Chair of Nano and Quantum Sensors
TUM School of Computation, Information and Technology
Technical University of Munich

Cavity optomechanics with hexagonal boron nitride mechanical resonators

PhD thesis

Irene Sánchez Arribas

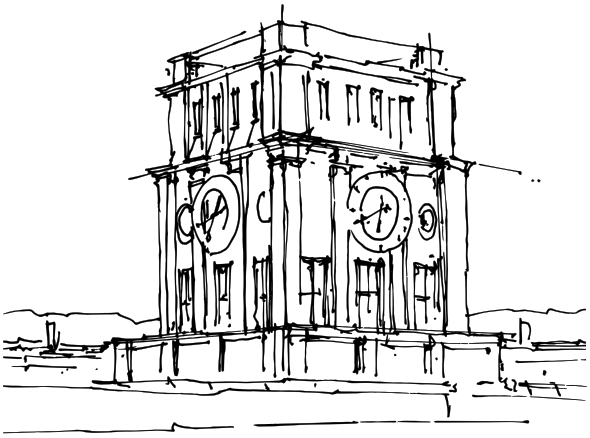

Technische Universität München
TUM School of Computation, Information and Technology

Cavity optomechanics with hexagonal boron nitride mechanical resonators

Irene Sánchez Arribas

Vollständiger Abdruck der von der TUM School of Computation, Information and Technology der Technischen Universität München zur Erlangung einer

Doktorin der Naturwissenschaften (Dr. rer. nat.)

genehmigten Dissertation.

Vorsitz:
Prof. Dr. Bernhard Wolfrum

Prüfer*innen der Dissertation:
1. Prof. Dr. Eva Weig
2. Prof. Dr. Elke Scheer

Die Dissertation wurde am 20.04.2023 bei der Technischen Universität München eingereicht und durch die TUM School of Computation, Information and Technology am 27.06.2023 angenommen.

A Julia, Chelo y Pepe.
A mi abuela.

Abstract

THE radiation pressure force, combined with an optical cavity, offers a tool to manipulate and control the mechanical motion of micro- and nanomechanical resonators. Bringing its backaction effects together with mechanical resonators capable of hosting optically active defects – like quantum emitters or spin qubits – which are susceptible to strain, could enable the realization of hybrid quantum devices. Some van der Waals materials, such as hexagonal boron nitride (hBN) or tungsten diselenide (WSe_2), fulfill these conditions. However, and until this day, the backaction from the radiation pressure force has not been observed with mechanical resonators made from van der Waals materials at optical wavelengths. Indeed, its effects were hidden by other more prominent forces like photothermal ones.

In this work, we demonstrate radiation pressure backaction effects on an hBN mechanical resonator at room temperature and in the telecom optical regime ($\lambda = 1550\,\mathrm{nm}$). The cavity optomechanical platform we present consists of a high finesse optical Fabry-Pérot microcavity. It is formed by two fiber mirrors facing each other and separated by a cavity length of $41\,\mu\mathrm{m}$. The empty cavity has a finesse as large as $\mathcal{F} = 194\,000$. We insert the mechanical resonator in the middle of the cavity, forming a membrane-in-the-middle optomechanical system. The hBN mechanical resonator is mechanically exfoliated and dry-transferred onto a hole patterned on a low-stress SiN stripe suitable to be inserted into the cavity. The hole serves as a circular frame for the hBN resonators. Before demonstrating the dynamical backaction effects, we characterize the mechanical response of the sample on a Michelson interferometer. We find that the mechanical modes of the hBN resonator and the heavier SiN stripe hybridize. Furthermore, we characterize the static optomechanical couplings of the system by placing the sample in the middle of the cavity and studying the dependence of the cavity resonance as a function of the sample's position. Finally, and for the first time, we explore the optical spring effect and optomechanical damping of an hBN mechanical resonator experimentally, reaching single-photon coupling strengths up to $g_0/2\pi = 1000\,\mathrm{Hz}$. The cavity optomechanics platform presented in this work unlocks a tool that will accelerate the research of emitter-optomechanics or spin-optomechanics with hBN and other van der Waals materials.

Zusammenfassung

Die Bewegung mikro- und nanomechanischer Resonatoren lässt sich mithilfe des Strahlungsdrucks eines Lichtfeldes manipulieren und steuern. In Resonatoren aus kristallinen Materialien können Materialdefekte als Quantenemitter oder Spin Qubits fungieren. Da viele dieser Defekte an die mechanische Spannung des Materials koppeln, würde eine Steuerung solcher mechanischer Resonatoren mit Strahlungsdruckkräften eine Vielzahl hybrider Quantenbauelemente ermöglichen. Einige van der Waals Materialien, wie z.B. hexagonales Bornitrid (hBN) oder Wolframdiselenid (WSe_2), können geeignete Defekte für Quantenanwendungen beherbergen. Bis heute ist jedoch keine Kontrolle mechanischer Resonatoren aus van der Waals Materialien mit Strahlungsdruckkräften gelungen, da in bisherigen Experimenten andere Einflüsse, z.B. photothermische Kräfte, dominieren.

In dieser Arbeit zeigen wir Strahlungsdruckrückwirkungskräfte auf einen mechanischen Resonator aus hBN bei Raumtemperatur bei der technisch relevanten Wellenlänge von $\lambda = 1550\,\text{nm}$. Die von uns vorgestellte Kavitätsoptomechanik-Plattform besteht aus einer durch zwei Faserspiegel gebildeten optischen Mikrokavität mit sehr hoher Finesse. Bei der leeren Kavität beträgt die Finesse $\mathcal{F} = 194\,000$. Wir setzen einen mechanischen Resonator aus hBN in die Mitte dieser Kavität ein, wodurch ein optomechanisches membrane-in-the-middle System ensteht. Den hBN Resonator stellen wir her, indem hBN exfoliert und auf eine gelochte, spannungsarme SiN Membran übertragen wird. Das Loch im SiN dient dabei als Rahmen für den hBN Resonator. Wir charakterisieren zunächst das mechanische Modenspektrum der Resonatoren mit einem Michelson-Interferometer und stellen fest, dass die Moden des hBN Resonators und der viel schwereren SiN Membran hybridisieren. Den so vorcharakterisierten Resonator platzieren wir anschließend in der Mitte der optischen Kavität und bestimmen die statische optomechanische Kopplung des Systems, die durch die Verschiebung der Resonanzfrequenz der optischen Kavität als Funktion der Position der Membran gegeben ist. Abschließend demonstrieren wir erstmals den “optical spring effect” und optomechanische Dämpfung an einem mechanischen hBN Resonator mit einer Einzelphotonenkopplungsstärke von bis zu $g_0/2\pi = 1000\,\text{Hz}$. Die in dieser Arbeit vorgestellte kavitäts-Optomechanik Plattform ermöglicht die Erforschung hybrider Quantenbauelemente, in denen die Materialdefekte in hBN oder anderen van der Waals Materialien mit den mechanischen Resonanzen und dadurch mit dem Lichtfeld wechselwirken.

Parts of this thesis have been published in the following article:

I. Sánchez Arribas, T. Taniguchi, K. Watanabe, E. M. Weig, *"Radiation pressure backaction on a hexagonal boron nitride resonator"*, Nano Lett. **23**, 6301–6307 (2023), Ref. [1].
The published work has been explicitly written by the author. Therefore, the thesis partly contains passages of the original publication.

Contents

1

Introduction

IMAGINE yourself lying on the grass in the English Garden in Munich on a sunny day. You will soon feel warm enough to perhaps consider jumping into the river. This happens because light is composed of electromagnetic waves that carry energy. Your body absorbs this energy, which is then transformed into heat. What will be harder for you to realize, actually impossible, is that the very same waves also carry momentum, exerting a force on you – pushing you! This force is called *radiation pressure force*, and the reason we don't feel it in our daily lives is because it is extremely weak. To give you an idea, the magnitude of the force the rays of the Sun exert on us is about 1 μN, similar to the force exerted by the weight of a grain of salt.

But someone did realize that light could push: Johannes Kepler. He observed that one of the two tails of a comet always points away from the Sun, and thus suggested in 1619 that the Sun's light could move the comet's particles away [2]. James C. Maxwell, with his theory of electromagnetism, developed the concept of light as being electromagnetic waves which carry momentum. In 1873, in his "A treatise on Electricity and Magnetism" [3, p. 792-793], he stated for the first time that the momentum transfer upon the reflection of light on a surface could lead to a radiation pressure force. Adolpho Bartoli arrived independently to a similar conclusion using thermodynamics principles in 1876 [4].

The first successful experimental demonstrations of radiation pressure came in 1900 by Peter N. Lebedew [5] and in 1901 by Ernest F. Nichols and Gordon F. Hull [6, 7]. Their experiments were done using a torsion balance and arc lamps as light sources, but the experimental errors were large[1] due in part to the weakness of the force, as well as to experimental difficulties. A technological revolution was necessary to increase the magnitude of the radiation pressure and hence its observable effects. This revolution happened in the 1960s and was the invention of the laser [10]. Since then, radiation pressure has enabled many applications, from the ability to hold micro and nanometer-size systems like bacteria [11] and DNA [12] with the use of optical tweezers, invented by Arthur Ashkin in the 70s [13], to the propulsion of spacecrafts with solar sails [14].

Around the same time Ashkin was developing the optical tweezers, Vladimir B. Braginsky studied the effects of radiation pressure when the electromagnetic radiation is confined within a hollow

[1] Initially, Nichols and Hull claimed an experimental error of only 1% with respect to Maxwell's predictions [6, 7]. Around thirty years later, the experiments from Alice Golsen [8] and Mary Bell and S. E. Green [9] highlighted that the experimental error from Nichols and Hull must have been around 10%.

metal box used as a microwave cavity. He focused on the particular case when one of the walls of the box is capable of moving around an equilibrium position, becoming then a mechanical oscillator [15, 16]. In his pioneer work, he demonstrated that the finite life time of the cavity leads to a retardation between the radiation pressure force and the actual position of the movable wall. These time lag effects make the force capable of extracting or giving energy to the mechanical resonator, in other words, capable of cooling or heating it. Interestingly, the cavity is at the same time a powerful and precise measurement tool of the resonator's motion. The field of research studying the interaction mediated by the radiation pressure force of an electromagnetic cavity and a mechanical resonator is called cavity optomechanics [17, 18]. This mature research field, which has been studied over three decades, has many-fold applications, such as the detection of weak signals like forces [19–22], masses [23] and accelerations [24]; the sensing of displacements with an imprecision below the standard quantum limit [25–27]; the cool down of a mechanical resonator to or close to its ground state [28, 29]; the manipulation of the quantum states of light [30]; the investigation of quantum gravity effects [31, 32]; the development of gravitational waves detectors [33–35]; or the realization of electro-opto-mechanical transducers [29, 36].

An approach to increase the optomechanical interaction is to reduce the mass of the mechanical oscillators, and therefore make them more susceptible to experience the radiation pressure force. The ultimate limit in reducing the mass of an oscillator is the atomic thickness. Indeed, there has been increasing efforts in performing optomechanical experiments with carbon nanotubes [37–40], nanowires [20] and van der Waals materials [41–44]. In this thesis we want to pursue this direction and study radiation pressure backaction effects on mechanical resonators made out of hexagonal boron nitride (hBN) – a type of van der Waals material – using a telecom cavity.

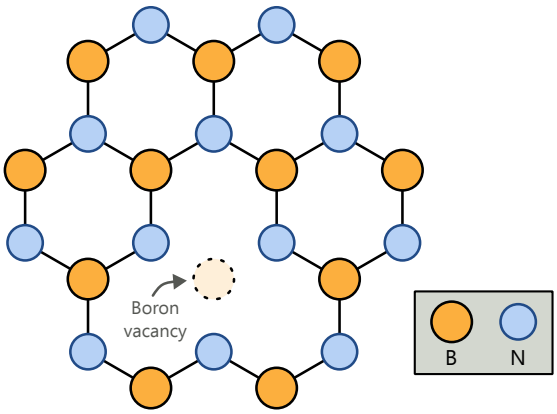

Figure 1.1: Illustration of the lattice structure of hexagonal boron nitride (hBN). Boron and nitrogen atoms are represented as orange and blue circles, respectively. The atomic bonds are depicted as black solid lines. The missing boron atom in the center illustrates a type of magnetically optically active defect, a negatively charged boron vacancy center (V_B^-).

Figure 1.1 depicts the atomic structure of a monolayer of hBN viewed from atop. It is composed of boron (B, orange circles) and nitrogen atoms (N, blue circles) arranged in a hexagonal lattice in a similar way to graphene. From the mechanics point of view, this layered crystal is an interesting material because of its large in-plane Young's modulus of 392 GPa [45] and breaking strain of 12.5 % [46]. These, together with the recent development of patterning methods [47, 48], have

opened the door to the engineering of mechanical resonators with high quality factors and tunable frequencies. On top of that, hBN is transparent in the visible and infrared part of the optical spectrum due to its wide bandgap of 6 eV [49], which makes it less prone to photothermal heating than other van der Waals materials like graphene. Indeed, photothermal forces, rather than radiation pressure, were responsible for the optomechanical backaction observed in other resonators made from van der Waals materials in the optical regime, limiting their performance so far [50–52].

But an even more interesting characteristic of this type of layered material is its large variety of single-photon emitters. They span from the UV to the low infrared part of the spectrum [53, 54] and are capable of operating at room temperature and even up to 800 K [55]. In addition, they are tunable via strain or electric fields [56–59], which adds new means of control of the emitters' properties. Over the past three years, several groups [60–62] have demonstrated optically detected magnetic resonance in negatively charged boron vacancy defects (V_B^-), together with coherent control of the spins [63, 64]. Such defects, illustrated as the missing boron atom in Figure 1.1, are also sensitive to strain [65, 66], and consequently could be coupled to the mechanical motion. One can envision a system composed of hBN where its mechanical motion interacts with the light field via radiation pressure and at the same time with the defects through strain gradients, realizing a hybrid quantum system [67–70]. A possible transduction scheme is illustrated in Figure 1.2a, which has been successfully implemented to couple telecom photons to spin qubits made of NV centers in diamond [71].

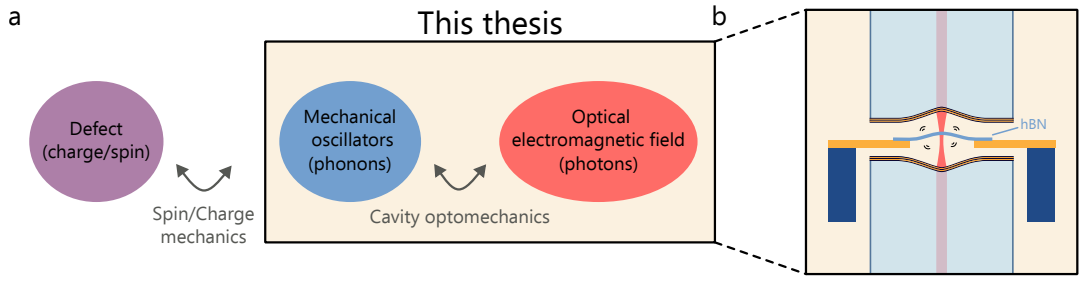

Figure 1.2: Towards hybrid quantum systems with hBN. (a) Schematic illustration of a possible transduction scheme between between telecom photons and the defects in hBN resonators. (b) Illustration of our experimental platform for cavity optomechanics with hBN resonators. The cavity is formed by two fiber mirrors facing each other. In the middle of the optical mode (red) we place an hBN mechanical resonator (blue).

In this work we focus on the right part of the transduction scheme and demonstrate the control and modification of the mechanical motion of hBN resonators through cavity optomechanics. Our experimental platform is illustrated in Figure 1.2b. It consists on a fiber-based optical microcavity operated at $\lambda = 1550\,\text{nm}$ with an hBN mechanical resonator placed in the middle of the cavity, forming a membrane-in-the-middle optomechanical system [72].

This thesis is structured as follows. Chapter 2 introduces the theoretical foundations necessary to understand the radiation pressure backaction effects for the particular case of a membrane-in-the-middle optomechanical system. In Chapter 3 we present and describe the experimental setup, which I constructed over the course of the first four years of my PhD. The first part contains

the details on the production of the fiber mirrors, the cavity assembly and cavity characterization, which is the core of the experiment. The second part is dedicated to the thermal and vibration stability of the experiment and to the locking scheme used to stabilize the cavity length. Chapter 4 focuses on the fabrication and mechanical characterization of the hBN resonators. Due to the geometrical constrains of the cavity, the hBN resonators have to be fabricated on top of a larger SiN membrane, which is also a mechanical oscillator itself. The mechanical modes of the two resonators hybridize, which we show at the end of Chapter 4. In Chapter 5, we present the full cavity optomechanical system. We first explore the optomechanical couplings by mapping the static properties of the radiation pressure interaction as a function of the position of the resonator within the optical cavity. We conclude the chapter by demonstrating the effects of the retarded radiation pressure force on the mechanical properties of the hBN mechanical resonator. Finally, in Chapter 6, we summarize the main achievements of this work and we discuss some possible improvements and directions for future experiments.

2

Cavity optomechanics

THIS thesis studies the interaction of an optical cavity with a mechanical membrane resonator, a *cavity optomechanical system*. Before diving into the experimental results, we need to establish the common language and terminology that I will employ in the rest of this thesis. This is the purpose of this chapter.

Three are the main theoretical concepts that I will summarize: the mechanical resonator, the optical cavity and finally their interaction when the mechanical resonator is incorporated in the middle of the cavity (cavity optomechanics). The three are well-established fields of research, and are explained in extreme detail in many textbooks and research articles. To avoid repetitions, I decided to introduce them here in the most pedagogical way I could find, keeping the necessary level of completeness to faithfully cover the topics relevant to this thesis. If the reader is looking for a careful and thorough mathematical treatment, here is the literature I found most instructive: for the mathematical treatment of non-noisy and noisy signals in the time and frequency domain, Refs. [73, 74]; the concept of harmonic oscillator and mechanical resonators, Refs. [75, 76]; the basics on optical cavities and optical modes, Refs. [77, 78]; and the fundamentals on cavity optomechanics, Refs. [17, 18].

2.1 Mathematical definitions

Let $x(t)$ be a time-dependent physical process, for example, the time varying amplitude of a guitar string, or the electrical signal generated by a photodetector upon arrival of laser light. In the lab, we could directly measure this time dependence by using, for instance, an oscilloscope. However, sometimes it is more convenient to work with the frequency domain representation of the signal, $x(\omega)$. The time and frequency domain are related by the Fourier theory. Here we use the convention adopted in the optomechanics community for the Fourier transform of the signal $x(t)$ [17, 79],

$$\mathcal{F}[x(t)](\omega) = x(\omega) = \int_{-\infty}^{\infty} x(t) e^{i\omega t}\, dt, \tag{2.1}$$

with $\omega = 2\pi f$ the angular frequency and $i \in \mathbb{C}$ the imaginary unit. Recall here that $x(\omega)$ has units of $x(t)$ per Hertz. The inverse Fourier transform is then

$$\mathcal{F}^{-1}[x(\omega)](t) = x(t) = \int_{-\infty}^{\infty} x(\omega) e^{-i\omega t}\, \frac{d\omega}{2\pi}. \tag{2.2}$$

Spectrum analyzers are in this case the devices used in laboratories to measure the Fourier transform of $x(t)$, i.e. its frequency spectrum $x(\omega)$.

The beauty of working in the frequency domain is that the convolution integral of time domain methods is replaced by a simple multiplication, making calculations often simpler. Let's see when this can become handy: imagine a linear system having one input and one output, where $x(t)$ is the input signal and $y(t)$ the output. $y(t)$ could be, for instance, the displacement of a mechanical resonator from its equilibrium position when experiencing a force $x(t)$. Assuming the system to be time-invariant, then the two are related via the system's impulse response $h(t)$ [80]

$$y(t) = \int_{-\infty}^{\infty} x(t)h(t-t')\,dt'. \tag{2.3}$$

This integral equation might look a little complicated. If we compute the Fourier transform, we get

$$y(\omega) = h(\omega)x(\omega), \tag{2.4}$$

where we refer to $h(\omega)$ as the system's frequency response. Equation 2.4 suggests that if we find a way to measure $y(\omega)$ for a controlled and known input $x(\omega)$ we can compute $h(\omega)$, and from then on predict any output of the system for a new, completely different type of input as long as we can compute its Fourier transform $x(\omega)$. This is very useful, and devices like the Vector Network Analyzer are constantly used in labs to measure $h(\omega)$.

But, what happens when we *cannot* compute the Fourier transform of $x(t)$? This is a very common problem as many processes are random in nature, like noisy signals, making it impossible[1] to calculate $x(\omega)$. Actually, this is of crucial importance for this thesis, as most of the experiments are carried out on mechanical resonators whose motion is driven by a fluctuating random force. Therefore, one has to find another way to treat those signals in the frequency domain. We circumvent this problem mathematically[2] by defining the *power spectral density* (PSD) $S_{xx}(\omega)$ of a sample function $x(t)$ as the expected value of the Fourier transform [73]

$$S_{xx}(\omega) = \lim_{T\to\infty} \frac{E[|x_T(\omega)|^2]}{2T}, \tag{2.5}$$

where $x_T(\omega)$ is the Fourier transform of $x(t)$ evaluated over the time interval $-T < t < T$ (also called gated Fourier transform[3]) . $E[|x_T(\omega)|^2]$ denotes the expected value of $|x_T(\omega)|^2$, i.e. the average of $|x_T(\omega)|^2$ over many independent experimental runs. One can think of the PSD as the noise power density per unit of frequency.

It can be shown that the power spectral density follows a relation similar to Eq. 2.4 [73]:

$$S_{yy}(\omega) = |h(\omega)|^2 S_{xx}(\omega). \tag{2.6}$$

[1] The time function of a stationary random process is not absolutely integrable, and therefore is not Fourier transformable [73].

[2] We assume an ergodic process (and therefore stationary), which means that the ensemble properties can be measured by time averaging long enough, and the statistical properties are time independent. We also assume a process of finite intensity [73].

[3] The gated Fourier transform is equivalent to defining a new sample function $x_T(t)$ such as $x_T(t) = 0$ if $|t| > T$ and $x_T(t) = x(t)$ otherwise [73].

Once we know the power transfer function of our system $|h(\omega)|^2$, we can also predict how it will behave under a noisy input with a given power spectral density. We remark that S_{xx} is defined for both positive and negative frequencies and is commonly referred in the literature as *double-sided PSD*. If $x(t)$ is real-valued, like most physical signals, then one can define the *single-sided PSD* $S_x(\omega)$

$$S_x(\omega) = 2S_{xx}(\omega), \quad \omega > 0, \tag{2.7}$$

which is the one we will employ here.

Another useful property of a stationary random process is that the time average of the mean-square value $\langle\overline{x^2(t)}\rangle$ is equal to the mean-square value of $x(t)$, $\overline{x^2(t)}$, and is related to the PSD in the following way [73]:

$$\langle\overline{x^2(t)}\rangle = \overline{x^2(t)} = \int_0^\infty S_x(\omega)\frac{d\omega}{2\pi}. \tag{2.8}$$

where we have introduced the notation for the mean-square value $\overline{x^2(t)} = E[x^2(t)]$. Equation 2.8 is very relevant for this work because it states that we can calculate the mean-square of a random process by computing the area under the PSD, which is experimentally accessible.

2.2 Mechanical resonators

The heart of this thesis consists on fabricating mechanical resonators at the nanometer scale and making them interact with light. Specifically, we use a set of two-dimensional resonators called *membranes*. The every-day example would be the membranes from the acoustic drums. We say that they are two-dimensional because the thickness of the membrane is orders of magnitude smaller than its lateral dimension, i.e., these devices have a large aspect-ratio. In this section we start by explaining the simplest resonator, the one-dimensional harmonic oscillator. We continue studying how, even in the absence of any external active forces, the resonator's motion is always driven by the fluctuations of the environment. We finish by describing the real 2D motion of the membranes and how we can map it into a set of individual harmonic oscillators, conveniently simplifying our system.

2.2.1 One-dimensional damped harmonic oscillator

The harmonic oscillator is a physics model representing a system that, when displaced from its equilibrium position, experiences a restoring force $F(t)$ proportional to the displacement $z(t)$, following Hooke's law $F(t) = -kz(t)$. The simplest harmonic oscillator is a mass on a spring of stiffness k (Fig. 2.1). Many phenomena in nature can be modeled as harmonic oscillators: bungee jumping, the vibrations of a diving board, an electron rotating around the nucleus of an atom... This makes the harmonic oscillator one of the most used toy models in physics.

Our mechanical resonators are very well represented as harmonic oscillators when vibrating with small amplitudes and when the resonator's mechanical modes are isolated[4]. If they would only experience the restoring force, they would oscillate forever around the equilibrium position, since

[4]Isolated here means that the mechanical resonances are far apart such that there is no spectral overlap between mechanical modes.

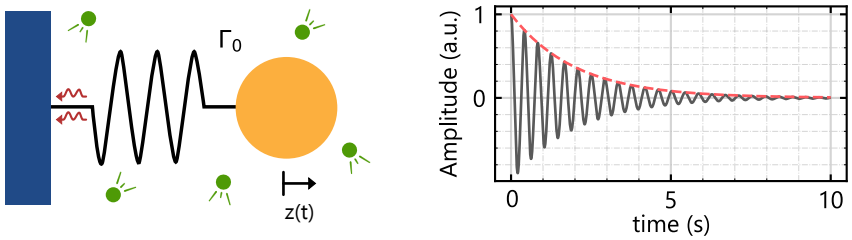

Figure 2.1: Non-driven damped harmonic oscillator. Illustration of a non-driven damped harmonic oscillator represented as a mass (orange) on a spring (black). The oscillator is damped via radiation to the substrate (red wavy arrows) and the random impacts of gas molecules, represented as green beads. The right graph shows in gray the amplitude decay of the resonator $z(t)$ as a function of time once displaced from its equilibrium position (Eq. 2.10 with $\Omega_0 = 15\,\mathrm{rad\,Hz}$ and $\Gamma_0 = 1\,\mathrm{rad\,Hz}$) . The red dashed line depicts the exponential decay $\exp(-\Gamma_0 t/2)$.

there is no mechanism for them to loose energy. In reality, there is a plethora of damping mechanisms – e.g. bending losses, radiation to the substrate[5], and gas damping among others [76, 81] – that dissipate the energy of the resonator [82].

Let $z(t)$ represent the time-dependent amplitude of the damped vibrational mode, m its effective mass, and Γ_0 the energy decay rate (assumed frequency independent here[6]). The differential equation of motion reads

$$m\ddot{z}(t) + \Gamma_0 \dot{z}(t) + m\Omega_0^2 z(t) = F(t), \tag{2.9}$$

where we have included an external force $F(t)$ that drives the resonator and $\Omega_0 = \sqrt{k/m}$ the resonator's natural frequency. The effective mass accounts for having a continuum mechanical structure instead of a point mass, and can be calculated by equating the kinetic energy of the mechanical structure to the potential energy that a point mass m would have [76]. For example, the effective mass of the fundamental mode of a circular membrane is approximately a quarter of its physical mass m_0, $m = 0.27 m_0$ [75].

Let's solve Eq. 2.9 first for the particular case when $F(t) = 0$, i.e. the mode is undriven. We also consider a vibrational mode whose resonance frequency is several orders of magnitude larger than its amplitude decay rate, $\Omega_0 \gg \Gamma_0/2$ – the resonators we use in this work satisfy this condition, with typically $\Omega_0/\Gamma_0 > 1000$. In that case, one can solve Eq. 2.9 easily and obtain the vibrational mode's time dependent amplitude response

$$z(t) = z_0 \exp\left(-\frac{\Gamma_0 t}{2}\right) \cos\left(t\Omega_0 \sqrt{1 - \Gamma_0^2/(4\Omega_0^2)}\right), \tag{2.10}$$

where z_0 is the amplitude of the oscillations at $t = 0$. We can see that the system oscillates around its equilibrium position, here set at 0, but its amplitude decays exponentially in time at a rate $\Gamma_0/2$ (Fig. 2.1). In most of the literature, instead of the energy decay rate, one uses the dimensionless quality factor Q. The latter can be approximated as $Q = \Omega_0/\Gamma_0$ for $\Omega_0 \gg \Gamma_0/2$.

[5] Also commonly referred to as clamping losses [76].

[6] The frequency dependence, if there is any, of the different types of damping is diverse. The reader is referred to Refs. [81, 82] for an extensive study.

Solving Eq. 2.9 for a specific driving force $F(t)$ is generally difficult in the time domain. However, as explained in Section 2.1, we can use the Fourier transform to make these calculations easier, obtaining

$$m\left[(\Omega_0^2-\omega^2)+i\Gamma_0\omega\right]z(\omega)=F(\omega). \tag{2.11}$$

Following Eq. 2.4, the amplitude's frequency response then reads

$$z(\omega)=\frac{1}{m\left[(\Omega_0^2-\omega^2)+i\Gamma_0\omega\right]}F(\omega)=\chi_m(\omega)F(\omega). \tag{2.12}$$

where we have introduced the *mechanical susceptibility*, $\chi_m(\omega)$.

Finally, we introduce the concept of *zero-point fluctuations* z_{zpf} of a quantum harmonic oscillator

$$z_{\mathrm{zpf}}=\sqrt{\frac{\hbar}{2m\Omega_0}}, \tag{2.13}$$

which is the minimum amplitude of the resonator when it is at its lowest possible energy[7], i.e. in the quantum ground state [79].

2.2.2 Thermal noise

Even in the absence of any external active forces actuating the mechanical resonator (for example, a piezo shaking the sample), it moves. This motion occurs because the resonator is coupled through the dissipation mechanisms to, and in thermal equilibrium with the environment, which is at a non-zero temperature T_{bath}. For example, in case of gas damping, the resonator looses energy due to the random collisions with the gas molecules. These random collisions also lead to a fluctuating force F_{th} that drives the motion of the resonator. Any fluctuations associated with a particular dissipation channel will lead to a force whose power spectral density is given by, using the *fluctuation-dissipation theorem* [83]

$$S_{F_{\mathrm{th}}}=\frac{4k_BT_{\mathrm{bath}}}{\omega}\,\mathrm{Im}\left(\chi_m(\omega)\right)=4mk_BT_{\mathrm{bath}}\Gamma_0, \tag{2.14}$$

where k_B is the Boltzmann constant. We highlight that the dissipation mechanism is hidden in $\mathrm{Im}\left(\chi_m(\omega)\right)=m\Gamma_0\omega$, different damping processes will have different forms of Γ_0 [82, 84]. Since we have assumed Γ_0 is frequency-independent, the thermal force is spectrally flat.

We have just found a way to express the power spectral density of the random force driving our mechanical resonators. Recalling the definitions of power spectral densities, we can recover the displacement power spectrum of a resonator driven by a thermal noise,

$$S_z(\omega)=|\chi_m(\omega)|^2S_{F_{\mathrm{th}}}=\frac{4k_BT_{\mathrm{bath}}\Gamma_0}{m\left(\left(\Omega_0^2-\omega^2\right)^2+\Gamma_0^2\omega^2\right)}. \tag{2.15}$$

[7] Strictly speaking it is the root-mean square zero-point uncertainty of the mechanical ground state wave function.

If we look at a frequency range close to the resonance frequency ($\omega \sim \Omega_0$) and assume $\Gamma_0 \ll \Omega_0$, Eq. 2.15 can be simplified to a Lorentzian with full width at half maximum (FWHM) Γ_0

$$S_z(\omega) \simeq \frac{k_B T_{\text{bath}} \Gamma_0}{m\Omega_0^2 \Big(\big(\omega - \Omega_0\big)^2 + \big(\Gamma_0/2\big)^2 \Big)}. \tag{2.16}$$

We can make use of the equations derived in Section 2.1 and compute the mean-squared displacement of the resonator

$$\langle \overline{z^2(t)} \rangle = \int_0^\infty S_z(\omega) \frac{d\omega}{2\pi} = \frac{k_B T_{\text{bath}}}{m\Omega_0^2}. \tag{2.17}$$

Its root-mean square (rms) displacement is then

$$z_{\text{rms}} = \sqrt{\frac{k_B T_{\text{bath}}}{m\Omega_0^2}}, \tag{2.18}$$

which represents the average amplitude of the oscillations of a mechanical resonator driven by thermal noise.

2.2.3 Modal analysis of two-dimensional resonators

In the previous section we have assumed our resonators (or one of its degrees of freedom) can be simplified as a harmonic oscillator: a point mass oscillating around its equilibrium position. But real resonators, like a drum-head or a guitar string, are continuous bodies, with a volume, that can move in many ways. If we are interested in the mode shapes and want to predict the resonance frequencies, we need to solve the equation of motion for each particular geometry.

Membranes are two-dimensional mechanical resonators whose vibrational properties are dominated by their in-plane tension N. This can occur either when the membrane is thin enough[8] so that the bending rigidity is negligible or when it has a very high in-plane tension. On the other hand, when the bending rigidity dominates the mechanical behavior, we refer to the resonator as *plate*.

Let's consider an undamped membrane of thickness d_m and arbitrary geometry. Its surface lies in the xy plane and it has an in-plane tension given by $N = \sigma d_m$, where σ is the in-plane stress. The membrane is oscillating along the z direction (shown on left side of Fig. 2.2), with a time-dependent *out of plane* deflection represented by a function $a(x, y, t)$. The equation of motion of $a(x, y, t)$ is given by the two-dimensional wave equation

$$\nabla^2 a - \frac{\rho}{\sigma} \frac{\partial^2 a}{\partial t^2} = 0, \tag{2.19}$$

where ∇^2 is the two-dimensional Laplacian operator and ρ the physical density of the membrane, and where we have neglected the membrane's bending rigidity [75]. Equation 2.19 is usually solved by separating the spatial and time components, $a(x, y, t) = \sum_n u_n(x, y) z_n(t)$. In the latter we have reflected that the total deflection can be decomposed as a sum of an infinite number

[8] Thin enough means that the membrane's thickness d_m is way smaller than its lateral dimensions ($d_m \ll L_x, L_y$).

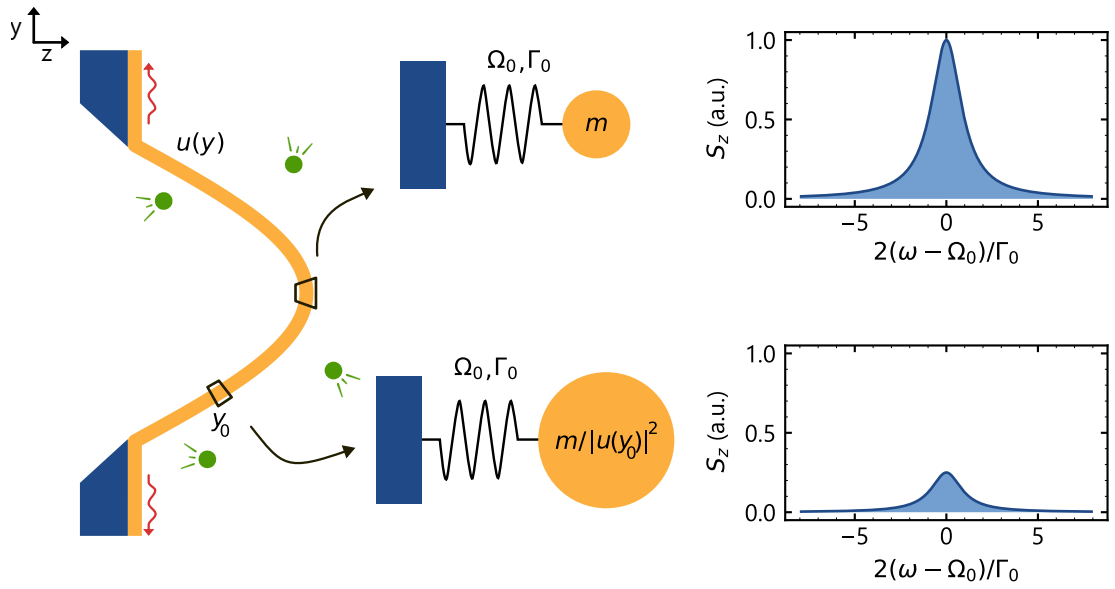

Figure 2.2: Mapping a two-dimensional motion into individual harmonic oscillators. Cross section of a SiN membrane (orange) that is oscillating along the z axis with a mode profile $u(y)$. The membrane is damped by gas molecules (green beads) and the radiation to the substrate (red wavy arrows) with a total damping rate Γ_0. The point of maximum deflection is mapped into a harmonic oscillator with effective mass m and PSD S_z. A position with $u(y_0) = 0.5$ would be mapped into a harmonic oscillator of $m' = 4m$ and hence have a PSD four times smaller.

of independent modes, where the mode shape information of each one resides in $u_n(x, y)$ and its time dependence in $z_n(t)$. By selecting the coordinate system in a smart way and imposing clamped boundary conditions [75], we can solve Eq. 2.19 for a variety of membrane geometries and obtain the discrete resonance frequencies Ω_n, mode shapes $u_n(x, y)$ and time dependencies $z_n(t)$. The solution to the temporal part of Eq. 2.19 is the one of an undamped harmonic oscillator $z_n(t) = z_{\mathrm{n,max}} \cos(\Omega_n\, t)$, with $z_{n,\mathrm{max}}$ the maximum amplitude.

In this thesis, we normalize the mode shapes $u_n(x, y)$ so that the maximum of its absolute value is unity. With this convention, the mode shapes $u_n(x, y)$ are unitless, implying that $z_n(t)$ has units of distance and corresponds to the resonator's real displacement [75]. That means, a mode with a displacement of z_{max} at the point of maximum deflection, will have a deflection $a_n(x_{\mathrm{max}}, y_{\mathrm{max}}, t) = z_{\mathrm{max}} \cos(\Omega_n\, t)$. The amplitude a_n will be smaller by a factor of $u_n(x_0, y_0)$ at any other point (x_0, y_0). Interestingly, we can see that at each position the mode behaves like a harmonic oscillator – we have reduced our 2D problem into a single degree of freedom. This normalization condition and its implication for our measurements are illustrated in Figure 2.2.

We could complicate the situation a bit more and imagine that the membrane is damped and driven by a thermal force. We would need to include those terms into Eq. 2.19. Due to the separation of variables, we will obtain the same solution for the mode shapes. In this case, the time evolution $z(t)$ will be given by the one of a thermally driven damped harmonic oscillator, that we derived in Section 2.2.1, and will have an associated PSD $S_z(\omega)$. However, even if $z_n(t)$ is the same

for all points on the membrane, one would expect $S_z(\omega)$ to depend on the membrane's position because the amplitude does. We therefore need some other quantity carrying the mode shape information within $S_z(\omega)$. For that, we introduce the definition of the effective mass at a particular point (x_0, y_0):

$$m(x_0, y_0) = \frac{\int \rho(x, y, z)|u_n(x, y)|^2 \, dxdydz}{|u_n(x_0, y_0)|^2}. \tag{2.20}$$

We can see that for a particular mode, the effective mass is the lowest at the point of maximum deflection ($|u_n(x, y)| = 1$). This is due to the chosen normalization condition.

In the following we summarize the solution to the wave equation for the resonator geometries relevant to this thesis: rectangular and circular membranes, and circular plates.

Rectangular membranes

The resonance frequency of the (m, n) modes of a rectangular membrane of lateral dimensions L_x and L_y are given by

$$\Omega_{mn}/2\pi = \frac{1}{2}\sqrt{\frac{\sigma}{\rho}\left[\left(\frac{m}{L_x}\right)^2 + \left(\frac{n}{L_y}\right)^2\right]}, \tag{2.21}$$

with $m, n = 1, 2, 3...$ [75]. Their mode shapes are

$$u_{mn}(x, y) = \sin\left(\frac{m\pi x}{L_x}\right)\sin\left(\frac{n\pi y}{L_y}\right), \tag{2.22}$$

where we use the normalization condition so that $|u_{mn}(x, y)|$ has a maximum value of unity. Figure 2.3a shows the first 3 modes of a rectangular membrane.

Circular membranes

The resonance frequency of the (m, n) modes of a circular membrane of radius r_0 are given by

$$\Omega_{mn}/2\pi = \frac{\alpha_{mn}}{2\pi r_0}\sqrt{\frac{\sigma}{\rho}}, \tag{2.23}$$

with $m = 0, 1, 2, ...$ and $n = 1, 2, ...$[75]. The mode shapes in polar coordinates (s, ϕ) are

$$u_{mn}(s, \phi) = K_m \cos(m\phi) J_m\left(\frac{\alpha_{mn} s}{r_0}\right), \tag{2.24}$$

where K_m is a normalization constant selected so that the maximum of $|u_{mn}(s, \phi)|$ is unity, J_m denotes the m^{th} Bessel function of the first kind and α_{mn} is a number determined from the solutions to $J_m(\alpha_{mn}) = 0$. Figure 2.3b depicts the first 6 different modes of a circular membrane. The values of α_{mn} can be found in Ref. [75].

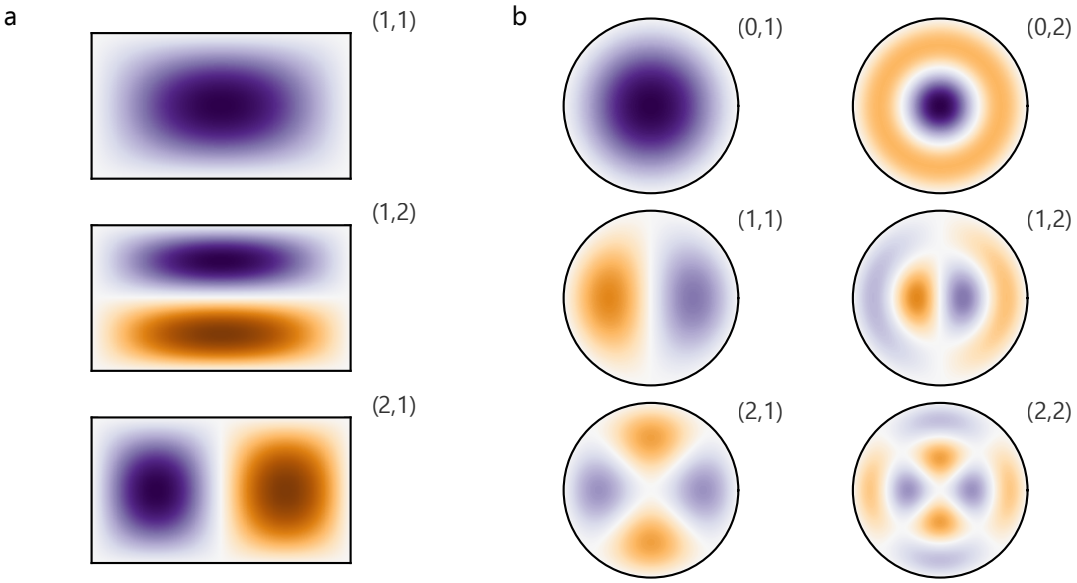

Figure 2.3: Membrane mode shapes. (a) Rectangular membrane modes (Eq. 2.22). (b) Circular membrane modes (Eq. 2.24). In both cases, the mode number (m, n) is specified on the top right corner of each mode shape. Dark orange and dark purple depict areas with high amplitude but opposite phase.

Circular plates

The mechanical behavior of plates is governed by the bending rigidity. Equation 2.19 is no longer valid and takes now the form

$$\nabla^2(\nabla^2 a) - \frac{\rho}{D}\frac{\partial^2 a}{\partial t^2} = 0, \tag{2.25}$$

where $D = \dfrac{E d_m^3}{12(1-\nu^2)}$ is the bending rigidity, E the Young's modulus and ν the Poisson ratio[76]. The resonance frequencies are given by

$$\Omega_{mn}/2\pi = \frac{\alpha_{mn}}{2\pi r_0^2}\sqrt{\frac{D}{d_m \rho}}, \tag{2.26}$$

where the values of the mode dependent constants α_{mn} can be found in Ref. [76].

2.3 Optical cavity

An optical cavity is a three-dimensional resonator containing electromagnetic waves in the optical domain that reflect back and forth between the resonator's walls. If the waves traveling inside the cavity can be approximated as plane waves, the study of their propagation can be reduced from a three- to a one-dimensional problem. In Section 2.3.1 we introduce the concept of transfer matrices, a mathematical formalism used to derive the amplitude of plane waves propagating through different media. This powerful tool allows us to understand the interference phenomena occurring inside the cavity. In particular, in Section 2.3.2 we will use it to introduce the concept

of a Fabry-Pérot optical cavity and derive its resonance frequencies, together with the reflected, transmitted and circulating optical fields.

2.3.1 Transfer matrix formalism

The transfer matrix (TM) method is a tool to derive the field amplitudes of an electromagnetic plane wave traveling through an interface, a single medium or a set of them [85, 86]. Each medium is considered to be a planar layer of finite thickness and perfectly-smooth infinite surface that lies in the xy plane. Here, we will only consider the electric field and assume that it propagates along the z direction, perpendicular to the layer's or interface's surface (case of normal incidence). Let's

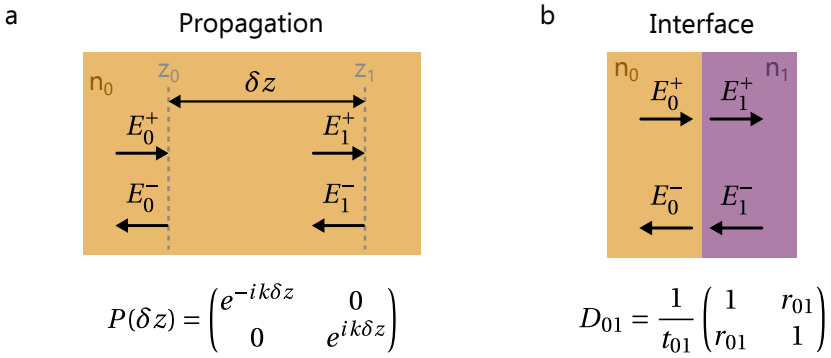

Figure 2.4: Transfer matrix of plane waves through a layered system. (a) Propagation matrix $P(\delta z)$ of a plane wave of wave number k traveling a distance δz through a medium with refractive index n_0. (b) interface matrix D_{01} of plane wave crossing an interface between two media of different refractive index, n_0 and n_1. The coefficients r_{01} and t_{01} are the Fresnel reflection and transmission amplitude coefficients.

start with the simplest case, a plane wave traveling along a single medium (Fig. 2.4a). The plane wave $E(z)$ at z_0 will be given by a forward and backward traveling wave with field amplitudes E_0^+ and E_0^-, respectively,

$$E(z_0) = E_0 = E_0^+ e^{ikz_0} + E_0^- e^{-ikz_0}, \tag{2.27}$$

where $k = 2\pi n/\lambda$ is the wave number, n the medium's *complex* refractive index and λ the wavelength in vacuum. The imaginary part of the refractive index accounts for any optical losses in the medium. From now on we will always assume the refractive index is complex unless stated otherwise. The above expression results in a complex-valued electric field; the real electric field at a particular time t and position z will be given by $E(z,\,t) = \mathrm{Re}\left[E(z)e^{-i\omega t}\right]$. At another position $z_1 = z_0 + \delta z$, the plane wave will be

$$\begin{aligned} E(z_1) &= E_0^+ e^{ikz_1} + E_0^- e^{-ikz_1} \\ &= E_0^+ e^{ik\delta z} e^{ikz_0} + E_0^- e^{-ik\delta z} e^{-ikz_0} \\ &:= E_1^+ e^{ikz_0} + E_1^- e^{-ikz_0} = E_1. \end{aligned} \tag{2.28}$$

The amplitude of the fields at each position are linked through a matrix equation:

$$\begin{pmatrix} E_0^+ \\ E_0^- \end{pmatrix} = \begin{pmatrix} e^{-ik\delta z} & 0 \\ 0 & e^{ik\delta z} \end{pmatrix} \begin{pmatrix} E_1^+ \\ E_1^- \end{pmatrix} = P(\delta z) \begin{pmatrix} E_1^+ \\ E_1^- \end{pmatrix}. \tag{2.29}$$

where we have introduced $P(\delta z)$, the *propagation matrix* for a distance δz.

We can do the same thing to relate the amplitudes of the fields upon reflection and transmission through an interface (Fig. 2.4b). First, let's remind ourselves the expressions of the Fresnel reflection r_{ij} and transmission t_{ij} amplitude coefficients for a wave propagating from the i^{th}- to the j^{th}-medium [78]

$$r_{ij} = \frac{n_i - n_j}{n_i + n_j}, \quad t_{ij} = \frac{2n_i}{n_i + n_j}. \tag{2.30}$$

Then, the field amplitudes in the left medium (n_0), are related to the ones in the right medium (n_1) through

$$\begin{aligned} E_1^+ &= E_0^+ t_{01} + E_1^- r_{10} \\ E_0^- &= E_0^+ r_{01} + E_1^- t_{10}, \end{aligned} \tag{2.31}$$

which can be reformulated in matrix notation as[9]

$$\begin{pmatrix} E_0^+ \\ E_0^- \end{pmatrix} = \frac{1}{t_{01}} \begin{pmatrix} 1 & r_{01} \\ r_{01} & 1 \end{pmatrix} \begin{pmatrix} E_1^+ \\ E_1^- \end{pmatrix} = D_{01} \begin{pmatrix} E_1^+ \\ E_1^- \end{pmatrix}. \tag{2.32}$$

In the last expression we have introduced the *interface matrix* D_{01} between layer 0 and 1. The interface and propagation matrices are the two building blocks from the transfer matrix formalism. For normal incidence, the transmission and reflection power coefficients are given by [78]

$$\mathcal{R}_{01} = |r_{01}|^2, \quad \mathcal{T}_{01} = \frac{n_1}{n_0} |t_{01}|^2. \tag{2.33}$$

Now, we can construct the matrix M of a system composed of N layers, numbered from 0 to $N-1$, where the first and last one are semi-infinite

$$\begin{pmatrix} E_0^+ \\ E_0^- \end{pmatrix} = D_{01} P(\delta z_1) D_{12} ... P(\delta z_{N-2}) D_{N-2N-1} \begin{pmatrix} E_{N-1}^+ \\ E_{N-1}^- \end{pmatrix} = M \begin{pmatrix} E_{N-1}^+ \\ E_{N-1}^- \end{pmatrix}. \tag{2.34}$$

We recall that computing M is straightforward when we know the refractive indices and thicknesses of each of the layers. Then, one can compute each of the matrix elements from the transfer matrix of the system M

$$M = \begin{pmatrix} M_{00} & M_{01} \\ M_{10} & M_{11} \end{pmatrix}, \tag{2.35}$$

from which one can extract the reflection and transmission amplitude coefficients of the composed system,

$$r = \left.\frac{E_0^-}{E_0^+}\right|_{E_N^-=0} = \frac{M_{10}}{M_{00}}, \quad t = \left.\frac{E_{N-1}^+}{E_0^+}\right|_{E_N^-=0} = \frac{1}{M_{00}}. \tag{2.36}$$

The power coefficients are therefore

$$\mathcal{R} = |r|^2, \quad \mathcal{T} = \frac{n_{N-1}}{n_0} |t|^2, \tag{2.37}$$

[9] Using $r_{10} = -r_{01}$ and $t_{01} t_{10} - r_{01} r_{10} = 1$

and satisfy the conservation of energy in case of a lossless system $\mathcal{R}+\mathcal{T}=1$. If the system had any losses $\mathcal{L}$, then the conservation of energy would be $\mathcal{R}+\mathcal{T}+\mathcal{L}=1$. Equation 2.35 can be reformulated using Eq. 2.36, obtaining

$$M=\frac{1}{t}\begin{pmatrix}1 & -r\\ r & t^2-r^2\end{pmatrix}. \tag{2.38}$$

We can use this formalism to derive the reflection and transmission coefficients of a dielectric slab or *membrane* of thickness d_m and refractive index n_m embedded in vacuum ($n_0=1$) [87]. In this case, they read

$$r_m=\frac{(1-n_m^2)\sin(kn_md_m)}{2in_m\cos(kn_md_m)+(n_m^2+1)\sin(kn_md_m)}, \tag{2.39}$$

$$t_m=\frac{2in_m}{2in_m\cos(kn_md_m)+(n_m^2+1)\sin(kn_md_m)}. \tag{2.40}$$

Figure 2.5 shows the amplitude coefficients (Eq. 2.39 and Eq. 2.40) for a membrane made of hBN for different membrane thicknesses and $\lambda=1550\,\mathrm{nm}$.

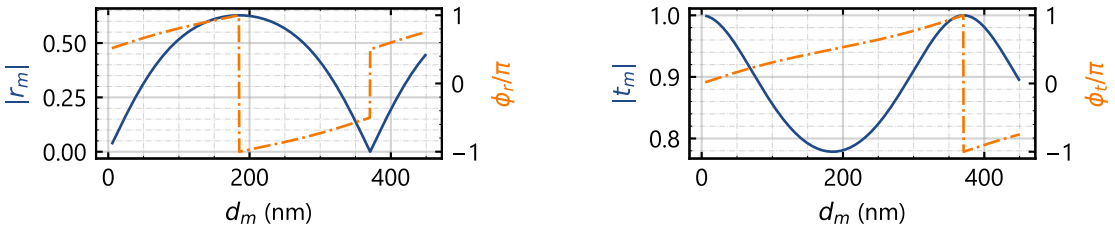

Figure 2.5: Amplitude coefficients of an hBN membrane versus membrane thickness $\mathbf{d_m}$. Magnitude (blue) and phase (orange) of the reflection and transmission amplitude coefficients, $r_m=|r_m|e^{i\phi_r}$ and $t_m=|t_m|e^{i\phi_t}$, for an hBN membrane at $\lambda=1550\,\mathrm{nm}$. The refractive index from hBN is $n_m=2.1$ [88].

Another interesting example is the one of a distributed Bragg reflector (DBR). The derivation of the coefficients r_{DBR} and t_{DBR} can be found in Appendix A. A DBR consists of N layer pairs sputtered on a substrate with refractive index n_s. Each layer has a thickness $d_i=\lambda n_i/4$, with $i=\{1,2\}$. Assuming the material sputtered first after the substrate is the one with the highest refractive index, $n_1>(n_2,n_s)$, the transfer matrix takes the form

$$M=\frac{(-1)^N}{i|t_{\mathrm{DBR}}|}\begin{pmatrix}1 & -|r_{\mathrm{DBR}}|\\ |r_{\mathrm{DBR}}| & -1\end{pmatrix}. \tag{2.41}$$

2.3.2 Fabry-Pérot cavity

Resonance condition via Transfer matrix

A Fabry-Pérot cavity is an optical resonator composed of two reflective mirrors separated by a distance L_{cav}, which is illustrated in Figure 2.6a. Here, we are going to assume that the mirrors are highly-reflective DBRs, both with the same even number of layer pairs, sputtered on the same substrate and with small, non-equal losses $\mathcal{L}_i$, which is the case that concerns this thesis. The

losses at each mirror are related to the transmission and reflection power coefficients through $\mathcal{L}_i = 1 - \mathcal{R}_i - \mathcal{T}_i$. Then, we can derive cavity's transfer matrix M_{cav}

$$M_{\text{cav}} = \frac{1}{i|t_{\text{DBR},1}|}\begin{pmatrix} 1 & -|r_{\text{DBR},1}| \\ |r_{\text{DBR},1}| & -1 \end{pmatrix}\begin{pmatrix} e^{-i\delta} & 0 \\ 0 & e^{i\delta} \end{pmatrix}\frac{1}{i|t_{\text{DBR},2}|}\begin{pmatrix} 1 & -|r_{\text{DBR},2}| \\ |r_{\text{DBR},2}| & -1 \end{pmatrix}, \tag{2.42}$$

where we have introduced $\delta = kL_{\text{cav}}$. Changing the notation for convenience to $r_i = |r_{\text{DBR,i}}|$ and $t_i = |t_{\text{DBR,i}}|$, and using Eq. 2.36 we obtain the cavity reflection and transmission coefficients

$$r_{\text{cav}} = \frac{E_0^-}{E_0^+} = \frac{r_1 - r_2 e^{2i\delta}}{-1 + r_1 r_2 e^{2i\delta}}, \tag{2.43}$$

$$t_{\text{cav}} = \frac{E_t^+}{E_0^+} = \frac{t_1 t_2 e^{i\delta}}{-1 + r_1 r_2 e^{2i\delta}}. \tag{2.44}$$

Once we have computed M_{cav}, we can reuse the transfer matrix formalism to calculate the amplitude of the field circulating inside the cavity, also known as intracavity field. The field amplitudes on the right side of the left mirror are related to the amplitudes after the output mirror

$$\begin{pmatrix} E_c^+ \\ E_c^- \end{pmatrix} = \begin{pmatrix} e^{-i\delta} & 0 \\ 0 & e^{i\delta} \end{pmatrix}\frac{1}{i\,t_2}\begin{pmatrix} 1 & -r_2 \\ r_2 & -1 \end{pmatrix}\begin{pmatrix} E_t^+ \\ E_t^- \end{pmatrix}, \tag{2.45}$$

and through Eq. 2.42 we can express the amplitude of the field circulating inside the cavity E_c^+ as a function the input field E_0^+

$$\left.\frac{E_c^+}{E_0^+}\right|_{E_t^-=0} = \frac{-i\,t_1}{-1 + r_1 r_2 e^{2i\delta}}. \tag{2.46}$$

The fractional power of the transmitted, reflected and circulating fields are

$$\left|\frac{E_0^-}{E_0^+}\right|^2 = \frac{r_1^2 + r_2^2 - 2r_1 r_2 \cos(2kL_{\text{cav}})}{1 + r_1^2 r_2^2 - 2r_1 r_2 \cos(2kL_{\text{cav}})}, \tag{2.47}$$

$$\left|\frac{E_t^+}{E_0^+}\right|^2 = \frac{t_1^2 t_2^2}{1 + r_1^2 r_2^2 - 2r_1 r_2 \cos(2kL_{\text{cav}})}, \tag{2.48}$$

$$\left|\frac{E_c^+}{E_0^+}\right|^2 = \frac{t_1^2}{1 + r_1^2 r_2^2 - 2r_1 r_2 \cos(2kL_{\text{cav}})}. \tag{2.49}$$

We have used the word fractional power because the actual power carried by a plane wave of amplitude E across a surface A is $P = \epsilon_0 c|E|^2 A/2$ – where ϵ_0 is the vacuum permittivity – but the relative powers maintain the relations expressed above [78, 89].

What do these equations tell us? If we look at the behavior of either of the fields as a function of the *round-trip phase* $\phi_{\text{rt}} = 2kL_{\text{cav}}$ (Fig. 2.6), we observe a resonance behavior every time ϕ_{rt} satisfies the condition

$$\phi_{\text{rt}} = 2\pi q,\ q \in \mathbb{N}. \tag{2.50}$$

We can explore this resonance condition in two ways. The first one is fixing the cavity length L_{cav} and sweeping the frequency of the incoming optical field $\omega = 2\pi c/\lambda$ and therefore sweeping k.

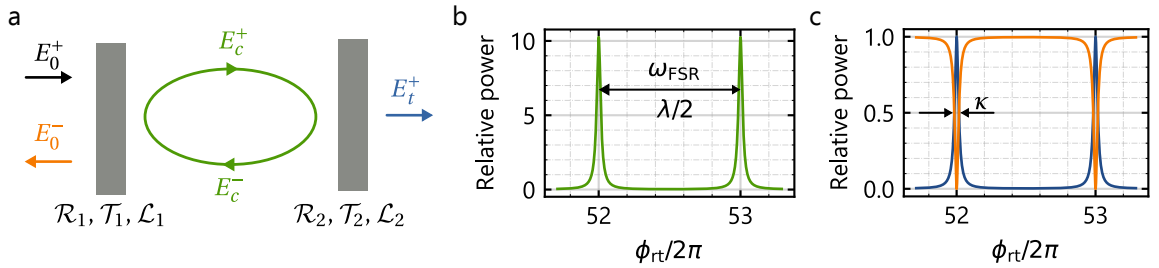

Figure 2.6: The Fabry-Pérot cavity. (a) Illustration of a Fabry-Pérot cavity and the electric fields involved. (b) Circulating relative power as a function of the round-trip phase ϕ_{rt}. (c) Transmitted (blue) and reflected (orange) relative power. Both (b) and (c) show two resonances with mode number $q = 52$ and $q = 53$.

In that case, we will observe that the resonances or *cavity longitudinal modes* are separated in frequency space by the free spectral range

$$\omega_{FSR} = \frac{c\pi}{L_{cav}}, \tag{2.51}$$

with resonance frequencies

$$\omega_q = q\frac{c\pi}{L_{cav}}, \tag{2.52}$$

where q is known as the cavity *longitudinal mode number*. Second, we can keep the laser frequency fixed and change the cavity length instead. Now the resonant modes will appear at cavity lengths that are multiples of half the laser wavelength:

$$L_q = q\frac{\lambda}{2}. \tag{2.53}$$

The second thing we realize is that the resonances have a finite width. In frequency space, the full width at half maximum κ is called the cavity linewidth, the rate at which the cavity energy – and hence the number of photons inside the cavity – decays. We introduce the concept of cavity finesse

$$\mathcal{F} = \frac{\omega_{FSR}}{\kappa}, \tag{2.54}$$

which is related to the number of round-trips N_{rt} the photons do before leaving the cavity via $N_{rt} = \mathcal{F}/\pi$ [90]. The other striking feature from Figure 2.6b is that the circulating power is enhanced with respect to the incoming one. The enhancement factor is given by the finesse $|E_c^+|^2 = \mathcal{T}_1\mathcal{F}^2/\pi^2|E_0^+|^2$. The finesse is also related to the round-trip losses $\mathcal{L}_{tot} = \mathcal{T}_1 + \mathcal{T}_2 + \mathcal{L}_1 + \mathcal{L}_2$ via

$$\mathcal{F} = \frac{2\pi}{\mathcal{L}_{tot}}. \tag{2.55}$$

Here, each mirror's transmission contributes to $\mathcal{L}_{tot}$ because it is a channel through which photons leave the cavity.

We can use Eq. 2.54 and Eq. 2.55 to define the *external couplings* or the rate at which the photons leave either of the mirrors, $\kappa_{i,e} = \omega_{FSR}\mathcal{T}_i/(2\pi)$, with $i = \{1,2\}$. With the former definition[10], we can

[10] We can also define the internal loss rate as $\kappa_0 = \omega_{FSR}(\mathcal{L}_1 + \mathcal{L}_2)/(2\pi)$, such that $\kappa = \kappa_0 + \kappa_{1,e} + \kappa_{2,e}$.

reformulate Eqs. 2.47-2.49 under the assumption of highly reflective mirrors[11] and for small cavity detunings Δ around resonance, $\omega = \omega_q + \Delta$ with $\Delta \ll \omega_{\mathrm{FSR}}$,

$$\left|\frac{E_r^+}{E_0^+}\right|^2 \simeq 1 - \frac{\kappa_{1,e}^2}{\Delta^2 + (\kappa/2)^2}, \quad \left|\frac{E_t^+}{E_0^+}\right|^2 \simeq \frac{\kappa_{1,e}\kappa_{2,e}}{\Delta^2 + (\kappa/2)^2} \quad \text{and} \quad \left|\frac{E_c^+}{E_0^+}\right|^2 \simeq \frac{\omega_{\mathrm{FSR}}}{2\pi}\frac{\kappa_{1,e}}{\Delta^2 + (\kappa/2)^2}. \tag{2.56}$$

In the latter, the equation of the circulating power has been scaled by a factor $n_{\mathrm{vac}}/n_s = 1/n_s$ so that the electric field amplitude matches the square root of the power, which is what is measured in the experiments[12]. The other two field amplitudes already match the square root of the measured power. These equations represent a Lorentzian with full width at half maximum κ.

We can also extract the number of photons circulating inside the cavity from the transmitted power P_t, which is what we usually measure with the photodetectors. First, we recall that the number of photons circulating inside the cavity n_c equals the total energy stored inside the cavity U_c divided by the energy of a single photon, $n_c = U_c/\hbar\omega_q$. Second, the energy inside the cavity is given by the circulating power P_c times the cavity round-trip time $\tau_{\mathrm{rt}} = 2L_{\mathrm{cav}}/c = 2\pi/\omega_{\mathrm{FSR}}$, $U_c = P_c\tau_{\mathrm{rt}}$. And finally, realizing (Eq. 2.56) that the relative circulating and transmitted powers are linked via

$$P_c = \frac{\omega_{\mathrm{FSR}}}{2\pi\kappa_{2,e}}P_t, \tag{2.57}$$

the circulating photon number is

$$n_c = \frac{P_t}{\kappa_{2,e}\hbar\omega_q}. \tag{2.58}$$

Optical modes in a concave cavity

So far we have only considered plane waves traveling in one direction, which was enough to explore the concept of optical resonance and to derive the longitudinal cavity modes. But these longitudinal modes living inside the cavity have a spatially-dependent intensity profile, which depends on the geometry of the cavity mirrors. The different spatial intensity profiles are called *transversal cavity modes*. These modes are a solution to the Helmholtz wave equation with the boundary conditions imposed by the mirrors. For our experiments, we use two concave mirrors, a type of stable two-mirror resonator. In this particular case, the Gaussian-Hermite modes form a complete set of solutions.

Each mode is characterized by three indices: the already introduced longitudinal mode number q and the transverse mode numbers m and n. The longitudinal mode number is often omitted in the literature, referring to the modes simply as $\mathrm{TEM}_{\mathrm{mn}}$, where TEM stands for transverse-electromagnetic. The electric field of the (q, m, n) mode $E_{q,m,n}(\mathbf{r})$ at a position $\mathbf{r} = (x, y, z)$ is given by [77]

$$E^{\pm}_{q,m,n}(\mathbf{r}) = \rho_{q,m,n}(\mathbf{r})e^{\pm i\theta_{q,m,n}(\mathbf{r})}, \tag{2.59}$$

where $\rho_{(q,m,n)}(\mathbf{r})$ is the amplitude

$$\rho_{q,m,n}(\mathbf{r}) = \frac{H_m(\sqrt{2}x/w(z))H_n(\sqrt{2}y/w(z))}{\sqrt{\pi 2^{m+n-1}n!m!L_{\mathrm{cav}}}}e^{-\frac{r^2}{w^2(z)}} \tag{2.60}$$

[11] If $\mathcal{R} \sim 1$, we can neglect terms of order of $\mathcal{O}(\mathcal{T}_i^2)$. Then $r_1 r_2 = \sqrt{1-\mathcal{L}_{\mathrm{tot}}} \sim 1 - \mathcal{L}_{\mathrm{tot}}/2$ and $\mathrm{R}_1\mathrm{R}_2 \sim 1 - \mathcal{L}_{\mathrm{tot}} + \mathcal{L}_{\mathrm{tot}}^2/4$.

[12] This comes from the definition of the transmission power coefficient (Eq. 2.37).

and $\theta_{q,m,n}(\mathbf{r})$

$$\theta_{q,m,n}(\mathbf{r}) = kz - (m+n+1)\Psi_G(z) + \frac{r^2}{w^2(z)}\frac{z}{z_R} + (q-1)\frac{\pi}{2} \tag{2.61}$$

the phase. The function H_m is the m^{th} Hermite polynomial, $w(z)$ the beam waist, z_R the Rayleigh range and $\Psi_G(z)$ the Gouy phase. The last four quantities depend solely on the radius of curvature of the mirrors R_i with $i \in [1,2]$ and the cavity length L_{cav}, so before giving their expressions we will introduce for convenience the g parameter of each mirror, $g_i = 1 - L_{\text{cav}}/R_i$. The beam waist is then given by

$$w(z) = w_0\sqrt{1+(z/z_R)^2}, \quad \text{with} \quad w_0^2 = \frac{L_{\text{cav}}\lambda}{\pi}\sqrt{\frac{g_1 g_2(1-g_1 g_2)}{(g_1+g_2-2g_1 g_2)^2}}, \tag{2.62}$$

and the Raleigh range

$$z_R = \frac{\pi w_0^2}{\lambda}, \tag{2.63}$$

Finally the Gouy phase follows

$$\Psi_G(z) = \arctan(z/z_R). \tag{2.64}$$

The resonance condition for each mode reads

$$\omega_{q,m,n} = 2\pi\frac{c}{2L_{\text{cav}}}\left(q + (m+n+1)\frac{\Delta\Psi_G^{\text{tr}}}{\pi}\right) \tag{2.65}$$

with $\Delta\Psi_G^{\text{tr}} = \cos^{-1}\left(\sqrt{g_1 g_2}\right)$ the change of Gouy phase in a round-trip [77].

In this thesis, we mainly work with the fundamental transversal mode, the TEM_{00}, which is a Gaussian mode. In the following, we will always refer to this one just as *cavity mode*, unless specified otherwise.

2.4 Membrane in the middle of a Fabry-Pérot cavity

In the previous section we have derived the resonance condition of an empty Fabry-Pérot (FP) cavity via the transfer matrix formalism. We are going to use it here as well to understand the radiation pressure force that the light inside the cavity exerts on a membrane placed in the middle of it, and obtain the expression of the optomechanical couplings.

The standard membrane-in-the-middle (MIM) system consists of a Fabry-Pérot cavity of length L_{cav} that is divided into two subcavities by placing a dielectric slab, referred as membrane, in between the mirrors (Fig. 2.7). Now, the circulating field is split into two, one on the left side of the membrane with forward and backward amplitudes E_l^+ and E_l^- and another one on the right side, with E_r^+ and E_r^-, respectively. In the following, we are going to consider that the wavelength or frequency of the laser is fixed and study the resonances of the MIM system by changing its cavity length. For a membrane's position z, the transfer matrix will read

$$M_{\text{MIM}} = \frac{1}{it_1}\begin{pmatrix}1 & -r_1\\ r_1 & -1\end{pmatrix}\begin{pmatrix}e^{-i\delta_l} & 0\\ 0 & e^{i\delta_l}\end{pmatrix}\frac{1}{t_m}\begin{pmatrix}1 & -r_m\\ r & t_m^2-r_m^2\end{pmatrix}\begin{pmatrix}e^{-i\delta_r} & 0\\ 0 & e^{i\delta_r}\end{pmatrix}\frac{1}{it_2}\begin{pmatrix}1 & -r_2\\ r_2 & -1\end{pmatrix}, \tag{2.66}$$

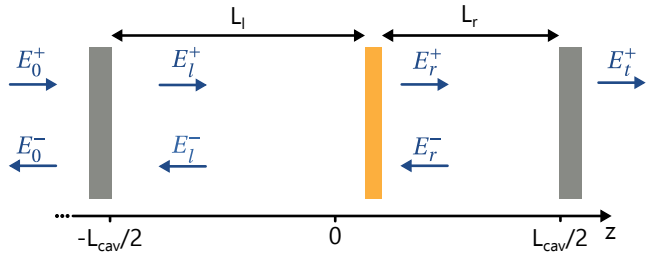

Figure 2.7: The membrane-in-the-middle system. It consists of two mirrors (dark gray) separated by a distance L_{cav} and a dielectric slab or membrane (orange) of thickness d_m. The empty Fabry-Pérot appears now divided in two sub-cavities, on the left and on the right of the membrane.

where r_i, t_i with $i \in [1,2]$ are the reflection and transmission coefficients of the mirrors, and r_m, t_m the ones of the membrane (Eq. 2.39 and Eq. 2.40). δ_l and δ_r denote the phase acquired by the field at each side of the membrane, given by

$$\delta_l = kL_l = k\big(L_{\text{cav}}/2 + z - d_m/2\big), \tag{2.67}$$

$$\delta_r = kL_r = k\big(L_{\text{cav}}/2 - z - d_m/2\big). \tag{2.68}$$

Let's try to understand the effect of adding the dielectric slab to the cavity by looking at its transmission T for different membrane reflection coefficients r_m as a function of the cavity length and membrane's position (Fig. 2.8). For simplicity, we will assume that the membrane is lossless – the case of a lossy membrane will be discussed at the end of this section. Setting $r_m = 0$ (Fig. 2.8a) creates the same effect as having an empty cavity. In that case, as we change the cavity length, we observe a set of resonances in transmission separated by multiples of $\lambda/2$, as expected for a Fabry-Pérot cavity. Since the membrane is completely transparent, the resonances do not depend on the membrane's position.

Figure 2.8b displays the system's transmission for a membrane with $|r_m| = 0.48$ ($d_m = 100\,\text{nm}$, $n_m = 2$). The resonance cavity lengths $L_q(z)$ now oscillate with respect to the membrane's position with a periodicity of $\lambda/2$. The cavity length detuning for the mode number q, defined as

$$\Delta L_q(z) = L_q(z) - L_q, \tag{2.69}$$

is always negative or close to zero $\Delta L_q < 0$ for this membrane, where L_q denotes the empty resonance cavity length. Intuitively, one can think that the membrane increases the optical path length inside the cavity by $n_m d_m$, and therefore we need to *shrink* the cavity to compensate for that increase and keep the cavity resonant[13]. The absolute change of cavity length will be maximized when the membrane is placed at the antinode because the largest portion of the light intensity is confined within the dielectric. The opposite effect occurs at the nodes, where the smallest portion of the intensity lies in the membrane. This is depicted on the bottom illustrations in Figure 2.8, which show the relative power $|E|^2$ inside the cavity when the membrane sits in a node (orange circle) and antinode (red circle) for the mode number $q = 10$. Because q is even in this case, the

[13]This is an intuitive picture. The exact expression for ΔL_q is given in the next section, and does not depend on the product $n_m d_m$ but on the phase and magnitude of the reflection coefficient r_m.

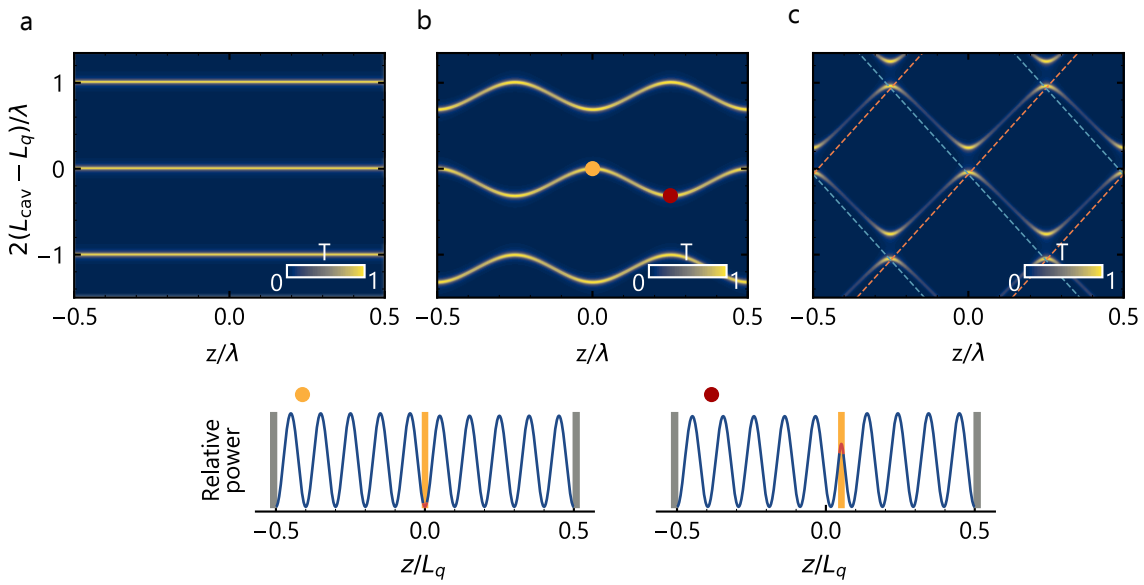

Figure 2.8: Transmission of a MIM system. Transmission coefficient T of a MIM system with mirror reflection coefficients $r_1 = r_2 = 0.95$ as a function of cavity length L_{cav} and membrane's position z. (a) Empty cavity ($|r_m| = 0$). (b) Membrane with $|r_m| = 0.48$. (c) Membrane with $|r_m| = 0.89$. L_q is the resonant cavity length with mode number $q = 10$ (Eq. 2.53). The blue and orange dashed lines are the resonance condition for left and right subcavities, respectively (Eq. 2.67 and Eq. 2.68). The two bottom graphs depict the relative power $|E|^2 = |E^+ + E^-|^2$ inside the cavity for the membrane placed at the node (orange circle) and antinode (red circle) of the system in (b).

cavity presents a node at $z = 0$. For odd values of q, the cavity has an antinode at $z = 0$, which explains why the resonance curves are shifted by $\lambda/4$ as a function of the membrane's position for even and odd mode numbers.

Now let's consider the other extreme case, when the membrane reflectivity approaches 1. The two subcavities are well separated by the highly reflective membrane, each of them satisfying the resonance condition $L_{l,r} = q_{r,l}\lambda/2$, with $L_{l,r}$ given by the definitions in Eq. 2.67 and Eq. 2.68. Figure 2.8c shows the cavity transmission for $|r_m| = 0.89$. The resonant cavity lengths for both subcavities $L_{l,r}$ are depicted in the figure as well, as dark orange and light blue dashed lines, orange for the right and blue for the left subcavities, respectively. We observe that the light is transmitted through the cavity when the system is resonant for both subcavities. For example, when the membrane sits in the middle ($z = 0$), if the MIM cavity is resonant for an even mode number q, both cavities are also resonant with $q_{l,r} = q/2$, as can be seen on the intensity profile at the bottom left in Figure 2.8. If we increase the membrane's position ($z > 0$), the right subcavity shrinks, and to bring the resonance back we need to increase the cavity length. Consequently, the orange line has a positive slope in z. The opposite occurs to the left subcavity (blue line).

We remark that the cavity linewidth κ is also modulated by the presence of the membrane. Even when the membrane does not introduce any losses, its presence still alters the fields distribution inside the cavity and consequently the energy stored inside. The finesse, on the contrary, remains constant for the case of a symmetric cavity ($r_1 = r_2$). Figure 2.9 shows the dependence of the cavity

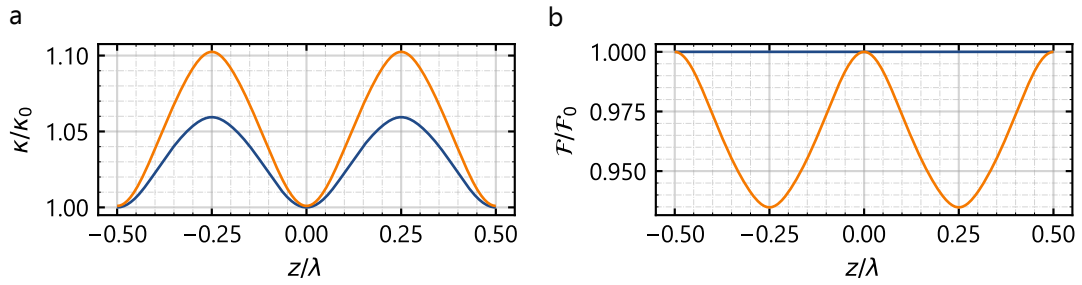

Figure 2.9: Linewidth and finesse of a MIM system with symmetric mirrors. (a) The linewidth of the cavity κ is modulated as the membrane changes its position z even for a lossless membrane (blue curve). Adding losses to the membrane ($\mathrm{Im}(n_m) = 2 \cdot 10^{-3}$) increases the modulation (orange line). The data is normalized to the minimum linewidth for the lossless case. (b) Cavity finesse as a function of sample position for the same configurations as in (a). The finesse is normalized to the lossless membrane finesse, which is constant.

linewidth and finesse for a membrane with and without losses.

Resonance condition and cavity frequency shift

The resonance condition of a MIM system can be obtained easily via the transfer matrix under the assumption of highly reflective mirrors $r_1 = r_2 \simeq 1$ [91]. The fields on the left and on the right side of the cavity are related through

$$\begin{pmatrix} E_l^+ \\ E_l^- \end{pmatrix} = \begin{pmatrix} e^{-i\delta_l} & 0 \\ 0 & e^{i\delta_l} \end{pmatrix} \frac{1}{t_m} \begin{pmatrix} 1 & -r_m \\ r & t_m^2 - r_m^2 \end{pmatrix} \begin{pmatrix} e^{-i\delta_r} & 0 \\ 0 & e^{i\delta_r} \end{pmatrix} \begin{pmatrix} E_r^+ \\ E_r^- \end{pmatrix} = M \begin{pmatrix} E_r^+ \\ E_r^- \end{pmatrix}. \tag{2.70}$$

If $r_1 = r_2 \simeq 1$, then $E_l^- = -E_l^+$ and $E_r^- = -E_r^+$, and we can express all in terms of E_l^+ and E_r^+. This leads to a relation between the matrix elements

$$(M_{00} - M_{01}) = (M_{11} - M_{10}), \tag{2.71}$$

which is the resonance condition. Replacing their expressions, we obtain

$$|r_m| \cos(2kz) = -\cos(L_{\mathrm{cav}} - d_m + \phi_r), \tag{2.72}$$

where we have used $r_m = |r_m| e^{i\phi_r}$, $t_m = |t_m| e^{i\phi_t}$ and that for a dielectric membrane $t_m^2 - r_m^2 = -e^{i2\phi_r}$ [91]. We can expand the above expression around resonance $L_{\mathrm{cav}} = L_q + \Delta L_q(z)$, yielding

$$\Delta L_q(z) = \frac{\cos^{-1}\left((-1)^{q+1} |r_m| \cos(2zk)\right) - \phi_r}{k}, \tag{2.73}$$

where we have used the approximation $L_{\mathrm{cav}} - d_m \simeq L_{\mathrm{cav}}$. The last approximation is valid for all the samples studied in this thesis, with a maximum membrane thickness of around 200 nm compared to cavity lengths of around 40 µm. The expression of ΔL_q shows that the offset with respect to the empty cavity length L_q is basically given by the complex phase of the membrane reflection coefficient ϕ_r.

We can transform the cavity length change into a frequency detuning when $\Delta L_q \ll L_q$ using

$$\Delta_{\text{cav}}(z) = q\pi c\Big(\frac{1}{L_q + \Delta L_q(z)} - \frac{1}{L_q}\Big) \simeq -q\pi c\frac{\Delta L_q(z)}{L_q^2}, \tag{2.74}$$

which can be understood as a change of cavity resonance frequency[14], $\omega_{\text{cav}}(z) = \omega_q + \Delta_{\text{cav}}(z)$. The frequency of the cavity therefore follows the same dependence as the length detuning but with opposite sign. We can expand $\omega_{\text{cav}}(z)$ as a function of its derivatives,

$$\omega_{\text{cav}}(z) = \omega_q + \frac{\partial\omega_{\text{cav}}}{\partial z}z + \frac{\partial^2\omega_{\text{cav}}}{\partial z^2}z^2 + \mathcal{O}(3). \tag{2.75}$$

This brings us to the definition of the linear dispersive frequency shift, or simply *linear dispersive coupling*[15] $G(z) := \partial\omega_{\text{cav}}/\partial z$. Using Eq. 2.73 and Eq. 2.74, the dispersive coupling of a MIM system is

$$G(z) = \frac{q\pi c}{L_q^2}\frac{2|r_m|\sin(2kz)(-1)^{q+2}}{\sqrt{1-|r_m|^2\cos^2(2kz)}}, \tag{2.76}$$

and the quadratic dispersive coupling $G^{(2)}(z)$

$$G^{(2)}(z) := \frac{\partial^2\omega_{\text{cav}}(z)}{\partial^2 z} = \frac{q\pi c}{L_q^2}4k(-1)^{q+2}\frac{|r_m|(1-|r_m|^2)\cos(2kz)}{\big(1-|r_m|^2\cos^2(2kz)\big)^{3/2}}. \tag{2.77}$$

For a MIM system, the linear coupling vanishes at the nodes and antinodes, where the quadratic coupling is the strongest, and the absolute value of the coupling reaches its maxima at sample positions which are odd multiples of $\pm\lambda/8$. The quadratic coupling is intrinsic to MIM systems and offers new functionalities beyond the linear optomechanical systems [72, 87, 92, 93], and has recently been used to generate non classical energy squeezing of macroscopic mechanical oscillators [94] and to cool down levitated nanoparticles [95].

Looking at Eq. 2.76 and Eq. 2.77, there are two approaches to increase the couplings. The first one is to increase the absolute value of the reflection coefficient of the membrane, which can be done for example by designing membranes with an incorporated photonic crystal [96–98]. The second is decreasing the cavity length, which is best achieved with fiber cavities. As we will see later, the fiber mirrors can have a very small radius of curvature that, combined with their small mirror diameters, make the construction of cavities with lengths down to tens of micrometers possible [90, 99]. Figure 2.10 shows both linear and dispersive couplings for a MIM system with different membrane and cavity length configurations.

[14] Strictly speaking, what is changing in the resonance condition is the cavity length because the frequency of the laser is kept fixed. However, with Eq. 2.74 we convert a change of cavity length ΔL_q into an effective frequency change Δ_{cav}.

[15] In the standard cavity optomechanics literature G is defined with a negative sign $G(z) = -\partial\omega_{\text{cav}}/\partial z$ [17, 18]. The sign arises because in the used toy model, a cavity with a movable mirror, an increase or the resonator's position – or cavity length – produces a decrease in the cavity resonance frequency. However, in the MIM system, the sign of the coupling depends on the membrane position in a non trivial way through Eq. 2.76.

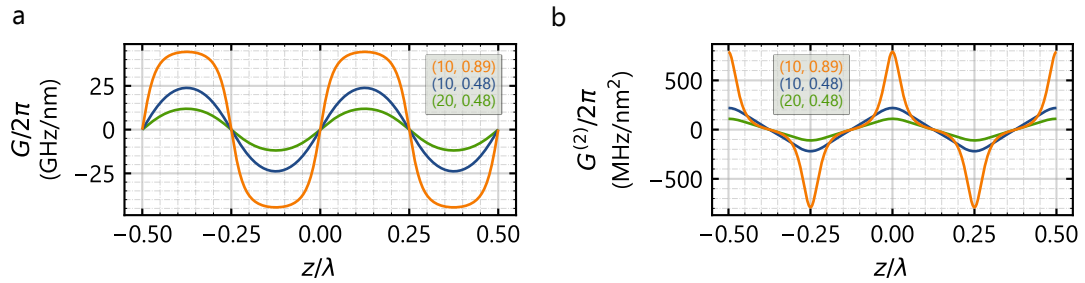

Figure 2.10: Linear and quadratic dispersive couplings. (a) Linear and (b) quadratic dispersive couplings for different cavity mode numbers q and membrane reflectivity $|r_m|$, and $\lambda = 1500\,\text{nm}$. Orange, blue and green lines are generated with parameters $(q, |r_m|)$, (10, 0.89), (10, 0.48), (20, 0.48), respectively.

2.4.1 The static optical force

An object immersed in an electromagnetic field experiences a force F because electromagnetic waves carry momentum. This force, acting on a surface A, exerts a light pressure or *radiation pressure* on the object. In the MIM system, the plane waves travel all in the z direction, resulting in a net force F also in the z direction that only depends on the field amplitudes at each side of the membrane

$$F = \frac{P_0}{c}\left(\left|\frac{E_l^+}{E_0^+}\right|^2 + \left|\frac{E_l^-}{E_0^+}\right|^2 - \left|\frac{E_r^+}{E_0^+}\right|^2 - \left|\frac{E_r^-}{E_0^+}\right|^2\right), \tag{2.78}$$

with P_0 being the incident light power on the cavity [89, 100]. To be able to predict and understand the force, we need to look at the field distributions on the left and right side of the membrane.

Figure 2.12 shows the transmission T (Fig. 2.11a) and reflection R (Fig. 2.12b) of a MIM system with $|r_m| = 0.48$, $r_1 = r_2 = 0.95$ and $q = 10$ as a function of cavity length and membrane's position. The value of both coefficients on resonance is symmetric with respect to the membrane displacement, $T^{\text{res}}(z) = T^{\text{res}}(-z)$ and $R^{\text{res}}(z) = R^{\text{res}}(-z)$, which is a consequence of having mirrors with equal reflectivity. If we look at the maximum of the relative power of the fields on the left and right side of the membrane, $|E_i|^2 = |E_i^+ + E_i^-|^2$ with $i = \{l, r\}$, we observe a different behavior (Fig. 2.11c and Fig. 2.11d). The intensity of the left circulating field is not symmetric with respect to the membrane's position. It is maximized when the membrane is moved to the right side of the node and minimized when moved in the other direction, and reaches both extrema at displacements of the membrane of $z = +\lambda/8$ and $z = -\lambda/8$, respectively. The right circulating power, on the contrary, behaves symmetrically with respect to the membrane's displacement, and it is maximized at the nodes and antinodes and minimized for $z = \pm\lambda/8$. We also recall that the maximum of the left relative power is 85 and its minimum 9, whereas for the right relative power the values are 40 and 31, respectively. Therefore, the left power varies more strongly with respect to the membrane's position than the right power, because the right subcavity is pumped less efficiently due to the presence of the membrane. Figure 2.11e shows the power distribution inside the cavity when the membrane is at $z = -\lambda/8$ (orange circle in Fig. 2.12a) and at $z = +\lambda/8$ (red circle in Fig. 2.11a) to illustrate the effect just discussed.

The consequence of this field distribution is a non-zero radiation pressure force for cavity lengths

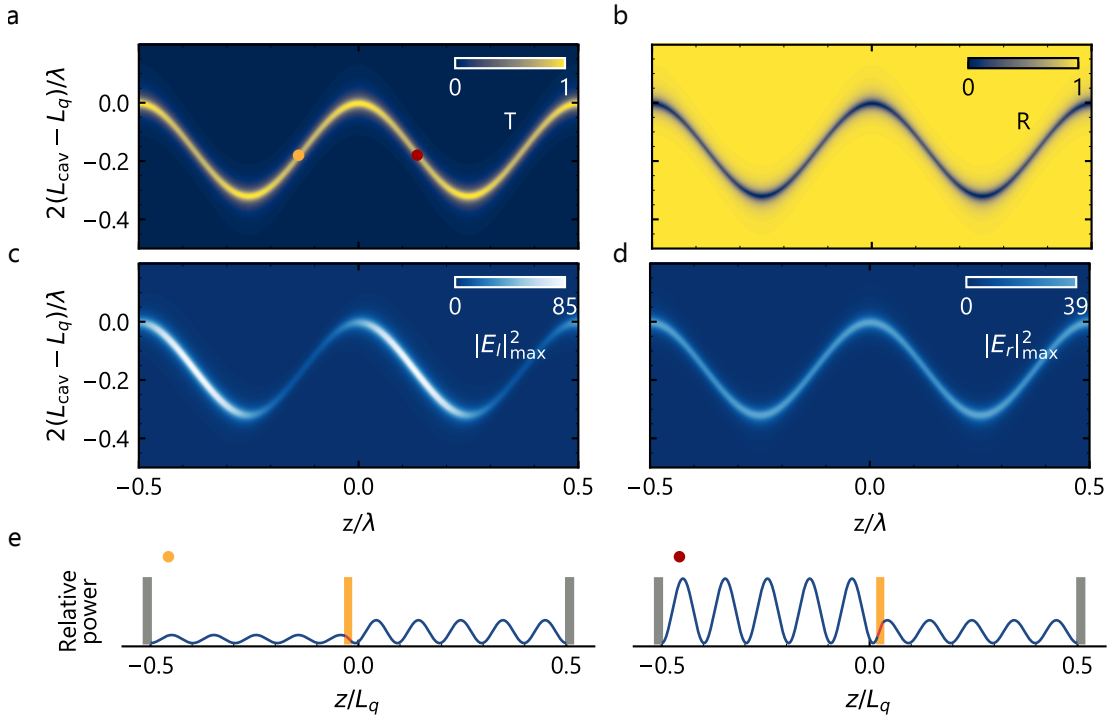

Figure 2.11: Fields at each subcavity in a MIM system. (a) Transmission and (b) reflection coefficient for $r_1 = r_2 = 0.95$, $|r_m| = 0.48$ and $q = 10$ as a function of cavity length and membrane's position z. (c) Maximum of the relative power $|E_l|^2$ in the left subcavity. (d) Same as (c) but in the right subcavity $|E_r|^2$. (e) Field amplitudes inside the cavity at the left (orange circle in (a)) and right side of the node (red circle in (a)).

and membrane's positions close to the resonance condition (Fig. 2.12a). The sign and magnitude of the force depend on the relative powers inside each subcavity, following Eq. 2.78. At the nodes and antinodes the force vanishes (see the power distributions at the bottom graphs of Fig. 2.8). We say that this force is a *static* optical force because we are assuming that the field inside the cavity reacts instantaneously to a change of sample position or cavity length[16].

Imagine now that the membrane is allowed to oscillate, like the one depicted in Figure 2.12c. The optical force will have an optical potential V associated to it so that $F = -\partial V/\partial z$. This will be added to the intrinsic mechanical potential of the resonator, contributing with an extra *optical spring* k_{opt} to the natural stiffness of the resonator,

$$k_{\text{opt}}(z) = -\frac{\partial F(z)}{\partial z}, \tag{2.79}$$

shown in Figure 2.12b. One can also induce new local minima in the potential by using very high optical powers, resulting in a bistable behavior of the optical resonator (see e.g. Refs. [100, 101] for the early experiments). We highlight here that, in principle, we do not need the cavity to induce

[16]This is equivalent to change the membrane's position in a adiabatic manner, i.e. slow enough compared to the time constants of the system.

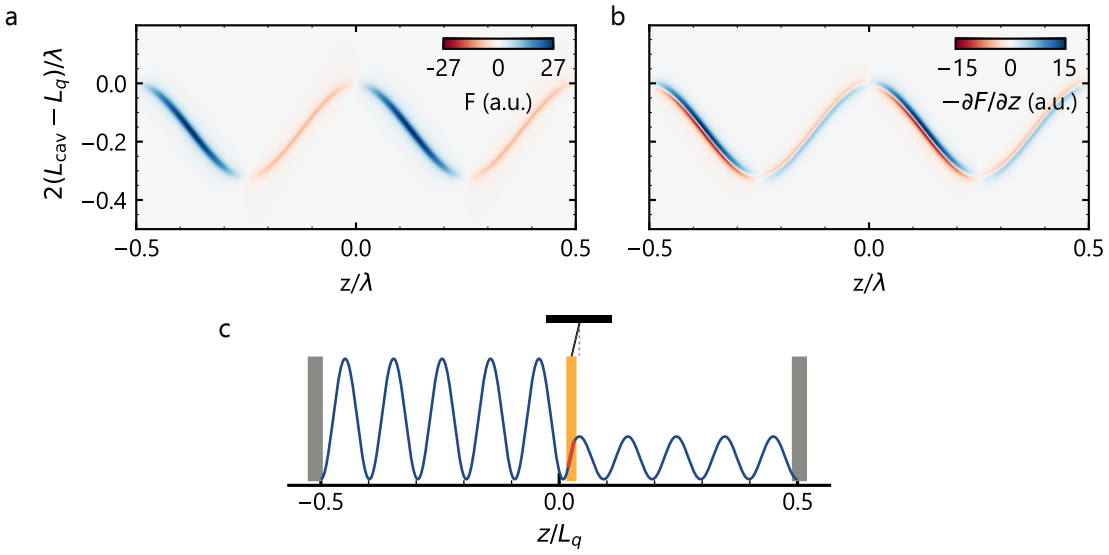

Figure 2.12: Radiation pressure force in a MIM system. (a) Radiation pressure force and (b) optical spring for $r_1 = r_2 = 0.95$, $|r_m| = 0.48$ and $q = 10$ as a function of cavity length and membrane's position z (same system as in Fig. 2.11). (c) Sketch of a membrane inside the cavity able to oscillate around its equilibrium position.

a new optical potential, just the standing waves naturally living inside. For example, radiation pressure forces have been used to confine membrane-like pendulums and modify optically their spring constant by just using the standing waves created between an incoming plane wave and its reflection [102].

2.4.2 The dynamical optical force

In the previous section we explained how the resonances of the optical cavity together with the field amplitudes depend on the membrane's position along the cavity axis z, leading to a static radiation pressure force acting on the membrane. We assumed that the field inside the cavity responds instantaneously to the displacement of the membrane or change of cavity length. This holds true when the respective change happens at a speed slower than the cavity energy decay rate, κ. Let's go back to the oscillating membrane depicted in Figure 2.12c. When oscillating, the membrane will change the optical resonance of the cavity, which acts back on the membrane by changing the radiation pressure force. If the membrane's oscillation frequency Ω_0 is comparable or larger than κ, the intensity cannot completely track the mechanical motion, leading to time lag effects. The radiation pressure force is no longer static but depends on the membrane's history at a previous time, it is therefore a *dynamical* force. Because the force is non-conservative, the work done on the mechanical oscillator upon an oscillation cycle is non-zero, resulting in a system capable of extracting or giving energy to the oscillator. This has consequences on the mechanical response of the resonator that we will discuss in the following.

The system's dynamics is described by two coupled nonlinear differential equations describing the optical field amplitude and resonator's mechanical displacement. They can be linearized if we

consider small membrane displacements only, and assume that the intracavity field is in a steady-state with small fluctuations around it. Their derivation can be found in standard optomechanics text books [17, 18]. The main consequence of the dynamical backaction is that the mechanical susceptibility of the resonator, given by Eq. 2.12, is modified to

$$\chi_{\mathrm{OM}}(\omega) = \frac{1}{m\left[\Omega_0^2 + \delta(\Omega^2) - \omega^2 - i\omega\left(\Gamma_0 + \Gamma_{\mathrm{opt}}\right)\right]}. \tag{2.80}$$

This leads to an optical spring, i.e. a modification of the natural frequency of the resonator due to the radiation pressure $\Omega_m^2 = \Omega_0^2 + \delta(\Omega^2)$ given by

$$\delta(\Omega^2) = 2\Omega_0 g^2\Big(\frac{\Omega_0 + \Delta}{(\Omega_0 + \Delta)^2 + (\kappa/2)^2} - \frac{\Omega_0 - \Delta}{(\Omega_0 - \Delta)^2 + (\kappa/2)^2}\Big), \tag{2.81}$$

where $g = \sqrt{n_c} g_0$ denotes the optomechanical coupling strength, which is the product of the square root of the number of circulating photons inside the cavity and the single-photon coupling strength g_0. The latter depends on the zero-point fluctuations $z_{\mathrm{zpf}} = \sqrt{\hbar/(2m\Omega_0)}$ and the dispersive linear coupling G through $g_0 = G z_{\mathrm{zpf}}$; it is a measure of the frequency shift of a single photon caused by the smallest possible displacement of the resonator, z_{zpf}. Here, Δ is the laser detuning: the frequency difference between the laser used to drive the cavity ω_l and the cavity resonance ω_{cav}, $\Delta = \omega_l - \omega_{\mathrm{cav}}$. We note that the circulating photon number n_c is also a function of the detuning and its dependence is given by Eq. 2.56 and Eq. 2.58. For small frequency shifts $\delta(\Omega^2) \ll \Omega_0$, Eq. 2.81 can be approximated to

$$\Omega_m \simeq \Omega_0 + \frac{1}{2\Omega_0}\delta(\Omega^2), \tag{2.82}$$

where we have used that $\sqrt{1+x} \simeq 1 + x/2$ if $x \ll 1$.

The damping of the resonator is also modified to $\Gamma_m = \Gamma_0 + \Gamma_{\mathrm{opt}}$ with Γ_{opt} being the optomechanical damping rate

$$\Gamma_{\mathrm{opt}} = 2g^2\frac{\kappa}{2}\Big(\frac{1}{(\Omega_0 + \Delta)^2 + (\kappa/2)^2} - \frac{1}{(\Omega_0 - \Delta)^2 + (\kappa/2)^2}\Big). \tag{2.83}$$

Figure 2.13 shows the optical spring effect and the optomechanical damping for a system with parameters $\kappa = 26\,\Omega_0$, $g_0 = \Omega_0/1500$, $Q = 7600$, and $n_c^{\max} = n_c(\Delta = 0) = 60000$. One observes that for negative detunings, i.e. a red detuned laser, the mechanical mode softens, whereas it stiffens for positive detunings (blue detuned laser). For negative detunings, the cavity extracts thermal energy from the resonator, increasing the mechanical linewidth. The opposite occurs for positive detunings. This is equivalent to cooling or heating the resonator, with the new effective temperature Γ_{eff} given by

$$T_{\mathrm{eff}} = T_{\mathrm{bath}}\frac{\Gamma_0}{\Gamma_m}, \tag{2.84}$$

where T_{bath} denotes the bath temperature [17]. When the overall mechanical linewidth $\Gamma_m = \Gamma_0 + \Gamma_{\mathrm{opt}}$ becomes negative (orange area in Fig. 2.13) an optomechanical instability arises: the amplitude of the resonator grows exponentially until reaching a steady-state, where it oscillates at a fixed amplitude. These oscillations are called self-sustained oscillations [17, 103].

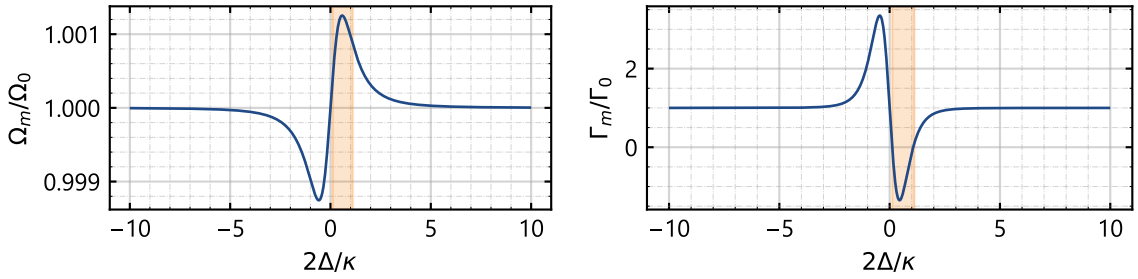

Figure 2.13: Dynamical backaction. Optical spring effect (left) and optomechanical damping (right) for an optomechanical system with $\kappa = 26\Omega_0$, $g_0 = \Omega_0/1500$ and $Q = 7600$. The intracavity photon number n_c follows Eq. 2.58 with $n_c^{\max} = 60000$. The orange area highlights the detunings for which the mechanical resonator undergoes self-sustained oscillations.

Optomechanical backaction has many applications and a very rich set of physical phenomena can arise depending on the explored parameter space (g_0, κ, Γ_0, Ω_0, n_c, Δ). One of most straightforward applications is the cool-down of mechanical resonators to their ground state, necessary for quantum applications. A requirement for an optomechanical system to be able to perform quantum experiments is having a quantum cooperativity, $C_q = 4g^2/(\kappa\Omega_0(n_{\text{th}}+1/2))$, larger than 1 [17]. In the last expression n_{th} is the phonon thermal occupation number,

$$n_{\text{th}} = \frac{k_B T_{\text{bath}}}{\hbar\Omega_0}. \tag{2.85}$$

To have a large C_q it is therefore necessary to have low phonon occupation numbers. For gigahertz resonators, the ground state is easily reachable with conventional dilution refrigerators capable of reaching temperatures down to a few millikelvin. However, for megahertz or lower frequency resonators extra means of cooling need to come into play [104, 105]. Optomechanical systems can be cooled down to the ground state through radiation pressure backaction only when they are operated in the resolved-sideband regime $\Omega_0 \gg \kappa$. In that case, the minimum phonon occupation number is given by [17]

$$n_{\text{ph,min}} = \left(\frac{\kappa}{4\Omega_0}\right)^2 < 1. \tag{2.86}$$

For the unresolved-sideband regime ($\Omega_0 < \kappa$), on the contrary, the minimum phonon number is larger than one

$$n_{\text{ph,min}} = \frac{\kappa}{4\Omega_0} \gg 1. \tag{2.87}$$

One can, nevertheless, use other mechanisms to provide additional cooling, like active feedback [106] or dissipative coupling [107, 108]. For both resolved-sideband and unresolved-sideband regimes, the final phonon number $n_{\text{ph,f}}$ due to the optomechanical backaction of a red detuned laser is

$$n_{\text{ph,f}} = \frac{\Gamma_0 n_{\text{th}} + \Gamma_{\text{opt}} n_{\text{ph,min}}}{\Gamma_m}, \tag{2.88}$$

where one has to use the corresponding expression for $n_{\text{ph,min}}$ [17]. Our experiments occur in the unresolved-sideband regime and at room temperature. Additionally, the natural linewidth

Γ_0 of our resonators is comparable to the optomechanical linewidth $\Gamma_0 \sim \Gamma_{\text{opt}}$. In this particular situation, one can neglect the second term in Eq. 2.88 so that the final phonon number can be approximated to $n_{\text{ph,f}} \simeq n_{\text{th}}\Gamma_0/\Gamma_m$.

Another useful application from the radiation pressure backaction is the direct control of the mechanical properties of the resonator via light forces. The manipulation of the amplitude of the resonator, and consequently the mechanical stress field, can be used to control other degrees of freedom like spins, realizing hybrid quantum systems [68, 71]. This could have interesting technological applications like bridging the gap between telecom photons and spin-qubits.

Dissipative dynamical backaction

Any mechanism resulting in a change of the radiation pressure force with the membrane's position will exert a backaction on the resonator. In the dispersive case discussed so far, it is the difference in photon number caused by the field distribution on both sides of the subcavities. Dissipative mechanisms can also alter the photon number inside the cavity, which manifests as a modulation of the cavity linewidth with the sample position $\kappa = \kappa(z)$ [107]. The linewidth modulation in a MIM system can originate from membrane absorption [109], membrane scattering due to surface imperfections or membrane misalignment [110], or simply from the modulation of the input couplings [91].

In equivalence with the dispersive case, we can define the *dissipative* linear and quadratic couplings

$$G_\kappa(z) = \frac{\partial\kappa(z)}{\partial z} \quad \text{and} \quad G_\kappa^{(2)}(z) = \frac{\partial^2\kappa(z)}{\partial z^2}. \tag{2.89}$$

Figure 2.14 shows the dissipative couplings in a symmetric MIM system ($r_1 = r_2 = 0.95$) with $q = 10$ and $\lambda = 1550\,\text{nm}$ for a membrane with absorption $\text{Im}(n_m) = 2\cdot10^{-3}$ and without absorption, the same settings as in Figure 2.9a. We recall that in a MIM system there is always a dissipative coupling, even with a lossless membrane and no scattering, due to the field's distribution inside the subcavities (see Fig. 2.9), which is what we referred to as modulation of the input couplings. Nevertheless, the dissipative coupling is negligible to the dispersive one in the case of a lossless membrane (more than three orders of magnitude smaller), as can be seen comparing the blue curve in Figure 2.14a with blue one in Figure 2.10a.

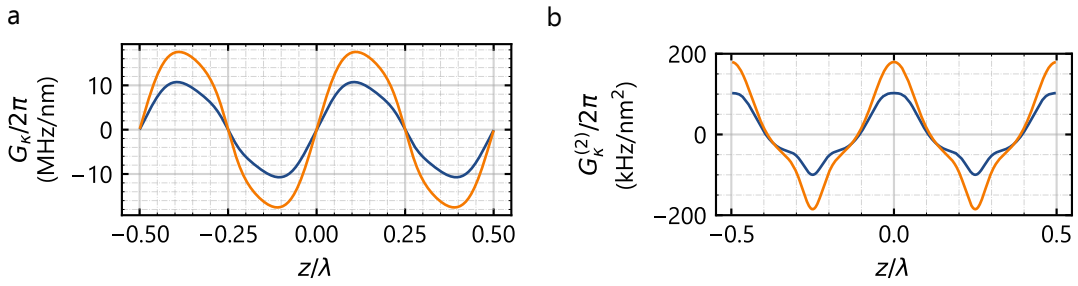

Figure 2.14: Dissipative couplings. (a) Linear dissipative and (b) quadratic couplings for a membrane of reflection $|r_m| = 0.48$ without losses (blue) and with $\text{Im}(n_m) = 2\cdot10^{-3}$ (orange), obtained numerically with the transfer matrix method.

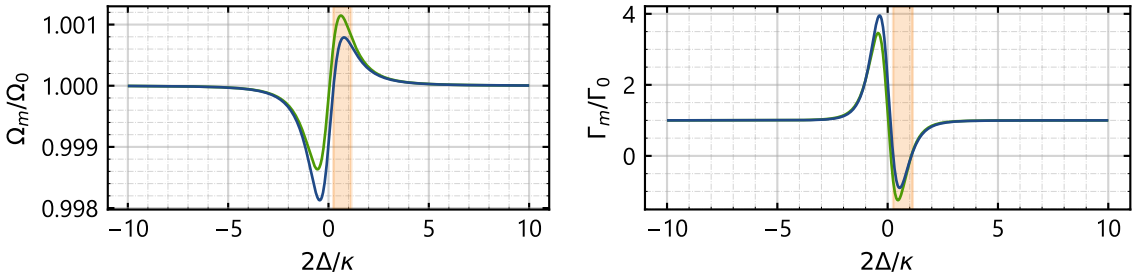

Figure 2.15: Dissipative and dispersive dynamical backaction. Optical spring effect (left) and optomechanical damping (right) for the same system as in Figure 2.13 ($\kappa = 26\Omega_0$, $g_0 = \Omega_0/1500$, $Q = 7600$, $n_c^{\max} = 60000$) with additional $g_{0,\kappa} = -g_0/4$ (blue line) and $g_{0,\kappa} = -g_0/20$ (green line). The orange area highlights the detunings for which the mechanical resonator undergoes self-sustained oscillations.

In case of membrane absorption, the optical spring and optomechanical damping take the form

$$\delta(\Omega^2) = 2\Omega_0 g^2\Big(\frac{\Omega_0+\Delta}{(\Omega_0+\Delta)^2+(\kappa/2)^2} - \frac{\Omega_0-\Delta}{(\Omega_0-\Delta)^2+(\kappa/2)^2}\Big) + 2\Omega_0 g g_\kappa \frac{\kappa}{2}\Big(\frac{1}{(\Omega_0+\Delta)^2+(\kappa/2)^2} + \frac{1}{(\Omega_0-\Delta)^2+(\kappa/2)^2}\Big), \quad (2.90)$$

and

$$\Gamma_{\text{opt}} = 2g^2\frac{\kappa}{2}\Big(\frac{1}{(\Omega_0+\Delta)^2+(\kappa/2)^2} - \frac{1}{(\Omega_0-\Delta)^2+(\kappa/2)^2}\Big) - 2g g_\kappa\Big(\frac{\Omega_0-\Delta}{(\Omega_0+\Delta)^2+(\kappa/2)^2} + \frac{\Omega_0+\Delta}{(\Omega_0-\Delta)^2+(\kappa/2)^2}\Big), \quad (2.91)$$

where $g_\kappa = \sqrt{n_c}g_{0,\kappa}$ [109]. In this case, $g_{0,\kappa}$ is the single-photon dissipative coupling strength $g_{0,\kappa} = G_\kappa z_{\text{zpf}}$. Figure 2.15 shows the dissipative couplings for the same system as in Figure 2.13 with an additional dissipative coupling of $g_{0,\kappa} = -g_0/4$ (blue line) and $g_{0,\kappa} = -g_0/20$ (green line). The dissipative coupling adds an asymmetry with respect to $\Delta = 0$ not present in the purely dispersive case. For $g_{0,\kappa} < g_0/20$ the contribution to the optical spring and damping is almost not distinguishable from the purely dispersive case (Fig. 2.13).

3

Our 1550 nm setup for cavity optomechanics

When I joined the Nanomechanics group at the University of Konstanz (now the Nano and Quantum Sensors group at TUM), the cavity optomechanics team was working with fiber-based Fabry-Pérot microcavities operating at a wavelength of 780 nm [111, 112]. The absorption of SiN membranes – the resonators we were using at that time – in the visible range, together with the huge optomechanical couplings, made the optomechanical experiments extremely difficult. Actually, we could not observe dynamical backaction effects at all due to the nonlinearities of the system [112]. We therefore decided to switch to telecom wavelengths, also benefiting from the advanced fiber technology and cheaper prices. This was the first goal of my PhD project: the design and construction of a complete cavity-optomechanical setup operating at $\lambda = 1550\,\text{nm}$. This chapter is fully dedicated to this work.

The cavity is the essence of any cavity optomechanics experiment. We use fiber-based Fabry-Pérot cavities (FFPCs), formed between the end facets of two optical fibers that serve as the cavity mirrors. Section 3.1 focuses on the production of the fiber mirrors, their characterization, and the cavity assembly. Section 3.2 and Section 3.3 introduce the optical and electrical setup, respectively, necessary to pump and characterize the cavities and perform the dynamical backaction experiments. Section 3.4 presents the cavity characterization methods. In order to reduce gas damping, our experiments are carried out in vacuum – the vacuum system is described in Section 3.5. To perform optomechanical experiments in the membrane-in-the-middle configuration, the sample has to be brought, as the name suggests, to the middle of the cavity. This is done through a positioning system presented in Section 3.6. The thermal stability of the setup is investigated in Section 3.7. After moving to Munich, we realized that the experiment was suffering from mechanical noise originating from the acoustic noise present in the new lab. We designed an acoustic shielding box to improve the mechanical stability of the setup; its performance is analyzed in Section 3.8. Finally, in Section 3.9 we describe the locking scheme used to stabilize the cavity length.

3.1 The fiber based Fabry-Pérot cavity

Fiber-based Fabry-Pérot cavities were developed back in the early 2000s in the context of cavity quantum electrodynamics [99, 113–116]. The trigger for this research was the need for short cavities, capable of confining the electric field in a small volume while maintaining a high finesse. The major breakthrough came in 2006 [99, 116], when laser ablation was used for the first time to produce concave shapes at the fiber tips in a controlled manner.

Our aim is to perform cavity optomechanical experiments with low dimensional materials, such as van der Waals materials or carbon nanotubes. To increase the dispersive coupling G, the easiest and most straightforward option is to decrease the cavity length (Eq. 2.76). This is best achieved with fiber-based cavities and it is the approach we decided to take. We also target fabricating cavities with large finesse, because it boosts the circulating photon number – and consequently the coupling strength g – and contributes to maintaining small cavity linewidths $\kappa = \omega_{\mathrm{FSR}}/\mathcal{F}$. Additionally, both a high finesse and small beam waists w_0 are desirable if we ever want to combine our setup with a single-photon or spin degree of freedom, since the atom-cavity cooperativity scales as $C \propto \mathcal{F}/w_0^2$ [99].

3.1.1 Production of microscopic mirrors

Fiber preparation

The fibers employed in our lab are copper-coated single-mode (SM) and multimode (MM) fibers[1]. We first prepare the work space by covering the table with aluminum foil to avoid dust contamination. We cut the fibers into 140 cm-long segments and remove approximately 35 mm of the coating of one of the two fiber ends with a copper etching solution[2]. The solution's residues on the fibers must be cleaned with DI water first and later with IPA. We cleave the uncoated fiber ends with a Fujikura CT-101 cleaver to have a flat surface at the fiber end, only accepting cleaves with angles[3] below 1°.

The fibers are loaded into an aluminum holder that was designed by Matthias Mader (LMU) and fabricated at the workshop of the University of Konstanz. The holders have to be previously cleaned in three subsequent ultrasonic baths (DI water and soap, DI water, IPA) and baked at 130 °C for 1 h. Each holder accommodates 11 fibers and every one of them has to protrude the edge of the holder by the same amount (1 mm), since the mirror coating properties depend strongly on the distance from the fibers to the target of the sputtering machine [117].

CO_2 laser ablation

To be able to build stable cavities with lengths between 10 µm to 100 µm, we have to fabricate mirrors with a radius of curvature (ROC) in the 40-400 µm range. This parameter space opens the possibility of creating cavities in the near-planar ($L_{\mathrm{cav}} \ll R_1, R_2$) and concentric ($R_1 = R_2 = L_{\mathrm{cav}}/2$) configurations [77], where R_1 and R_2 are the input and output mirror's ROC. Near-planar cavities

[1] Art Photonics GmbH. Pure-silica SM, step index: *9/125 Cu.* Ge-doped MM, graded index: *50/125 Cu.*

[2] 36% solution of $FeCl_3$, dissolving 38 g of solute in 65 mL of water.

[3] The cleave angle is measured by the fiber splicer (Fujikura FSM-100P).

are desirable to obtain cavities insensitive to length fluctuations, while concentric ones are better when the aim is to reduce the cavity beam waist. On the other hand, to couple light in or out of the cavity through one of its ports, the overlap between the cavity mode and the fiber mode has to be maximized, which depends on the cavity length and mirror radius as well. Assuming both modes are Gaussian modes, the coupling efficiency ϵ is given by [99, 118]

$$\epsilon = \frac{4}{\left(\frac{w_f}{w_m} + \frac{w_m}{w_f}\right) + \left(\frac{\pi n_f w_f w_m}{\lambda R}\right)}, \tag{3.1}$$

where w_f is the fiber beam waist, $n_f = 1.46$ its refractive index and R the mirror's ROC. The Art Photonics SM fibers that we use yield $w_f = 5.29\,\mu\text{m}$. For our cavities, the output fiber is multimode, ensuring a coupling efficiency close to unity independently of the mirror's ROC. Figure 3.1a shows the coupling efficiency for the case of symmetric cavities ($R_1 = R_2$) as a function of the cavity length. The efficiency is nearly 1 for cavity lengths between 20 µm and 60 µm and mirrors with ROCs larger than 150 µm, which is the parameter range we aim for.

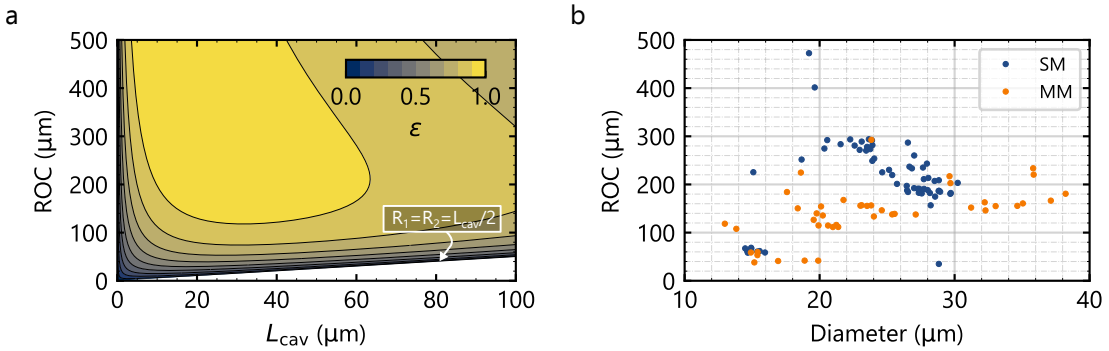

Figure 3.1: Mode matching efficiency and mirrors ROC. (a) Mode matching efficiency ϵ for a cavity with symmetric radius of curvature (ROC), $R_1 = R_2$, as a function of the cavity length. The white area under the line $R_1 = R_2 = L_{\text{cav}}/2$, highlighted with a white arrow, corresponds to unstable resonator configurations. (b) ROCs vs mirror diameter of the processed SM and MM fibers.

After determining the mirror parameters, we place the holders into plastic boxes for dust protection and bring them to the CO_2 laser ablation setup from Prof. Hunger's group in the Karlsruhe Institute of Technology (see Jonathan Körber's bachelor thesis [119] for more details on the setup and Refs. [99, 120] on the laser ablation technique). The fiber tips are shot with pulses of a duration of t ~ 100-200 µs and powers in the range of 1 W to 10 W depending on the targeted ROC. The number of pulses varies between 100 and 300. Afterwards, the fiber surface is reconstructed using an optical profilometer incorporated in the setup. The indentations are fit to a 2D Gaussian profile, whose full width at $1/e$ gives an estimate of the useful mirror diameter [99]. The radius of curvature is determined by fitting a parabola to the center of the indentation. At a later stage, we built an additional optical profilometer in our labs in Konstanz to be able to perform these measurements onsite (see Section 3.1.2).

In June 2018, we manufactured a batch of telecom fiber mirrors comprising a total of 45 MM and 66 SM fibers. Figure 3.1b shows their ROCs as a function of the mirror diameters. The major-

ity of the SM fibers have ROCs between 200 and 300 µm, with diameters between 20 and 30 µm; the MM fibers mostly have diameters between 100 and 200 µm. A smaller number of fibers are processed with mirror ROCs in the range 40-60 µm, suitable to build shorter cavities with smaller beam waists.

Coating

A commercial high-reflective coating (*LaserOptik GmbH*) was deposited on the fiber tips via ion beam sputtering. Each mirror is a distributed Bragg reflector (DBR) consisting of 18 pairs of Ta_2O_5 and SiO_2 layers and a final layer of Ta_2O_5. Each layer has a thickness of $\lambda/(4n)$, with n being the layer's refractive index and λ the wavelength in vacuum. The last layer of Ta_2O_5 is added because it is the material with lowest losses, and consequently it should be the layer facing the largest concentration of the electric field. The thickness of each layer is determined by the mirror's operational wavelength, which is $\lambda = 1550$ nm in our case. Given the refractive indices of the materials at that wavelength, $n_{Ta_2O_5} = 2.0856$ and $n_{SiO_2} = 1.4694$ [121], the expected thicknesses are $t_{Ta_2O_5} = 185.8$ nm and $t_{SiO_2} = 263.7$ nm. The number of layer pairs, on the other hand, is a consequence of the desired mirror's transmission. The coating run is designed to produce mirrors with a transmission of $\mathcal{T} = 10$ ppm to obtain a high finesse $\mathcal{F} > 100,000$ (Eq. 2.55). Figure 3.2a shows the DBR's transmission as a function of the wavelength. The blue line was measured by LaserOptik; the orange line shows our transfer matrix calculations for the given coating parameters. The inset shows a close up to the DBR band centered at 1550 nm. Figure 3.2b and Fig. 3.2c display the photograph of an uncoated and coated telecom fiber, respectively. The coating has a calculated thickness of 8.3 µm, and therefore the coated tip of the fiber is expected to have a larger diameter, with upper limit of 141.6 µm.

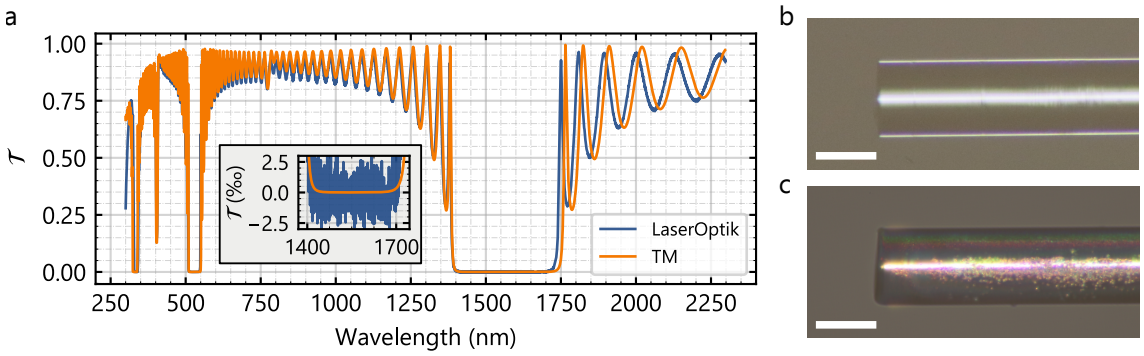

Figure 3.2: Fiber mirrors. (a) Measured (blue) and calculated (orange) DBR transmission $\mathcal{T}$ as a function of wavelength. The calculations were done using the transfer matrix formalism. (b) Uncoated telecom fiber. (c) DBR coated telecom fiber. In both cases the scale bar is 100 µm.

3.1.2 Mirror surface reconstruction

The relevant geometrical parameters of the laser-machined fiber tips are extracted by reconstructing their surfaces using an optical profilometer. The working principle is based on phase shifting interferometry measurements [122]. The main component of our phase shifting interferometer is

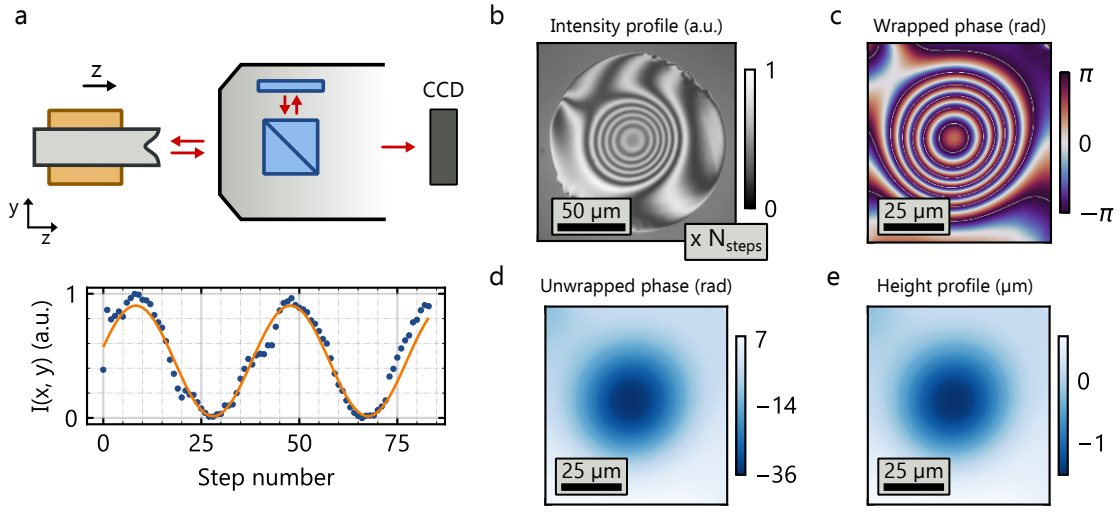

Figure 3.3: Phase shifting interferometry. (a) Sketch of the Mireau interferometry objective with incorporated beam splitter and fixed mirror. The fiber with the indentation is glued to a piezo element (orange square) that moves the fiber in the z direction in steps. A first calibration of the piezo allows to map the z movement with the intensity modulation $I = A\sin(4\pi z/\lambda+\phi_0)+B$ that is used at a later stage for the demodulation (Eq. 3.5 and Eq. 3.6). After calibration, the z position is varied N_{steps}-times and an interferometry intensity profile (b) is recorded with the CCD camera at each position. (c) Wrapped and (d) unwrapped phase for a close up around the center of the indentation. (e) Reconstructed height profile.

a Mireau interferometry objective (20x Nikon DI Interferometry Objective). This special objective has a built-in beam splitter and reference mirror (Fig. 3.3a), so that the images formed on a CCD camera chip present the standard fringe pattern from a Michelson interferometer (Fig. 3.3b). The fringes are produced by the profile-dependent phase difference $\varphi(x, y)$ that originates from the difference in optical paths due to the surface profile $z(x, y)$. In the ideal scenario of homogeneous illumination and perfectly balanced arms of the Michelson interferometer, the intensity on the camera chip will be

$$I(x, y) = I_{\text{dc}} + I_{\text{ac}}\cos\big(\varphi(x, y)\big). \tag{3.2}$$

As in a Michelson interferometer, two points separated by consecutive bright fringes correspond to a height difference of $\lambda/2$, which is a phase change of $\Delta\varphi(x, y) = 2\pi$. One could in theory count fringes and reconstruct the surface. Doing this, however, one cannot distinguish changes in intensity due to spurious mechanisms not related to height differences, like inhomogeneous illumination, that result in a position dependent DC component of the intensity, $I_{\text{dc}}(x, y)$. To eliminate them, one introduces a controlled phase element $\phi(z)$ that depends on the fiber position z, so that now the intensity profile becomes

$$I(x, y, z) = I_{\text{dc}}(x, y) + I_{\text{ac}}\cos\big(\varphi(x, y) + \phi(z)\big), \tag{3.3}$$

that can be expanded to

$$I(x, y, z) = I_{\text{dc}}(x, y) + I_{\text{ac}}\big[\cos\big(\varphi(x, y)\big)\cos\big(\phi(z)\big) - \sin\big(\varphi(x, y)\big)\sin\big(\phi(z)\big)\big]. \tag{3.4}$$

The phase $\phi(z)$ is shifted by changing the distance of the fiber surface to the objective, and at each position z an intensity profile is recorded $I(x, y, z)$. If the position of the fiber mirror is displaced

by Δz, then the change of controlled phase is $\Delta\phi = 4\pi\Delta z/\lambda$. By changing the position in steps of $\Delta z < \lambda/2$ over several half-wavelengths, every pixel $(x, y,)$ is scanned through several fringes, i.e. the local intensity $I(x, y)$ oscillates in a controlled manner with a $\lambda/2$ periodicity, but with a fixed $\varphi(x, y)$. One can fit Eq. 3.4 to $\cos(\phi(z))$ and $\sin(\phi(z))$, obtaining two quadrature signals which allow us to extract the desired phase factor $\varphi(x, y)$. This method is called, for obvious reasons, phase shifting interferometry; we illustrate its working principle in Figure 3.3.

Let M be the number of scanned periods, and N the number of z steps per period, each quadrature is obtained as [123]

$$X(x, y) = \sum_{i=0}^{MN-1} I(x, y, z_i)\cos(4\pi z_i/\lambda) \tag{3.5}$$

$$Y(x, y) = \sum_{i=0}^{MN-1} I(x, y, z_i)\sin(4\pi z_i/\lambda), \tag{3.6}$$

from which

$$\varphi_w(x, y) = \tan^{-1}(Y/X) \tag{3.7}$$

The result of Eq. 3.7 is a phase $\varphi_w(x, y)$ going from $-\pi$ to π. We need to *unwrap* $\varphi_w(x, y)$ to obtain the accumulated phase, $\varphi(x, y)$. To that end, $\varphi_w(x, y)$ is fed to a phase-unwrapping algorithm [122]. After that, the height profile is calculated as

$$z(x, y) = \frac{\lambda\varphi(x, y)}{4\pi}. \tag{3.8}$$

The initial version of the profilometer was designed and constructed by Alexandre Brieussel. The fiber is mounted on a fiber holder that its glued on a piezo element; the piezo is used to change the z position of the fiber. The piezo is connected to the DAC port of an Arduino DUE board that, after passing through a home-build amplifier, can generate voltages between 5.5 V and 27.5 V, in steps of minimum 5 mV. The sample is illuminated with a red LED ($\lambda = 632$ nm). The setup was upgraded by changing the old Thorlabs CCD camera to a Zelux Thorlabs camera, with a larger CCD chip size. This, together with a larger focal length lens ($f = 200$ mm), increased the lateral resolution of the setup from 360 nm/px up to 170 nm/px. A picture of the setup is shown Fig. 3.4a. The original Matlab code, written by Alexandre Brieussel, was modified to incorporate the new camera and corrected to produce the right phase profiles.

Our vertical resolution is limited by the phase-reconstruction analysis. To illustrate this, Figure 3.4b shows a cross-section of the surface profile (blue) and its derivative amplified by a factor of 10 (orange) for the SM fiber mirror of cavity C9 (see Table 3.1). The surface presents small jumps that are more appreciable when looking at its derivative. As measure of the resolution in the z direction we can take the root mean square of the derivative of the profile, yielding a resolution of 55 nm. The jumps' origin is unclear and was not studied because they do not affect the mirror's geometrical parameters, which are only influenced by features at larger length scales. The jumps could originate from the unwrapping algorithm – right now the code uses the built-in unwrap function from Matlab R2021a, but there are more sophisticated algorithms [124]. Additionally, the cosine and sine factors in Eq. 3.5 and Eq. 3.6 are currently obtained by running a calibration prior to acquiring all the interferometry images (see the caption in Figure 3.3). One could fit the same function to each of the pixels instead to get a better extraction of the reconstructed phase.

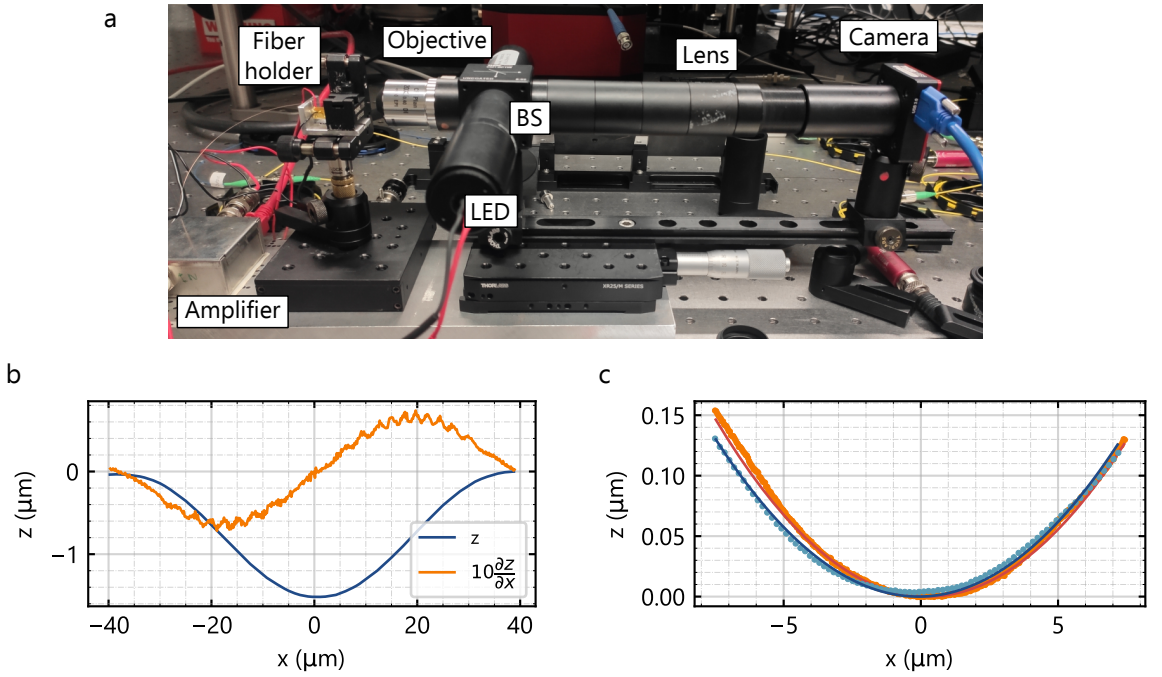

Figure 3.4: Optical profilometer components and performance. (a) Our phase shifting interferometer consists of, from left to right: a home-built amplifier, a Thorlabs fiber holder glued to a piezo element, a Mireau interferometry objective, a beam splitter (BS), a 200 nm focal length lens, a red LED, a Thorlabs Zelux camera and an Arduino DUE board (not shown). (b) Cross section of the height profile (blue) of the SM fiber mirror of cavity C9 (see Table 3.1), together with its derivative amplified by a factor of 10 (orange), measured with our setup at TUM. (c) Cross section of the profile in (b) around its center. Dots are experimental data and solid lines parabola fits. The blue data was measured at TUM and the orange data at KIT.

After the height profile is obtained, we fit the data to a 2D Gaussian with a linear background to extract the mirror diameter [99]. Finally, we fit a 2D parabola in an area of $15 \times 15\,\mu m^2$ around the center of the mirror, from which the radius of curvature and asymmetry are obtained[4]. We re-measured few of the fibers fabricated and characterized at KIT with our optical profilometer to compare their performance. The setup at KIT had a horizontal resolution of 41 nm/px. Both analysis yield the same mirror depths and radii of curvature within 5 %. Figure 3.4c shows the data around the center of the same mirror as in Figure 3.4b measured at KIT (data as orange dots, parabola fit as red line) and re-measured at TUM (data as blue dots, parabola fit as blue line). The setup at KIT yields a mean ROC of $R = 205.8\,\mu m$ and ours $R = 207.2\,\mu m$ for this particular example.

3.1.3 Cavity assembly

To form a cavity we select two fiber mirrors: a single-mode one and a multimode one (Fig. 3.5a). Each fiber is glued to a silicon v-groove (Fig. 3.5b, top) and each v-groove is glued to a shear piezo

[4] All mirrors have some degree of asymmetry due to the shooting process resulting in an elliptic parabola. The asymmetric is defined as $\epsilon = R_x/R_y - 1$, with $R_{x,y}$ the ROC in each direction.

(PZT) (Fig. 3.5b, bottom). The piezos, when fed with a voltage, allow us to tune the distance between the fibers within the piezos' range[5]. The piezos are fixed by UV-epoxy to a quartz block that serves as a base for the the whole cavity (Fig. 3.5b, bottom). The v-groove from the MM fiber, with the fiber glued on it, is the last element to be glued in the cavity assembly – it is glued to its piezo with Stycast glue. All degrees of freedom between the fibers (x, y, z directions and angles) are fine-tuned during the curing of the Stycast glue. Although it takes 24 h to cure, the alignment is done during the first 12 h. Once it is cured, the cavity is a monolithic device (Fig. 3.5b, bottom): neither the fibers nor any of the other cavity components can be removed or changed without damaging other parts. This rigid design ensures a good mechanical and thermal stability compared to other cavity designs where the fibers can be retracted at a later stage [20, 125]. Of course, the big expense is that it is complicated to insert the sample in between the fibers, which are separated by only 40 µm (less than half of the diameter of a hair!).

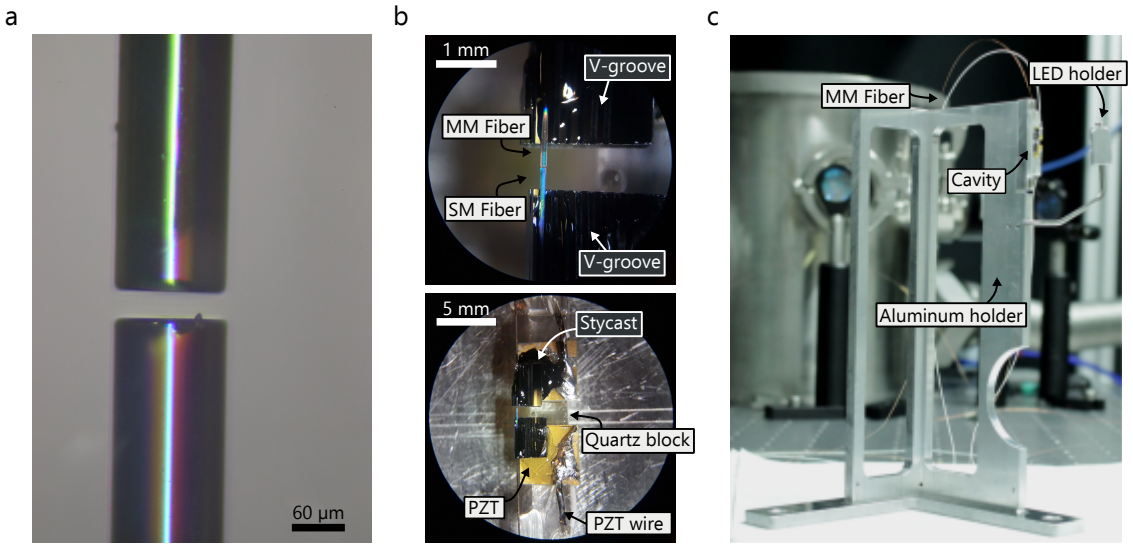

Figure 3.5: Fiber-based microcavity. (a) Image of a single-mode (top) and multimode (bottom) fiber facing each other separated by a distance $L_{cav} \simeq 40\,\mu m$. (b) Photograph of the final device. The two fibers are glued to silicon v-grooves with Dymax UV-epoxy. Both v-grooves are glued to shear piezos: the SM fiber's v-groove with Dymax UV-epoxy and the MM fiber's v-groove with Stycast (black glue). (c) The cavity is glued with Dymax epoxy to an aluminum holder that is placed later inside the vacuum chamber.

The gluing and aligning process is explained in great detail in the PhD theses from Sebastian Stapfner [111] and Felix Rochau [112], with the following modifications. The fast curing UV-epoxy used to glue the single-mode fiber was changed from the old Dymax OP 4-20632 to Dymax OP-24-REV-B (liquid) or Dymax OP-29 (viscous), both yielding good results. The reason for the change was that Dymax stopped the fabrication of the OP 4-20632. We also changed the stereo microscope (x4 magnification) used for fiber alignment to a higher magnification tube lens system (magnification adjustable up to x37), providing a better optical access and easier alignment. The tube lens belongs to the setup used to transfer the van der Waals materials and is described

[5] Scanning both piezos symmetrically with a ramp waveform of peak amplitude $V_p = 10\,V$ that is amplified with a HV amplifier produces a cavity length change of around $\Delta L \simeq 1.6\,\mu m$ (see Appendix B.1).

in Section 4.2.

Finally, the cavity is mounted on an aluminum holder or frame as shown in Figure 3.5c. The frame's constraint is that the cavity must be located at a height matching the one of the sample when placed on the positioning stages. We designed the holder with Louis Kukk's assistance, who produced it at the workshop of the University of Konstanz. It contains a LED holder looking like a light pole that is used to provide extra illumination to the optical access of the setup. The latter is necessary to monitor the insertion of the sample into the cavity.

3.2 Optical setup

All components of our optical setup, shown in Figure 3.6, are fiber based. The fibers from the cavity are fusion-spliced to commercial fibers with a Fujikura FSM-100 splicer. The cavity's SM fiber is spliced to a Tholarbs SMF28 fiber and the cavity's MM fiber to a graded-index Thorlabs GI50D fiber. The rest of the fiber connections are done with standard FC/APC connectors.

The setup has three different light sources and respective light paths: the lock laser ($\lambda = 1550\,\text{nm}$), the probe laser ($\lambda = 1550\,\text{nm}$) and a 1310 nm-SLED. Each wavelength is depicted with one color in Figure 3.6, blue for 1550 nm and red for 1310 nm. In the following we describe each of the light paths.

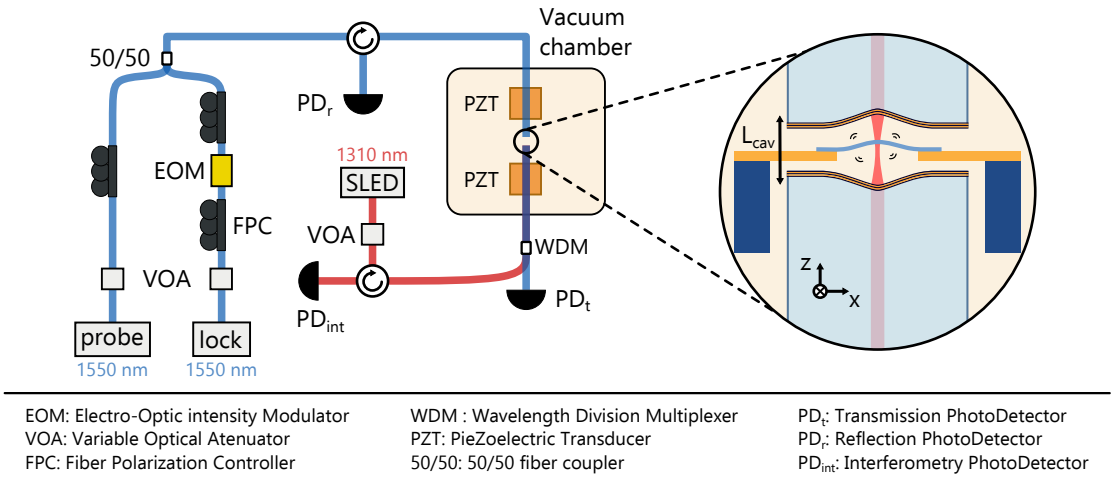

Figure 3.6: Optical setup. The lock laser is used to characterize the cavity. The cavity is locked to this laser when performing dynamical backaction experiments. The probe laser is used to scan the laser frequency across the cavity resonance when the cavity is locked to exert an optical force on the resonator. The SLED, whose wavelength is outside the DBR coating band, is employed for interferometry measurements. The fiber polarization controllers have a $\lambda/4$-$\lambda/2$-$\lambda/4$ configuration.

The lock laser is an ultra-low noise telecom fiber laser (NKT Koheras Basik E15) that we use as main light source to perform all the cavity characterization measurements and the cavity-to-laser locks. For this reason, we refer to this laser as *lock laser*, even for the cavity characterization measurements where the cavity is not locked. The laser is operated at its maximum power, $P = 40\,\text{mW}$,

where it operates at its best noise performance[6]. Because we need to use very low input powers to avoid nonlinear cavity effects ($P_{\text{in}} < 30\,\mu\text{W}$, cavity dependent), we use fiber-based optical variable attenuators (VOA, Thorlabs V1550A, maximum attenuation of 25 dB) at different stages to reduce the power. We employ an electro-optic analog intensity modulator (EOM, iXblue MXAN-LN-10) to generate sidebands that are used for the heterodyne measurements and to generate the error signal for the cavity lock (see Section 3.9). The fibers of the EOM are panda polarization maintaining (PM) fibers. We place a fiber polarization controller (FPC) between the laser and the EOM to match the laser's polarization to the EOM's. An additional FPC after the EOM allows us rotate the linear polarization to match the target cavity polarization direction. The cavity polarization mode splitting is introduced later in Section 3.4. Finally, the lock laser meets with the probe laser by means of a 50/50 fiber optic coupler (Thorlabs, TN1550R5A2).

The probe laser is a tunable laser (Newport, Velocity TLB-6728) with a mode-hop free wide tuning range of 50 nm (1520-1570 nm) and a fine-tuning range of 30 GHz. We use this laser for dynamical backaction experiments, where we use the laser's fine-tuning option to scan the probe laser's frequency across the cavity resonance. We use an additional VOA to attenuate the laser power and a FPC to select the desired polarization. The laser is finally connected to the other port of the 50/50 fiber optic coupler.

One of the outputs of the 50/50 coupler is connected to port 1 of a fiber circulator (Thorlabs, 6015-3-APC). Port 2 of the circulator is directly connected to the cavity SM fiber, sending the light from both the probe and lock laser to the cavity. The cavity reflection is sent to a fast photodetector (Thorlabs PDB435C-A, 350 MHz bandwidth) connected to port 3 of the circulator. We refer to this photodetector as reflection photodetector, PD_{r}. The light transmitted from the cavity is sent to a 1310/1550 nm wavelength division multiplexer (WDM, Thorlabs WD1350A). The 1550 nm port is connected to the transmission photodetector (PD_{t}) that detects the cavity transmission at $\lambda = 1550\,\text{nm}$.

The other port of the WDM is connected to the light path from the 1310 nm-SLED. The SLED's wavelength is outside the mirror coating band – we therefore use it to perform interferometry measurements when the sample is inserted. The light from the SLED is attenuated with a VOA and then sent to port 1 of a 1310 nm circulator (Thorlabs CIR1310-APC). Port 2 is connected to the 1310 port of the WDM. The light reflected back from the cavity at 1310 nm goes again through the WDM and is sent to a photodetector connected to port 3 of the 1310 circulator. We refer to this detector as interferometer detector, PD_{int}. The detectors used for transmission and interferometry depend on the exact measurement and are described in the next section.

3.3 Electrical setup

Light is converted to electrical signals through photodetectors (PDs). Depending on the frequencies and magnitude of the signals we aim to detect, we need to use PDs with different bandwidths and gains, respectively.

The transmission detector needs to have large gains to be able to detect the small transmitted powers, which are in the order of 1 μW or smaller. When the transmission port is used to create

[6] This is specified by the supplier.

the error signal for the lock, we need a detector with a high gain to provide a good signal but with a large enough bandwidth to be able to resolve the demodulation sidebands (remember that gain and bandwidth compete against each other [126]). For those cases, we use a home-built detector[7] with an RF bandwidth of 30 MHz and RF and DC gain of −0.7 V/μW. The DC output has an offset of 25 mV. For the cavity characterization and the measurements of the dispersive and dissipative couplings, which do not require large bandwidths, we use a commercial variable gain photodetector (Femto OE200) with gains from 0.1 V/μW to 10^5 V/μW. The largest bandwidth for this detector is 500 kHz. If for any reason the Femto detector is used to measure the 1310 nm signal, the selected gain has to be scaled down by a factor 0.92 to account for the different responsivity at different wavelengths.

The detector used for the 1310 nm signals is another home-built detector with the same specs as the home-built one previously described. The reflection photodetector (Thorlabs PDB435C-A, 350 MHz bandwidth) has a DC and RF gain of 0.01 V/μW.

We perform mainly three types of measurements: the characterization of the cavity to extract the relevant empty cavity parameters, the measurement of the static dispersive and dissipative couplings, and the measurement of dynamical backaction, usually in that order for a given cavity. The electronics involved in each of them depend on the required cavity length scan range and whether the cavity length needs to be stabilized (locked) or not. In all cases, a ramp waveform is generated by a Keysight arbitrary waveform generator (AWG, Keysight 33521B series) with a frequency of 9 Hz and a peak voltage V_p (maximum of $V_\mathrm{p} = 10$ V). The corresponding peak-to-peak voltage, when directly sent to one of the piezos without amplification, corresponds to a maximum frequency detuning of $\Delta_\mathrm{max}/2\pi = \pm 26$ GHz (see Appendix B.1). The output of the AWG is sent to an analog lock box (designed and built by Anton Scheich, chair of T. Hänsch at LMU, Munich), which has an input range of ±14 V. The lock box can attenuate the input signal and change its offset with potentiometers, and has a maximum output of ±10 V. We describe the specifics regarding each measurement in the following paragraphs.

Cavity characterization

Figure 3.7a displays the electronic equipment involved in this measurement. For convenience, some optical components are cut off through a fade, but they can be recovered from Figure 3.6. The output of the lock box (PI, from proportional-integral controller) is sent directly to one of the piezos. In principle the lock box is not necessary, because it basically mimics the output of the AWG, but we keep it to avoid moving devices around. Since the cavity linewidths are in the megahertz regime, the frequency detuning of $\Delta_\mathrm{max}/2\pi = \pm 26$ GHz provided by the piezo scan is enough to scan through a cavity resonance. The other piezo is used to bring the cavity in resonance. It is fed with a DC voltage generated by a UHFLI Zurich instruments lock-in amplifier[8] (aux port, ±10 V) that is amplified by a home-built HV amplifier. The amplifier has an input of ±10 V, a gain

[7] The detector was originally designed by Stephan Manus (LMU), and has some modifications from Felix Rochau and Alexandre Brieussel. It was built by the electronic workshop of the University of Konstanz. For more details on the detector see Ref. [112].

[8] The UHFLI is a powerful device. As we will see later, we mainly use it to generate the error signal to stabilize the cavity length. Still, its 600 MHz-bandwidth is not necessary for our experiments, but since it was available we use it given all its functionalities.

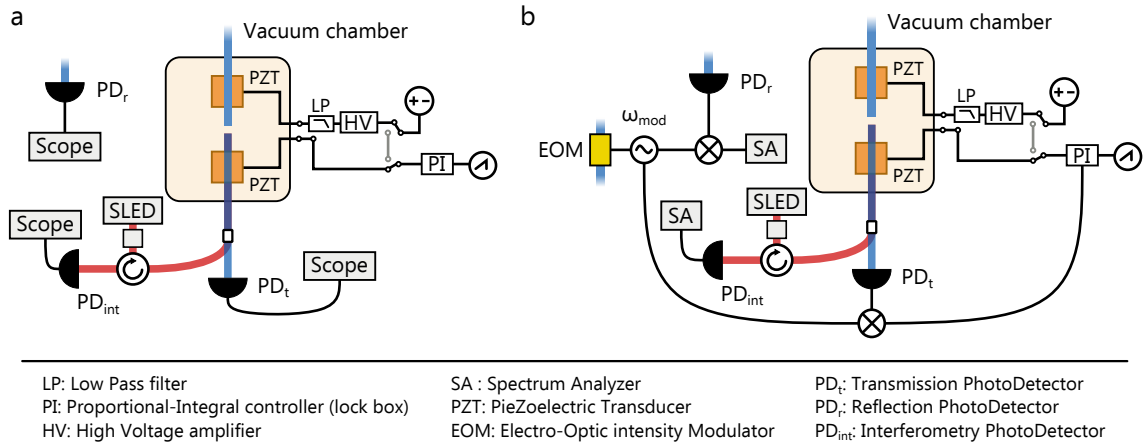

Figure 3.7: Electrical setup. Electronics involved in (a) the cavity characterization measurement and (b) in the dynamical backaction experiment. In both cases, the cavity is brought in resonance by feeding the upper piezo with a HV-amplified DC voltage. The cavity length is scanned by sending a ramp waveform to the lower piezo. In (a), we record the DC traces of the transmission, reflection and interferometry detectors with oscilloscopes. In (b), the RF outputs of the reflection and interferometry detectors are connected to spectrum analyzers to measure the mechanical response of the resonators. The DC component of all detectors, although not shown, is monitored with oscilloscopes as well. The EOM modulates the lock laser at ω_{mod}. We demodulate the transmission signal at the same frequency, which we use to stabilize the cavity length through the lower piezo (see main text for details). The low pass filter has a cutoff frequency of 16 Hz in both cases. For convenience, some optical components are cut off through a fade in both (a) and (b), but they can be recovered from Figure 3.6.

of 40 V/V and a bandwidth of 20 kHz. Its output is protected with a low pass filter (cutoff frequency of 16 Hz). The reflection and transmission of the cavity are recorded by the Thorlabs and Femto detectors, respectively.

Dynamical backaction

Although the dynamical backaction experiments are the last measurements we usually perform, its electrical components, shown in Figure 3.7b, are very similar to the cavity characterization ones: they both require a similar piezo scan range. Consequently, we display them together in the same figure. The cavity is brought on resonance with the amplified DC voltage sent to one of the piezos as described in the previous subsection. We use the UHFLI Zurich instruments lock-in amplifier to generate an RF signal at ω_{mod} to produce sidebands on the lock laser. In this case, we use the home-built photodetector with bandwidth of 30 MHz in transmission. The RF output from the transmission PD is sent back to the lock-in and demodulated at ω_{mod}. One of the quadratures is sent through a lock-in's aux port to the lock box and employed as error signal for the lock (similar to a PDH technique but not quite the same, as explained in Section 3.9). The lock box has now two inputs: the scan generated by the AWG and the error signal. By flipping a switch, the scan is disconnected from the output of the lock box and the proportional-integral (PI) controller of the lock box sends a control signal to the piezo, that stabilizes the cavity length to the set point of the error signal. The P and I gains can be tuned with potentiometers.

The spectral response of the mechanical resonators is measured from the reflected light from the cavity via the Thorlabs detector. The RF output of the detector is sent to the lock-in and demodulated at ω_{mod} to separate the contributions form the lock and probe lasers. The PSD of the demodulated signal is measured with a spectrum analyzer (Rhode & Schwarz FSVR7).

Static dispersive and dissipative couplings

The dispersive coupling of our samples lead to cavity detunings larger than 100 GHz, outside the scan range of the AWG. To be able to resolve them, the output of the lock box is sent to the home-built high voltage amplifier (gain of 40 V/V and a bandwidth of 20 kHz), shown in Figure 3.8. We change the filter of its output to a cutoff frequency of 160 Hz to be able to resolve the scan, and send it directly to both piezos, that are scanned symmetrically. The maximum frequency detuning is $\Delta_{\mathrm{max}}/2\pi = \pm 4.5\,\mathrm{THz}$ for a $V_{\mathrm{p}} = 10\,\mathrm{V}$ scan, enough to resolve up to three free spectral ranges in most of our cavities. The piezos show a nonlinear response – a polynomial of second order – due to the large input voltages[9]. The piezo scan to frequency conversion is explained in detail in Appendix B.1. The cavity reflection and transmission are measured with the Thorlabs and Femto detectors, respectively.

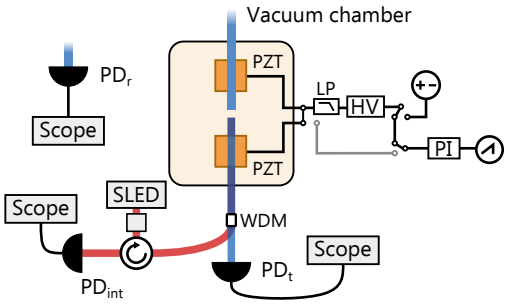

LP: Low Pass filter
PI: Proportional-Integral controller (lock box)
HV: High Voltage amplifier
WDM: Wavelength Division Multiplexer
PZT: PieZoelectric Transducer
PD$_r$: Reflection PhotoDetector
PD$_{int}$: Interferometry PhotoDetector
PD$_t$: Transmission PhotoDetector

Figure 3.8: Electrical setup for measuring the static couplings. Both piezos are driven symmetrically with a ramp amplified with a high voltage amplifier. The low pass filter has a cutoff frequency of 160 Hz. The transmission photodetector is the high gain Femto OE200. Some optical components are cut off through a fade, but they can be recovered from Figure 3.6.

3.4 Fiber cavity characterization

The transmission, reflection and circulating fields (Eq. 2.56) of a Fabry-Pérot cavity are completely determined by the cavity linewidth κ, free spectral range ω_{FSR} – and therefore cavity length L_{cav}

[9] After amplification, a ramp amplitude of $V_{\mathrm{p}} = 10\,\mathrm{V}$ is transformed into $V_{\mathrm{p}} = 400\,\mathrm{V}$. We always specify the ramp waveform's amplitude V_{p} in terms of the output of the AWG *before* it is amplified, because this is what we monitor and change in the experiment. To obtain the voltage at the piezo one has to multiply V_{p} times the amplifier's gain (40 V/V).

– and external couplings, $\kappa_{1,e}$ and $\kappa_{2,e}$. In a fiber-based Fabry-Pérot cavity, however, one needs to also take into account the mode-filtering from the fiber core: the mode matching between the fiber Gaussian mode and the one from the cavity (Eq. 3.1) [127]. Additionally, in most of our fiber mirrors the center of the mirror does not necessarily match the center of the core of the fiber, which reduces the mode matching even more. Figure 3.9a shows the center mismatch of one of our fiber mirrors. Gallego and coauthors [127] did an extensive experimental and theoretical study on fiber core filtering effect. For us, it is sufficient to know that the cavity's response equations are now changed into

$$\left|\frac{E_0^-}{E_0^+}\right|^2 = \left|\beta - \frac{\kappa_{1,e}\alpha^2}{\kappa/2 - i\Delta}\right|^2, \tag{3.9}$$

$$\left|\frac{E_t}{E_0^+}\right|^2 = \frac{\kappa_{1,e}\kappa_{2,e}|\alpha|^2|\alpha_2|^2}{(\kappa/2)^2 + \Delta^2}. \tag{3.10}$$

Let's look first at the reflection using Figure 3.9b as reference. Two fields are relevant in this case,

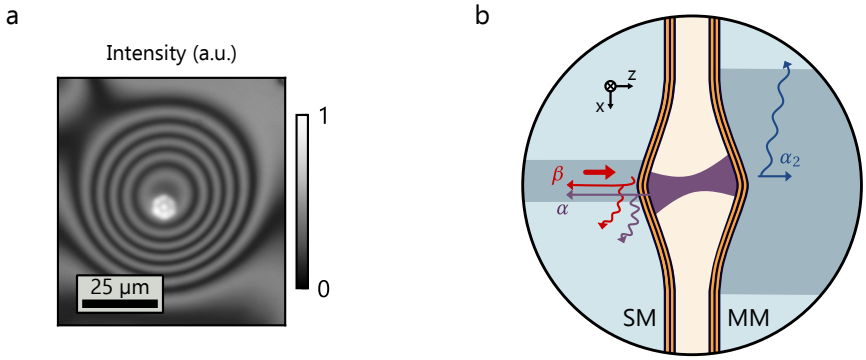

Figure 3.9: Fiber filtering. (a) Interferometry image of a mirror profile with the fiber core illuminated (bright white circle in the middle). The image shows a typical offset between the mirror's center and the fiber core of 4 µm. This particular fiber mirror was used as SM fiber for cavity C8 (Table 3.1), which has $|\beta|^2 = 0.6$. (b) Sketch illustrating the fiber filtering contribution to the reflected and transmitted fields in a fiber-based microcavity. The gray shaded areas depict the fiber core for both SM (9 µm-diameter) and MM fiber (50 µm-diameter). See the main text for a detailed explanation.

the one that is prompt reflected from the first mirror (red) and the one corresponding to the circulating field inside the cavity that leaks out through the first mirror (purple). Each of them will have a different mode matching efficiency with respect to the Gaussian mode from the fiber-core: β accounts for the mode matching efficiency between the prompt reflection and the fiber, and α between the field leaking from the cavity and the fiber. The part that is not mode matched is lost in the cladding (wavy-arrows). On top of that, they do not necessarily have to be in phase, which means that α and β are complex numbers. The value $|\beta|^2$ receives the name of *prompt reflection* and is the fraction of light power reflected from the cavity when it is far from resonance. When we measure the reflection response in the lab, we cannot distinguish between $\kappa_{1,e}$ and α, so we redefine the input coupling to $\kappa^*_{1,e} = \kappa_{1,e}\alpha^2$; dropping the superscript asterisk for convenience, we obtain

$$\left|\frac{E_0^-}{E_0^+}\right|^2 = |S_{11}|^2 = \left|\beta - \frac{\kappa_{1,e}}{\kappa/2 - i\Delta}\right|^2. \tag{3.11}$$

The filtering effect form the fiber core leads to an asymmetry in the reflection response that is not present in standard Fabry-Pérot cavities, and a shifting of the minimum of the reflection compared to the maximum of the transmission.

The transmission case (blue in Fig. 3.9b) is easier; α_2 is the mode matching between the cavity and transmission fiber modes. Similarly, we can define $\kappa^*_{2,e} = \kappa_{2,e}|\alpha_2|^2$, leading to

$$\left|\frac{E_t}{E_0^+}\right|^2 = |S_{21}|^2 = \frac{|\kappa_{1,e}|\kappa_{2,e}}{(\kappa/2)^2 + \Delta^2}, \tag{3.12}$$

where we have dropped the superscript asterisk again. In the last two expressions we have introduced the scattering matrix notation for the transmission and reflection from the cavity, $|S_{21}|^2$ and $|S_{11}|^2$, respectively. We note that with the new definition of the external couplings they are no longer a measure of the mirrors' transmission (see Section 2.3.2).

3.4.1 Power calibrations

To fit Eq. 3.11 and Eq. 3.12 and extract all cavity parameters we need to know the transmitted, reflected and input powers precisely. The gain of all photodetectors has to be very well characterized and the losses of all fiber connections minimized. The fiber connectors are cleaned and inspected with a fiber microscope. In general, the losses upon fiber splicing[10] (≤ 0.01 dB) are lower than the ones in the FP/APC fiber connectors, which are around 0.25 dB. The transmission of each of the fiber components (circulators, WDMs, fiber splitters) must also be characterized.

After these calibrations, we can calculate the transmitted power as $P_t = V_t/(G_t T_t)$, where V_t is the voltage measured at the oscilloscope, G_t the gain of the transmission detector and T_t the product of the transmission of each of the fiber components/connectors involved in the transmission light path. The reflected power follows $P_r = V_r/(G_r T_r)$, similarly.

The input power of the cavity can be measured from the off-resonant cavity reflection if the prompt reflection of the cavity $|\beta|^2$ is known. In that case,

$$P_0 = \frac{V_r}{G_r T_{23} |\beta|^2}, \tag{3.13}$$

with T_{23} being the circulator's transmission from port 2 to 3. To measure the cavity prompt reflection we use a fiber retroreflector (Thorlabs, P5-SMF28ER-P01-1) with a known[11] reflection power coefficient of 0.97. The prompt reflection is then measured as

$$|\beta|^2 = 0.97 \frac{V_r^{\text{cav}}}{V_r^{\text{rr}}}. \tag{3.14}$$

V_r^{cav} denotes the measured voltage at the oscilloscope from the off-resonant cavity reflection and V_r^{rr} the one from the retroreflector.

3.4.2 Linewidth and external couplings

We bring the cavity on resonance by sending a DC voltage to one of the piezos; at the same time we scan the cavity length by sending a ramp waveform to the other one (see Section 3.3). The time axis

[10] They are measured by the splicer. If any splice has losses larger than 0.01 dB we redo the splice.

[11] We cannot measure this value. We take the one provided in the spec sheet.

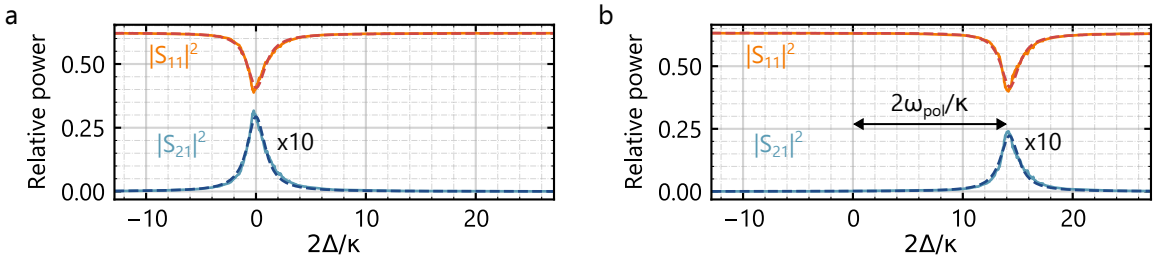

Figure 3.10: Cavity characterization. Cavity reflection $|S_{11}|^2$ and transmission $|S_{21}|^2$ for the lower frequency (a) and higher frequency (b) polarization mode of the cavity for an input power of $P_0 = 22\,\mu W$. For this cavity (C8, see Table 3.1), the polarization splitting and mean linewidth (of the two polarizations) are $\omega_{pol}/2\pi = 133.5\,MHz$ and $\kappa/2\pi = 18.7\,MHz$, respectively.

of the oscilloscope is transformed into frequency by modulating sidebands with the EOM. One can calibrate the voltage to frequency conversion for a particular ramp peak-amplitude V_p and piezo, so that the sidebands are no longer needed. For the 9 Hz ramp, we obtain a calibration factor[12] of $-2.6\,GHz/V$, specified to ramp peak voltages V_p. The transformation between time and frequency of the oscilloscope's traces and the piezo scan calibration are carefully described in Appendix B.1. Figure 3.10 shows the transmission $|S_{21}|^2$ and reflection $|S_{11}|^2$ of the two non-degenerate polarization modes of the cavity, together with the theoretical fits using Eq. 3.11 and Eq. 3.12. The fit results of all the cavities constructed during this work are presented in Section 3.4.4. The polarization mode splitting originates from the fiber mirrors' ellipticity [128, 129].

Nonlinear effects

If the cavity is pumped with sufficiently high optical powers, the expansion and contraction of the mirrors changes the optical path length inside the cavity. This effect is proportional to the circulating photon number n_c and is therefore a nonlinearity of the Kerr type [130, 131]. In this case, the circulating photon number is no longer given by a Lorentzian function (Eq. 2.56 and Eq. 2.58). Instead, one has to find the solution to the nonlinear equation

$$\frac{n_c}{n_{in,crit}}\left[(\mathcal{K}n_c - \Delta)^2 + (\kappa/2)^2\right] = \kappa\frac{n_{in}}{n_{in,crit}}, \tag{3.15}$$

where $\mathcal{K}$ is the Kerr nonlinear coefficient, n_{in} the input photon rate and $n_{in,crit} = \kappa^2/(3\sqrt{3}|\mathcal{K}|)$ [131].

Let's take a look at the behavior of the photon number as a function of the input power through the ratio $n_{in}/n_{in,crit}$ (Fig. 3.11a). For values of $n_{in}/n_{in,crit} \ll 1$ (blue line), the circulating photon number follows a Lorentzian function characteristic from a linear cavity. In this case, Eq. 3.15 has a unique solution. As we increase the input power, the maximum of the cavity resonance is shifted towards negative detunings and the left side of the curve gets increasingly steep. This is characteristic of systems with a negative Kerr nonlinearity ($\mathcal{K} < 0$), which is the case of our cavities

[12] This value was measured for the piezo of the SM fiber of cavity C8 (see Table 3.1). A different piezo will have a different value. The sign of the calibration factor depends on how the piezos are glued. For this cavity, the cavity length increases for positive voltages, therefore the frequency decreases and the sign is negative.

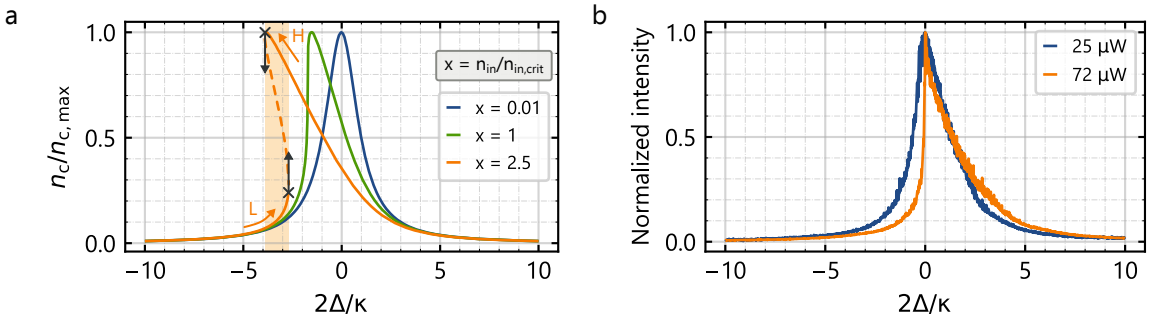

Figure 3.11: Cavity nonlinear response. (a) Normalized circulating photon number versus cavity detuning for different values of the ratio $n_{\text{in}}/n_{\text{in,crit}}$. The curves are generated solving Eq. 3.15 using the parameters $\mathcal{K}/2\pi = -240\,\text{Hz/photon}$ and $\kappa/2\pi = 18\,\text{MHz}$. The python code used to solve the nonlinear equation was provided by Philipp Bredol. (b) Normalized nonlinear cavity transmission for different input powers. The detuning is swept from negative to positive values, and is set to 0 at the point of maximum transmission. The blue curve ($P_0 = 25\,\mu\text{W}$) is slightly asymmetric around the cavity detuning. The orange line ($P_0 = 72\,\mu\text{W}$) shows a clear bistable behavior manifested as an infinitely steep transition from the lower to the higher branch.

as we will see later. When $n_{\text{in}}/n_{\text{in,crit}} = 1$ (green line), the system reaches the critical point. If the input power is further increased so that $n_{\text{in}}/n_{\text{in,crit}} > 1$ (orange curve), then Eq. 3.15 has three solutions for a particular detuning range. From the three solutions, only two are stable, both of them depicted as solid orange lines in the figure. Among them, one has a larger photon number (top solid line) than the other (bottom solid line). We label them as high (H) and low (L) photon number solution. The bistable regime is highlighted with a orange shaded area in Figure 3.11a and the unstable solution is depicted as an orange dashed line. This leads to an optical bistability: the behavior of the cavity depends on the direction in which we sweep the frequency detuning, giving rise to a hysteresis of the photon number with respect to the detuning's sweep direction [99, 132]. For example, if we start from negative detunings in the low photon number solution, when the system reaches the bifurcation point (black lower cross), it jumps to the high photon number solution. The jump is indicated with a black arrow that points upwards. On the contrary, if we start sweeping from positive detunings, the system starts in the high photon number solution until it reaches the other bifurcation point (higher black cross). Then, it falls down into the low photon number solution. The latter is represented by a downwards pointing black arrow.

Figure 3.11b shows the normalized experimental cavity transmission for different input powers. The detuning is swept from negative to positive values and set to zero at the point of maximum transmission[13]. As the power is increased, the cavity response becomes more and more steep for negative detunings: our cavity has a negative Kerr nonlinearity. The sign of the nonlinearity is better understood if we start on the high photon number solution. First, we need to remember that when we change the cavity detuning, what we are really doing is changing the cavity length with the fiber mirrors' piezos. If we start with a shorter cavity (positive detuning, higher photon number solution), the photon number builds up as the cavity length is increased. This means that the detuning is swept towards negative values. The mirrors' expansion compensates the cavity length increase from the mirrors' piezos [99]. This effectively manifests as having a high photon

[13] We did not measure the relative detuning shift between the linear and nonlinear cavity response.

number at longer cavity lengths, i.e. negative detunings, compared to what we would expect for a linear cavity. We usually start observing a nonlinear behavior for input powers around 25 µW, manifested as a slight deviation from the expected Lorentzian trend (Fig. 3.11b, blue solid line). We measure a bistable behavior for input powers beyond 35 µW approximately. In the example we show the extreme case for $P_0 = 72\,\mu W$ (Fig. 3.11b, orange line). Because the detuning is swept from negative to positive values, the orange line sharply transitions between the low to the high photon number solution at the bifurcation point.

If the readers are familiar with the nonlinear response of a mechanical resonator, they could wonder: why does the nonlinear cavity response look like the amplitude response of a nonlinear mechanical oscillator [133] with a negative Duffing parameter? Indeed, both problems are equivalent, but the difference is the starting point. For our case, Equation 3.15 is derived using the Hamiltonian formulation and input output theory of a cavity with a Kerr nonlinearity [131]. The Duffing model, on the contrary, starts directly from the equation of motion of a damped, driven oscillator in a nonlinear potential. David Zöpfl demonstrates the equivalence of both approaches in his PhD thesis [134].

3.4.3 Cavity length and free spectral range

When we build the cavity we estimate the cavity length from the images taken with a camera, using the fiber diameter as length reference (considering the increased diameter due to the DBR coating). This is, however, just quick and underestimates the cavity length because it does not consider the depth of the mirror indentation, DBR penetration depth, or any angle from the imaging process.

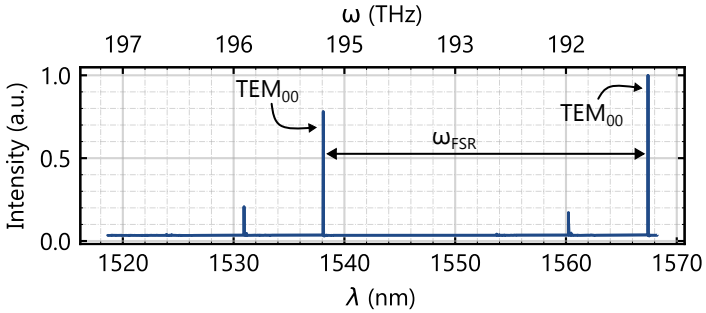

Figure 3.12: Free spectral range. Cavity transmission as a function of laser wavelength. The separation between the longitudinal modes reveals a free spectral range of 3.58 THz. The detector was saturated for the TEM_{00} on the right of the graph and therefore the relative intensity between the fundamental and higher order transversal modes carries no useful information.

To measure the cavity length and free spectral range precisely we ground both cavity piezos and use the tunable option of the probe laser to scan over two free spectral ranges. We record the cavity transmission and reflection while tuning the laser's wavelength. We identify the FSRs by locating the TEM_{00} mode. In non-fiber based cavities, one can identify the transversal cavity modes by imaging them. Because our cavity is fiber coupled, this is not possible. However, considering that we obtain input coupling efficiencies > 90 % for the SM fiber to cavity Gaussian modes (see

Fig. 3.1a), and that for higher order cavity modes the couplings are more than three orders of magnitude smaller[14], it is safe to assume that the peaks with highest transmission belong to the TEM_{00}. From their separation we extract the free spectral range and cavity length. Figure 3.12 shows a typical transmission spectrum as a function of the laser wavelength. The TEM_{00} mode is pointed with an arrow; the smaller peaks correspond to higher order transversal modes. In order to resolve the higher order transversal modes, we had to crank up the detector gain, which means the detector is saturated for the TEM_{00} on the right of the graph – for this reason the relative height between the TEM_{00} and higher order modes has no useful information. The intensity variation between both TEM_{00} is due to the wavelength dependent power variations of the tunable laser.

3.4.4 Summary of the fabricated cavities

Over the course of this PhD thesis I fabricated a total of nine fiber cavities. Their parameters are presented in Table 3.1. The ones that we used for published work have the reference next to the cavity name. We do not show cavities C1 and C2 because they are not well aligned and present many higher order modes. C5 was unusable because the Stycast glue did not properly cure and the cavity got misaligned afterwards. All cavities besides C3 and C8 were characterized during the fabrication process, not under vacuum and not with vibration isolation. Their values may slightly differ if they are characterized again under different measurement conditions.

Table 3.1: Experimental cavity parameters. The cavity with an asterisk broke and is no longer operational. All measurements (except for C3 and C8) were done under atmospheric pressure and without acoustic shielding. The prompt reflection is the mean value of both polarizations (they typically deviate by ~ 3 %). The displayed finesse and $|S_{21}|^2_{\max}$ are the highest of the two polarizations. Missing values are indicated with a hyphen.

Cavity name	ROC (µm) SM, MM	$\kappa/2\pi$ (MHz) pol1, pol2	$\omega_{\text{pol}}/2\pi$ (MHz)	L_{cav} (µm)	$\omega_{\text{FSR}}/2\pi$ (MHz)	$\mathcal{F}\cdot 10^{-3}$	$\lvert\beta\rvert^2$	$\lvert S_{21}\rvert^2_{\max}$
C3 [135]	191, 139	17, 19	74	43.8	3.42	200	0.6	0.012
C4*	278, 138	46, 48	250	38.2	3.94	85	0.6	0.014
C6	255, 60	68, 68	360	28.7	5.2	76	0.7	–
C7	274, 126	46, 46	86	76.4	1.96	43	0.5	–
C8 [1]	191, 136	18, 18	133	41.8	3.58	194	0.6	0.03
C9	206, 146	41, 40	88	40	3.75	91	0.45	0.007

3.5 Vacuum system

The cavity and mechanical resonators are kept inside a vacuum chamber to reduce gas damping. We designed the vacuum chamber and manufactured it in the workshop from the Univer-

[14]The couplings can be calculated numerically computing the overlap integral of the mode profiles at the mirror surfaces [118]. After the cavity Gaussian mode, the cavity modes TEM_{mn} with largest coupling are the ones with mode number (m, n): (0, 4), (4, 0), (2, 2), which are degenerate in frequency.

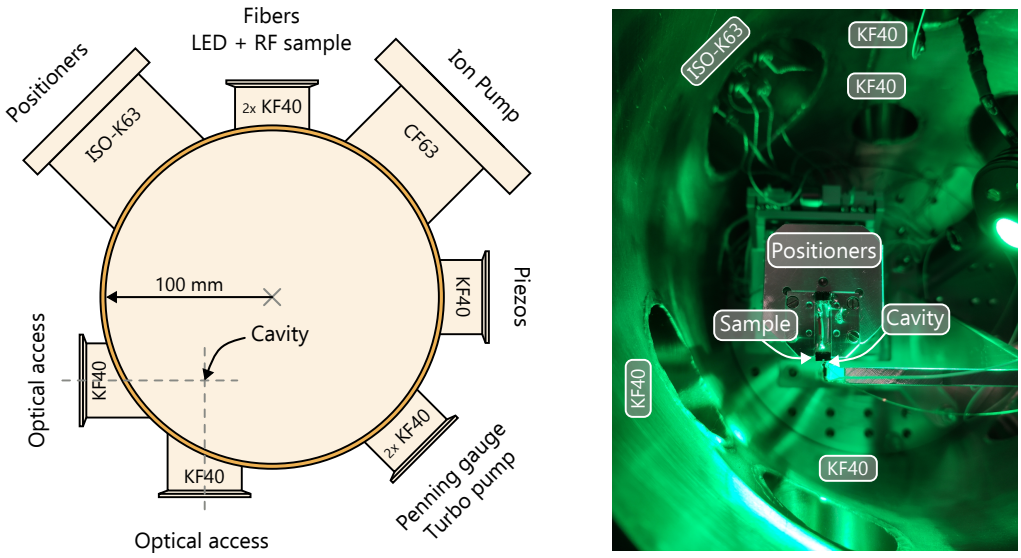

Figure 3.13: Vacuum chamber. Left: sketch to scale of the vacuum chamber (top view). The different flange types are depicted within each vacuum tube; the symbol 2x indicates that there are two flanges of that type stacked in the vertical direction. The purpose of each flange is written outside of it. Right: top view photograph of the inside of the chamber with the cavity, positioners and sample included.

sity of Konstanz with the assistance from Louis Kukk. The geometrical constrains for the design were:

- The chamber should be big enough to accommodate the sample's positioners and the cavity holder.
- It should contain two optical access ports to monitor the sample position at perpendicular directions. These ports' position should match the height of the cavity and positioning system.
- It should contain ports for the different optical, electrical and vacuum connections: the fibers, an LED for illumination, an RF connection to drive the sample, the electrical connections of the positioners, the electrical connection of the cavity piezos, a vacuum penning gauge, an ion pump and a turbopump.

All components from the vacuum chamber are made out of stainless steal. A sketch to scale of the chamber, together with a photograph of its inside, are shown in Figure 3.13. The chamber is pumped first with a turbo molecular pump (Pfeiffer vacuum, HiCube 80 Classic) for two days. After reaching a pressure $\leq 8.5 \times 10^{-6}$ mbar, we start the ion pump in parallel (Gamma Vacuum, TiTan 75S). The two pumps run together until the pressure in the chamber is $\leq 1.9 \times 10^{-6}$ mbar, which usually takes from one to two days. After the base pressure is reached, we close the valve from the turbopump and run them together for half a day. From there on, the turbopump can be turned off, vented and disconnected. The lowest pressure we have measured at the chamber with

the penning gauge[15] (Leybold Penning PTR 90) is 7×10^{-7} mbar. The ultimate pressure of the ion pump is 10^{-11} mbar, but we are most likely limited by leaks in the vacuum connectors – most of them are O-rings – and in the electrical and fiber feedthroughs. Nevertheless, the vacuum is good enough to run the ion pump continuously, which was not the case with the previous version of the setup (the old cuvette-type vacuum setup suffered from many leaks and it was difficult to start the ion pump at all) [111, 112].

Only with the turbopump we already reach pressures low enough[16] so that gas damping is no longer the main energy dissipation mechanism of our mechanical resonators. However, our experiment suffers from the mechanical vibrations of the turbopump. Consequently, we only use the turbopump to be able to reach a minimum pressure from which we can work with the ion pump exclusively, which is vibration free in the frequency range of interest.

3.6 Position control

The sample is brought into the cavity with a stick-slip positioning system[17] from Smaract GmbH. It consists of three linear stages that move the sample in the x, y and z directions and two goniometers used to control the sample alignment with respect to the cavity mode axis. The x and y stages have a travel of 30 mm and the z stage of 21 mm. The 5D-stage is driven with a MCS2 controller. The positioners can be used in the step mode (stick-slip movement, steps in the micrometer range) or in the scan mode (sub-nanometer resolution). We use the step function to bring the sample inside the cavity and to perform the angle alignments. The scan function, with a range of 3 µm, is used to map the static couplings by changing the sample position along the cavity axis (z-axis).

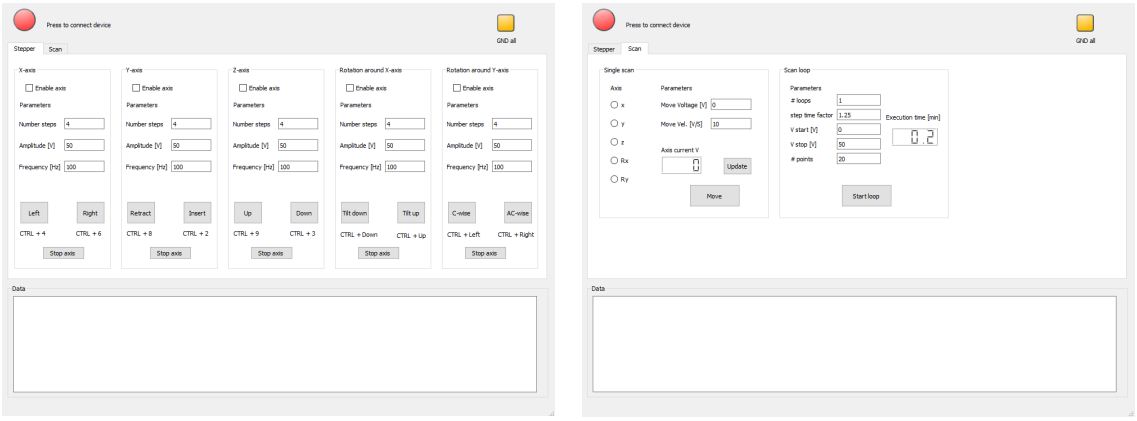

Figure 3.14: Positioners graphical user interface. The GUI has two tabs, one for the step movement (left) and another for the scans (right). Each axis' step motion can also be controlled with keyboard shortcuts.

[15] The ion pump gauge, located inside the pump, gives smaller values than the penning. We always take the largest of the two as reference.

[16] The Q factor of most micron-sized mechanical resonators is pressure independent below 10^{-4} mbar [136].

[17] The part numbers for the x, y and z stages and both goniometers are, respectively: SLS-5252-D-HV, SLS-5252-D-HV, SLC-1730-D-HV, SGO-77.5r2-HV, SGO-60.5r2-HV.

Back in 2019 when we purchased the positioners, Smaract could only provide C-libraries to communicate with the MCS2 (most companies provide their libraries at least in C, Python and LabView). Because I was not used to C, and I had already coded all the other lab instruments in Python, I developed our own Python software to control the positioners using standard SCPI commands and the application programming interface provided by Smaract. On top of that, the positioner's GUI was not user friendly, so I created our own using Qt Designer and Python, which became really handy, especially when inserting the sample. A snapshot of the GUI is shown in Figure 3.14.

After some recent exchanges with the company, the new firmware version has indeed a Python library. I would advise the reader, if planning to use these positioners, to switch to that one, which should be more stable.

3.7 Thermal stability

Temperature drifts in the lab cause the positioners to expand and contract, resulting in a drift of the sample's position. They also lead to fluctuations of the mechanical resonator's resonance frequency, to cavity length changes, and to fluctuations of the laser's wavelength. The last two are particularly detrimental for our measurements, especially when we need to stabilize the cavity length. They result in drifts of the cavity resonance condition, which, depending on the magnitude of the drift, can or cannot be compensated by the feedback loop sent to the cavity piezos.

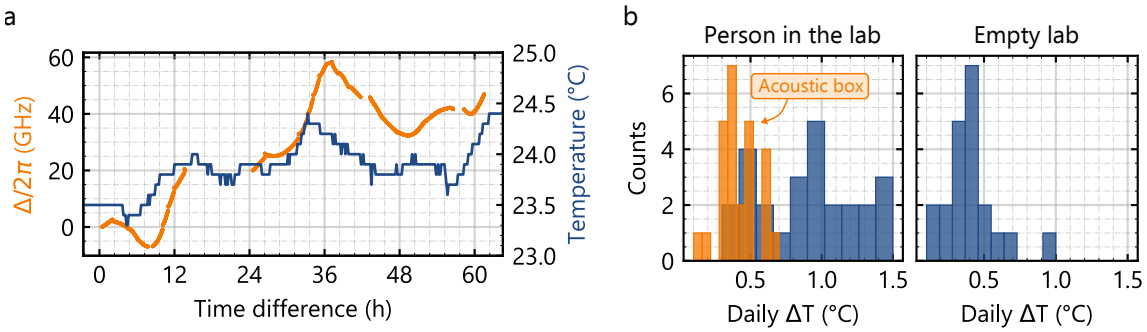

Figure 3.15: Thermal stability of the setup. (a) Drift of the cavity frequency (orange, left y axis) and lab temperature (blue, right y axis) as a function of time. The measurement started the evening of July 1st, 2022. (b) Histogram of the maximum daily temperature difference when there is someone in the lab (left, time span of 26 days) and not (right, time span of 21 days). Blue bins are measurements of the lab temperature and orange bins of the temperature inside the acoustic shielding box.

The cavity thermal stability can be estimated by monitoring the drift of the cavity resonance condition as a function of time and correlate the drifts with the temperature in the lab. With this method, however, we cannot distinguish between laser wavelength fluctuations and cavity length fluctuations due to thermal expansion. Figure 3.15a shows such a measurement for cavity C8. The orange dots represent the cavity frequency shift as a function of time; the blue line is the temperature inside the lab at the Center for Nanotechnology and Nanomaterials (ZNN). For this measurement the acoustic shielding box (see Section 3.8) was open, so that the walls of the vac-

uum chamber are thermalized with the lab temperature. We observe a delayed response of the cavity resonance frequency with respect to the lab temperature, which is expected because the cavity and chamber walls are separated by vacuum. From the data, we extract an estimation[18] of the temperature drifts of 60 GHz/°C.

We can perform similar measurements when we insert the sample inside the fiber cavity to study the thermal drifts of the sample position. In this case, we use the 1330 nm-interferometer to count interference fringes as a function of time (and therefore temperature). We measure a shift of the sample position along the z direction of 1.2 µm/°C. Taking into account that we usually measure at sample positions with a coupling $G = 330$ MHz/nm, this translates into a cavity frequency shift of around 400 GHz/°C, an order of magnitude larger than the empty cavity temperature drift. It becomes clear that our experiment is limited by thermal drifts of the sample and not the cavity.

Figure 3.15b shows the maximum daily temperature difference in the laboratory (blue) and inside the acoustic shielding box (orange) over 25 days for two situations: when there is a person inside the lab (left) and when not (right). As soon as one enters the lab to measure, it starts to heat up. The maximum temperature difference is 1.5 °C. The acoustic isolation box reduces the magnitude of the change to half a degree. The temperature inside the isolation box can increase as much as half a degree (Fig. 3.15b, orange bins) in a time span of 4.5 h. Assuming that increase is linear (which it is not, it is faster at the beginning), this implies a frequency shift of around 50 MHz/s – this is two times the cavity linewidth! Consequently, when we lock the cavity for the dynamical backaction experiments, the lock point and the cavity transfer function change massively during the measurement time – it's impossible to measure. Luckily, the acoustic shielding delays the thermalization of the chamber with respect to the lab, which usually leaves us with a couple of hours of measurement time before the experiment starts to heat up significantly. We recall that leaving the lab to avoid the fast temperature increase is not an option with the current setup configuration: the lock box is an analog device (see Section 3.3), so that one has to be in the lab to re-lock or unlock depending on the measurement. On top of that, the cavity locks are very unstable with the sample inserted. They are lost after 15 to 20 minutes in the best case due to the temperature fluctuations of the lab itself (Fig. 3.15b, right).

Since we cannot change the lab's air conditioning settings, the only possible solution is to feed back on the sample position with the interferometer. We did not have time to implement it due to time constrains, but the Smaract positioners allow it.

3.8 Vibration isolation

After moving the labs to the ZNN (TUM, Garching), we observed that the setup was suffering from an unknown mechanical noise that we did not have in Konstanz. In both labs the vacuum chamber was directly placed on top of a floating optical table.

Figure 3.16a shows in blue the cavity transmission as a function of cavity detuning with the sample inserted and placed at a cavity node, where it is less sensitive to mechanical vibrations of the sample. These vibrations lead to cavity fluctuations of about 20 GHz at the cavity node, making it

[18] For the estimation we use parts of the data where the lab temperature and frequency shift vary linearly with time.

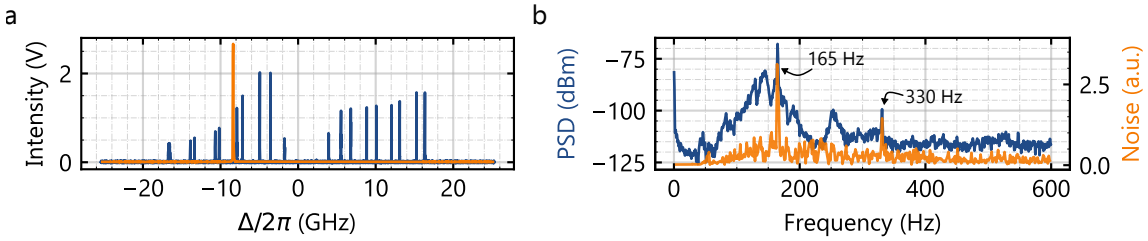

Figure 3.16: Mechanical noise at the ZNN. (a) Fluctuations in the cavity resonance frequency at the cavity node for a cavity without acoustic isolation (blue). The orange line shows the response of the same cavity with the sample at the node when it is acoustically shielded. (b) Power spectral density (1 Hz bandwidth) of the sample vibrations (blue, left y axis) measured with the 1330 nm-SLED and the lab's acoustic noise (orange, right y axis) measured with the microphone of a mobile phone (see main text for details).

impossible to lock the cavity. We identified the acoustic noise from the ZNN facilities as the source of the mechanical noise. Figure 3.16b displays in blue the power spectral density (bandwidth of 1 Hz) of the sample vibrations measured with the cavity's interferometer and in orange the lab's acoustic noise[19]. Both share two very pronounced peaks at 165 Hz and 330 Hz and a wider feature around 165 Hz. To suppress the mechanical vibrations, we built an acoustic isolation box made by hand (literally[20]). The box, shown in Figure 3.18a, is made out of plywood and composite foams (two layers, 2 cm-thick each, density of 120 kg/m^3).

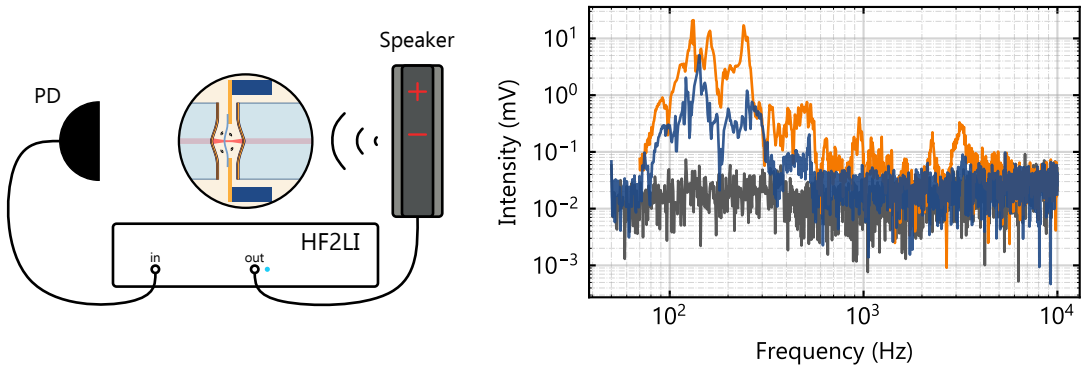

Figure 3.17: Positioners mechanical response. Left: We drive a UE Boom 2 speaker with a HF2LI Zurich lock-in to mechanically excite the setup with the sample inside the cavity. We record the mechanical vibrations of the sample with the interferometry photodetector. Right: Mechanical response of the setup with (blue) and without (orange) acoustic isolation box for a drive amplitude of 50 V_{rms} and an interferometer input power of 273 µW. The gray line is the noise floor with acoustic isolation.

To measure the performance of the acoustic isolation box, we drive an Ultimate Ears Boom 2

[19] The acoustic noise was measured with the microphone of a Samsung SM-J710F phone and the FFT spectrum of the Phyphox App. The measurements were done inside the lab and at the ZNN corridors (far away from vacuum pumps, compressors, etc.). In the latter, the noise peaks at 165 Hz and 330 Hz had a larger magnitude.

[20] Upon arrival to TUM, we had no workshop associated and the guests' waiting time for other workshops was larger than three months. We had to build it ourselves instead.

speaker (frequency range 90 Hz-20 kHz as specified from the company) with a Zurich Instruments HF2LI lock-in (Fig. 3.17). The sound from the speakers excites the setup mechanically and we record the interferometer signal from the cavity when the sample is placed at half an interferometry fringe, the point of maximum sensitivity. We do this measurement placing the speakers on top of the optical table without acoustic damping (vacuum chamber on top of the table directly, orange data in Fig. 3.17) and with the whole setup inside the box (blue data in Fig. 3.17), which is closed. We achieve a noise suppression factor of 20 and 74 for the 165 Hz and 330 Hz ZNN acoustic noise's frequencies, respectively. These measurements also give information about the positioners' mechanical transfer function, which resonates in the range between 80 Hz and 500 Hz – the mean noise suppression factor in this range is 5.5. The two resonances above 2 kHz are attributed to the fibers or the fiber holder, which can be measured by taking the sample out and we using the same principle to measure the empty cavity mechanical response. We highlight that we cannot distinguish between the isolation from the air vibrations and from the vibrations transferred through the optical table. Just by placing the chamber on top of the foam the mechanical noise got already reduced significantly, without the need of closing the box completely. This is an indication that part of the vibrations are also transferred through the optical table.

After the box installation, the cavity can easily be locked at the node and antinode. Figure 3.16a shows in orange the cavity transmission with the sample at the node when the setup is acoustically shielded. The improvement in the mechanical stability of the setup also manifests in the empty cavity parameters as a reduction in the scattering of the cavity linewidth (Fig. 3.18b): the standard deviation of the linewidth is reduced by a factor of 5 from $\sigma_{\text{std}} = 1.4\,\text{MHz}$ to $\sigma_{\text{std}} = 0.3\,\text{MHz}$ when the box is closed. The mean value stays the same for both cases: $\mu = 18.5\,\text{MHz}$.

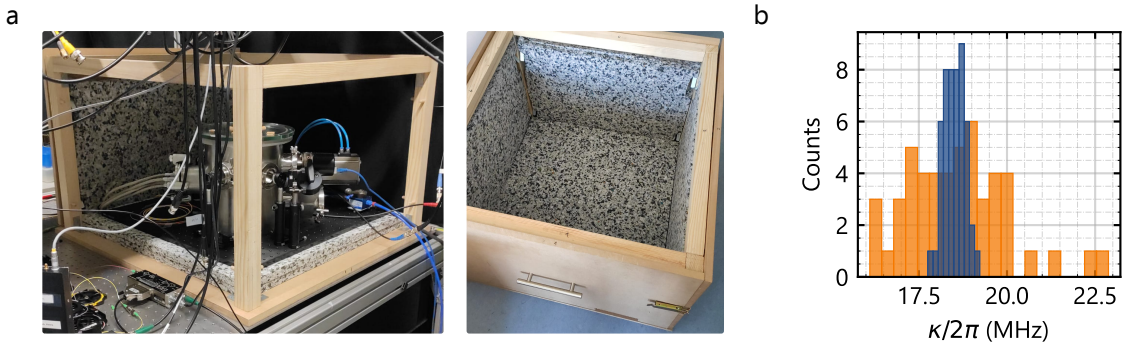

Figure 3.18: Acoustic isolation box. (a) Photographs of the acoustic isolation box. (b) Histogram of the cavity linewidth (C8) for a total of 50 measurements. Blue (10 bins) and orange (20 bins) bins are measured with the acoustic box closed and open, respectively. The mean μ and standard deviation σ_{std} of the linewidth are $\mu = 18.5\,\text{MHz}$ and $\sigma_{\text{std}} = 1.4\,\text{MHz}$ when the box is open, and $\mu = 18.5\,\text{MHz}$ and $\sigma_{\text{std}} = 0.3\,\text{MHz}$ when it is closed.

3.9 Active cavity stabilization

The cavity is locked to an error signal generated in a similar fashion to the one from the standard Pound-Drever-Hall (PDH) frequency stabilization technique [137]. In this section we derive the mathematical expression of our error signal and discuss our locking-scheme. The first modification to the standard PDH technique is that we do not use the cavity reflection but the transmission to generate the error signal. The reason for this is that, when using the reflection, the phase modulation oscillates in time due to the standing waves present in the cavity reflection. This leads to time drifts of the error signal.

The second difference is that we do not use an electro-optic phase modulator but an electro-optic analog intensity modulator. Chapter 10 from Ref. [89] gives a good description of the difference between the two. In an analog intensity EOM, the light beam is split into two arms (or waveguides) by a beam splitter, and recombined before its output, like in a Mach-Zehnder interferometer. By applying a DC voltage V_{dc} to the EOM, one can change the relative phase between both arms. The DC voltage that generates a phase shift between the arms of π is called the half-wave voltage V_π; at that voltage the light from both arms destructively interferes with each other. By changing V_{dc}, one can choose the working point of the interferometer fringe.

Adding an RF component of amplitude V_{rf} to the voltage at a frequency ω_{mod} produces an amplitude modulation. The laser's electric field, $E_l = E_0/2e^{i\omega_l t} + c.c.$, after the EOM is then

$$E(t) = \frac{E_0}{4} e^{i\omega_l t}\left(e^{i\theta_1(t)} + e^{i\theta_2(t)}\right) + c.c., \tag{3.16}$$

where $c.c.$ denotes the complex conjugate, and $\theta_1(t)$ and $\theta_2(t)$ the phase acquired at each arm, which are given by [138]

$$\theta_1(t) = \beta\cos(\omega_{\mathrm{mod}}t + \pi), \quad \theta_2 = \beta\cos(\omega_{\mathrm{mod}}t) + \phi_B. \tag{3.17}$$

In the last expression we have introduced the bias voltage $\phi_B = \pi V_{\mathrm{dc}}/V_\pi$, the modulation depth $\beta = \pi V_{\mathrm{rf}}/V_\pi$, and a π phase difference between the arms that occurs when the RF drive is applied to both of them simultaneously (like our EOM, which is a Y-based Mach-Zehnder interferometer). We can use the Jacobi-Anger expansion to obtain

$$E(t) = \frac{E_0}{4} e^{i\omega_l t}\left[J_0(\beta)\left(1 + e^{i\phi_B}\right) + \sum_{q=1}^{\infty} i^q J_q(\beta)\left(e^{iq\pi} + e^{i\phi_B}\right)\left(e^{iq\omega_{\mathrm{mod}}t} + e^{-iq\omega_{\mathrm{mod}}t}\right)\right] + c.c., \tag{3.18}$$

where $J_q(\beta)$ is the q^{th}-Bessel function of the first kind and we have employed that $i^{-q} = (-1)^q i^q$ and $J_{-q}(\beta) = (-1)^q J_q(\beta)$. The field transmitted through the EOM is composed of a carrier oscillating at ω_l and a series of sidebands at frequencies $\omega_l \pm q\omega_{\mathrm{mod}}$, similar to the standard phase modulation. We can re-write Eq. 3.18 as

$$E(t) = e^{i\omega_l t}\left[E_c + \sum_{q=1}^{\infty} E_q\left(e^{iq\omega_{\mathrm{mod}}t} + e^{-iq\omega_{\mathrm{mod}}t}\right)\right] + c.c., \tag{3.19}$$

where have introduced the carrier and sidebands amplitudes, E_c and E_q, respectively. The main difference with respect to the phase modulation is hidden in the carrier's and sideband's amplitude dependencies on the bias voltage: the amplitude ratio between sidebands and carrier is not

only determined by the Bessel functions but by ϕ_B. One can, for instance, set the bias voltage so that either the carrier is suppressed or the sidebands are, controlling their relative amplitudes. This is convenient when we want to nicely resolve the sidebands when we use them as calibration tones to convert scan voltages into frequency detunings.

The field transmitted through the cavity will be

$$E_t(t) = e^{i\omega_l t}\Big[E_c H(\Delta) + \sum_{q=1}^{\infty} E_q\big(H(\Delta + q\omega_{\mathrm{mod}})e^{iq\omega_{\mathrm{mod}}t} + H(\Delta - q\omega_{\mathrm{mod}})e^{-iq\omega_{\mathrm{mod}}t}\big)\Big] + c.c., \tag{3.20}$$

with $H(\Delta)$ the cavity transmission function and $\Delta = \omega_l - \omega_{\mathrm{cav}}$. The transmission detector measures the light intensity $I \propto |E_t|^2$; it will have a DC and a RF component $I = I_{\mathrm{dc}} + I_{\mathrm{rf}}$, where

$$I_{\mathrm{dc}} \propto |E_c H(\Delta)|^2 + \sum_{q=1}^{\infty}\Big(|E_q H(\Delta + q\omega_{\mathrm{mod}})|^2 + |E_q H(\Delta - q\omega_{\mathrm{mod}})|^2\Big) \tag{3.21}$$

and

$$\begin{aligned} I_{\mathrm{rf}} \propto & \Big(E_c^* H(\Delta) E_1 H(\Delta + \omega_{\mathrm{mod}}) + E_c H(\Delta) E_1^* H^*(\Delta - \omega_{\mathrm{mod}})\Big)e^{i\omega_{\mathrm{mod}}t} \\ & + \Big(E_c H(\Delta) E_1^* H(\Delta + \omega_{\mathrm{mod}})^* + E_c^* H(\Delta) E_1 H(\Delta - \omega_{\mathrm{mod}})\Big)e^{-i\omega_{\mathrm{mod}}t} \\ & + \sum_{q=2}^{\infty}\Big(\mathcal{O}(q\omega_{\mathrm{mod}}t) + \mathcal{O}(-q\omega_{\mathrm{mod}}t)\Big). \end{aligned} \tag{3.22}$$

In the last expression we have neglected the terms oscillating at ω_l or faster, because they are filtered by the photodetector. Taking into account that the detector used for transmission measurements has a bandwidth of 30 MHz and that we employ modulation frequencies ω_{mod} in the range 20 MHz to 30 MHz, we can neglect all terms oscillating with $q \geq 2$, too. Finally, introducing for convenience the factor K

$$K = E_c^* H(\Delta) E_1 H(\Delta + \omega_{\mathrm{mod}}) + E_c H(\Delta) E_1^* H^*(\Delta - \omega_{\mathrm{mod}}), \tag{3.23}$$

and expressing the complex exponential as sine and cosine, the RF intensity becomes

$$I_{\mathrm{rf}} \propto 2\,\mathrm{Re}(K)\cos(\omega_{\mathrm{mod}}t) + 2\,\mathrm{Im}(K)\sin(\omega_{\mathrm{mod}}t). \tag{3.24}$$

We can demodulate I_{rf} at ω_{mod}, obtaining the in-phase component $X = 2\,\mathrm{Re}(K)$ and the quadrature component $Y = 2\,\mathrm{Im}(K)$.

In our experiment, the demodulation is done electronically by the UHFLI lock-in amplifier (we also use its internal gains to amplify the error signal), which generates the modulation signal sent to the EOM as well. We typically use values $V_{\mathrm{dc}} = 6.5\,\mathrm{V}$, $V_{\mathrm{rf}} = 0.75\,\mathrm{V}$, which translate[21] into $\beta = 0.6$ and $\phi_B = 0.78\pi$. Figure 3.19a shows the experimental and calculated (Eq. 3.24) in phase (dark and light blue) and quadrature (orange and red) components for $\omega_{\mathrm{mod}}/2\pi = 30\,\mathrm{MHz}$ and cavity C8. We always observe an asymmetry between the sidebands, but we have not investigated it.

[21] Experimentally, the DC voltage at which the beams are in phase V_0 is not zero. This implies $\phi_B = \pi(V_{\mathrm{dc}} - V_0)/(V_\pi - V_0)$. Similarly, $\beta = \pi V_{\mathrm{rf}}/(V_\pi - V_0)$. For our EOM, $V_0 \simeq 2.2\,\mathrm{V}$ and $V_\pi \simeq 7.7\,\mathrm{V}$. Both shift in time due to temperature fluctuations and have to be measured.

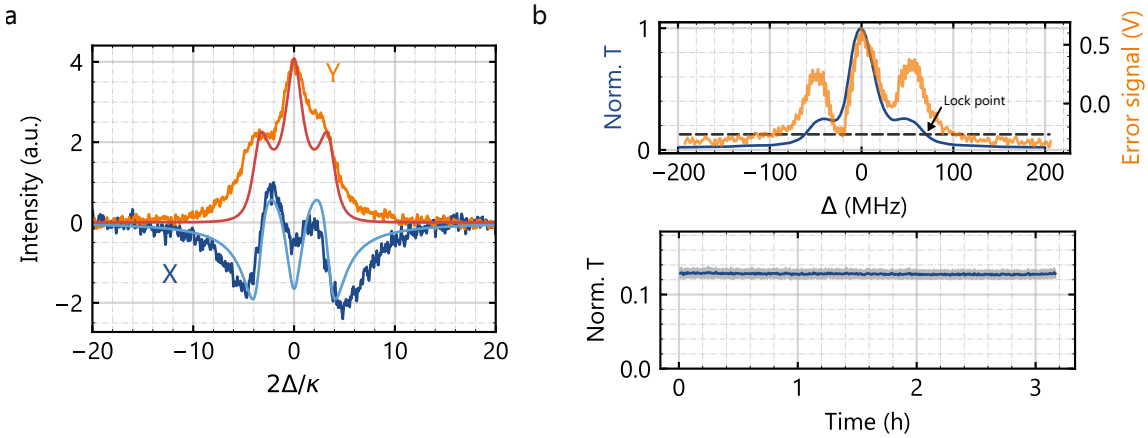

Figure 3.19: Cavity stabilization. (a) Quadrature measurements (orange, dark blue) with $\omega_{\mathrm{mod}}/2\pi$ = 30 MHz for cavity C8. Red and light blue solid lines are calculated using Eq. 3.18 and Eq. 3.24 and scaled to match in amplitude the experimental values. (b) Top: cavity transmission and error signal before locking the cavity for $\omega_{\mathrm{mod}}/2\pi = 50$ MHz. Bottom: locked cavity transmission (blue) as a function of time. The gray shaded area is the transmission's standard deviation. The lock point is at $\Delta_{\mathrm{l}}/2\pi = -70$ MHz and is pointed at with an arrow in the top graph. These measurements were done with an empty cavity (no sample loaded).

In Figure 3.19b we display an example of a standard lock configuration with an empty cavity (C8). The top graph shows in blue the normalized cavity transmission and in orange the error signal before the lock takes place. In this particular measurement we used a modulation frequency of 50 MHz. We always use the Y-quadrature and lock at a laser detuning of around $\Delta_{\mathrm{l}}/2\pi = (\omega_{\mathrm{l}} - \omega_{\mathrm{cav}})/2\pi = -70$ MHz, i.e. the laser is red detuned with respect to the cavity. We choose this value of Δ_{l} as a compromise between having a good signal in reflection and a good transduction from frequency fluctuations to voltages, and minimizing the backaction from the lock. The bottom graph shows the normalized cavity transmission when the cavity is locked as a function of time. The lock of the empty cavity is very stable and can last more than 3 h. As explained at the end of Section 3.7, the lock stability is reduced to 15 to 20 minutes at best with the sample inserted due to the thermal fluctuations in the lab.

4

Fabrication and characterization of suspended hBN resonators

THE second part of any cavity optomechanical system is the mechanical resonator. In our experiments we employ circular membranes or plates made out of hBN – in this chapter, we will use the terms *drum* and *drum-head* as synonyms for circular resonator. The short cavity length and the fiber dimensions restrict the geometry of the samples that can be inserted in the cavity, as illustrated in Figure 4.1. The hBN resonators need to be clamped to a substrate capable of fitting in a gap of some tens of micrometers. For this purpose, we choose commercially available low-stress SiN membranes (Norcada Inc.), which consist of a layer of SiN grown on top of a 200 µm-thick silicon chip. The reasons for our choice are three-fold. First, SiN membranes can be patterned using standard photolithography techniques, which allows us to create the circular frames for the drums (Fig. 4.1, patterned SiN in orange) – in this chapter we will refer to the circular frames simply as *holes*. Second, their small thickness of few hundreds of nanometers makes it possible to insert the sample in the cavity. Third, their window opening of 500 µm × 500 µm is larger than the fiber diameter (125 µm); this leaves some freedom in the positioning of the hBN resonator within the cavity and permits probing the sample at different positions.

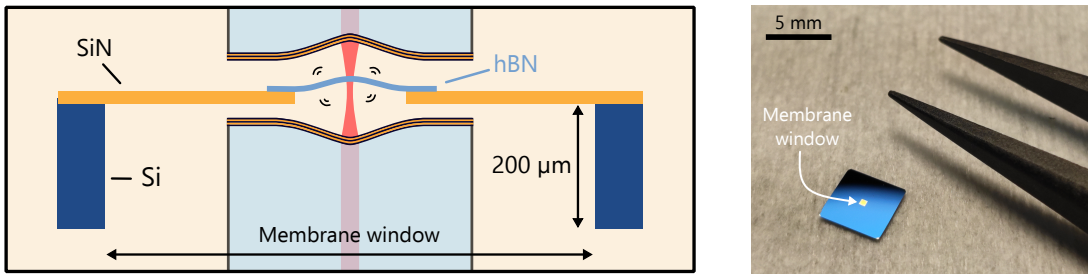

Figure 4.1: Sample geometrical constrains. Left: Sketch of the fiber cavity and sample. The short cavity length of $L_{cav} \sim 40\,\mu m$ and fiber diameter of 125 µm limit the possible geometries of the samples that can be inserted in the cavity. SiN membranes (SiN in orange, Si frame in dark blue) overcome these constrains. Right: Image of a 200 nm-thick low-stress SiN membrane chip sitting next to some lab tweezers. The membrane window opening appears as a yellow square at the sample's center.

This chapter begins by explaining the fabrication of the SiN membranes used as mechanical support of the hBN drums (Section 4.1). Section 4.2 introduces the transfer process used to place the hBN flakes on the circular frame patterned on the SiN membrane. To be able to insert the sample inside the cavity, we need to cleave the SiN chips – this is described in Section 4.3. Once the samples are fabricated, we characterize their mechanical properties in a Michelson interferometer (Section 4.4). Because the samples consist of an hBN drum on top of a larger and heavier SiN resonator, the modes of the mechanical resonators can hybridize. The chapter concludes with a study of the hybridization between the hBN and SiN resonators (Section 4.5).

4.1 SiN membranes as frames for hBN circular resonators

The holes acting as frames for the hBN resonators are transferred onto the SiN membranes via photolithography and reactive ion etching. Since the membranes provided by Norcada do not require any cleaning before processing, the fabrication starts directly by applying an adhesion promoter (HMDS) in vapor phase before spin coating the samples with a 850 nm-thick layer of AZ MIR 701 14 cPs photoresist. After the spin coating, the samples are soft baked with a hotplate at 90 °C for 60 s and subsequently exposed with a UV maskless aligner (Heidelberg MLA100) with an exposure dose of 250 mJ/cm^2. The resist is then developed for 60 s in AZ MIF 726 developer, followed by 30 s of rinsing in deionized (DI) water (Fig. 4.2a). The samples are dried very gently with an air gun, paying attention not to break the fragile SiN membrane. If there are any remaining water residues on the sample, they are removed with an O_2 plasma (Alpha Plasma Q150, 500 W, 90 Pa, 100 sccm, 3 min).

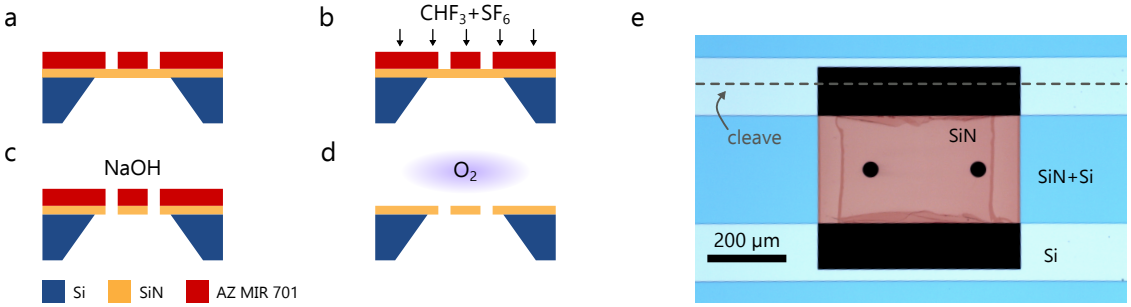

Figure 4.2: Process flow for patterning low-stress SiN membranes. (a) A layer of AZ MIR 701 photoresist is spin coated, exposed with UV light (250 mJ/cm^2), and developed with AZ MIF 726. (b) RIE-ICP etching using the resist as etch mask. (c) Resist removal in a NaOH 0.5 mol/L solution. (d) Final structure and cleaning with an O_2 plasma. (e) Brightfield microscopy image of a patterned 100 nm-thick low-stress SiN membrane. Areas with only SiN appear as orange; areas with only Si appear as white/slight-green; areas with SiN and Si appear as light blue; the black background depicts parts of the membrane window where the SiN was removed. There are some resist residues remaining on the back side of the SiN membrane (darker orange), which remain there sometimes even after plasma cleaning. The gray dashed line depicts the direction along which the sample is cleaved at a later stage to be able to be inserted in the optical cavity.

The next step is the selective removal of SiN to create the holes where we stamp the van der Waals materials. This is done with an inductively coupled plasma etching process (PlasmaPro 80 ICP RIE) at a pressure of 5×10^{-3} mbar; the etching step uses a combination of two gases: 14 sccm of

CHF_3 and 6 sccm of SF_6 (Fig. 4.2b). This particular recipe etches both SiN and Si, with etch rates of 2.1 nm/s and 7.5 nm/s, respectively. The resist etch rate is approximately 5 nm/s. The resist is then removed by dipping the sample in a 0.5 mol/L solution of NaOH for 3 min (Fig. 4.2c); the sample is subsequently rinsed for 30 s in DI water and 30 s in isopropanol (IPA). We help the drying process by blowing the sample with an air gun very gently. Finally, any resist left overs are removed with an O_2 plasma (Fig. 4.2d, 500 W, 90 Pa, 100 sccm, 4 min).

Figure 4.2e shows a brightfield microscopy image of a 100 nm-thick low-stress SiN membrane after fabrication and O_2 plasma cleaning. The transferred patter consists of a wide stripe of dimensions 282 µm × 500 µm with two holes with a diameter of 40 µm. We pattern the big stripe on the SiN because the membrane has to be released from the Si frame so that it does not break afterwards when the sample is cleaved (see Section 4.3). The cleave direction is highlighted as a gray dashed line in Figure 4.2e. This particular sample still has some resist resides on the backside of the stripe even after O_2 plasma cleaning. We found that this usually happens if a thick layer of resist penetrated on the backside of the membrane during the spin coating process. Leaving the sample longer in the O_2 plasma does not help in this case. Instead, one can place the sample in a Piranha solution (H_2SO_4:H_2O_2, 3:1) for 4 to 8 minutes to remove the remaining resist residues. Afterwards, the sample should be rinsed in two subsequent baths of DI water (1 min each) and finally 1 min in IPA. We blow the sample with an air gun very gently to assist the drying process.

During this work we have tried different pattern designs. The diameter of the holes has to be ≥ 30 µm to avoid clipping losses of the cavity mode at the edges of the holes (see Section 5.1.2). The number of holes has to be also minimized. The reason for this is that, during the stamping of the van der Waals materials, the PDMS stamp (see Section 4.2) tends to get stuck in any profile irregularities, like the holes themselves, making the release of the stamp more difficult. We usually have two holes at the end, one for the hBN flake and the second for reference measurements like the design shown in Figure 4.2e. Moreover, adding extra holes to the design complicates the mechanical mode spectrum of the SiN stripe itself, which deviates more from the ideal rectangular geometry introduced in Section 2.2.3.

In the introduction to this chapter and in this section we have only discussed patterning low-stress SiN membranes. Norcada offers high-stress ($\sigma \simeq 1$ GPa) stoichiometric Si_3N_4 membranes as well. We have tried patterning Norcada high-stress membranes with photolithography and RIE-ICP etching without success, in the cleanroom facilities from both the University of Konstanz and from the ZNN (Garching, TUM). This is the reason why we work with the low-stress version. Moving to high-stress Si_3N_4 would have two main advantages for us. On the one hand, the resonance frequency of the modes from the Si_3N_4 stripe will be pushed towards higher frequencies due to the larger stress. This would be beneficial to avoid, up to a certain extent, the hybridization between the mechanical modes of the hBN resonator and the ones from the stripe itself [139]. We will discuss the hybridization later in Section 4.5. On the other hand, we would benefit from its lower optical absorption at telecom wavelengths [140]. Norcada offers these days high-stress membranes with custom made patterns, which would possibly be the easiest solution. Alternatively, we could fabricate our own custom patterned high-stress membranes following other established recipes [97, 141, 142].

4.2 Mechanical exfoliation and deterministic transfer of hBN

The hBN flakes are obtained by mechanically exfoliating bulk crystals and transferred to the patterned SiN holes with the all-dry viscoelastic method [143]. The process steps are the following. First, we exfoliate hBN from bulk crystals – grown by T. Taniguchi and K. Watanabe – with blue Nitto tape (Fig. 4.3a). We cut a piece of polydimethilsiloxane (PDMS) of approximately 5x5 mm^2 and place it on top of a microscope slide, which serves as a mechanical support for the PDMS stamp. The Nitto tape is gently pressed against the PDMS (Fig. 4.3b) and peeled off quickly. Part of the hBN flakes are transferred to the PDMS stamp (Fig. 4.3c). We inspect the PDMS with hBN flakes optically with a microscope, and identify flakes with areas large enough to cover the SiN holes and with thicknesses between 10 nm and 200 nm. The thickness of the flakes can be estimated[1] by their color contrast, but has to be measured at a later stage with an atomic force microscope (AFM). The glass slide with PDMS on top is subsequently flipped upside down and placed in a Thorlabs micropositioning stage (XYZ and two goniometers). The glass slide with the

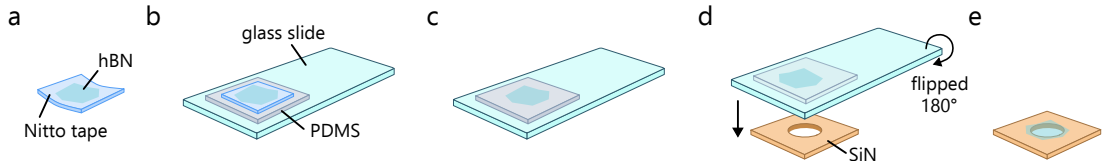

Figure 4.3: Deterministic dry-transfer of van der Waals materials. (a) hBN is exfoliated from its bulk form using blue Nitto tape. (b) The blue tape with hBN is brought in contact to a PDMS stamp previously placed on a glass slide. (c) The Nitto tape is peeled off quickly, leaving hBN flakes behind on the PDMS. (d) The glass slide is flipped upside down, with the PDMS facing toward the substrate. The PDMS stamp is aligned with respect to the hole with the help of a micropositioning stage, and brought in contact with the substrate. The process is monitored with a camera. (e) By slowly peeling off the PDMS, the hBN flake gets transferred onto the substrate.

stamp is brought downwards toward the patterned substrate (Fig. 4.3d); this process is monitored optically with a camera and a lens tube system[2] that has an adjustable magnification of up to x37. The position of the flake with respect to the hole is adjusted with the help of the positioning stage. Once the alignment is finished, the two are slowly brought in contact. Sometimes big[3] air bubbles remain between the flake and the substrate; by waiting long enough with the PDMS stamp in contact one can get rid of most of them. Finally, the PDMS stamp is very slowly peeled off. If the transfer is successful, the flake stays on the substrate, forming a suspended drum on the SiN membrane (Fig. 4.3e).

The process that we just described is common to any type of substrate, like a patterned SiN membrane or just a patterned Si chip. When working with SiN membranes, however, one has to pay attention to a few extra things because one risks breaking the membrane. In general, it is desirable to have some degree of tilt between the SiN sample and the PDMS stamp, so that the first point of contact of the PDMS is far away from the SiN membrane window – this implies that the last point

[1] Performing a good thickness estimation requires some experience and hours of stamping. This task could be automated by studying the contrast to thickness relation under a fixed illumination setting.

[2] Edmund Optics, 12.5X High Precision Zoom Lens Kit.

[3] Big here means big enough so that they are resolved with the imaging system.

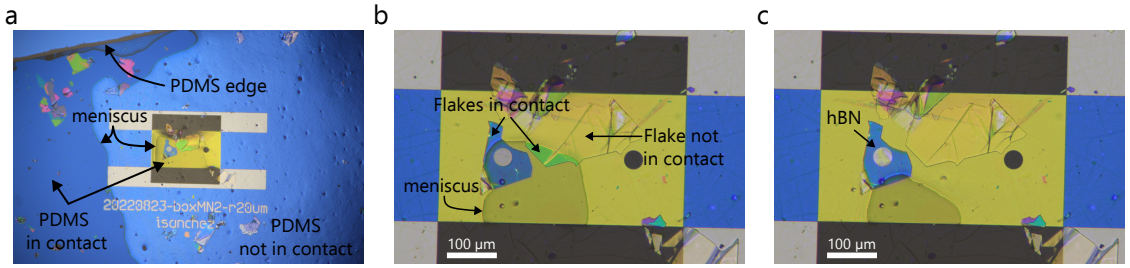

Figure 4.4: Deterministic dry-transfer of van der Waals materials. Photographs of the transfer process of an hBN flake (blue) onto a 40 µm-diameter hole patterned on a 200 nm-thick SiN membrane (yellow). Areas were the PDMS is in contact with the substrate appear darker. The meniscus from the PDMS is highlighted with an arrow.

the PDMS touches during the peeling off from the sample is also not the membrane, otherwise the membrane would be pulled out and break. Figure 4.4a shows a photograph taken during the stamping of the drum used in Ref. [1]. Parts that are in contact with the PDMS appear darker than the ones that are not. The point of contact was towards the left side of the membrane. Figure 4.4b-c are zooms into the membrane window at different points of the release of the PDMS. Parts of the flakes that are in contact with the substrate appear as colorful, like the blue flake on the hole, and those that are not appear as transparent. The speed at which the meniscus – the interface between the areas in contact and not in contact with the PDMS – advances can be controlled with the z-positioning stage.

The mechanical transfer makes the SiN membranes and hBN flakes buckle (Fig. 4.5). At the end, we press the flakes against the SiN membrane and later we pull them off with the PDMS stamp – this leads to uneven tensioning and bulging of the hBN resonators, and can be detrimental to the mechanical properties of the hBN drums [45, 144]. In particular, they cause a deviation of the experimental mechanical mode shapes of the drum with respect to what is expected for ideal circular membranes (see Fig. 2.3); this effect is investigated in Section 4.5.

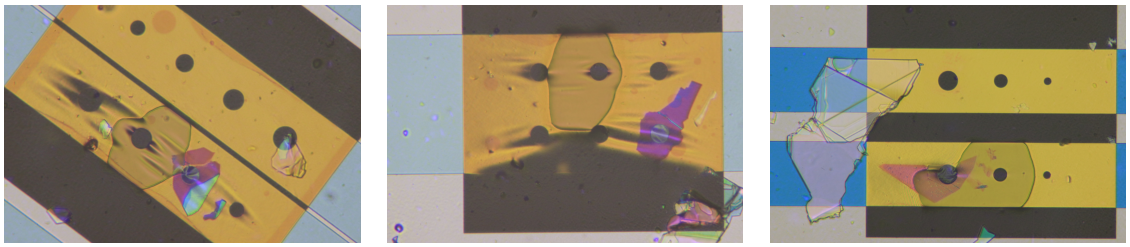

Figure 4.5: Example of a dry transfer process. Photographs of the stamping process of three different samples. During the peeling off of the PDMS, the SiN membrane and the flakes get dragged, causing the hBN and SiN membrane to buckle and wrinkle.

We have mentioned before that we look for flakes with thicknesses between 10 nm and 200 nm. The choice of this thickness range results as a compromise between having a large membrane mechanical amplitude and enough dispersive coupling. On the one hand, the mechanical am-

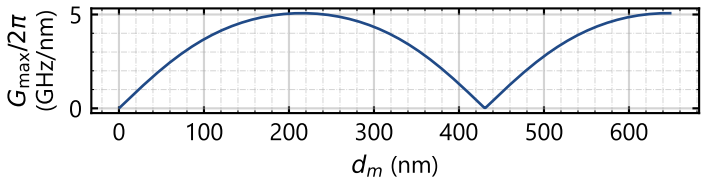

Figure 4.6: Flake thickness and maximum dispersive optomechanical coupling. The blue line is generated using Eq. 2.76 with the following parameters: hBN refractive index at $\lambda = 1550\,\text{nm}$, $n = 2.1$ [88]; cavity length, $L_{\text{cav}} = 40\,\mu\text{m}$ and sample position, $z = \lambda/8$.

plitude is inversely proportional to the effective mass (Eq. 2.16), and consequently to the flake's thickness d_m. The limit here is a mono layer flake. On the other hand, flakes thinner than 10 nm present almost no dispersive coupling due to their small reflectivity (Fig. 2.5). The upper limit of 200 nm can easily be understood by looking at the behavior of maximum dispersive coupling[4] as a function of the flake's thickness (Fig. 4.6). Because of the periodic behavior, it is pointless to use flakes thicker than 200 nm, which suffer from lower mechanical amplitudes.

O_2 plasma cleaning

Both the Nitto tape and the PDMS stamp leave polymer residues on the flakes, which can potentially be detrimental for the optical properties of the cavity. Figure 4.7a shows AFM tapping mode scans of an hBN flake stamped on a 200 nm-thick patterned low-stress SiN membrane before (left) and after (right) cleaning the sample with an O_2 plasma (600 W, 90 Pa, 4 min, 100 sccm). The RMS roughness of the hBN flake surface (yellow area) decreases from 2.6 nm to 880 pm after the cleaning step. The height profile across the white lines are depicted in Figure 4.7b.

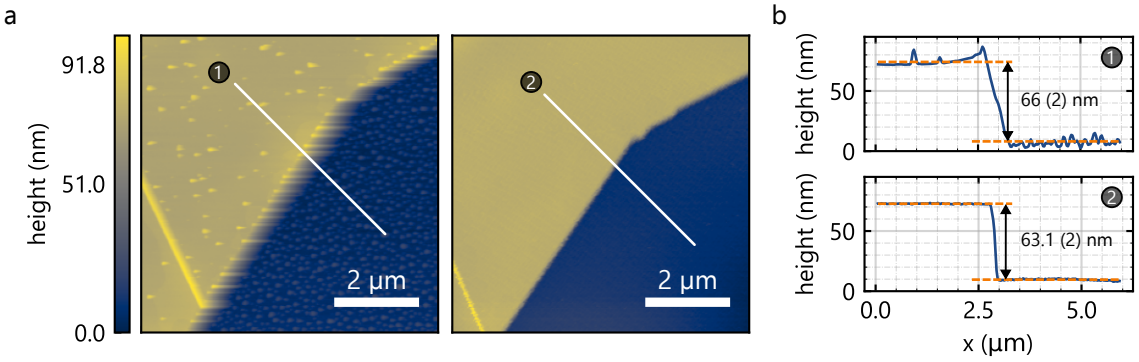

Figure 4.7: O_2 plasma cleaning. (a) Tapping mode AFM scan of an hBN sample prior to (left) and after (right) O_2 plasma cleaning (600 W, 90 Pa, 4 min, 100 sccm, Alpha Plasma Q150). (b) Height traces across the white lines labeled with the number 1 and 2. The change of flake thickness reveals an etch rate for this plasma settings of approximate 1.3 nm/min.

The O_2 plasma also etches the flakes; from this measurement we estimate a maximum etch rate of 1.3 nm/min. After this measurement we decided to reduce the plasma power to 300 W in order to decrease the etching rate, but we have not measured its value. A thorough study of the influence

[4] This happens at membrane positions which are odd multiples of $\pm\lambda/8$, see Section 2.4.

of the plasma on the flake's thickness and its mechanical properties should be conducted in the future.

Ralf Messmer carried out a detailed characterization of the PDMS residues on the samples [145]; following his work, we perform a two-step cleaning process. First, to remove the residues from the Nitto tape we put the PDMS stamp with the exfoliated flakes on top into an O_2 plasma (300 W, 90 Pa, 3 min, 100 sccm, Alpha Plasma Q150). Second, we treat the sample with another O_2 plasma step (300 W, 90 Pa, 3 min, 100 sccm, Alpha Plasma Q150) after the stamping process to remove residues from the PDMS stamp itself.

4.3 Cleaving the sample

The samples have to be cleaved to be inserted in the cavity. To that end, we mount them on a custom made holder (fabricated by Louis Kukk) that ensures that the patterned SiN membrane is protected and not in contact with any other parts of the holder (Fig. 4.8a). We use a diamond scribe to scratch across the entire backside of the SiN chip (Fig. 4.8b). By applying some pressure on the sample, it breaks along the Si crystal direction (Fig. 4.8c). Finally, the SiN chip is glued to a sample holder with conductive silver paste (Fig. 4.8d). The sample holder accommodates a piezo element to be able to drive the sample if necessary. The newest version of the sample holder, which is not the one shown in Figure 4.8d but in Figure 4.8e, is made of a PCB board. Both the sample and top side of the piezo are connected to ground (GND), avoiding an electrical potential difference between the sample and the fiber mirrors. The piezo is glued to both versions of the sample holder with indium soldering paste[5].

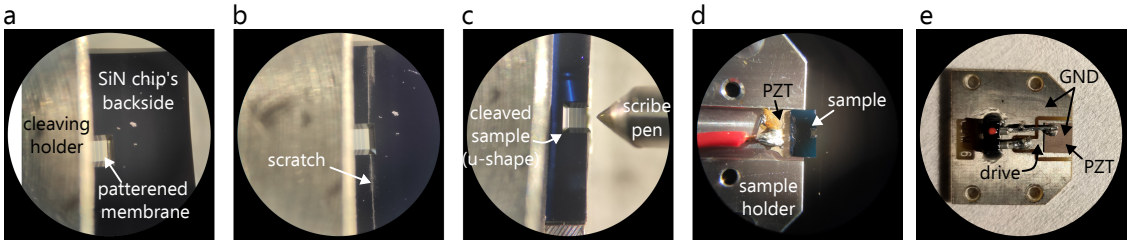

Figure 4.8: Cleaving the SiN chips. (a) Top view of a SiN chip placed upside down inside the cleaving holder. The patterned SiN (three stripes) can be seen upon zooming into the picture. (b) Same chip after scratching its backside with a diamond scribe. (c) After cleaving, the sample presents a characteristic u-shape. If there are remaining pieces of the Si frame they can, most of the time, be removed with the tip of the scribe. (d) Sample glued to the sample holder. The piezo element appears as orange below the soldered cable. In the image, the sample is not connected to ground but to the RF drive. (e) Newest version of the sample holder without sample on it. It is made of a PCB board. The top side of the piezo and consequently the sample are connected to ground (GND). Only the small part of the sample holder into which the backside of piezo is glued is connected to the RF drive.

Jana Ochs (née Huber) and Felix Rochau compared the mechanical cleaving process to a laser cutting method [146]. They found that the latter produces a lot of dirt with respect to the mechanical approach. This is the reason why we use the cleaving process presented in this section.

[5]Indium corporation. Low temperature Pb-Free paste, alloy E1 (NCSMQ80).

4.4 Mechanical characterization methods

The mechanical properties of the sample are characterized in a standard Michelson interferometer, operated at room temperature and equipped with a He-Ne laser ($\lambda = 632\,\text{nm}$, $180\,\mu\text{W}$). Figure 4.9a shows a sketch of the interferometer. The sample is mounted on a 3-axis positioning system[6] and placed inside a vacuum chamber to reduce gas damping ($< 10^{-4}$ mbar). The interference from the light reflected from the sample and the reference arm is detected via a fast photodetector (home-built photodetector[7], bandwidth of 30 MHz) and sent to a spectrum analyzer (SA). We actively stabilize the signal to the middle of the Michelson interferometer fringe by mounting the reference arm mirror on a piezoelectric transducer (PZT) controlled with a proportional-integral feedback loop (PI, same lock box as the ones described in Section 3.3). We send a ramp waveform

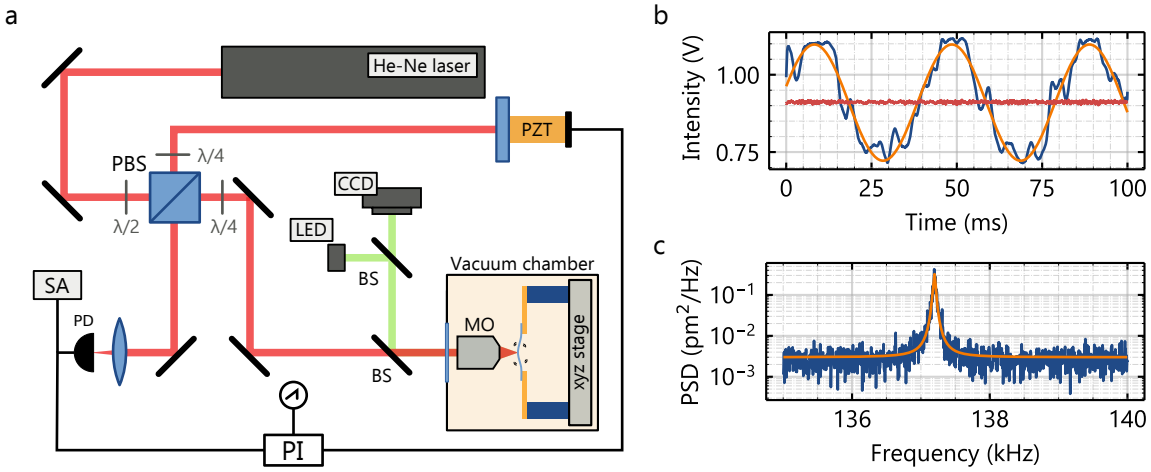

Figure 4.9: Mechanical characterization of the samples. (a) Schematic of the Michelson interferometer setup, with the following acronyms: spectrum analyzer (SA), polarizing beam splitter (PBS), beam splitter (BS), proportional-integral controller (PI), photodetector (PD), piezoelectric transducer (PZT). (b) Signal from the photodetector as a function of time while scanning the mirror's position (blue) and actively stabilizing to the middle of the fringe (red). The orange line is a fit to the photodetector signal using Eq. 4.1. (c) Displacement power spectral density of the fundamental mode of the 200 nm-thick SiN stripe shown in Figure 4.10a. See Figure 4.10a and Section 4.5 for more details on the sample's geometrical parameters.

generated with a Agilent arbitrary waveform generator to the piezo element. The ramp has a peak voltage of $V_\text{p} = 10\,\text{V}$ and a frequency of 10 Hz. The voltage $V(t)$ measured by the photodetector, as a function of the mirror position $z(t)$, is given by

$$V(t) = V_\text{dc} + V_\text{rf}\cos\left(\frac{4\pi z(t)}{\lambda} + \phi_0\right); \tag{4.1}$$

the displacement of the mirror with the ramp waveform scans the interferometer over 3-bright-fringes of fringe amplitude $V_\text{rf} = 180\,\text{mV}$ (Fig. 4.9b, blue line), which corresponds to a mirror displacement $\Delta z = \lambda$. If we lock the interferometer at the middle of the fringe, where the voltage depends linearly on the mirror position, a small displacement of the sample $\delta z(t)$ – driven, for

[6] Attocube ECSx3030.

[7] The detector is described in Section 3.3. Reference [112] provides more information about it.

instance, by the thermal noise (see Section 2.2.2)– will be translated into a small voltage around the DC value $V(t) = V_{\mathrm{dc}} + \delta V(t)$, with

$$\delta V(t) = V_{\mathrm{rf}} \frac{4\pi \delta z(t)}{\lambda}. \tag{4.2}$$

The expression above is valid as long as $\delta V(t) \ll V_{\mathrm{rf}}$. This way of converting voltages into displacement based on the fringe pattern of the Michelson interferometer has been used for decades [147–150]. In particular, Ref. [148] describes it in a very pedagogical manner and proposes an easy undergraduate experiment to understand its working principle.

Using Eq. 4.2 we can transform the voltage power spectral density S_V (V^2/Hz), measured by the spectrum analyzer, into displacement power spectral density S_z (m^2/Hz). This method, in contrast to the thermomechanical calibration [75], does not require any knowledge about the resonator's effective mass or the environment's temperature. Figure 4.9b displays the experimental signal $V(t)$ as a function of time in blue; the orange line is a fit using Eq. 4.1; the red line is the reflection signal when the interferometer is locked at half the fringe. From the fitting parameters we extract the conversion efficiency $\alpha = \lambda/(4\pi V_{rf})$. The voltage PSDs measured at the spectrum analyzer are transformed to displacement using[8]

$$S_z = \alpha^2 S_V. \tag{4.3}$$

We fit Eq. 2.16 to the experimental S_z and extract the effective mass[9] m, resonance frequency Ω_0, linewidth Γ_0 and quality factor $Q = \Omega_0/\Gamma_0$ of the detected mechanical modes. Figure 4.9c depicts the displacement PSD (blue) of the fundamental mode of a low-stress SiN stripe together with the Lorentzian fit (orange). The fit yields $\Omega_0/2\pi = 137.2\,\mathrm{kHz}$, $\Gamma_0/2\pi = 38\,\mathrm{Hz}$, $Q = 3600$, $m = 282\,\mathrm{ng}$.

The conversion efficiency for the measurements shown in Figure 4.9 is $\alpha = 0.29\,(5)\,\mu\mathrm{m/V}$, and is limited by the fringe amplitude V_{rf}. A better optical alignment should lead to better efficiencies. The minimum detectable signal, i.e. the sensitivity of the measurement η, is given by the noise floor and yields for these measurements $\eta = 0.003\,\mathrm{pm}^2/\mathrm{Hz}$.

4.5 hBN and SiN modes hybridization

This section is based on the Supporting Information of our publication:

I. Sánchez Arribas, T. Taniguchi, K. Watanabe, E. M. Weig, *"Radiation pressure back-action on a hexagonal boron nitride resonator"*, Nano Lett. **23**, 6301–6307 (2023), Ref. [1]. The published work has been explicitly written by the author. Therefore, the section partly contains passages of the original publication.

Our samples consist, at the end of the day, of a circular hBN drum-head resonator suspended on a larger and heavier SiN resonator. If the resonant modes of both resonators are close in frequency

[8] If the reader is planning to use this formula, check the output units from the spectrum analyzer and make sure to transform from RMS to peak voltages if necessary.

[9] To extract the effective mass we assume the resonator is thermalized with the environment $T_{\mathrm{bath}} = 24.7\,^{\circ}\mathrm{C}$.

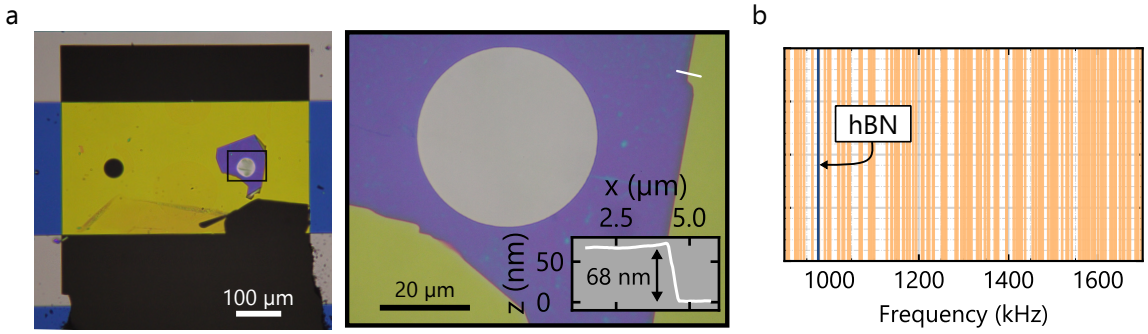

Figure 4.10: The "resonator on a resonator". (a) Left: Microscopy image of 40 µm-diameter hBN drum (blue) resting on a 200 nm-thick low-stress SiN stripe ($500 \times 281\,\mu m^2$, yellow). A piece of the SiN stripe broke during cleaving. The image has an enhanced phase contrast obtained by closing enough the microscope's condenser aperture. The latter reveals bulging or uneven tensioning of the circular hBN drum. Right: zoom into the black rectangle of the left image without enhanced phase contrast, together with an AFM height profile along the white line on the top-right corner of the micrograph. (b) Calculated resonance frequencies for the hBN drum (blue, fundamental mode) and SiN stripe (orange, higher order modes up to $m, n = 30$). See the main text for the parameters of the calculations.

and the mechanical modes are coupled together, they can hybridize [139, 151–153]. In our system, the coupling mechanism is mediated by strain. Let's have a look at the sample shown in Figure 4.10a. The sample consists of a 40 µm-diameter hBN drum suspended on a 200 nm-thick low-stress SiN stripe of dimensions $500 \times 281\,\mu m^2$; a part piece of the SiN stripe broke during the cleaving of the sample. The flake has a thickness[10] of $d_m = 68$ nm (inset in Fig. 4.10a, right). We can predict the frequency of the fundamental mode of the hBN drum resonator through Eq. 2.26 , yielding[11] $\Omega_0/2\pi = 970$ kHz. We can measure the frequency of the fundamental mode of the SiN stripe using the Michelson interferometer. The mode, displayed in the previous section in Figure 4.9c, reveals $\Omega_0/2\pi = 137.2$ kHz; approximating the geometry of the stripe to a perfect rectangle, we get an estimate of the stripe's stress σ using Eq. 2.21, $\sigma = 14$ MPa; with σ we can predict the frequency of the higher modes. Figure 4.10b shows the calculated resonance frequencies for the fundamental mode of the hBN drum (blue) and the higher order modes of the SiN stripe (orange), up to $(m, n) = (30, 30)$. The spectrum of frequencies of the SiN stripe is very dense, and consequently one should expect the modes to hybridize.

We note here that we have used the equation of a rectangular membrane (Eq. 2.21) – and not a plate – to predict the mode frequencies of the SiN stripe. We have therefore neglected its bending rigidity, which may not seem justified given the small value of the estimated stress $\sigma = 14$ MPa. Nevertheless, we assume it behaves as a membrane due to the results Jana Ochs obtained in her master thesis [146]. She studied the mechanical response of resonators very similar to ours. The resonators were $500 \times 30\,\mu m^2$-stripes patterned on a low-stress 200 nm-thick SiN membrane (Norcada): only one lateral dimension differs from our resonators by approximately a factor of 10. The

[10] After the AFM measurement the flake was cleaned again with an O_2 plasma. The latter etched the flake, which was observed as a change of color contrast under the microscope. We did not re-measure its thickness, so that the value $d_m = 68$ nm is an upper limit to the real thickness. More information on this is given in Section 5.1.3.

[11] For hBN we use $\rho = 2100\,kg/m^3$ [154], $E = 300$ GPa [145] and $\nu = 0.211$ [155].

SiN chip was cleaved in the same way as the one from this work. She measured a final stress of $\sigma = 90\,\text{MPa}$, of the same order of magnitude than our estimation. She observed that the frequency versus mode number dependence follows the linear trend characteristic of resonator whose motion is governed by the in-plane tension (Eq. 2.21), like a membrane or a string in the one dimensional case [76]. If the bending stiffness cannot be neglected, the mode frequency shows on the contrary a quadratic dependence on the mode number [76]. Given her results and the similarities between both systems, we assume we can neglect the SiN stripe's bending rigidity. The validity of this assumption should be checked in the future by performing similar measurements.

Let's have a look at the experimental mechanical spectra of our sample. Figure 4.11a displays the thermomechanical motion's power spectral density measured at different positions: the orange and blue lines are measured on the hBN flake, outside and on the circular resonator, respectively (orange and blue left triangles in the inset of Fig. 4.11a). Both measurements display a pronounced resonance at 322.6 kHz attributed to the SiN stripe; the wider feature next to it, at 322.0 kHz, is noise from the He-Ne laser. For frequencies above 1 MHz a plethora of peaks start arising on the hBN resonator that are not present in the spectra measured on the SiN stripe. The right part of Figure 4.11a shows the frequency range between 1.5 MHz and 1.6 MHz as an example.

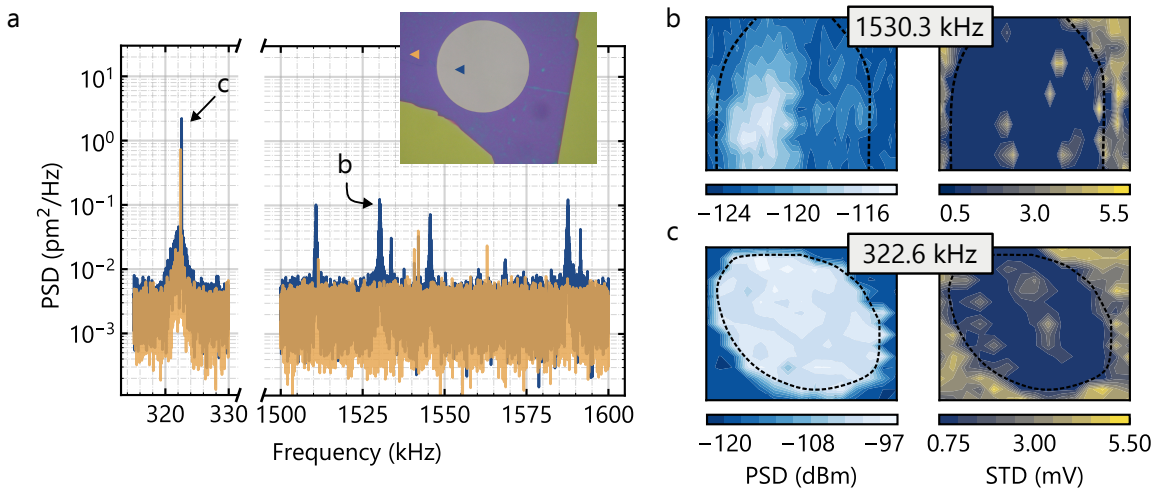

Figure 4.11: Thermomechanical spectra. (a) Power spectral density (PSD) on the suspended flake (blue line, measured at the blue triangle in the inset) and on the flake resting on the SiN stripe (orange line, orange triangle in the inset). The arrows depict the modes used in (b) and (c). (b) Left: Maximum of the PSD in dBm for the 1530.3 kHz mode as a function of spatial position measured with a bandwidth of 1 Hz. Right: standard deviation (STD) of the reflection signal; for positions outside the circular drum the lock is lost and the STD of the reflection is large. The black dashed lines represent the edges of the circular drum and are estimated from the STD colormap. Due to hysteresis in the positioner's scan directions the plot is distorted and not to scale. (c) Same as (b) but for the mode at 322.6 kHz.

To gain more insight into the mode's spatial dependence, we map the mode shapes of some of these resonances. The mode shapes are obtained by recording the spectra while scanning the sample position along the drum's surface. At each position of the scan measurements we record the PSD with the spectrum analyzer and the reflection signal with an oscilloscope. The travel range of the reference arm mirror is not long enough to cover for changes in reflection when the

sample is scanned over regions of different material. For this reason, every time the scans go over a different material, i. e. outside the circular membrane, the lock is lost. Figure 4.11b shows the maximum of the PSD in dBm of the mode at 1530.3 kHz measured with a 1 Hz bandwidth (left colormap) and the standard deviation (STD) of the reflection signal (right colormap), for a 32×11 scan. The standard deviation of the reflection signal is used to draw the edges of the resonator depicted as dashed black lines. The travel range of the scanning mode of our positioning system is too small to cover the whole drum-head and we have to use the stepper function. The latter suffers from a strong hysteresis, and consequently the colormap's x and y axis are not to scale and distorted; for spatial reference, the measured edges of the drum, drawn as guidelines to the eye from the maps of the standard deviation, are depicted as black dashed lines superimposed to the colormaps. The mode shape reveals that the mechanical mode is confined within the circular resonator, with a prominent lobe on the left side. Similar mode shapes have been observed for exfoliated hBN resonators [45]. We attribute the deviation from the expectation for the fundamental mode an ideal circular resonator (see Section 2.2.3) to the uneven tensioning and/or bulging of the resonator resulting from the transfer process. A closer look into the sample shows indeed hints of bulging (Fig. 4.10a, left). Figure 4.11c displays the same measurements but for the SiN mode at 322.6 kHz and a 15×15 scan. The peak amplitude of this mode remains constant over the scanned area at 100 ± 1 dBm. All this suggests that the modes appearing at frequencies larger than 1 MHz, undetectable on the SiN stripe, originate purely from the hBN circular resonator or result from hybridization between the modes intrinsic to the hBN drum-head and the SiN stripe ones [139, 152, 153].

To further investigate the degree of hybridization, we measure the effective mass of all modes starting from the fundamental mode of the SiN stripe at 137.2 kHz until 1.7 MHz. Any hybridization between the heavy SiN stripe and the hBN drum will result in an increase of the effective mass of the hBN resonator [139]. Figure 4.12a displays the effective mass as a function of resonance frequency. The data points are obtained from fitting the response of the resonator driven by thermal noise (Eq. 2.16) measured at different positions – now is a good moment to remember that the effective mass is position dependent, as explained in Section 2.2.3 and in Figure 2.2. Blue markers depict measurements taken on the free-standing hBN resonator, whereas orange ones depict measurements taken on the flake resting on the SiN stripe. Different marker shapes indicate measurements taken at different locations. The orange line represents the theoretical effective mass of an ideal rectangular SiN stripe of dimensions $500 \times 281 \times 0.2\,\mu\text{m}^3$, $m^{\text{th}}_{\text{SiN}} = 0.25 m_0 = 21.5$ ng, with m_0 the physical mass. This value sets a lower limit for the effective mass of pure SiN modes in case of an ideal rectangular geometry. Similarly, using a mass density of $2100\,\text{kg/m}^3$ [154], we predict for the fundamental mode of the hBN drum $m^{\text{th}}_{\text{hBN}} = 0.26 m_0 = 46.7$ pg, shown as blue dashed line in Figure 4.12a. This is the lower limit of the effective mass of the fundamental mode[12] of an ideal hBN drum. From our data we observe that the effective masses measured outside the circular drum (orange markers) stay close to the theoretical limit for SiN, which is what we expect as no hybridization should occur. However, the modes measured on the free standing hBN resonator (blue data set) start to deviate from the SiN limit toward lower masses for frequencies above 1 MHz: this is a sign of mode hybridization. The effective mass in this case reaches a minimum value of 520 pg at 1675.2 kHz. Since the spectrum of modes of the SiN is very dense above 400 kHz

[12] In contrast to a rectangular membrane, the effective mass of a circular membrane is mode dependent. The effective mass at the point of maximum deflection decreases for higher order modes [75].

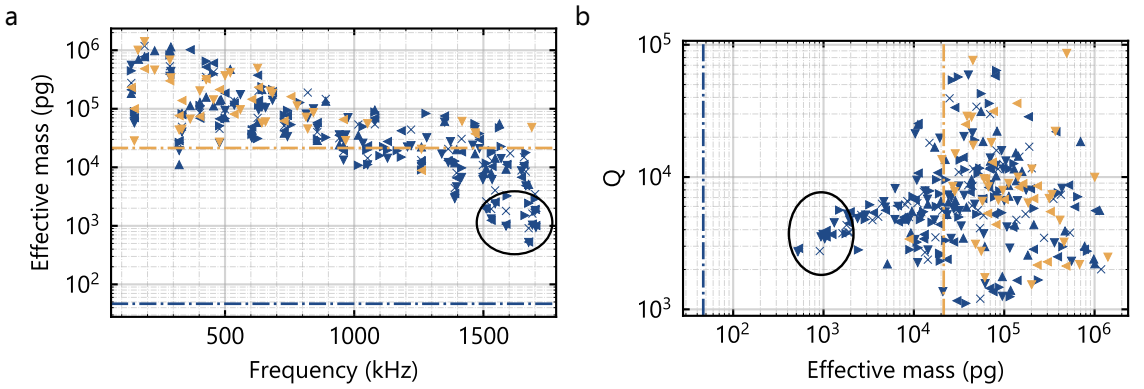

Figure 4.12: Effective mass and quality factor. (a) Experimentally determined effective mass versus resonance frequency. (b) Quality factor versus effective mass. Blue markers are resonances measured on the hBN drum whereas orange markers depict resonances measured on the hBN on top of SiN. Different marker shapes indicate measurements taken at different positions. Up, down, left, and right triangles indicate measurements done in the upper, bottom, left and right side of the hBN drum. The cross depicts the center. Dashed lines represent the theoretical effective masses for ideal circular hBN (blue) and rectangular SiN (orange) resonators at the point of maximum deflection (see Fig. 2.2). The black ovals highlight the interval in which the dynamical backaction measurements from Chapter 5 take place.

and around the estimated fundamental frequency of the hBN drum (Fig. 4.10b), we expect some degree of hybridization for all hBN modes. We were not able to identify the textbook modes of a circular membrane in our sample and we attribute this to the large bulging originating from the dry transfer (see Section 4.2 and Fig. 4.11a) [45, 144]. Nevertheless, we consider that the modes with effective masses more than an order of magnitude smaller than the limit for the SiN resonator have a very pronounced hBN drum-head character. Those are the modes we use to demonstrate dynamical backaction on the hBN resonator in the following chapter.

Figure 4.12b shows the dependence of the quality factor with the effective mass. The modes with an effective mass below 2 ng (black oval in Fig. 4.12b), with a strong circular resonator character, have quality factors in the range $Q \in [2000, 6000]$. This is in agreement with other measured Q factors of large diameter drums made from van der Waals materials [156, 157]. These Q factors may be influenced by the hybridization with the SiN modes though, which have Q factors in a similar range.

We conclude this chapter by highlighting that the performance of our mechanical resonator is limited, on the one hand, by the hybridization between the modes from the low-stress SiN stripe and the ones from the hBN resonator. This can be improved by using high-stress Si_3N_4 as a support for the hBN drums, pushing the Si_3N_4 resonances to higher frequencies and allowing resolution of the distinct mode shapes. On the other hand, the mechanical imperfections originating from the dry transfer are also detrimental for the mechanical properties. This can be improved by using more gentle transfer mechanisms like a wet transfer [139].

5

Cavity optomechanics with hBN resonators

THE attempts to observe radiation pressure effects on hBN mechanical resonators are very scarce. The first available platforms for hBN cavity optomechanics experiments are mechanically exfoliated hBN resonators coupled to the near-field of a microdisk cavity [158, 159]. Indeed, Shandilya and colleagues [158] were able to measure the thermal motion of an hBN beam through its optomechanical interaction with a silicon microdisk cavity in the telecom regime for the first time. However, no optomechanical backaction was observed.

In this chapter, we report the first experimental demonstration of radiation pressure backaction with a hexagonal boron nitride resonator. The mechanical resonator is inserted in the middle of our fiber-based microcavity (cavity C8 from Table 3.1), realizing a membrane-in-the-middle optomechanical system. The chapter begins with the characterization of the dispersive and dissipative couplings (Section 5.1), which is done by mapping the dependence of the properties of the cavity resonance with respect to the resonator's position along the cavity mode axis. In Section 5.2 we characterize the mechanical response of the resonator's modes using the cavity as read-out mechanism. Section 5.3 presents the dynamical backaction effects of the retarded radiation pressure force on the mechanical resonator, which manifest as an optical spring and optomechanical damping. For some mechanical modes we observe a reverse optical spring with respect to the detuning of the laser exerting the optical force. These measurements, introduced in Section 5.4, conclude this chapter.

Parts of this chapter are based on our publication:

I. Sánchez Arribas, T. Taniguchi, K. Watanabe, E. M. Weig, *"Radiation pressure backaction on a hexagonal boron nitride resonator"*, Nano Lett. **23**, 6301–6307 (2023), Ref. [1]. The published work has been explicitly written by the author. Therefore, the chapter partly contains passages of the original publication.

5.1 Static optomechanical couplings

The goal of this section is to determine the linear and quadratic dispersive and dissipative optomechanical couplings of different samples. This is achieved by mapping the behavior of the transmission of the cavity as a function of the membrane's position, in the same way we derived the expressions of the couplings in Section 2.4. Prior to the measurements we need to align the sample with respect to the cavity mode. We do so by first aligning by eye the sample's surface so that it is perpendicular to the fiber axis. Then, we perform several transmission maps as a function of the sample's position and change the sample's angle[1] with respect to the fibers to maximize the cavity's transmitted power. We also change the sample's angle to minimize the presence of higher order optical modes [160].

In Section 5.1.1 we first describe the standard measurement routine. To that end, we employ a standard 30 nm-thick SiN stripe without hBN or any patterned holes, a type of sample we have been working with for years [112, 135]. The next step is to understand if the added etched holes on the SiN stripe introduce any scattering losses or dispersive effects. We analyze this in Section 5.1.2. Finally, our results on hBN membranes are presented in Section 5.1.3. All results presented in this chapter are done with cavity C8.

5.1.1 Measurement description with a SiN test sample

Figure 5.1 summarizes the measurement routine. The sample's position is changed N-times from z_0 to z_{N-1} (Fig. 5.1a). At each position we record a cavity transmission $|S_{21}|^2$ and a cavity reflection $|S_{11}|^2$ spectrum with the oscilloscope, with a large resolution of typically 10^6 samples, as a function of the cavity length. The latter is scanned by sending the same ramp waveform to both piezos and is transformed into frequency detuning Δ (Eq. 2.74) with the help of the sidebands generated by the EOM. We only use one laser, the lock laser, and its polarization is set to match the cavity's lower frequency polarization ($|\kappa_{1,e}|/2\pi = 1.34\,\text{MHz}$, $\kappa_{2,e}/2\pi = 1.80\,\text{MHz}$, $\kappa/2\pi = 18.5\,\text{MHz}$, Fig. 3.10a). The electrical equipment involved in these measurements is described in detail in Section 3.3. $|S_{21}|^2$ and $|S_{11}|^2$ are determined using the calibration procedure explained in Section 3.4.1 with an extra step: due to the large frequency detuning scans ($\Delta/2\pi > 25\,\text{GHz}$), we need to consider the finite sampling rate of the oscilloscope as well, which effectively behaves as having a detector whose gain depends on the amplitude of the scan sent to the cavity piezos (see Appendix B.2).

Figure 5.1b shows as an example a total of $N = 350$ transmission spectra as a function of the detuning Δ and sample's position z, for a ramp waveform of frequency $f = 9\,\text{Hz}$ and peak amplitude $V_\text{p} = 1.6\,\text{V}$. The waveform is amplified with a high voltage amplifier (see Section 3.3). The sample consists of a patterned[2] 30 nm-thick SiN stripe (Norcada NX5050X) and is cleaved following the procedure described in Section 4.3. We set the position to $z = 0$ and the detuning to $\Delta = 0$ when the sample is at a node of the cavity. The dashed line depicts the resonance frequency when the cavity is empty. The cavity's transmission follows the sinusoidal behavior with $\lambda/2$-periodicity expected for a membrane-in-the-middle experiment when the cavity piezos are scanned symmetrically. The $\lambda/2$-periodicity was introduced and explained in detail in Section 2.4. The sample's

[1] We can change two angles with the positioning system. We always iterate over both of them.
[2] The stripe's dimensions are $80 \times 500\,\mu\text{m}^2$.

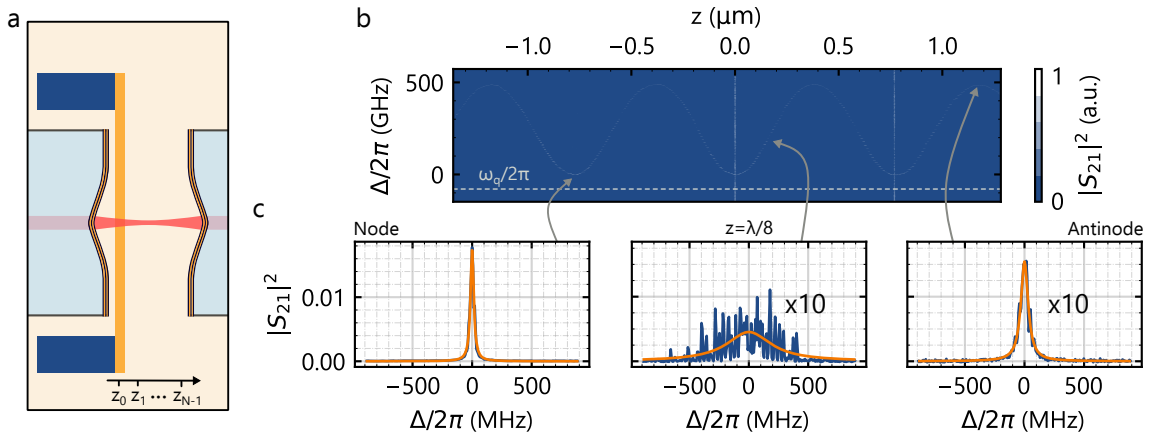

Figure 5.1: Measurement routine. (a) The sample's position is changed N-times from z_0 until z_{N-1}. At each position we record a transmission and reflection spectrum as a function of the frequency detuning Δ. (b) Cavity transmission $|S_{21}|^2$ versus sample's position z and frequency detuning Δ. The white dashed line depicts the empty cavity resonance. (c) Example of three spectra (blue) taken at the node, $z = \lambda/8$ and antinode. The orange solid lines are Lorentzian fits to the data. For this measurement we use an input power of $P_0 = 17\,\mu$W. The detuning is set to 0 at the center of the Lorentzian function for these plots.

position z is changed by sending a voltage to the z-axis of the positioners from 5 V to 55 V for this particular example. The voltage sent to the positioners can be transformed into displacement z either by using the fringe pattern of the 1310 nm-interferometer as reference or the sinusoidal behavior of the cavity resonance transmission itself (Fig. 5.1b). The calibration from voltages to position is explained in Appendix B.3.

To measure the dispersive and dissipative coupling, we fit a Lorentzian function to each transmission spectrum. The fit's parameters are the cavity linewidth κ, the center of the Lorentzian and its amplitude. Figure 5.1c depicts three examples at the most representative positions: the cavity node, antinode and at the point of maximum dispersive coupling $z = \lambda/8$. The cavity response (blue data) is well represented by a Lorentzian function (orange solid line) for sample's positions very close to the cavity node and antinode, where the dispersive coupling is the smallest and close to 0. However, at $z = \lambda/8$ and positions far away from the cavity nodes and antinodes, any mechanical vibrations – coming from the sample, the positioning stage or the cavity mirrors – are converted into cavity frequency fluctuations due to the large dispersive coupling. The frequency fluctuations, which are larger than the cavity linewidth, lead to a broadened cavity frequency response and overestimated cavity linewidth κ from the fits.

From the center of the Lorentzian we extract the detuning of the cavity resonance Δ_{cav} as a function of the sample's position, which is displayed in Figure 5.2a. In the measurements we set the detuning to $\Delta_{\mathrm{cav}} = 0$ when the sample is placed at the cavity node, removing the offset with respect to the empty cavity resonance introduced by the complex phase of the membrane's reflection coefficient ϕ_r (Eq. 2.73 and Eq. 2.74). The missing points in Figure 5.2a are failed fits and occur at positions either with a large dispersive coupling – where the signal is weak and very broad – or at positions where there is scattering to higher order optical modes. To extract the linear dispersive coupling G we perform a numerical derivative of the data (Fig. 5.2b, blue dots). The quadratic dis-

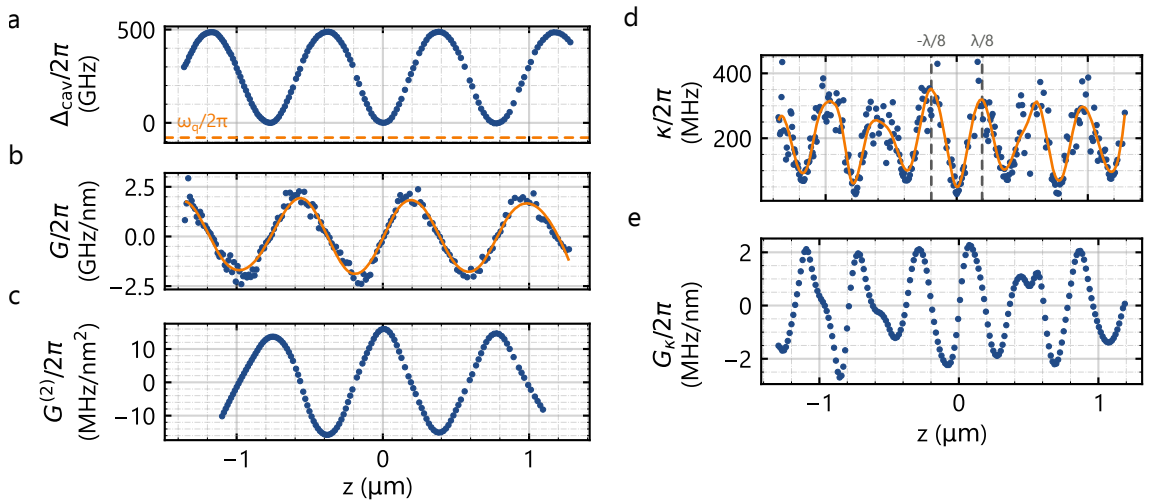

Figure 5.2: Experimental optomechanical couplings. (a) Cavity detuning (dots) versus sample position z along the cavity mode axis. The coordinate $z = 0$ corresponds to the sample sitting in an optical field node. (b) Linear dispersive coupling G obtained by doing a numerical derivative of the data in (a). The orange solid line is a spline used to smooth the data. (c) Quadratic dispersive coupling $G^{(2)}$ calculated from the numerical derivative of the spline in (b). (d) Cavity linewidth (blue) and spline to the data (orange) as a function of sample position. The two gray dashed lines highlight the positions $z = \pm\lambda/8$. (e) Dissipative coupling extracted from the numerical derivative of the spline in (d).

persive coupling $G^{(2)}$ (Fig. 5.2c) is obtained by smoothing the data from the linear coupling with a spline (orange line in Fig. 5.2b) and doing a numerical derivative again.

Figure 5.2d shows the cavity linewidth κ extracted from the Lorentzian fits as a function of the sample's position. It presents local minima at the node and antinode and local maxima at odd multiples of $z = \lambda/8$, the latter resulting from the linewidth broadening due to the frequency fluctuations. We estimate the dissipative coupling G_κ by smoothing the experimental $\kappa(z)$ with a spline (orange line in Fig. 5.2d) and performing a numerical derivative. The results are presented in Figure 5.2e. We recall that because the linewidth is overestimated so is the dissipative coupling.

An alternative to extract the cavity linewidth is to use the value of the cavity transmission at resonance $|S_{21}|^2_{\max} = |S_{21}|^2(\Delta = 0)$. Because we know the cavity's external couplings $\kappa_{1,e}$ and $\kappa_{2,e}$ from the previously measured empty cavity response, and assuming they do not depend on the sample's position, we can use Eq. 3.12 to obtain

$$\kappa_{s_{21}}(z) = 2\sqrt{\frac{|\kappa_{1,e}|\kappa_{2,e}}{|S_{21}|^2_{\max}(z)}}, \tag{5.1}$$

where we name the linewidth as $\kappa_{s_{21}}$ to emphasize that it is obtained from the cavity's transmission $|S_{21}|^2$ on resonance.

Figure 5.3a shows the linewidth calculated using Eq. 5.1. The linewidth presents again local minima at the nodes and antinodes, and the values of $\kappa_{s_{21}}$ coincide with the ones extracted from the

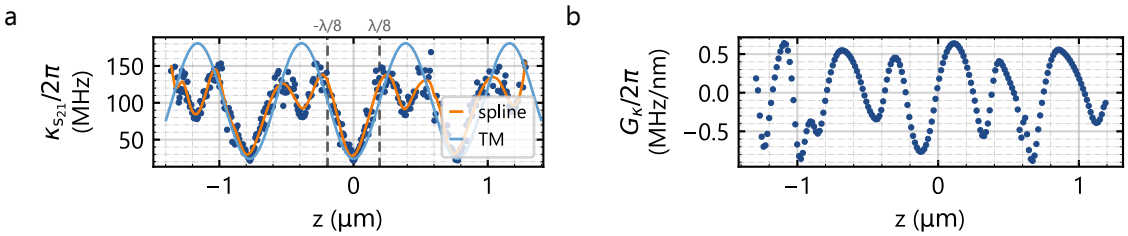

Figure 5.3: Cavity linewidth and dispersive coupling from the cavity transmission. (a) Cavity linewidth extracted using Eq. 5.1. The orange line is a spline to smooth the data. The blue solid line shows the transfer matrix calculations with a SiN thickness of $d_m = 30\,\text{nm}$, $\text{Re}(n) = 2.1$ and $\text{Im}(n) = 1.4 \times 10^{-4}$. The two gray dashed lines highlight the positions $z = \pm\lambda/8$. (b) Dissipative linear coupling extracted from the smoothed data (orange line) in (a).

Lorentzian fit (Fig. 5.2d) at those positions. However, they are significantly reduced for the other sample positions and now the local maxima do not happen at odd multiples of $\lambda/8$ but slightly closer to the antinode. We often observe the dips at the antinodes in most of the measurements performed in this work with different samples and with cavity C8, and in those done by Felix Rochau (Refs. [112, 135]) with cavity C3 and a symmetrical scan of the fiber mirrors[3]. A similar dip was observed in the work by Sankey et al. [110] with a normal Fabry-Pérot cavity and stoichiometric Si_3N_4 membrane operated at $\lambda = 1064\,\text{nm}$. The dips could originate from scattering to higher order modes by a small misalignment of the membrane with respect to the cavity mode axis. However, due to difficulties of aligning the membrane with respect to the cavity because of the small cavity length, we have not investigated this effect.

We cross-check the measurements with the transfer matrix calculations, displayed as a light blue solid line in Figure 5.3a (membrane thickness $d_m = 30\,\text{nm}$, $\text{Re}(n) = 2.1$ and $\text{Im}(n) = 1.4 \times 10^{-4}$ at $\lambda = 1550\,\text{nm}$). The employed imaginary part of the refractive index is an order of magnitude larger than the value of $\text{Im}(n) = 1.2 \times 10^{-5}$ measured by Steinlechner and colleagues [161] on Norcada low-stress SiN membranes at telecom wavelengths. Using their measured refractive index, we expect a maximum linewidth modulation of $\kappa/2\pi = 35\,\text{MHz}$, a factor of 4 smaller than what we observe. This suggests that the SiN's absorption is not the main factor contributing to the large κ and supports the hypothesis of scattering as main loss mechanism.

5.1.2 Clipping losses from the circular frame

In this section we study the scattering and clipping losses introduced by the circular holes etched on the SiN that serve as frames for the hBN resonators. We fabricate a test sample (Fig. 5.4a) consisting of a 200 nm-thick SiN stripe (Norcada NX5050D) with seven etched holes of decreasing diameter (80 μm, 65 μm, 50 μm, 40 μm, 30 μm, 20 μm and 10 μm).

Figure 5.4b shows the cavity detuning as a function of the sample's position for the following diameters: 80 μm (green), 50 μm (red), 40 μm (orange) and 30 μm (blue) – the color code matches the one in the legend from Fig. 5.4c. For diameters ≤ 20 μm the clipping losses are too large and

[3] All measurements in this work (C8) are done with a symmetrical scan of the fiber mirrors. Felix Rochau did measurements with a non-symmetric scan and with a symmetric scan [112].

the cavity mode is lost, so consequently there is no data to show. The detuning does not exhibit a $\lambda/2$-periodicity for any of the holes, indicating an absence of dispersive coupling. The drift is due to lab temperature changes[4], and has a maximum value in absolute terms of $|\Delta_{\mathrm{cav}}|/2\pi = 1.25\,\mathrm{GHz}$ for the 80 µm-hole. In comparison, we note that a 30 nm-thick SiN stripe produces a maximum detuning of 500 GHz (Fig. 5.2a). Because of the lack of dispersive optomechanical coupling, it is sufficient to scan the cavity piezos without amplifying the signal from the waveform generator. We use a scan waveform of amplitude $V_{\mathrm{p}} = 3\,\mathrm{V}$ and input power of $P_0 = 18.5\,\mu\mathrm{W}$.

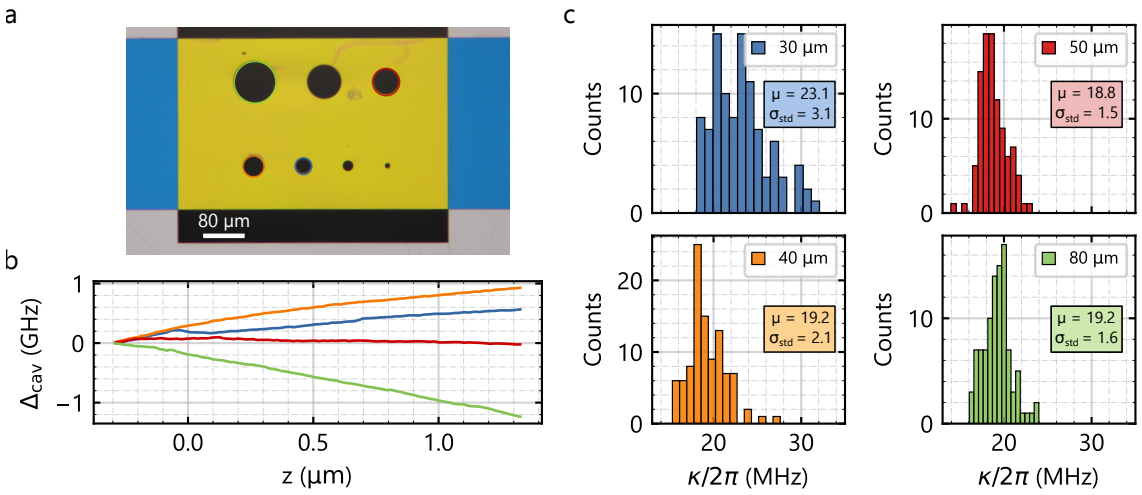

Figure 5.4: Clipping from the circular frames. (a) Microscope image of the sample used for the test. The holes used for the measurement have a false-colored rim according to the legend in (c). (b) Normalized cavity detuning as a function of sample position for different hole diameters (same color code as in (c)). The maximum detuning of all measurements is $|\Delta_{\mathrm{cav}}|/2\pi = 1.25\,\mathrm{GHz}$. The measurement consists of a total of $N = 100$ z-steps. (c) Histogram of cavity linewidth of the measurements in (b) for different hole diameters. The graphs include the mean value μ and standard deviation σ_{std} of the histogram in units of MHz. The measurements were done with the acoustic shielding box open.

Figure 5.4c depicts a histogram of the cavity linewidth of the z scans in Figure 5.4b for each of the holes, which were performed without acoustic isolation. The mean μ and standard deviation σ_{std} of the linewidth are displayed in the graphs. The standard deviation from the holes with diameters of 50 µm and 80 µm corresponds to that of the empty cavity without acoustic isolation (see Fig. 3.18). It increases by a factor of 1.3 for the 40 µm-hole, but the mean value remains within the error of the measurement. However, σ_{std} doubles the empty cavity value for the 30 µm-hole, and the mean is displaced towards larger linewidths, a clear indication of light scattering. Overall, these measurements set a lower limit to the minimum diameter of the hBN drums to 30 µm, although 40 µm is preferable to avoid scattering effects.

[4]The measurements were done with the acoustic shielding box open. The detuning drift, when plotted versus time, matches the lab temperature change in a similar way to the measurements shown in Figure 3.15a.

5.1.3 Results with hBN resonators

Figure 5.5 shows the static optomechanical couplings for the 68 nm-thick hBN circular resonator characterized in Section 4.5. We point out that, after the AFM measurements, we performed an extra O_2 cleaning step after which the color contrast of the flake changed. This indicates that the flake was etched by the O_2 plasma (see Section 4.2), but we did not re-measure it with the AFM. We nevertheless use the AFM-measured thickness of 68 nm as label to distinguish the flake from the other ones measured in this work (Table 5.1). A microscope image of the flake is shown as an inset in Figure 5.5. We observe a sinusoidal pattern of the detuning (blue dots, Fig. 5.5a) that reaches a maximum of $\Delta_{cav}/2\pi = 600\,\text{GHz}$ when the sample is placed at the cavity antinodes. G is directly extracted from the measurement by performing a numerical derivative (blue dots, Fig. 5.5b) as explained in Section 5.1.1. We observe a maximum of $|G/2\pi| = 2.5\,\text{GHz/nm}$. As expected for a membrane-in-the-middle system, the quadratic dispersive coupling $G^{(2)}$ reaches a maximum at the cavity nodes and antinodes [110, 160], of value $|G^{(2)}/2\pi| = 25\,\text{MHz/nm}^2$ for our system (blue dots, Fig. 5.5c). The measurements are well reproduced by transfer matrix calculations (solid lines in Fig. 5.5a-c), using as input parameters a flake thickness of 58 nm and a flake refractive index of $n_{hBN} = 1.85$. Assuming a smaller thickness value is justified by the already mentioned observation that the flake was etched and is therefore thinner than the AFM value. The measurement is done with a voltage ramp waveform sent to the piezos of amplitude $V_p = 1.65\,\text{V}$ and input power $P_0 = 12\,\mu\text{W}$.

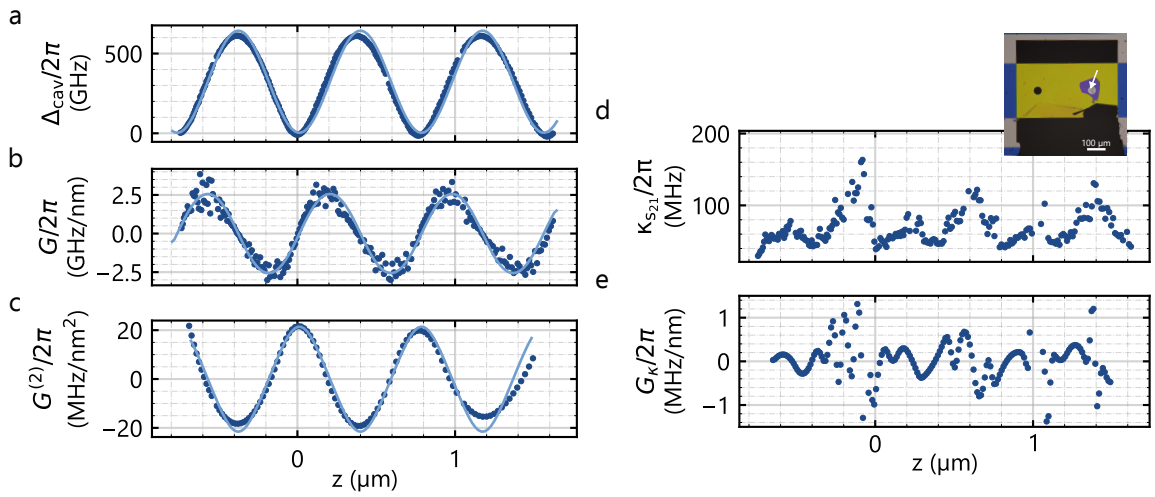

Figure 5.5: Static optomechanical couplings with a 68 nm-thick hBN membrane. (a) Cavity detuning (dots) versus sample position z along the cavity mode axis. We use an input power of $P_0 = 12\,\mu\text{W}$. The coordinate $z = 0$ corresponds to the sample sitting in an optical field node. (b) Dispersive and (c) quadratic dispersive coupling. The solid lines in (a), (b) and (c) are the result of transfer matrix calculations. (d) Cavity linewidth modulation and (e) corresponding dissipative coupling.

Any absorption or scattering from the flake will manifest as a modulation of the cavity linewidth κ, displayed in Figure 5.5d. hBN has a negligible absorption coefficient at telecom wavelengths [88, 162], and therefore the large cavity linewidths we observe cannot be attributed to optical absorption from the flake itself. Performing the same measurements shown in Figure 5.5a on the

SiN stripe hosting the flake results in modulations of similar magnitude (see Fig. 5.6b) that cannot be explained considering the absorption coefficient of SiN. This suggests that the losses in our system are dominated by scattering to higher order modes caused by a sample misalignment with respect to the cavity mode axis, and not by remaining impurities from the transfer process. The hypothesis is also consistent with the dips observed at the antinodes and the small scale ($z \ll \lambda$) variations of $\kappa_{s_{21}}(z)$. The linewidth modulation translates into the dissipative coupling $G_\kappa = \partial\kappa/\partial z$ (Fig. 5.5e). We highlight that dissipative coupling is more than three orders of magnitude smaller than the dispersive coupling and is therefore negligible in our system.

Excluding residual effects from the surrounding SiN membrane

To rule out an effect of the SiN membrane on the static optomechanical couplings, we design our sample with an additional empty hole of the same diameter (40 µm) used for reference measurements. Figure 5.6a , top panel, shows the cavity detuning Δ_{cav} as a function of the sample position when the empty hole is centered with the cavity mode. There is no modulation of the detuning with periodicity $\lambda/2$, indicating the absence of dispersive coupling. The constant drift is due to thermal drifts of the cavity. The SiN frame slightly modulates the linewidth (Fig. 5.6a, bottom panel), probably due to scattering of the mode at the edges, but remains very close to the empty cavity linewidth of 18.5 MHz, with some scattering around that value. Due to the absence of optomechanical coupling, the linewidth extracted from the Lorentzian fits κ matches the one from the resonant transmission $\kappa_{s_{21}}$.

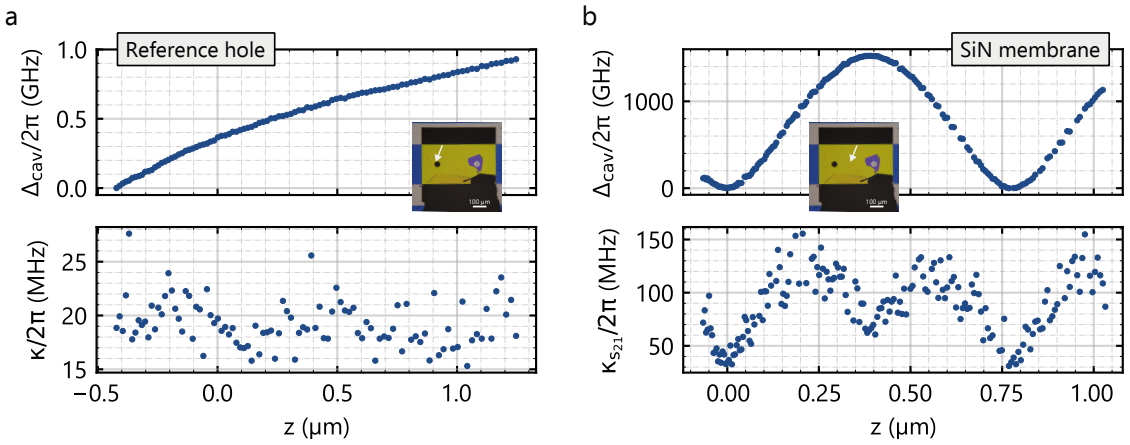

Figure 5.6: Effects from the SiN membrane. (a) Cavity detuning Δ_{cav} (top) and linewidth κ (bottom) when the empty hole is placed at the cavity mode. The position is indicated with a white arrow in the microscope image inset. The linewidth is extracted directly from the Lorentzian fits. (b) Same as (a) but with the SiN membrane center at the cavity mode. Due to the frequency fluctuations coming from the optomechanical coupling of the membrane, we extract the linewidth from the cavity transmission $\kappa_{s_{21}}$.

Figure 5.6b displays the detuning (top) and cavity linewidth (bottom) when the middle of the SiN membrane is centered with the cavity mode. The detuning, now periodic at $\lambda/2$, has a maximum value of $\Delta_{cav}/2\pi = 1520$ GHz. The cavity linewidth suffers a similar modulation as what is observed with the hBN flake. Neither the small absorption coefficient expected for hBN nor the larger one

for SiN accounts for the large modulation observed on both materials[5]. This was already discussed in the previous subsection and in Section 5.1.1.

Summary of the experimental linear optomechanical couplings

Table 5.1 summarizes the optomechanical couplings of the different samples studied in this work. We successfully fabricated a total of four hBN samples whose thickness d_m, measured with an AFM, is depicted in the second column. However, before placing the samples in the cavity, they were cleaned with an O_2 plasma that decreased their thickness, which manifested as a change of contrast in the microscope. Therefore, the values indicated are a upper limit to the real thickness the flakes had once inserted in the cavity. We estimate the flakes could be etched by around 10 nm from the transfer matrix calculations. The thinnest flake did not produce any observable dispersive coupling, which is expected from its small reflectivity (see Fig. 4.6 and its discussion in the main text).

Table 5.1: Linear optomechanical couplings. The thickness d_m of the hBN samples is an upper limit to the real value – the samples were etched after an O_2 plasma cleaning step but their thickness was not re-measured with the AFM. The thickness of the SiN membranes is the one specified by Norcada. The two bottom rows, with an asterisk next to the material, were measured by Felix Rochau [112]. Missing values are indicated with a hyphen.

Material	d_m (nm)	Cavity	λ (nm)	$\Delta_{\mathrm{cav}}^{\mathrm{max}}/2\pi$ (GHz)	$G_{\mathrm{max}}/2\pi$ (GHz/nm)	$\kappa_{s_{21}}/2\pi$ (MHz) min, max	$G_\kappa^{\mathrm{max}}/2\pi$ (MHz/nm)
hBN	177	C8	1550	1000	4	–	–
hBN [1]	68	C8	1550	600	25	30, 160	1
hBN	24	C8	1550	123	0.5	19, 200	4
hBN	16	C8	1550	0	0	18.5, 28	0.02
SiN	200	C8	1550	1520	6	30, 150	0.5
SiN	100	C8	1550	970	4	–	–
SiN	30	C8	1550	500	2.5	20, 150	0.5
Si_3N_4* [135]	30	C3	1550	240	1	20, 80	0.4
SiN*	30	–	780	1100	13.8	–	–

5.2 Mechanical modes inside the cavity

Before experimentally showing the effects of the retarded radiation pressure force on the mechanical properties of the resonators, we need to identify their mechanical resonances with the cavity. We do so by measuring the effective mass of each of the mechanical modes, with the intention of reproducing the results presented in Figure 4.12. For these measurements we use the 68 nm-thick

[5] For the 200 nm-thick SiN stripe we expect a maximum linewidth modulation of $\kappa/2\pi = 60$ MHz if we consider the membrane's absorption $\mathrm{Im}(n) = 1.2 \times 10^{-5}$ [161].

hBN drum-head whose mechanical properties and optomechanical couplings were characterized in Section 4.5 and Section 5.1.3, respectively. The drum has a diameter of 40 µm and rests on top of a 200 nm-thick SiN stripe (Fig. 4.10). The hBN drum is placed so that it is centered with respect to the cavity mode (inset in Fig. 5.5d).

We stabilize the cavity length to the lock laser as explained in Section 3.9 with the sample inserted $\Delta z = 10$ nm away from the cavity node. This position corresponds to $|G|/2\pi \simeq 275$ MHz/nm (Fig. 5.5). The lock detuning is $\Delta_l/2\pi = (\omega_l - \omega_{cav})/2\pi = -65$ MHz and we use a lock power of $P_l = 35.6$ µW. That corresponds to a number of photons circulating inside the cavity due to the lock laser[6] of around $n_l \simeq 14000$. Once the cavity is locked, we send the light reflected from the cavity to the spectrum analyzer and acquire the mechanical spectra. We measure the mechanical resonances between 137 kHz – the fundamental mode of the SiN stripe (Fig. 4.9c) – and 1700 kHz.

To extract the effective mass we need to transform the voltage PSD S_V into displacement PSD S_z. Let's pause for a second and think how the transduction of the setup works. The sample's displacement fluctuations are transformed into cavity frequency fluctuations S_ω through the optomechanical interaction

$$S_\omega(\omega) = G^2 S_z(\omega), \tag{5.2}$$

where we have assumed that the sample position is fixed at z and $G = G(z)$. The spectrum of the frequency fluctuations is transformed into a voltage spectrum through the transduction function $f(\omega, \Delta_l)$ of the lock scheme and the involved electronics [163]

$$S_V(\omega) = f(\omega, \Delta_l) S_\omega(\omega). \tag{5.3}$$

$f(\omega, \Delta_l)$ depends on the lock detuning Δ_l through the frequency response of the error signal, which at the same time depends on the lock laser's power. In our measurements, we keep Δ_l and P_l fixed and assume that $f(\omega, \Delta_l)$ is constant over the frequency range at which we measure the mechanical spectra. The displacement and voltage PSDs are finally related through

$$S_z(\omega) = \frac{1}{G^2 f(\omega, \Delta_l)} S_V = \alpha_{calib} S_V. \tag{5.4}$$

$f(\omega, \Delta_l)$ can be extracted by using a calibration tone, for example modulating the laser with an AOM (see e.g. Refs. [25, 72, 163]).

There are different unknowns in Eq. 5.4 depending of the type of optomechanical system. For instance, in most optomechanical experiments that are not in the membrane-in-the-middle configuration, there is no direct way to measure G. If the effective mass of the resonators is known, one also knows the mechanical response S_z. This allows one to extract the optomechanical coupling G by using directly the thermomechanical motion of the sample[7], as for example used in Ref. [25].

[6] For a mode with $\Omega_0/2\pi = 1590$ kHz and $g_0/2\pi = 1$ kHz, we calculate (Eq. 2.81 and Eq. 2.83) that this lock setting leads to an optical spring and optomechanical damping of $(\Omega_m - \Omega_0)/2\pi = -380$ Hz and $\Gamma_{opt}/2\pi = 10$ Hz, respectively.

[7] One can still do the same procedure if the effective mass is unknown, but instead of obtaining G one obtains g_0, where the effective mass is hidden in the dependency of g_0 in the zero-point fluctuations z_{zpf}. This is used in Ref. [163].

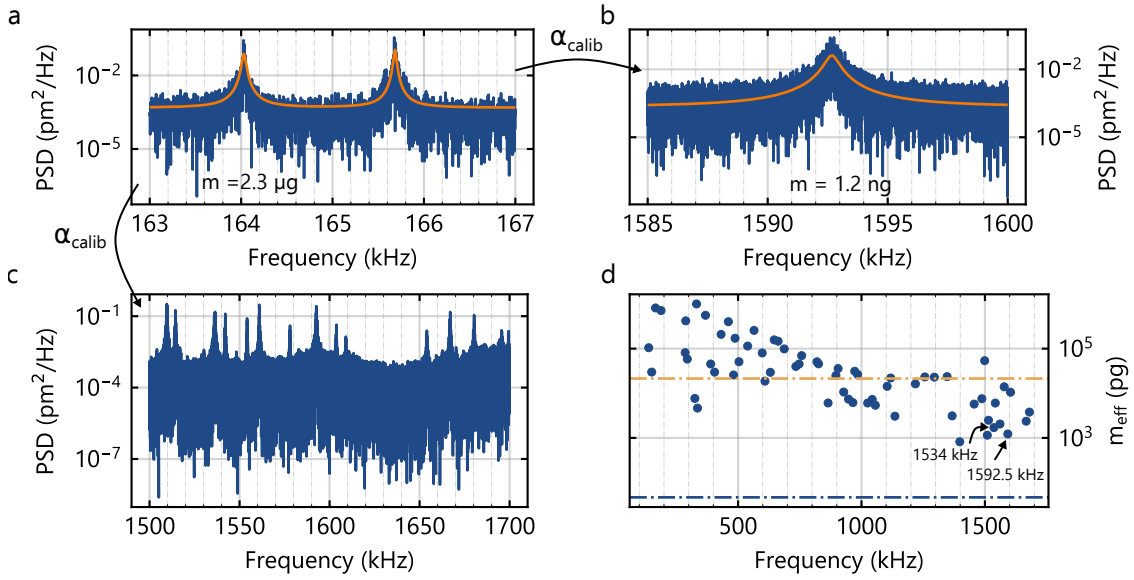

Figure 5.7: Mechanical spectra measured with the locked cavity. (a) Displacement PSD of two mechanical modes belonging to the SiN stripe. The one at 164 kHz (left), of known effective mass $m = 2.3\,\mu g$ and therefore S_z, is used to obtain α_{calib}. The orange solid line is a fit including two Lorentzian functions. (b) Displacement PSD of a hybrid mechanical mode at 1592.5 kHz after calibration. From the Lorentzian fit we extract m, Γ_0 and Ω_0. (c) Larger frequency range displaying the mechanical modes in the range where the mechanical modes of the SiN and hBN hybridize. (d) Experimental effective mass vs. mechanical frequency. The orange and blue dashed lines are the theoretical effective mass for an ideal rectangular SiN and circular hBN mechanical resonator, respectively, at the point of maximum deflection (see Fig. 2.2). All spectra are measured with the same lock settings (see main text) and same spectrum analyzer settings (1 Hz bandwidth, 4000 points, 5 kHz frequency span).

We use a similar approach and employ the SiN mode at $\Omega_0/2\pi = 164.0\,\text{kHz}$ of known effective mass $m = 2.3\,\mu g$ measured at the center of the hBN drum as reference for the calibration. The mode was well characterized in the Michelson interferometer (Fig. 4.12) – because we know S_z and measure S_V we can estimate α_{calib} from their quotient. We choose this mode because it does not show any optomechanical interaction with the cavity and consequently it is not affected by dynamical backaction effects[8]. Figure 5.7a shows the mechanical spectrum of the $\Omega_0/2\pi = 164.0\,\text{kHz}$ mode measured with the locked cavity. The mode gives $\alpha_{\text{calib}} = 9\,\text{pm}^2/\text{mV}^2$.

Figure 5.7b displays another mechanical mode at $\Omega_0/2\pi = 1592.5\,\text{kHz}$ after using the calibration factor to convert the voltage spectrum into displacement PSD. We fit Eq. 2.16 (orange solid line) to extract the resonance frequency, linewidth and effective mass. Figure 5.7c displays a larger frequency range showing many resonances, similar to what we measured previously in the Michelson interferometer . The effective masses are displayed in Figure 5.7d, and show a similar behavior than the ones measured with the Michelson interferometer (Section 4.5). The blue and orange dashed lines represent the theoretical effective mass of the fundamental mode of an ideal circular

[8]For each mode, the single-photon coupling strength g_0 is "weighted" by the spatial overlap η between the cavity mode intensity profile and mechanical mode profile, $g_0 = \eta G z_{\text{zpf}}$. Different mechanical modes can therefore have different couplings.

hBN resonator and rectangular SiN resonator, respectively, at the point of maximum deflection. At any other position one expects a larger effective mass (see Fig. 2.2). Again, this measurement allows us to distinguish the modes with a strong hBN character by selecting those with effective masses below 2 ng. The modes used to demonstrate radiation pressure backaction in the next section are highlighted with a dark arrow. The difference between the effective masses shown here with the ones from Figure 4.12 arise from the optomechanical interaction: because the cavity is locked, the effective spring constant (or effective mass) is modified by the presence of the lock laser. This can affect different modes at different magnitudes, given by the overlap of the mechanical modes with the optical one.

We conclude noting that these measurements are always done at the center of the hBN drum. Getting closer to the edges generates too many scattering losses and the cavity mode is lost. This, together with the fact that the cavity lock is lost when we perform a step movement with the positioning system, makes us unable to map the mode shapes inside the cavity with the current setup capabilities. In principle, we could use the 1330 nm-interferometer to perform those measurements. Unfortunately, the signal to noise ratio is not enough to resolve most of the modes due to the small fringe amplitudes ($V_{\mathrm{rf}} = 100\,\mathrm{mV}$) and the large wavelength (Eq. 4.2). Adding a second laser operating at shorter wavelengths, also outside the coating band of the mirrors, could enable interferometry measurements with a higher signal to noise ratio like in the Michelson setup.

5.3 Dynamical backaction

We observe the dynamical backaction effects of the radiation pressure force as a modification of the natural frequency and mechanical linewidth of the resonator, in other words: the optical spring effect and optomechanical damping (see Section 2.4.2). In the following, we present our results measured on the 68 nm-thick hBN drum-head whose mechanical properties and optomechanical couplings were characterized in Section 4.5 and Section 5.2, and Section 5.1.3, respectively.

5.3.1 Experiment description

The experiments are carried out in the following way. For each measurement, we place the sample at a position of known coupling G. This is achieved by placing the sample at the cavity node z_{node}, which is used as spatial reference, and displacing it by a certain amount Δz. The coupling at $G(z_{\mathrm{node}} + \Delta z)$ is extracted from the measurements of the optomechanical couplings (Fig. 5.5). We typically displace the sample by 10 nm to 20 nm from the cavity node, which correspond to linear couplings G below 500 MHz/nm. Positions with larger couplings are inaccessible due to the large frequency fluctuations caused by the mechanical noise of the setup (see Section 3.8). These make the cavity locks very unstable. The next step is to stabilize the cavity length. This is done by locking the cavity length to the frequency of the lock laser ω_{l}. We typically use a lock detuning $\Delta_{\mathrm{l}} = \omega_{\mathrm{l}} - \omega_{\mathrm{cav}}$ of around $\Delta_{\mathrm{l}}/2\pi = -70\,\mathrm{MHz}$ and a lock laser power of $P_{\mathrm{l}} = 35\,\mu\mathrm{W}$. Its polarization is set to match the one from the higher frequency polarization mode of the cavity (Fig. 3.10b, $|\kappa_{1,e}|/2\pi = 1.41\,\mathrm{MHz}$, $\kappa_{2,e}/2\pi = 1.42\,\mathrm{MHz}$, $\kappa/2\pi = 18.9\,\mathrm{MHz}$), and it is modulated with the EOM at $\omega_{\mathrm{mod}}/2\pi = 30\,\mathrm{MHz}$, producing two sidebands. We drive the EOM with the UHFLI with a signal of $V_{\mathrm{rf}} = 0.75\,\mathrm{V}$ and $V_{\mathrm{dc}} = 6.5\,\mathrm{V}$, which gives a sideband to lock power ratio of $P_{\mathrm{sb}}/P_{\mathrm{l}} = 0.25$. The latter is

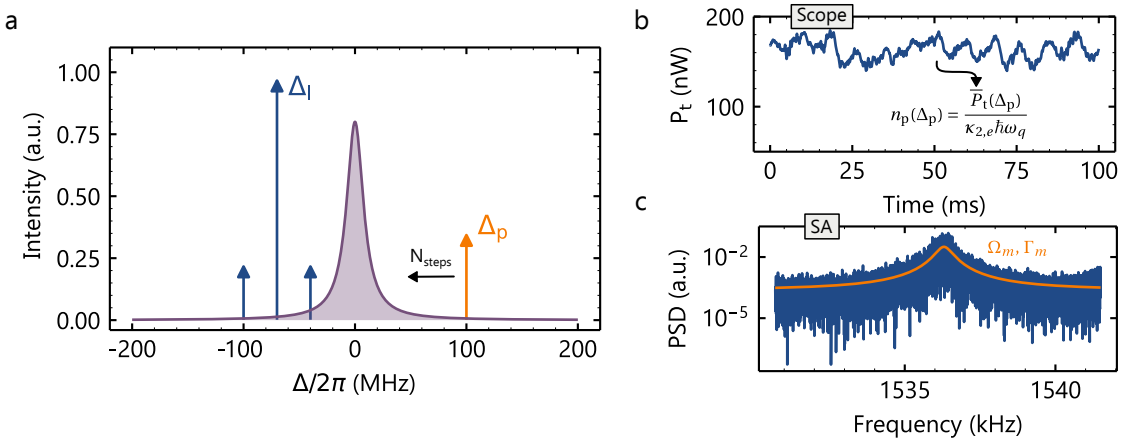

Figure 5.8: Measurement routine to probe dynamical backaction effects. (a) Illustration of the laser tones employed in the measurement as a function of their detuning Δ with respect to the cavity resonance. The lock laser is displayed as a blue arrow and has to sidebands separated by $\omega_{\text{mod}}/2\pi = 30\,\text{MHz}$. The probe laser is illustrated in orange. The x-axis is to scale and the y-axis is normalized to the lock laser's input power. The cavity transmission response is illustrated in purple and not to scale. After locking the cavity, the probe detuning is swept N_{steps}-times across the cavity resonance. At each probe detuning, we record a trace of the probe's transmitted power P_t (b) with the oscilloscope and a mechanical spectrum (c) of the reflection from the cavity with the spectrum analyzer (SA). From the mean of the probe's transmission $\overline{P_t}$ we extract the probe's circulating photon number n_{p}. We fit each mechanical spectrum to a Lorentzian response to extract Ω_m and Γ_m (orange solid line in (c)).

calculated using Eq. 3.18. The electronics involved in the locking procedure and a detailed analysis of the error signal used for the lock can be found in Section 3.3 and Section 3.9, respectively. We always record the cavity transmission, reflection, and error signal as a function of cavity detuning Δ before locking the cavity, getting traces similar to the ones shown in Figure 3.19b. Using the measured response of the cavity's transmission $P_t = f(\Delta) = |S_{21}|^2(\Delta)P_{\text{l}}$, we estimate the lock detuning from the transmitted power after locking $P_{\text{t,lock}}$, solving the inverse problem $\Delta_{\text{l}} = f^{-1}(P_{\text{t,lock}})$. The circulating number of photons inside the cavity due to the lock laser is also estimated from $P_{\text{t,lock}}$ through equation Eq. 2.58.

Once the cavity length is stabilized, we use a second laser (the probe laser) to exert a radiation pressure force. Its polarization is set to match the one from the lower frequency polarization mode of the cavity (Fig. 3.10a) and has a light power in the order of $P_{\text{p}} = 10\,\mu\text{W}$. Using both lasers with orthogonal cavity polarizations avoids interference effects. The probe detuning $\Delta_{\text{p}} = \omega_{\text{p}} - \omega_{\text{cav}}$ is swept N_{steps}-times across the cavity resonance by sending a voltage to the piezo of the tunable laser. It is transformed into frequency detuning following the calibration procedure described in Appendix B.4. Figure 5.8a displays the laser tones and the cavity response in the frequency space as a function of the cavity detuning $\Delta = \omega - \omega_{\text{cav}}$. The cavity transmission response is depicted in purple and calculated using the experimental parameters for the lower frequency polarization mode: $\kappa_{1,e}/2\pi = 1.34\,\text{MHz}$, $\kappa_{2,e}/2\pi = 1.80\,\text{MHz}$, $\kappa/2\pi = 18.5\,\text{MHz}$. The lock laser and its sidebands are shown as blue arrows, and the probe tone is represented in orange color.

At each probe detuning step we record the cavity transmission with the oscilloscope and a me-

chanical spectrum from the reflection signal with the spectrum analyzer. For the latter we use a bandwidth of 1 Hz and a total of 4000 points. The transmission detector measures the sum of the transmitted power due to the lock – which is constant[9] through the measurement and equal to $P_{\mathrm{t,lock}}$ – and the one from the probe which depends on Δ_{p}. To isolate the contribution of the probe's laser, we subtract the value $P_{\mathrm{t,lock}}$ from the experimental traces. Figure 5.8b shows as a example the probe laser's transmission for a particular probe detuning. We take the mean of the probe transmitted power, which oscillates due to residual frequency fluctuations, and use Eq. 2.58 to extract the circulating probe photon number n_{p}. Each mechanical spectrum is fitted to a Lorentzian function to extract the resonance frequency Ω_m and mechanical linewidth Γ_m (Fig. 5.8c). For a typical measurement, we sweep the probe detuning 100 times ($N_{\mathrm{steps}} = 100$), which takes around 4 minutes. For these measurements, because we are not interested in the effective mass, we do not calibrate the measured PSDs in volts to displacement PSDs.

5.3.2 Optical spring and optomechanical damping

Figure 5.9 shows the optical spring effect (Fig. 5.9b) and optomechanical damping (Fig. 5.9c) of the hBN hybrid mechanical mode with $\Omega_0/2\pi = 1533.759(8)\,\mathrm{kHz}$. The sample is positioned so that $G/2\pi = 330\,\mathrm{MHz/nm}$, and we use a lock detuning of $\Delta_{\mathrm{l}}/2\pi = -77\,\mathrm{MHz}$. The probe and lock input powers are $P_{\mathrm{p}} = 11\,\mu\mathrm{W}$ and $P_{\mathrm{l}} = 35.4\,\mu\mathrm{W}$, respectively. The linewidth and quality factor are $\Gamma_0/2\pi = 0.69(3)\,\mathrm{kHz}$ and $Q = 2200\,(80)$. The effective mass, measured in the previous section, is $m = 1.7(6)\,\mathrm{ng}$, yielding $z_{\mathrm{zpf}} = 1.78(7)\,\mathrm{fm}$. With these numbers, we expect a single-photon coupling strength of $g_0/2\pi = (G/2\pi)\,z_{\mathrm{zpf}} = 586\,\mathrm{Hz}$. We recall that the effective mass was measured with the lock red detuned – that means that the real effective mass can be actually smaller. Consequently, the calculated value $g_0/2\pi = 586\,\mathrm{Hz}$ is a lower limit for the single-photon coupling strength.

The circulating probe photon number seems at first sight to follow the Lorentzian shape characteristic from a linear cavity (Fig. 5.9a). A Lorentzian fit (solid line) reveals a loaded cavity linewidth of $\kappa/2\pi = 40.4(5)\,\mathrm{MHz}$ and finesse of $\mathcal{F} = 88700$. However, there is a hardly noticeable asymmetry between both branches of the Lorentzian, being the left side (negative detunings) more steep than the right one (positive detunings). This is an indication of a nonlinear response of the cavity (see Fig. 3.11).

The backaction of the probe leads to a softening (stiffening) of the mechanical frequency for negative (positive) detunings, with a maximum frequency shift of $|\delta\Omega/2\pi| = 2\,\mathrm{kHz}$ for negative detunings. The natural frequency has a slight negative slope stemming from drifts in the lock that originate from changes of the sample position due to slow temperature drifts in the laboratory. The data shows an asymmetry around the probe detuning as well, which is not predicted by the linear cavity optomechanics theory. Indeed, the mode shows a stronger softening than stiffening. The solid line is a fit to the optical spring using Eq. 2.81 together with a linear background. For the fit, we fix the cavity linewidth to the value obtained from the Lorentzian fit to the probe photon number, $\kappa/2\pi = 40.4\,\mathrm{MHz}$, assume negligible dissipative coupling, feed the equation with the experimentally measured probe photon number n_{p} and exclude the data on the heating side

[9] In reality, we have thermal drifts which cause small drifts of Δ_{l} and consequently of the lock laser's transmitted power of around 1 nW in 4 min, but it is measurement dependent. In that case, the final transmission as function of probe detuning $P_{\mathrm{t}}(\Delta_{\mathrm{p}})$ is a Lorentzian function coming from the probe $P_{\mathrm{t,probe}}(\Delta_{\mathrm{p}})$ on top of a linear background originating from the lock drift $P_{\mathrm{t,lock}}$. We fit a linear regression to the background to extract $P_{\mathrm{t,lock}}$.

($0<\Delta_p/2\pi<40$ MHz) due to the asymmetry in the optical spring. The only free parameter for the fit is g_0, and the best fit yields $g_0/2\pi = 710(10)$ Hz. This result is in good agreement with the independently extracted lower limit of $g_0/2\pi = 586$ Hz.

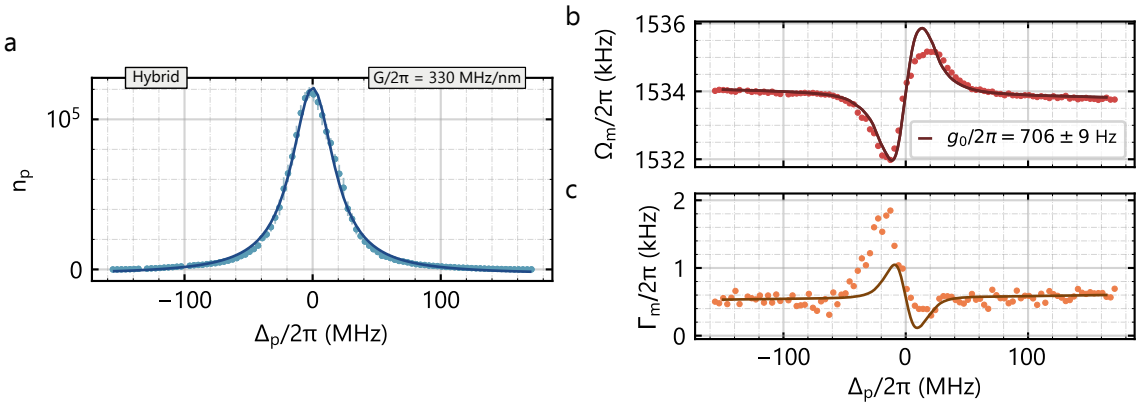

Figure 5.9: Radiation pressure backaction. (a) Experimental probe photon number n_p versus probe detuning Δ_p. The solid line is a Lorentzian fit with linewidth $\kappa/2\pi = 40.4$ MHz. (b) Optical spring effect and theoretical regression (solid line) with best fit parameter $g_0/2\pi = 710$ Hz. The fit excludes the data on the heating side ($0<\Delta_p/2\pi<40$ MHz) due to the asymmetry in the optical spring. (c) Mechanical damping and theory calculation (solid line) with the parameters from the fit in (b). The error bars for Ω_m and Γ_m, generated from the fits to Eq. 2.15, are omitted because they are not appreciable in the figure.

The regression reproduces the data trend except for positive detunings. We discard the possibility of an asymmetry induced by the dissipative coupling because of the small value of the single-photon dissipative coupling strength, $g_{0,\kappa}/2\pi = (G_\kappa/2\pi)z_{zpf} = 0.3$ Hz. As discussed in Section 4.5, the sample presents many resonances in the frequency range of interest, resulting from the hybridization between the dense SiN mechanical spectrum and the hBN resonator. These hybridized modes, which are close in frequency and have similar mode shapes, will modulate the intracavity field too. This can result in an intermode coupling which drives the other mechanical modes [164]. Consequently, the system is no longer represented by a single optical mode interacting with a single mechanical mode, which could explain the deviations from Eq. 2.81. Another possible, and perhaps more accurate explanation given the slight asymmetry of the photon number (Fig. 5.9a), is the presence of nonlinear effects. We have shown in Section 3.4.2 that the cavity response can become nonlinear for sufficiently high input powers due to the change of cavity length caused by the thermal expansion of the mirrors. The cavity resonance frequency consequently depends on the photon number, which is a nonlinearity of the Kerr type. The nonlinearity can contribute to the backaction effects as well. Zoepfl and colleagues [131] have developed the theory of Kerr backaction cooling and demonstrated the cooling of a cantilever resonator using this mechanism. In their experiments they show the optical spring effect and optomechanical damping of a cantilever coupled to superconducting cavity with a behavior very similar to ours: the optical spring is asymmetric with respect to the cavity detuning, and less pronounced for blue probe detunings; the optomechanical damping is stronger in the cooling side than in the heating side. This behavior is characteristic for systems with a negative Kerr nonlinearity, and leads to a more efficient cooling than the ideal linear systems. We will apply their theory to our data in the

next section.

Figure 5.9c shows the effective linewidth Γ_m (orange dots) as a function of the probe detuning. The solid line is the result of Eq. 2.83 using the parameters obtained from the fit of the optical spring. We observe a larger broadening (optomechanical cooling) than what is predicted by the theory for negative detunings, whereas the narrowing (optomechanical heating) found for positive detunings is less pronounced compared to the theoretical model. This again matches with the presence of a Kerr nonlinearity. In general, the experimental linewidths are broadened due to unavoidable mechanical fluctuations of the positioner stack and the SiN stripe itself. They are also the limiting factor of this experiment and the reason why we are unable to successfully lock the cavity at sample positions with higher coupling G. The fluctuations translate into cavity length noise, which directly affects the detuning and therefore turn into mechanical frequency noise. This leads to the overall broadening of the mechanical linewidth.

Overall, these results are the first demonstration of radiation pressure backaction at optical wavelengths on a hexagonal boron nitride mechanical resonator and, to the best of our knowledge, on a mechanical resonator made from a van der Waals material.

5.3.3 Power sweeps: hints of Kerr backaction cooling

Figure 5.10a shows the circulating probe photon number (top graph), optical spring (middle graph) and optomechanical damping (bottom graph) for a hybrid mode with $\Omega_0/2\pi = 1590.3(3)$ kHz. The sample is positioned so that $G/2\pi = 333$ MHz/nm, and we use $P_p = 11\,\mu$W, $P_l = 34.5\,\mu$W and a lock detuning of $\Delta_l/2\pi = -50$ MHz. The linewidth and quality factors are $\Gamma_0/2\pi = 572(20)$ Hz and $Q = 2700\,(100)$, respectively. The effective mass, measured in the previous section, is $m = 1.2(1)$ ng, yielding $z_{zpf} = 2.1$ fm. From these numbers, we calculate a value of $g_0/2\pi = 690$ Hz.

The photon number does not follow a Lorentzian trend, which can be an indication of a nonlinear cavity response. Because we cannot fit a Lorentzian, and since the sample is placed at a similar position than in the example from Figure 5.9, we take the linewidth's value from that measurement $\kappa/2\pi = 41$ MHz. The detuning is set to zero at the point of maximum photon number. This mode presents a larger coupling than the one at 1534 kHz, that manifests as a larger maximum frequency shift of $|\delta\Omega/2\pi| = 3$ kHz for the red detuned case. The optical spring shows a similar probe detuning dependence to the one from the mode in Figure 5.9. From the fit to the optical spring formula (Eq. 2.81), we obtain $g_0/2\pi = 1007(10)$ Hz, which leads to $z_{zpf} = 3.0$ fm and $m = 0.5$ ng, in good agreement with the value previously calculated. The fit to the optical spring excludes the data on the heating side ($0<\Delta_p/2\pi<40$ MHz) due to its asymmetry.

We now cool the resonator by fixing the probe laser's frequency to the red detuned value $\Delta_p/2\pi = -14.5$ MHz, highlighted as a gray dashed line in Figure 5.10a. To fix the probe detuning we first do a probe detuning sweep and measure the response of the cavity, similar to the measurements in Fig. 5.10a, top graph, but with smaller probe powers. This takes around 3 minutes. Then we set the wavelength of the laser so that it matches the target value given the cavity response and do the power sweep measurement. The cavity is locked at $\Delta_l/2\pi = -40$ MHz and with $P_l = 34.3\,\mu$W. The lock laser's circulating photon number is constant during the measurement and around $n_l \simeq 20\,000$. Figure 5.10b shows the optical spring (top graph) and mechanical linewidth (bottom graph) as a function of the circulating probe photon number. The probe's input power

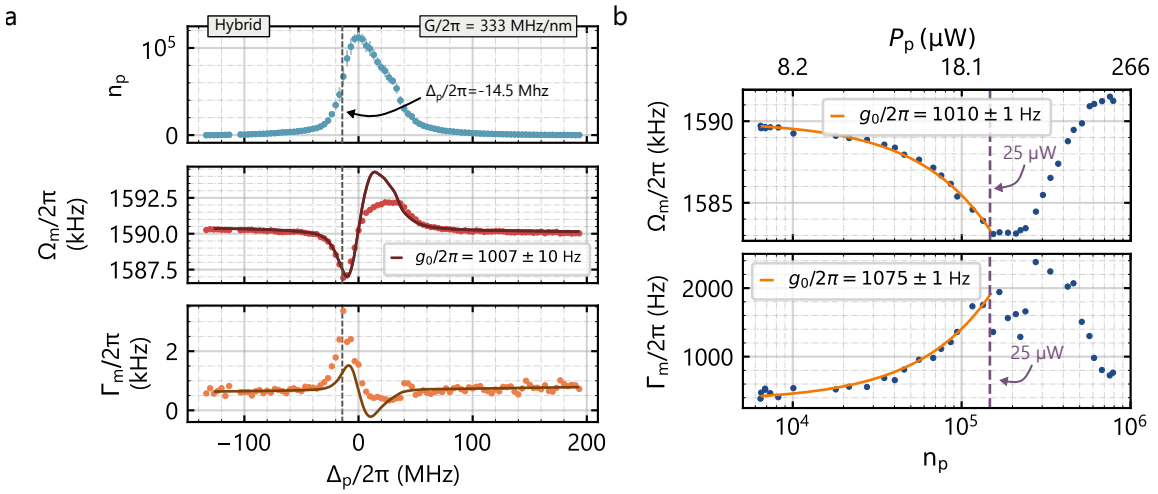

Figure 5.10: Dynamical backaction cooling. (a) Circulating probe photon number n_p (top graph), optical spring (middle graph) and optomechanical damping (bottom graph) versus probe detuning Δ_p for a hybrid mechanical mode at 1590 kHz. The solid line in the optical spring is a theory fit using the linear cavity optomechanics theory (Eq. 2.81) excluding the data on the heating side ($0<\Delta_p/2\pi<40$ MHz); the one in the mechanical damping is the calculation from the theory (Eq. 2.83) using the parameters from the fit to the optical spring. (b) Optical spring and mechanical damping for a fixed probe detuning ($\Delta_p/2\pi = -14.5$ MHz, gray dashed line in (a)) and varying circulating probe photon number n_p. The top x-axis reflects the probe input power P_p. The value $P_p = 25\,\mu$W is highlighted as a purple dashed line. The orange lines are linear regressions to the data.

was changed from $P_p = 7\,\mu$W to $P_p = 265\,\mu$W.

Both Ω_m and Γ_m depend linearly on the photon number for $n_p < 150\,000$, with slopes of different sign, as predicted from the theory (Eq. 2.82 and Eq. 2.83). The mechanical mode softens and cools down, which is the normal behavior for a red detuned probe. The frequency decreases by more than 5 kHz and the linewidth increases by almost an order of magnitude. The orange solid lines are linear fits, from which we can extract the single-photon coupling strength through Eq. 2.82 and Eq. 2.83 using the experimental values $\Delta_p/2\pi = -14.5$ MHz and $\kappa/2\pi = 41$ MHz. They yield $g_0/2\pi = 1010$ Hz and $g_0/2\pi = 1075$ Hz for Ω_m and Γ_m, respectively, both in very good agreement with the independent measurement in Figure 5.10a using the probe laser's detuning sweep.

For $n_p > 150\,000$, however, the data starts deviating from what we expect from the theory. Indeed, the mechanical frequency starts increasing again with a quadratic dependence in n_p, and the linewidth decreases. As explained in Section 3.4.2, the cavity starts presenting a clear nonlinear behavior for input input powers $P > 25\,\mu$W. That is also the power value at which we start observing a deviation between the linear optomechanics theory and the data, highlighted as a purple dashed line in Figure 5.10b. This is an indication that the behavior of the cavity maybe nonlinear, giving rise to other optomechanical effects. Our cavities present a negative Kerr: looking at Figure 3.11b we observe that the response of the cavity gets steeper for negative detunings, which also occurs for the photon number presented in Figure 5.10a. Figure 5.11 shows the measured optical

spring and damping (blue dots). The solid lines are theoretical curves[10] including the Kerr nonlinearity (Eq. S17 from Ref. [131]) with a value for the Kerr nonlinearity of $\mathcal{K}/2\pi = -240\,\mathrm{Hz/photon}$ and $g_0/2\pi = 900\,\mathrm{Hz}$. The photon number fed to the equation is calculated from a Lorentzian with full width at half maximum $\kappa/2\pi = 41\,\mathrm{MHz}$ and amplitude of $n_\mathrm{p}^\mathrm{max}$ ($n_\mathrm{p}^\mathrm{max} = 10^5$ orange line, $n_\mathrm{p}^\mathrm{max} = 2\cdot 10^5$ green line). The theoretical curve with $n_\mathrm{p}^\mathrm{max} = 10^5$ reproduces the optical spring very well. It underestimates, however, the linewidth for red detunings, but follows experimental data trend. We note that we have fed to the equation a linear (Lorentzian) photon number; to accurately describe the data one should use a nonlinear photon number dependency.

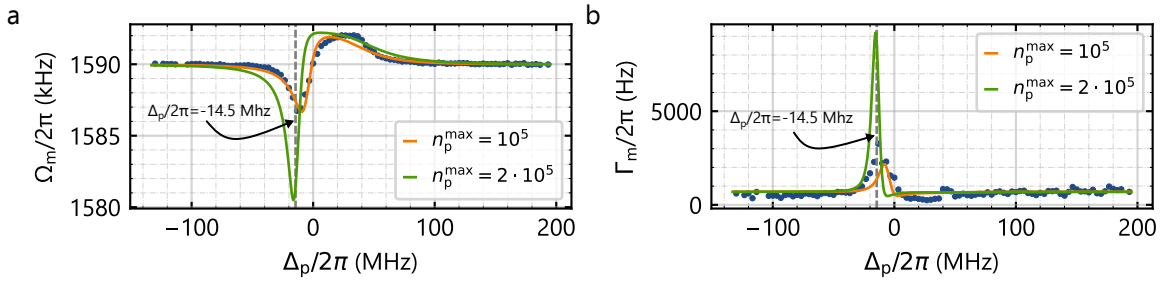

Figure 5.11: Dynamical backaction with a nonlinear cavity. (a) Experimental optical spring (blue dots) verus probe detuning Δ_p. The solid lines are calculated theoretical curves (Eq. S17 from Ref. [131]), which include the nonlinear response of the cavity. The curves use a Kerr nonlinearity of $\mathcal{K}/2\pi = -240$ hertz/photon and $g_0/2\pi = 900\,\mathrm{Hz}$. The equations are fed with a probe photon number of Lorentzian dependence (linear cavity) with $\kappa/2\pi = 41\,\mathrm{MHz}$ and amplitude $n_\mathrm{p}^\mathrm{max}$ ($n_\mathrm{p}^\mathrm{max} = 10^5$ and $n_\mathrm{p}^\mathrm{max} = 2\cdot 10^5$ for the orange and blue lines, respectively). (b) Experimental optomechanical damping (blue dots). The solid lines follow the same as in (a). The gray dashed line indicates the value $\Delta_\mathrm{p}/2\pi = -14.5\,\mathrm{MHz}$.

The nonlinear response can also give us an explanation on the unexpected dependencies of the optical spring and damping with the probe circulating photon number (Figure 5.10b). Let's take another look at Figure 5.11. The gray line highlights a fixed red detuning of $\Delta_\mathrm{p}/2\pi = -14.5\,\mathrm{MHz}$. We can observe that, as we increase the photon number, the curves are displaced towards negative detunings: the fixed probe detuning (gray dashed line in Fig. 5.11) is for the orange curve on the left side of the optical spring minima whereas it is on the right side for a two-fold increase in the photon number (green curve). If we had increased the photon number even further, the value $\Delta_\mathrm{p}/2\pi = -14.5\,\mathrm{MHz}$ would correspond to a positive optical spring. Same occurs with the optical damping. Consequently, both cooling and heating backaction shift to lower frequencies, which could very well explain what we observe in Figure 5.10b, as we use powers exceeding the linear regime of our cavity.

The asymmetry of the theoretical curves of the optical spring and optomechanical damping including the Kerr nonlinearity (Fig. 5.11) also matches the one from the measurements presented in the previous section (Fig. 5.9). However, in that case, the nonlinearity in the photon number is way less pronounced for a similar input power and similar coupling G. The reasons behind this are still unclear to the author. First, the measured nonlinear response differs from the ones

[10] The curves are not a fit to the data. The parameter space is large and it is important to know the shift of the nonlinear cavity response with respect to the linear cavity, which we do not know. Nevertheless, it serves to illustrate the Kerr backaction mechanism.

predicted by the theory (Fig. 3.11): we observe[11] an unexpected lower "bump" for a blue detuned probe (Fig. 5.10a and see also our previous work [135]). This could be an indication that the origin of the nonlinearity can be more complex than just the thermal effects explained in Section 3.4.2. A possible explanation for the bump is that, given the large number of photons, the mechanical oscillator jumps to another local minima of the mechanical potential modified by the optical potential from the radiation pressure [17]. Whether the jump occurs or not depends on the position history of the system, which is different for different measurements. Second, we remark that given the high number of photons inside the cavity the intrinsic Kerr nonlinearity from hBN could also come into play [130, 165].

The theory from Zoepfl and coauthors [131], on which I based this discussion, was published while I was writing this thesis. More data sets and a more careful analysis of the cavity nonlinear response should be done in the future to completely validate the results presented here. Nevertheless, we always observe an asymmetry in the optical spring and optomechanical damping of the negative Kerr type for almost all mechanical modes analyzed in this work. If further analyses validate the arguments exposed in this section, this would mean that we have cooled the mode of the hBN mechanical resonator with a Kerr enhanced radiation pressure backaction.

We conclude this section analyzing the cooling of the mechanical resonator. Figure 5.12 displays the resonator's effective temperature (Eq. 2.84) as a function of the probe photon number. The orange line is the fit used for the optical damping (Figure 5.10b). We cool down the resonator from room temperature to approximately 30 K. We note that, since we cannot measure the mechanical linewidth without locking the cavity, the value taken for the natural linewidth is already affected by the backaction of the red detuned lock. This implies that the measured effective temperatures are an upper limit to the real value. Because our optomechanical system is deeply in the unresolved sideband regime ($\Omega_0 \ll \kappa$), the minimum attainable photon number using radiation pressure backaction cooling with a linear cavity is $n_{\mathrm{ph,min}} = \kappa/(4\Omega_0) = 6.6$. This value is far from the final phonon number reached in the experiments $n_{\mathrm{ph,f}} \simeq n_{\mathrm{th}}\Gamma_0/\Gamma_m = 8\times10^5$, with $n_{\mathrm{th}} = 4\times10^6$. The difference is basically given by the large natural linewidth of $\Gamma_0/2\pi = 572\,\mathrm{Hz}$, which is comparable to the optomechanical damping $\Gamma_{\mathrm{opt,max}}/2\pi \sim 2000\,\mathrm{Hz}$ (Eq. 2.88).

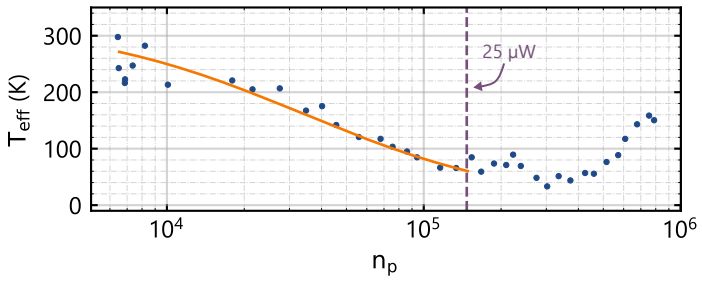

Figure 5.12: Effective mode temperature. The data is calculated using the measurements of the optomechanical damping (Fig. 5.10b) and Eq. 2.84. The solid line is the same linear regression to the mechanical damping in Fig. 5.10b. The purple dashed line highlights the input probe power of $P_{\mathrm{p}} = 25\,\mu\mathrm{W}$. Above that value the data starts deviating form the linear optomechanical theory.

[11] This was observed with different SiN stripes and different hBN flakes and cavity C8. Felix Rochau also observed this with high-stress Si_3N_4 stripes in cavity C3 with a completely different setup.

5.4 Reverse optical spring

The dynamical backaction experiments presented in Section 5.3 for the mechanical modes at 1534 kHz and 1590 kHz were also done with most of the mechanical modes with enough signal to noise ratio in the frequency range between 137 kHz and 3 MHz. We found a total of 5 modes with resonance frequencies below 500 kHz ($\Omega_0/2\pi = 255, 332, 354, 459$ and 481 kHz) that showed a reverse optical spring. As an example, Figure 5.13a displays the optical spring and damping as a function of the probe detuning for the mode at $\Omega_0/2\pi = 354$ kHz, which has $\Gamma_0/2\pi = 44$ Hz. The measurement parameters are $G/2\pi = 480$ MHz, $\Delta_l/2\pi = -50$ MHz, $P_l = 34\,\mu$W and $P_p = 15\,\mu$W. The photon number shows a Lorentzian response of linewidth $\kappa/2\pi = 50$ MHz, 10 MHz larger than the previous measurements because the sample is displaced further away from the cavity node at a point of larger coupling G. The frequency of the resonator behaves opposite to what is expected from the linear optomechanical backaction theory: the mode stiffens for a red detuned probe and softens for a blue detuned one. The maximum frequency shift is around $|\delta(\Omega)|/2\pi = 0.15$ kHz. The mode's mechanical linewidth increases with a red detuned probe as predicted by the theory, and it is not altered (at least that we can resolve) for the blue detuned case. Nevertheless, extracting the linewidth from this measurement is very difficult because the mode presents a low signal to noise ratio of 5.

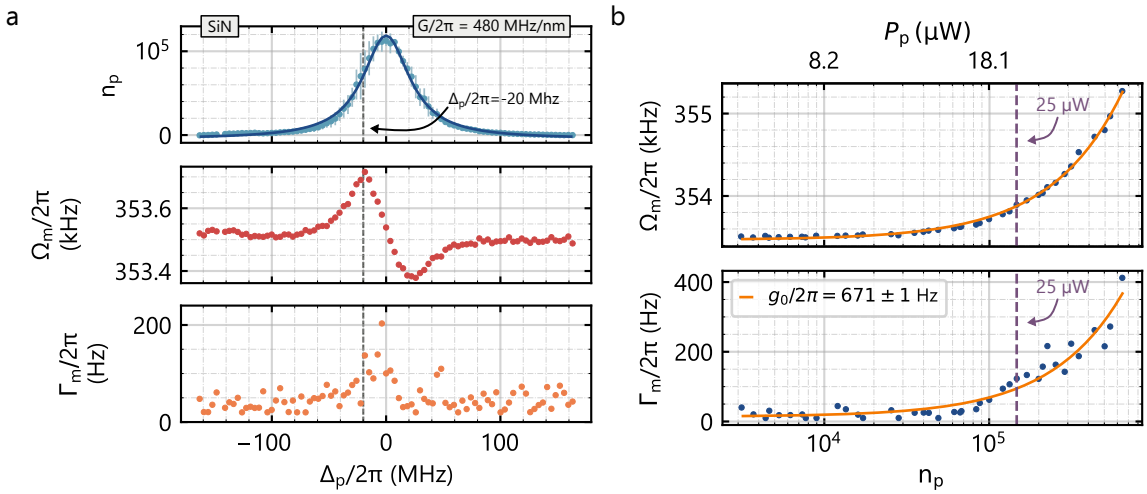

Figure 5.13: Reverse optical spring. (a) Circulating probe photon number n_p (top graph), optical spring (middle graph) and optomechanical damping (bottom graph) versus probe detuning Δ_p for a SiN mechanical mode at 353.5 kHz. The solid line in the probe photon number graph is a Lorentzian fit. (b) Optical spring and mechanical damping for a fixed probe detuning ($\Delta_p/2\pi = -20$ MHz, gray dashed line in (a)) and varying circulating probe photon number n_p. The top-x axis reflects the probe input power P_p. The value $P_p = 25\,\mu$W is highlighted as a purple dashed line. The orange lines are linear regressions to the data.

To confirm our observations we perform a power sweep by fixing the probe detuning to the red sideband side, $\Delta_p/2\pi = -20$ MHz and the lock to $\Delta_l/2\pi = -60$ MHz. Figure 5.13b shows the mechanical frequency and linewidth as a function of the probe photon number. Both depend linearly, with a positive slope, on the photon number. From the fit to the linewidth, which behaves according to the linear optomechanics theory, we extract a single-photon coupling rate of

$g_0/2\pi = 671(1)$ Hz. This mode also does not present a change of the sign of the slope for $n_p > 10^5$ in contrast with the mode at 1590 kHz. We currently do not have an explanation for the mechanism behind the reversed behavior of the optical spring with respect to the probe detuning, which should be subject of future experiments.

In conclusion, we have demonstrated radiation pressure backaction on an hBN resonator at telecom wavelengths. We have shown that the measured optical spring and optomechanical damping have an asymmetry that is not predicted by the linear cavity optomechanics theory. This asymmetry can be reproduced theoretically if we include a negative Kerr nonlinearity in the system. Additional experiments should be conducted to clarify the origin of the nonlinearity.

6

Conclusion and outlook

In this thesis we present an experimental platform to perform radiation pressure backaction experiments with micro- and nanomechanical resonators placed in the middle of an optical cavity. In particular, we study membrane mechanical resonators made of hexagonal boron nitride, a type of van der Waals material.

The first part of this work aims to introduce the reader into the insights of a membrane-in-the-middle (MIM) cavity optomechanical system. The standard cavity optomechanics literature [17, 18] covers the optomechanical interaction but for the toy model of an optical cavity with a movable mirror, which is effectively different to the MIM system. In the latter, the membrane splits the optical cavity into two subcavities. The radiation pressure arises in the MIM case due to the different optical field amplitudes at each side of the membrane. We explain the characteristics of the MIM system by introducing the transfer matrix formalism, the mathematical tool we use to compute the static optomechanical couplings.

In our experiment, the radiation pressure interaction is enabled thanks to a high-finesse optical cavity. The cavity is composed of two fiber mirrors which were machined through CO_2 laser ablation and coated with a distributed Bragg reflector. We introduce the effects specific to fiber cavities and explain carefully the cavity characterization methods. Throughout this work, I fabricated and characterized a total of nine fiber cavities with cavity lengths between 20 µm and 76 µm, and an empty cavity finesse up to $\mathcal{F} = 200\,000$. One of the cavities was used to demonstrate dynamical backaction in the ultrahigh-finesse regime [135], and another one to realize the first experimental evidence of radiation pressure backaction with a mechanical resonator made of hexagonal boron nitride [1].

Long lasting efforts were devoted to understand the limiting factors of our experiment. We found that the main source of instability is the sample positioning system for two main reasons. First, the short cavity lengths enable very large optomechanical couplings when the sample is inserted, with a maximum of around $G_{\mathrm{max}}/2\pi \simeq 3\,\mathrm{GHz/nm}$. This is, of course, beneficial from the point of view of the optomechanical interaction. However, it also means that we couple to tiniest mechanical noise. We found that the positioning system's mechanical response peaks at similar frequencies than the acoustic noise from the ZNN facilities, which translates into cavity frequency fluctuations larger than the cavity linewidth. With this noise it is impossible to stabilize the cavity length even when the sample is placed at the cavity node – the point of minimum coupling. To overcome

this limitation, we designed and characterized an acoustic isolation box protecting the setup from the mechanical noise. With the vibration isolation in place, we are able to stabilize the cavity and perform dynamical backaction experiments. Nevertheless, we are still limited to sample positions with couplings below $G/2\pi \simeq 500\,\mathrm{MHz/nm}$. A possible solution is to move the experiment to another building with lower mechanical noise – or with noise at frequencies where the positioners do not resonate – together with the design of a better mechanical isolation system. Second, the sample position drifts in time due to temperature changes in the lab, with a magnitude of about $1.2\,\mu\mathrm{m}/^{\circ}\mathrm{C}$. This leads to cavity lock drifts when the sample is inserted. These are temperature dependent. The best approach in this case is to use a feedback loop to stabilize the sample position. The current positioning system allows this.

The hBN mechanical resonators are fabricated by dry-transferring mechanically exfoliated hBN flakes on top of a low-stress SiN stripe resonator. We have characterized the mechanical spectra from both resonators using a Michelson interferometer and mapped some of the spatial profiles. The mode profiles from the hBN drum deviate from the what we would expect from an ideal circular membrane. We attribute this deviation to the dry-transfer technique: the pulling and pushing from the PDMS stamp against the flake results in a bulging of the hBN membrane which is appreciable under the microscope. This could explain the deviation from the ideal membrane behavior, which has also been observed in other experiments with dry-transferred hBN resonators [45]. A more gentle transfer technique, like a wet transfer, would be beneficial for the mechanical performance of the resonators [139]. We have also found that the modes from hBN and SiN resonators hybridize because they are close in resonance frequency and coupled through strain. We have measured this hybridization as a shift of the effective mass of the resonators, following the work from Ref. [139]. To avoid the hybridization one could change the low-stress SiN stripe to a high-stress Si_3N_4. With the same stripe dimensions, and using the conservative[1] value $\sigma = 400\,\mathrm{MPa}$, we expect the fundamental mode of the Si_3N_4 stripe to be at $\Omega_0/2\pi = 730\,\mathrm{kHz}$. This would isolate the fundamental mode of hBN from the sea of modes observed in Figure 4.11. Combined with the wet transfer, one could take a step further and engineer the mode spectrum of the Si_3N_4 in the same spirit as the phononic shielding [142] to push the frequencies even further away in the spectrum.

The main achievement of this thesis is the demonstration of dynamical backaction on an hBN mechanical resonator. We have measured the optical spring and optomechanical damping of different mechanical modes, with single-photon coupling strengths as high as $g_0/2\pi = 1000\,\mathrm{Hz}$. Both the optical spring and the optomechanical damping display an asymmetry with respect to the probe's laser detuning that is not explained by the linear cavity optomechanics theory. The photon number displays a nonlinear response as well. A theoretical framework including a Kerr nonlinearity is capable of reproducing the experimental trends we observe [131]. However, the source of the nonlinearity is still unclear and more experiments should be carried out to clarify its origin. These should include a thorough characterization of the thermal nonlinear response of the cavity.

The membrane-in-the-middle optomechanical platform presented here offers the possibility to study different types of mechanical resonators. In particular, to study resonators with incorpo-

[1] Norcada provides unpatterned high-stress membranes with $\sigma = 1\,\mathrm{GPa}$. We do not know if the stress changes for custom patterned membranes, so we take a conservative lower value for the calculations.

rated optically active defects, for which van der Waals materials are especially suited. Indeed, hBN is not the only material that has defects which are sensitive to strain [57, 63, 166], so do other van der Waals materials like WSe_2 [167–169]. The multi-mode fiber at the output of the cavity allows the incorporation of several wavelengths, enabling photoluminiscence experiments on-site. One could even go a step further and carefully design the DBR coating of the fiber mirrors to operate at different wavelength ranges. The latter could be used, for instance, to enhance the spontaneous emission rate from the quantum emitters through the Purcell effect [170, 171]. All this will open the door to new ways of studying the strain dependence of the optically active defects from hBN with an additional control of the mechanical properties through light, and a new step forward towards the realization of spin-optomechanics with van der Waals materials.

Appendices

A

Theoretical calculations

A.1 Transfer matrix of a DBR

We consider a DBR formed by N pairs of layers sputtered on a substrate with refractive index n_s. Layer 1 has a thickness of $d_1 = \lambda n_1/4$ and layer 2 $d_2 = \lambda n_2/4$. The propagation matrix for each layer is

$$\begin{pmatrix} -i & 0 \\ 0 & i \end{pmatrix}. \tag{A.1}$$

The transfer matrix of a layer pair, starting from layer 1,

$$M_{N=1} = \begin{pmatrix} -i & 0 \\ 0 & i \end{pmatrix} \frac{1}{t_{12}} \begin{pmatrix} 1 & -r_{12} \\ r_{12} & 1 \end{pmatrix} \begin{pmatrix} -i & 0 \\ 0 & i \end{pmatrix} \frac{1}{t_{21}} \begin{pmatrix} 1 & -r_{21} \\ r_{21} & 1 \end{pmatrix}, \tag{A.2}$$

$$M_{N=1} = \frac{1}{2} \begin{pmatrix} -\frac{n_1}{n_2} - \frac{n_2}{n_1} & +\frac{n_1}{n_2} - \frac{n_2}{n_1} \\ +\frac{n_1}{n_2} - \frac{n_2}{n_1} & -\frac{n_1}{n_2} - \frac{n_2}{n_1} \end{pmatrix}. \tag{A.3}$$

The N-layer matrix is therefore given by

$$M_N = M_{N=1}^N = \frac{1}{2} \begin{pmatrix} \left(-\frac{n_1}{n_2}\right)^N + \left(-\frac{n_2}{n_1}\right)^N & -\left(-\frac{n_1}{n_2}\right)^N + \left(-\frac{n_2}{n_1}\right)^N \\ -\left(-\frac{n_1}{n_2}\right)^N + \left(-\frac{n_2}{n_1}\right)^N & \left(-\frac{n_1}{n_2}\right)^N + \left(-\frac{n_2}{n_1}\right)^N \end{pmatrix}. \tag{A.4}$$

Usually, when the DBR is used within optical cavities, the side opposite to the substrate is the one facing the region of highest electric field intensity, and therefore where the material losses are more critical. For this reason, an additional layer of the material with lowest losses is added at the end of the coating, which is Ta_2O_5 in this case. The final matrix is therefore,

$$M = D_{s1} M_{N=1}^N \begin{pmatrix} -i & 0 \\ 0 & i \end{pmatrix} D_{1e}, \tag{A.5}$$

with M_{10} being the interface between material 1 and the external medium of refractive index n_e, which we assume to be vacuum ($n_e = 1$). The complete matrix reads

$$M = \frac{i}{2n_1 n_s}\begin{pmatrix} -n_1^2\left(-\frac{n_1}{n_2}\right)^N - n_e n_s\left(-\frac{n_2}{n_1}\right)^N & -n_1^2\left(-\frac{n_1}{n_2}\right)^N + n_e n_s\left(-\frac{n_2}{n_1}\right)^N \\ n_1^2\left(-\frac{n_1}{n_2}\right)^N - n_e n_s\left(-\frac{n_2}{n_1}\right)^N & n_1^2\left(-\frac{n_1}{n_2}\right)^N + n_e n_s\left(-\frac{n_2}{n_1}\right)^N \end{pmatrix}. \tag{A.6}$$

The reflection and transmission coefficients follow from Eq. 2.36

$$r_{\mathrm{DBR}} = \frac{-n_1^{2N+2} + n_e n_s n_2^{2N}}{n_1^{2N+2} + n_e n_s n_2^{2N}}, \tag{A.7}$$

$$t_{\mathrm{DBR}} = \frac{2i(-1)^N n_s n_1^{N+1} n_2^N}{n_1^{2N+2} + n_e n_s n_2^{2N}}. \tag{A.8}$$

We recall that if $n_1 > (n_2, n_e, n_s)$, and assuming lossless layers (negligible imaginary part of the complex refractive index), then $r_{\mathrm{DBR}} = -|r_{\mathrm{DBR}}|$ and $t_{\mathrm{DBR}} = i(-1)^N |t_{\mathrm{DBR}}|$.

A.2 Different notations for the amplitude coefficients

There are different ways in the literature to define the transmission amplitude coefficient through an interface (Fresnel coefficients). Most books and literature (Refs. [78, 85, 86, 89], to cite some) take the one we used here: $t_{01} = 2n_0/(n_0 + n_1)$, which results in the real field amplitudes. In that case, the transmission power coefficient $\mathcal{T}_i$ has to be scaled by the refractive index in both media with respect to $|t_{01}|$, $\mathcal{T}_i = n_1|t_{01}|^2/n_0$, so that energy conservation holds, $\mathcal{R}_i + \mathcal{T}_i = 1$. One can define the transmission amplitude coefficient in a way that it directly gives the right power values, but a "scaled" field amplitude. This is the convention employed in *Lasers* from Siegman [77], who defines

$$t_{01} = \frac{2\sqrt{n_0 n_1}}{n_0 + n_1}. \tag{A.9}$$

This results in field amplitudes which are "not real" but scaled by a refractive index factor. The advantage of this method is that one can compute directly the power transmission coefficient as $\mathcal{T}_i = |t_{01}|^2$. The reflection coefficient is defined in the same way in both cases.

B

Experimental calibrations

To perform some of our experiments, we have to change the sample's position, the cavity length or the probe laser's frequency – or a combination of some of them at the same time. This is done by sending electrical signals to the piezos composing the positioners stack, the cavity piezos or the piezo controlling the laser's internal cavity. It is therefore necessary to understand how these electrical signals are transformed into displacement or, when it applies, frequency detuning. This appendix summarizes the calibrations and procedures used to perform those transformations. In the main text, we have also highlighted how important it is to know the absolute transmission and reflected powers. The measurement of those quantities is also affected by the finite sampling rate of the used oscilloscopes. This adds an extra calibration step to our measurements of the optomechanical couplings (Section 5.1), which is also described in this appendix.

B.1 Cavity's piezo scan to frequency conversion

The voltage sent to the shear piezos hosting the fiber mirrors creates a shear strain in the piezo material. The deformation of the piezo element basically translates into a displacement of their top surfaces, where the fiber mirrors are glued. We scan the cavity length by sending a ramp waveform generated by an arbitrary waveform generator (AWG) to the piezos. The voltage sent to the piezos is converted into frequency detuning – which is equivalent to cavity length change through Eq. 2.74 – by modulating the lock laser with the EOM. Figure B.1a shows the cavity transmission (blue) and ramp waveform (orange) traces recorded with the oscilloscope. The sidebands appear at a time difference from the lock equal to Δt_{mod}, which corresponds to ω_{mod} in the frequency space. Another time difference Δt will therefore correspond to a detuning Δ

$$\Delta = \frac{\omega_{\text{mod}}}{\Delta t_{\text{mod}}} \Delta t.$$

The equation above is used to transform the time axis into frequency detuning. Δt_{mod} depends on the amplitude of the ramp voltage sent to the piezos: the larger the amplitude, the closer the sidebands will be to the laser tone for a fixed value of ω_{mod} because the change of cavity length is larger. In our experiments we keep fixed the frequency f of the ramp waveform and only change

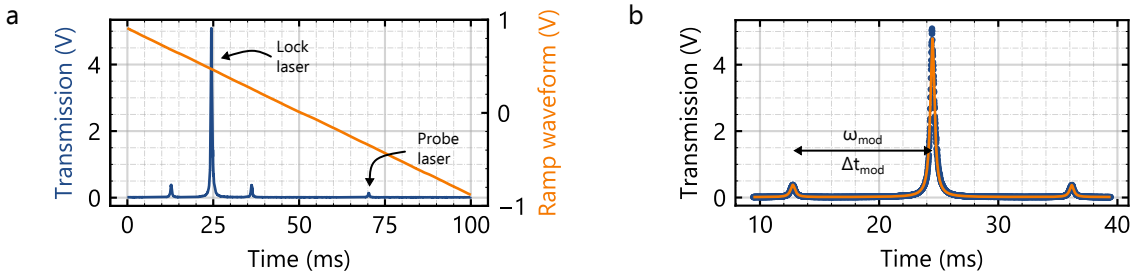

Figure B.1: Frequency calibration with EOM sidebands. (a) Oscilloscope time trace of the cavity transmission (blue) and ramp waveform sent to the piezos (orange). The lock laser has two sidebands, modulated with the EOM, at $\omega_{\mathrm{mod}}/2\pi = 530\,\mathrm{MHz}$. (b) Close up around the lock laser's peak. The transmission is fitted to three Lorentzian functions (orange line).

its peak amplitude V_{p}. The maximum detuning for a particular V_{p} will therefore be:

$$\Delta(V_{\mathrm{p}}) = \frac{\omega_{\mathrm{mod}}}{\Delta t_{\mathrm{mod}}(V_{\mathrm{p}})}\frac{T}{2},$$

where $T = 1/f$ is the ramp period. Measuring $\Delta(V_{\mathrm{p}})$ allows us to extract the voltage to frequency conversion, so that we do not need to run a frequency calibration for every measurement. The results of $\Delta(V_{\mathrm{p}})$ are presented in the next two sections for two distinct cases. First, when the waveform is sent to just one piezo, which is relevant for the cavity characterization measurements and dynamical backaction experiments, since we need a small detuning range. Second, when the waveform is sent to both fiber piezos after amplification with the HV amplifier. The latter is relevant when performing the measurement of the optomechanical couplings, where we need a larger detuning range. We recall that the calibrations are piezo dependent, and consequently need to be redone for each of them.

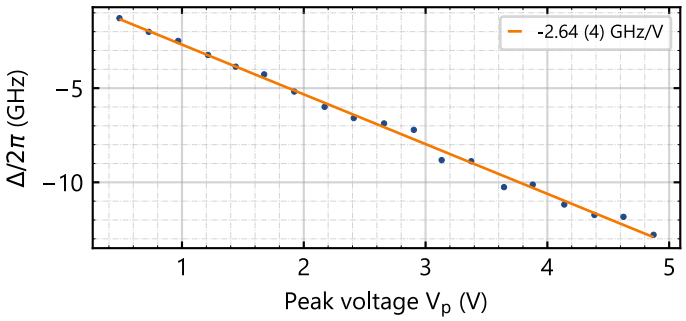

Figure B.2: Maximum frequency detuning vs. scan amplitude (peak voltage). Only the SM fiber mirror is scanned and without HV amplification. The data is fit to a linear regression (orange line) yielding a voltage to frequency conversion factor of $-2.64(4)$ GHz/V.

B.1.1 Without high voltage amplification

Figure B.2 displays the maximum detuning as a function of the peak voltage V_{p} of the ramp waveform used to scan the piezo of the SM fiber of cavity C8. The waveform is not amplified with

the HV amplifier. The voltage to frequency conversion is linear and gives a conversion factor of $-2.64(4)$ GHz/V. Consequently, we can scan up to $\Delta/2\pi \simeq -26$ GHz when we send a ramp voltage with $V_p = 10$ V to the piezo. The negative sign reflects the movement direction of the piezos. The shear piezos from this cavity (C8) are glued so that for positive voltages the cavity length increases, and therefore the frequency decreases, explaining the negative sign in the frequency detuning. We cross-check the calibration every time we characterize the empty cavity response, which happens every time we change the sample, and always get the same values within the error of the calibration.

B.1.2 With high voltage amplification

Figure B.3 depicts the maximum detuning as a function of the peak voltage V_p of the ramp waveform generated by the AWG. The ramp is used to scan the piezos of both the SM and MM fiber from cavity C8. The waveform is in this case amplified with the HV amplifier (gain of 40 V/V, see Section 3.3 for details), and sent symmetrically to both mirrors. The voltage to frequency conversion is not linear anymore due to the high voltages, which reach values up to 400 V. We fit two polynomials of second order, one for $V_p < 4$ V and another for $V_p > 4$ V, which are displayed in the figure. With the HV amplified signal, we get a maximum frequency detuning of $\Delta/2\pi \simeq -4.5$ THz for $V_p = 10$ V, large enough to scan more than two FSRs. We always specify the voltage V_p in terms of the output of the AWG *before* amplification because this is what we monitor and change in the experiment.

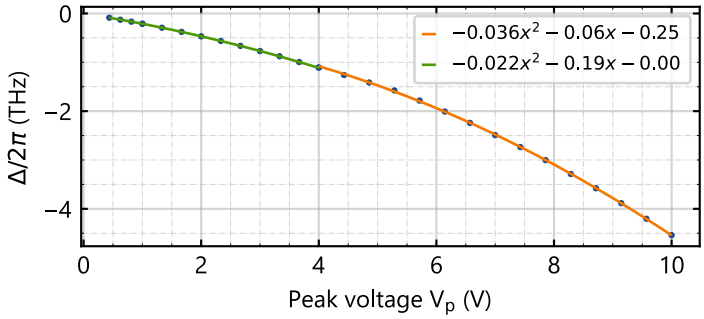

Figure B.3: Maximum frequency detuning vs. scan amplitude (peak voltage) with HV amplification. Both fiber mirrors are scanned symmetrically and the ramp waveform is amplified with the HV amplifier. The peak voltage V_p is the value at the output of the AWG *before* amplification. To obtain the voltage at the piezo one has to multiply V_p times the gain of the HV amplifier (40 V/V). The data is fit to two polynomials of second order, one for $V_p < 4$ V (green line) and another for $V_p > 4$ V (orange line). The polynomials are shown in the graph's label.

B.2 Oscilloscope finite sampling rate

Oscilloscopes have a finite sample rate. For large detuning scans, like the ones needed for the optomechanical coupling measurements (Section 5.1), the sample rate is not large enough to be able to resolve the complete height of the transmission peak. This effectively behaves as having a detector whose gain depends on the magnitude of the piezo scan, in other words, the voltage

sent to the piezos. We need to know this dependence to correctly extract the cavity linewidth from the maximum transmission (Eq. 5.1). To that end, we measure the height of a transmission peak as a function of the peak voltage of the ramp waveform sent to the piezos, with and without HV amplification. We do this for different oscilloscope's number of samples. The frequency of the ramp waveform is the same in all cases and equal to 9 Hz.

Figure B.3a displays such a measurement when we scan only one fiber mirror and without HV amplification, for 10^5 (orange, 100 kS) and 10^6 (blue, 1 MS) samples. There is a slight deviation for peak voltages above $V_p = 5$ V only in the 100 kS case . The normalized transmission reaches a minimum value of 0.95 at $V_p = 10$ V. The 1 MS case is not affected by the finite sampling rate. Figure B.3b shows the same measurement but for the case when the ramp waveform is amplified by the HV amplifier and sent to both fiber mirrors symmetrically. In this case, the finite sampling rate affects the traces very strongly. Already at $V_p = 0.2$ V the 100 kS trace decreases to 0.9 and it is at half of its value for $V_p = 1$ V. The 1 MS traces reach 0.9 at $V_p \sim 1.2$ V and 0.5 at $V_p \sim 5$ V. The gray solid lines are splines to smooth the data in both graphs. We treat this effect as having a detector whose gain depends on the amplitude of the scan, and use the splines to extract its value.

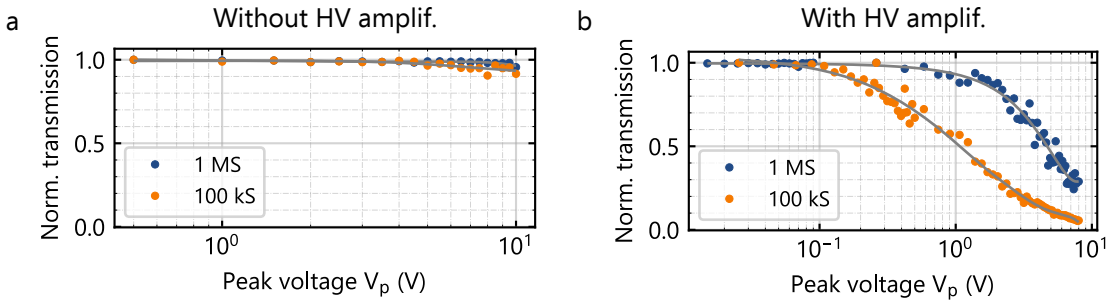

Figure B.4: Normalized transmission vs. peak voltage for different oscilloscope's number of samples. (a) Situation where only one fiber mirror is scanned with the ramp waveform of amplitude V_p. The normalized transmission is calculated by dividing the maximum of the cavity's transmission peak by its value when it is not affected by the oscilloscope's finite sampling rate. (b) Same as (a) but both fiber mirrors are scanned symmetrically with the waveform and with HV amplification.

B.3 Sample's position

The sample's position along the cavity axis (z direction) is changed by sending a DC voltage to the Smaract positioners' piezos involved in the z direction movement. We do not use the positioners' step function but the scan one. The voltage is sent internally by the MCS2 controller – we do not use an external voltage source – and can have values from 0 V to 100 V.

The z position of the sample depends consequently on the voltage $z(V)$. To find $z(V)$ we can either use the fringes of the 1310 nm interferometer or the dependence of the cavity detuning Δ_{cav} on the sample's position (Fig. 5.5a). Both of them are periodic on the sample's position with a period of $\lambda/2$ and can be fit to Eq. 4.1 to extract its Fourier component. Figure B.5a shows the cavity detuning (blue dots) of the measurements in Figure 5.5a as an example. The distance between the detuning's oscillations is larger for voltages smaller than 50 V than for voltages larger than that

value. This indicates that the piezos do not move linearly with respect to the applied voltage. We fit the data to the function

$$\Delta_{\mathrm{cav}}(V) = A\sin\left(\frac{2\pi}{(\lambda/2)}z(V) + \phi_0\right) + B, \tag{B.1}$$

which is equivalent to Eq. 4.1. Here, A, B and ϕ_0 are fit parameters. We tried different dependencies of $z(V)$ on the voltage and found that a polynomial of second order gives the best result: $z(V) = c_1 V + c_2 V^2$; c_1 and c_2 are consequently extracted from the fit as well. The regression is shown as an orange line in Figure B.5. From the fit we extract values for the coefficients, $c_1 = 21.8(3)\,\mathrm{nm/V}$ and $c_2 = 0.171(2)\,\mathrm{nm/V^2}$. Figure B.5b displays the function $z(V) = c_1 V + c_2 V^2$. Overall, the positioners move around a maximum of 3 µm.

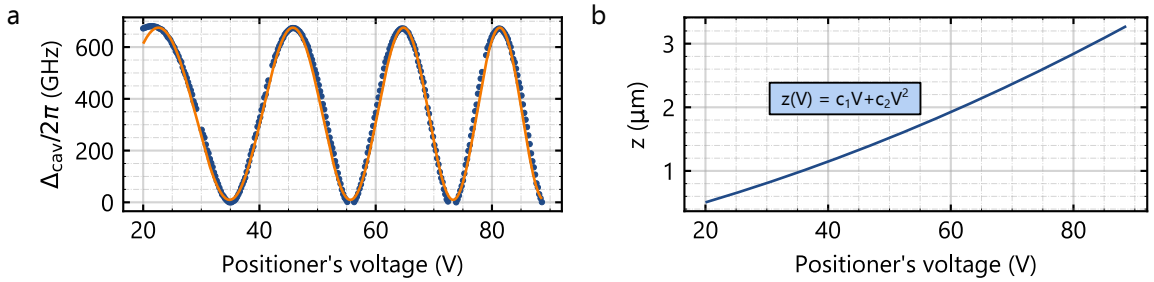

Figure B.5: Positioners' voltage to displacement conversion. (a) Cavity frequency detuning (data from Fig. 5.5a) versus positioners' voltage in the z axis. The data is fitted to Eq. B.1 (orange line) to extract the voltage dependency of the positioners' z-movement $z(V)$. (b) Positioners' displacement in the z direction vs. voltage $z(V) = c_1 V + c_2 V^2$, with the values for c_1 and c_2 extracted form the fit in (a).

B.4 Probe laser's frequency detuning

We can tune the frequency ω_{p} of the probe laser (Newport, Velocity TLB-6728) by sending a DC voltage V_{tlb} to one of its internal piezo electric transducers, that changes the position of one of the mirrors inside the laser's head. The laser's controller accepts DC voltages between −3 V and 3 V. To measure the voltage to frequency detuning conversion, we proceed as follows. We scan the cavity length by sending a ramp waveform to the SM fiber and send the light from both the probe and lock laser, and look at the cavity transmission. We observe a time trace similar to the one in Figure B.3a, where we can clearly identify the lock laser's and probe laser's transmission peak. Then, we sweep the DC voltage V_{tlb} N-times with voltages between −3 V and 3 V. The DC voltage sent to the TLB laser is generated using a Stahl-Electronics BS14 voltage source. At each voltage we record a time trace. During the data processing, we transform the time axis of the scope traces to frequency by using the procedure described in Appendix B.1. Then, we use the frequency of the lock laser as reference, which is fixed during the measurement, and measure the shift in frequency of the probe laser Δ as a function of V_{tlb} with respect to its value when $V_{\mathrm{tlb}} = 0\,\mathrm{V}$, $\Delta(V_{\mathrm{tlb}}) = \omega_{\mathrm{p}}(V_{\mathrm{tlb}}) - \omega_{\mathrm{p}}(0)$. Figure B.6 shows the results of the measurement. The frequency depends linearly on the DC voltage. We fit a linear regression yielding a voltage to frequency conversion factor of −275(20) MHz/V. The data deviates slightly from the linear trend for voltages below −2.8 V, but we always measure with voltages between −2.5 V and 2.5 V. This calibration is used to

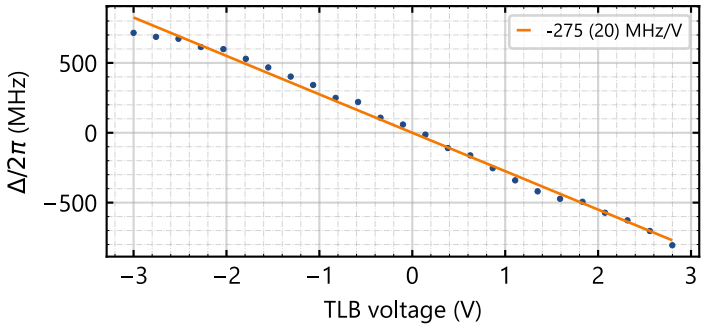

Figure B.6: Probe laser's voltage to frequency detuning conversion. The data (blue dots) follow a linear trend. The orange line is a linear fit which yields the voltage to frequency detuning conversion factor of −275(20) MHz/V.

convert the DC voltage into probe frequency detuning Δ, in other words, to generate the x-axis of the graphs in the dynamical backaction measurements (see Fig. 5.9 for example), without the offset from the cavity resonance ω_{cav}.

Acknowledgements

There are many people to whom I am grateful for their help, support and guidance over the five years and a half that this PhD project lasted. It's impossible to compress all of them in just a few paragraphs, but I hope these lines reflect my gratitude to most of them.

First of all, I want to thank you, Eva, for giving me the opportunity to work by your side and learn from you. I also want to express my deepest gratitude for your trust and constant support. Besides all the exciting science, I have learned from you the importance of being precise and paying attention to details. You have always encouraged my science-slammy side as well, and found the time to listen to my talks and to give me feedback, making them always better.

The next big thanks goes to Susi. As a Harry Potter fan, I can clearly tell that you are definitely a witch. I cannot count the times I have seen you doing your "Susi magic", saving us from administrative disasters without even asking for it. I can submit my thesis because of you. But specially thanks for always knocking on the door, with a great smile and full of energy, asking how my day went and sharing your stories with me. I can't wait to meet Shon the sheep!

It is my pleasure to acknowledge Prof. David Hunger for lending us his setup at KIT to create the fiber mirrors and for sharing his knowledge on fiber-based cavities with us. From his team, I want to specially thank Jonathan Körber who helped us during the machining of the fiber mirrors. I also want to thank Prof. Gary Steele, who let me visit his group for a month to learn the dry-transfer technique of van der Waals materials. From the Steele lab, I specially thank Felix Schmidt for teaching Khannan and me all we needed to know to get started in the 2D materials business.

I would like to acknowledge the other members of the cavity optomechanics team, with whom I've worked at different parts of this project. I want to specially thank Felix Rochau, who started working with the membrane-in-the-middle experiment before me. Without your help I would not have succeeded with this PhD. Thanks for having the patience for listening and answering my questions, for sharing with me what you learned, and for the times we spent in the lab. From you I have learned the endurance and resilience that is needed to work in this project – which was, at the end, the most important part :-). In the same spirit I have to thank Alexendre Brieussel, who also participated in the initial version of the cavity optomechanics experiment. You made me dive into the soldiering station as soon as I arrived and got me out of my comfort zone. From you I learned that sometimes in experimental science the best way to do something is to stop thinking and just try things around. The last member of the cavity optomechanics team is Ralf Messmer, who pushed the hBN part of this project a great deal. I hope you learned from me as much as I learned from you. It was always a pleasure working with you. With your questions, you made me understand better things that I thought I already knew, and discover new ones that I didn't. By the way, I cannot count the times I had to correct *aN optomechanical system* while writing this thesis.

Avishek, although you didn't work in the cavity optomechanics project you have been a men-

tor to me in the last year of this adventure. You were always eager to discuss the physics of our experiment, making the work presented in this thesis better in many ways. Thank you for everything.

My special thanks go to Louis Kukk. You helped me designing and constructing many of the mechanical parts of the setup even when I was in Munich already, always with a smile and patiently listening to my poor German when I dared to try. I had a lot of fun with you in all our joint projects. I will never forget the day I arrived to my office and found our newly built vacuum chamber wrapped in red present paper on top of my desk!

I also have to thank Matthias Hagner for organizing and maintaining the Nanolab from the University of Konstanz in such a great way.

I am forever grateful to the past members of the Nanomechanics group and the new ones from NQS: Katrin, Maximilian, Juliane, Felix, Ralf, Alex, Jana, Tuan, Yannick, Louis, Avi, Berke (Demiralp), Berke (Yalaman), Maira, Jonny, Ahmed, Philipp, Felix and Lukas. I enjoyed every moment we spent together: the wine festivals in Konstanz, Dönele essen, Christmas parties, cake breaks, LN2 ice cream sessions, BBQs, covid-Zoom coffee breaks and many more. Yannick, Tuan and Jana, my PhD and office P945 companions, thanks for these fantastic years together!

I want to thank my team of editors that helped improving this document: Eva, Jana and Avishek. But specially thanks to the two executive editors, Carmen and Yannick, who proof-read the whole document from A to Z, spotting my mistakes and providing constructive feedback.

Every German thesis needs a German abstract. I thank my official translator, Philipp, for improving the terrible version I gave him. Moreover, thank you for being in the office on an Easter Friday and giving me the code that solved the nonlinear equation of the circulating photon number in just 2 minutes.

During my PhD I had the great pleasure to belong to the OMT Marie-Curie training network. I thank my OMT friends and fellows, Giuseppe, Paolo, Alberto, Mohammad, Edouard, Sampo, Simon, Byoung-moo, Tasnimul, Mohamed, Corentin, Khannan, Tirth, Jossein and Charles for all the time we spent together in conferences and outside them. Specially thank you, Antonella, for organizing and coordinating such a wonderful experience. It was, for me, one of the best parts of my PhD. Also thank you for encouraging my science communication side, supporting me in my projects and for our inspiring conversations. I'm looking forward to our next encounter.

I was lucky to meet Ines Rodrigues during my short visit to the Steele lab. Ines, thank you for the fun times in Delft and for the ones at all the conferences we met after! You made me feel at home for the few months I was in Delft when I knew basically nobody. It's not so common to meet scientists that are great at their jobs and at the same time so positive and generous. I hope to see you sooner than later.

I was able to finish this thesis thanks to all the friends and family that supported me through this sometimes complicated journey. Thank you Domi and Georgia, for being such valuable friends and for the countless times I spent at your place in Zurich (which were, indeed, too many). Car, de mica en mica, s'omple la pica, y aquí estamos 8 años después de conocernos en Lausanne. Muchas gracias por acogerme en tu casa tantísimas veces, compartir conmigo tus amigas y amigos y por todos los momentos que hemos pasado juntas estos años. Gracias a mis amigos del Erasmus,

Andrew, Alba, Alejandro, Car, Andrés y Alberto, por todas las risas y el boost de energía que me han dado para seguir cada vez que nos hemos visto. A mis amigas en Granada, Juli, Pau, Mire, Ana, Tere, Elena, Zabi y Alba, por todos los años que llevamos ya juntas.

I want to thank my friends in Munich, the Key Alliance, for the wonderful times in this new city. Particularly Andy and Rich, who kept reminding me that there is sun outside the "bunker" of the lab with their jokes and our evenings together.

To my chosen family in Konstanz: Samu, Juls, Jule, Yannick and Sophia. Samu, you have been my big brother and confidant, and I couldn't have asked for a better person to spend the lock-down at our place in Am Briel. Muchas gracias Cariño. Juls and Jule, my mermaids, every Tuesday and Thursday I was looking forward to practice time in the Halle with you. You helped me escape from the lab – and other things – when I most needed it. You were my greatest support in Konstanz and I will always be grateful for that. Yannick and Sophia, well, what to say. I cannot make a list of all the things I am thankful for, it will just take too long. I am so happy to have met you and share countless memories with you. I can't wait to play Binokel in person again, of course with my chuleta, and be able to start a new set of entries in your guest book – it has simply been too long! And don't forget: Granada is waiting for you.

Yannick, here again, words fall short to express you my gratitude. You have shared with me the worst and best moments in the lab and you are in all my good memories at the Nanomechanics group in Konstanz and at NQS. Thank you for being my cinqueterre and vias ferratas partner, my office mate and sharing with me the love for coding. I leave NQS with a PhD and a best friend.

Carmen, no tengo palabras para agradecerte todo lo que has hecho por mi este magnífico año. Si he sobrevivido estos meses ha sido gracias a ti. Has compartido conmigo los mejores momentos del doctorado. De hecho, quizás hayan sido los mejores porque estabas tú a mi lado. Cuento los días para nuestra próxima aventura juntas.

And finally, I want to thank my parents and my sister. Este camino hubiese sido completamente distinto sin vuestro apoyo. A mi hermana, por crecer y seguir creciendo conmigo, compartiendo cada momento, cada risa y cada lágrima. A mis padres, por ser los cimientos de lo que mi hermana y yo somos ahora. Gracias por vuestro amor incondicional y por el incalculable esfuerzo que habéis puesto en darnos a las dos la oportunidad de escoger nuestro propio camino. Por enseñarnos la importancia de la empatía y de luchar por lo que se cree justo. Y, sobre todo, por siempre creer en nosotras incluso cuando nosotras no lo hacíamos. Esta tesis va dedicada a vosotros tres desde lo más profundo de mi corazón.

Garching,

19.04.2023

Bibliography

[1] I. Sánchez Arribas, T. Taniguchi, K. Watanabe, and E. M. Weig, "Radiation Pressure Backaction on a Hexagonal Boron Nitride Nanomechanical Resonator", Nano Lett. **23**, 6301–6307 (2023) (cit. on pp. v, 51, 65, 69, 75, 83, 97).

[2] J. Kepler, *De cometis libelli tres.* (Typis Andreae Apergiri, 1619) (cit. on p. 1).

[3] J. C. Maxwell, *A Treatise on Electricity and Magnetism, Vol. 2: Volume 2*, 2nd edition (Dover Publications Inc., New York, June 1954) (cit. on p. 1).

[4] A. G. Bartoli, *Sopra i movimenti prodotti dalla luce e dal calore* (Le Monnier, Italy, 1876) (cit. on p. 1).

[5] P. Lebedew, "Untersuchungen über die Druckkräfte des Lichtes", Annalen der Physik **311**, 433–458 (1901) (cit. on p. 1).

[6] E. F. Nichols and G. F. Hull, "A Preliminary Communication on the Pressure of Heat and Light Radiation", Phys. Rev. (Series I) **13**, 307–320 (1901) (cit. on p. 1).

[7] E. F. Nichols and G. F. Hull, "The Pressure Due to Radiation. (Second Paper.)", Phys. Rev. (Series I) **17**, 26–50 (1903) (cit. on p. 1).

[8] A. Golsen, "Über eine neue Messung des Strahlungsdrucks", Annalen der Physik **378**, 624–642 (1924) (cit. on p. 1).

[9] M. Bell and S. E. Green, "On radiometer action and the pressure of radiation", Proc. Phys. Soc. **45**, 320 (1933) (cit. on p. 1).

[10] A. L. Schawlow and C. H. Townes, "Infrared and Optical Masers", Phys. Rev. **112**, 1940–1949 (1958) (cit. on p. 1).

[11] A. Ashkin and J. M. Dziedzic, "Optical Trapping and Manipulation of Viruses and Bacteria", Science **235**, 1517–1520 (1987) (cit. on p. 1).

[12] M. D. Wang, H. Yin, R. Landick, J. Gelles, and S. M. Block, "Stretching DNA with optical tweezers", Biophysical Journal **72**, 1335–1346 (1997) (cit. on p. 1).

[13] A. Ashkin, "Acceleration and Trapping of Particles by Radiation Pressure", Phys. Rev. Lett. **24**, 156–159 (1970) (cit. on p. 1).

[14] G. Vulpetti, *Solar Sails* (Springer, New York, 2015) (cit. on p. 1).

[15] V. B. Braginsky and A. B. Manukin, "Ponderomotive Effects of Electromagnetic Radiation", Soviet Journal of Experimental and Theoretical Physics **25**, 653 (1967) (cit. on p. 2).

[16] V. B. Braginsky, A. B. Manukin, and M. Y. Tikhonov, "Investigation of Dissipative Ponderomotive Effects of Electromagnetic Radiation", Soviet Journal of Experimental and Theoretical Physics **31**, 829 (1970) (cit. on p. 2).

[17] M. Aspelmeyer, T. J. Kippenberg, and F. Marquardt, "Cavity optomechanics", Rev. Mod. Phys. **86**, 1391–1452 (2014) (cit. on pp. 2, 5, 24, 28, 29, 93, 97).

[18] M. Aspelmeyer, T. J. Kippenberg, and F. Marquardt, *Cavity Optomechanics* (Springer Berlin Heidelberg, 2014) (cit. on pp. 2, 5, 24, 28, 97).

[19] E. Gavartin, P. Verlot, and T. J. Kippenberg, "A hybrid on-chip optomechanical transducer for ultrasensitive force measurements", Nature Nanotech **7**, 509–514 (2012) (cit. on p. 2).

[20] F. Fogliano, B. Besga, A. Reigue, P. Heringlake, L. Mercier de Lépinay, C. Vaneph, J. Reichel, B. Pigeau, and O. Arcizet, "Mapping the Cavity Optomechanical Interaction with Subwavelength-Sized Ultrasensitive Nanomechanical Force Sensors", Phys. Rev. X **11**, 021009 (2021) (cit. on pp. 2, 40).

[21] P. E. Allain, L. Schwab, C. Mismer, M. Gely, E. Mairiaux, M. Hermouet, B. Walter, G. Leo, S. Hentz, M. Faucher, G. Jourdan, B. Legrand, and I. Favero, "Optomechanical resonating probe for very high frequency sensing of atomic forces", Nanoscale **12**, 2939–2945 (2020) (cit. on p. 2).

[22] R. Fischer, D. P. McNally, C. Reetz, G. G. T. Assumpção, T. Knief, Y. Lin, and C. A. Regal, "Spin detection with a micromechanical trampoline: towards magnetic resonance microscopy harnessing cavity optomechanics", New J. Phys. **21**, 043049 (2019) (cit. on p. 2).

[23] F. Liu, S. Alaie, Z. C. Leseman, and M. Hossein-Zadeh, "Sub-pg mass sensing and measurement with an optomechanical oscillator", Opt. Express, OE **21**, 19555–19567 (2013) (cit. on p. 2).

[24] A. G. Krause, M. Winger, T. D. Blasius, Q. Lin, and O. Painter, "A high-resolution microchip optomechanical accelerometer", Nature Photon **6**, 768–772 (2012) (cit. on p. 2).

[25] G. Anetsberger, O. Arcizet, Q. P. Unterreithmeier, R. Rivière, A. Schliesser, E. M. Weig, J. P. Kotthaus, and T. J. Kippenberg, "Near-field cavity optomechanics with nanomechanical oscillators", Nature Physics **5**, 909–914 (2009) (cit. on pp. 2, 84).

[26] J. D. Teufel, T. Donner, M. A. Castellanos-Beltran, J. W. Harlow, and K. W. Lehnert, "Nanomechanical motion measured with an imprecision below that at the standard quantum limit", Nature Nanotech **4**, 820–823 (2009) (cit. on p. 2).

[27] D. Mason, J. Chen, M. Rossi, Y. Tsaturyan, and A. Schliesser, "Continuous force and displacement measurement below the standard quantum limit", Nat. Phys. **15**, 745–749 (2019) (cit. on p. 2).

[28] I. Galinskiy, Y. Tsaturyan, M. Parniak, and E. S. Polzik, "Phonon counting thermometry of an ultracoherent membrane resonator near its motional ground state", Optica, OPTICA **7**, 718–725 (2020) (cit. on p. 2).

[29] B. M. Brubaker, J. M. Kindem, M. D. Urmey, S. Mittal, R. D. Delaney, P. S. Burns, M. R. Vissers, K. W. Lehnert, and C. A. Regal, "Optomechanical Ground-State Cooling in a Continuous and Efficient Electro-Optic Transducer", Phys. Rev. X **12**, 021062 (2022) (cit. on p. 2).

[30] J. Chen, M. Rossi, D. Mason, and A. Schliesser, "Entanglement of propagating optical modes via a mechanical interface", Nat Commun **11**, 943 (2020) (cit. on p. 2).

[31] S. P. Kumar and M. B. Plenio, "Quantum-optical tests of Planck-scale physics", Phys. Rev. A **97**, 063855 (2018) (cit. on p. 2).

[32] M. Bonaldi, A. Borrielli, A. Chowdhury, G. Di Giuseppe, W. Li, N. Malossi, F. Marino, B. Morana, R. Natali, P. Piergentili, G. A. Prodi, P. M. Sarro, E. Serra, P. Vezio, D. Vitali, and F. Marin, "Probing quantum gravity effects with quantum mechanical oscillators", Eur. Phys. J. D **74**, 178 (2020) (cit. on p. 2).

[33] Y. Ma, S. L. Danilishin, C. Zhao, H. Miao, W. Z. Korth, Y. Chen, R. L. Ward, and D. G. Blair, "Narrowing the Filter-Cavity Bandwidth in Gravitational-Wave Detectors via Optomechanical Interaction", Phys. Rev. Lett. **113**, 151102 (2014) (cit. on p. 2).

[34] J. Qin, C. Zhao, Y. Ma, X. Chen, L. Ju, and D. G. Blair, "Classical demonstration of frequency-dependent noise ellipse rotation using optomechanically induced transparency", Phys. Rev. A **89**, 041802 (2014) (cit. on p. 2).

[35] M. A. Page, M. Goryachev, H. Miao, Y. Chen, Y. Ma, D. Mason, M. Rossi, C. D. Blair, L. Ju, D. G. Blair, A. Schliesser, M. E. Tobar, and C. Zhao, "Gravitational wave detectors with broadband high frequency sensitivity", Commun Phys **4**, 1–8 (2021) (cit. on p. 2).

[36] A. P. Higginbotham, P. S. Burns, M. D. Urmey, R. W. Peterson, N. S. Kampel, B. M. Brubaker, G. Smith, K. W. Lehnert, and C. A. Regal, "Harnessing electro-optic correlations in an efficient mechanical converter", Nature Phys **14**, 1038–1042 (2018) (cit. on p. 2).

[37] I. Favero and K. Karrai, "Cavity cooling of a nanomechanical resonator by light scattering", New J. Phys. **10**, 095006 (2008) (cit. on p. 2).

[38] S. Stapfner, L. Ost, D. Hunger, J. Reichel, I. Favero, and E. M. Weig, "Cavity-enhanced optical detection of carbon nanotube Brownian motion", Appl. Phys. Lett. **102**, 151910 (2013) (cit. on p. 2).

[39] A. W. Barnard, M. Zhang, G. S. Wiederhecker, M. Lipson, and P. L. McEuen, "Real-time vibrations of a carbon nanotube", Nature **566**, 89–93 (2019) (cit. on p. 2).

[40] S. Blien, P. Steger, N. Hüttner, R. Graaf, and A. K. Hüttel, "Quantum capacitance mediated carbon nanotube optomechanics", Nat Commun **11**, 1636 (2020) (cit. on p. 2).

[41] X. Song, M. Oksanen, J. Li, P. J. Hakonen, and M. A. Sillanpää, "Graphene Optomechanics Realized at Microwave Frequencies", Phys. Rev. Lett. **113**, 027404 (2014) (cit. on p. 2).

[42] V. Singh, S. J. Bosman, B. H. Schneider, Y. M. Blanter, A. Castellanos-Gomez, and G. A. Steele, "Optomechanical coupling between a multilayer graphene mechanical resonator and a superconducting microwave cavity", Nature Nanotech **9**, 820–824 (2014) (cit. on p. 2).

[43] P. Weber, J. Güttinger, A. Noury, J. Vergara-Cruz, and A. Bachtold, "Force sensitivity of multilayer graphene optomechanical devices", Nat Commun **7**, 12496 (2016) (cit. on p. 2).

[44] I. A. D. Williamson, S. H. Mousavi, and Z. Wang, "Large Cavity-Optomechanical Coupling with Graphene at Infrared and Terahertz Frequencies", ACS Photonics **3**, 2353–2361 (2016) (cit. on p. 2).

[45] X.-Q. Zheng, J. Lee, and P. X.-L. Feng, "Hexagonal boron nitride nanomechanical resonators with spatially visualized motion", Microsyst Nanoeng **3**, 1–8 (2017) (cit. on pp. 2, 65, 72, 73, 98).

[46] A. Falin, Q. Cai, E. J. G. Santos, D. Scullion, D. Qian, R. Zhang, Z. Yang, S. Huang, K. Watanabe, T. Taniguchi, M. R. Barnett, Y. Chen, R. S. Ruoff, and L. H. Li, "Mechanical properties of atomically thin boron nitride and the role of interlayer interactions", Nat Commun **8**, 15815 (2017) (cit. on p. 2).

[47] C. Elbadawi, T. T. Tran, M. Kolíbal, T. Šikola, J. Scott, Q. Cai, L. H. Li, T. Taniguchi, K. Watanabe, M. Toth, I. Aharonovich, and C. Lobo, "Electron beam directed etching of hexagonal boron nitride", Nanoscale **8**, 16182–16186 (2016) (cit. on p. 2).

[48] S. Kim, J. E. Fröch, J. Christian, M. Straw, J. Bishop, D. Totonjian, K. Watanabe, T. Taniguchi, M. Toth, and I. Aharonovich, "Photonic crystal cavities from hexagonal boron nitride", Nat Commun **9**, 2623 (2018) (cit. on p. 2).

[49] G. Cassabois, P. Valvin, and B. Gil, "Hexagonal boron nitride is an indirect bandgap semiconductor", Nature Photon **10**, 262–266 (2016) (cit. on p. 3).

[50] R. A. Barton, I. R. Storch, V. P. Adiga, R. Sakakibara, B. R. Cipriany, B. Ilic, S. P. Wang, P. Ong, P. L. McEuen, J. M. Parpia, and H. G. Craighead, "Photothermal Self-Oscillation and Laser Cooling of Graphene Optomechanical Systems", Nano Lett. **12**, 4681–4686 (2012) (cit. on p. 3).

[51] H. M. Meyer, M. Breyer, and M. Köhl, "Monolayer graphene as dissipative membrane in an optical resonator", Appl. Phys. B **122**, 290 (2016) (cit. on p. 3).

[52] N. Morell, S. Tepsic, A. Reserbat-Plantey, A. Cepellotti, M. Manca, I. Epstein, A. Isacsson, X. Marie, F. Mauri, and A. Bachtold, "Optomechanical Measurement of Thermal Transport in Two-Dimensional MoSe2 Lattices", Nano Lett. **19**, 3143–3150 (2019) (cit. on p. 3).

[53] A. Kubanek, "Coherent Quantum Emitters in Hexagonal Boron Nitride", Advanced Quantum Technologies **5**, 2200009 (2022) (cit. on p. 3).

[54] I. Aharonovich, J.-P. Tetienne, and M. Toth, "Quantum Emitters in Hexagonal Boron Nitride", Nano Lett. **22**, 9227–9235 (2022) (cit. on p. 3).

[55] M. Kianinia, B. Regan, S. A. Tawfik, T. T. Tran, M. J. Ford, I. Aharonovich, and M. Toth, "Robust Solid-State Quantum System Operating at 800 K", ACS Photonics **4**, 768–773 (2017) (cit. on p. 3).

[56] G. Grosso, H. Moon, B. Lienhard, S. Ali, D. K. Efetov, M. M. Furchi, P. Jarillo-Herrero, M. J. Ford, I. Aharonovich, and D. Englund, "Tunable and high-purity room temperature single-photon emission from atomic defects in hexagonal boron nitride", Nature Communications **8**, 705 (2017) (cit. on p. 3).

[57] S. Li, J.-P. Chou, A. Hu, M. B. Plenio, P. Udvarhelyi, G. Thiering, M. Abdi, and A. Gali, "Giant shift upon strain on the fluorescence spectrum of VNNB color centers in h-BN", npj Quantum Inf **6**, 1–7 (2020) (cit. on pp. 3, 99).

[58] G. Noh, D. Choi, J.-H. Kim, D.-G. Im, Y.-H. Kim, H. Seo, and J. Lee, "Stark Tuning of Single-Photon Emitters in Hexagonal Boron Nitride", Nano Lett. **18**, 4710–4715 (2018) (cit. on p. 3).

[59] N. Nikolay, N. Mendelson, N. Sadzak, F. Böhm, T. T. Tran, B. Sontheimer, I. Aharonovich, and O. Benson, "Very Large and Reversible Stark-Shift Tuning of Single Emitters in Layered Hexagonal Boron Nitride", Phys. Rev. Appl. **11**, 041001 (2019) (cit. on p. 3).

[60] A. Gottscholl, M. Kianinia, V. Soltamov, S. Orlinskii, G. Mamin, C. Bradac, C. Kasper, K. Krambrock, A. Sperlich, M. Toth, I. Aharonovich, and V. Dyakonov, "Initialization and read-out of intrinsic spin defects in a van der Waals crystal at room temperature", Nat. Mater. **19**, 540–545 (2020) (cit. on p. 3).

[61] X. Gao, S. Pandey, M. Kianinia, J. Ahn, P. Ju, I. Aharonovich, N. Shivaram, and T. Li, "Femtosecond Laser Writing of Spin Defects in Hexagonal Boron Nitride", ACS Photonics **8**, 994–1000 (2021) (cit. on p. 3).

[62] H. L. Stern, Q. Gu, J. Jarman, S. Eizagirre Barker, N. Mendelson, D. Chugh, S. Schott, H. H. Tan, H. Sirringhaus, I. Aharonovich, and M. Atatüre, "Room-temperature optically detected magnetic resonance of single defects in hexagonal boron nitride", Nat Commun **13**, 618 (2022) (cit. on p. 3).

[63] A. Gottscholl, M. Diez, V. Soltamov, C. Kasper, A. Sperlich, M. Kianinia, C. Bradac, I. Aharonovich, and V. Dyakonov, "Room temperature coherent control of spin defects in hexagonal boron nitride", Science Advances **7**, eabf3630 (2021) (cit. on pp. 3, 99).

[64] X. Gao, B. Jiang, A. E. Llacsahuanga Allcca, K. Shen, M. A. Sadi, A. B. Solanki, P. Ju, Z. Xu, P. Upadhyaya, Y. P. Chen, S. A. Bhave, and T. Li, "High-Contrast Plasmonic-Enhanced Shallow Spin

Defects in Hexagonal Boron Nitride for Quantum Sensing", Nano Lett. **21**, 7708–7714 (2021) (cit. on p. 3).

[65] A. Gottscholl, M. Diez, V. Soltamov, C. Kasper, D. Krauße, A. Sperlich, M. Kianinia, C. Bradac, I. Aharonovich, and V. Dyakonov, "Spin defects in hBN as promising temperature, pressure and magnetic field quantum sensors", Nat Commun **12**, 1–8 (2021) (cit. on p. 3).

[66] X. Lyu, Q. Tan, L. Wu, C. Zhang, Z. Zhang, Z. Mu, J. Zúñiga-Pérez, H. Cai, and W. Gao, "Strain Quantum Sensing with Spin Defects in Hexagonal Boron Nitride", Nano Lett. **22**, 6553–6559 (2022) (cit. on p. 3).

[67] A. A. Clerk, K. W. Lehnert, P. Bertet, J. R. Petta, and Y. Nakamura, "Hybrid quantum systems with circuit quantum electrodynamics", Nat. Phys. **16**, 257–267 (2020) (cit. on p. 3).

[68] H. Wang and I. Lekavicius, "Coupling spins to nanomechanical resonators: Toward quantum spin-mechanics", Appl. Phys. Lett. **117**, 230501 (2020) (cit. on pp. 3, 30).

[69] M. Abdi, M.-J. Hwang, M. Aghtar, and M. B. Plenio, "Spin-Mechanical Scheme with Color Centers in Hexagonal Boron Nitride Membranes", Phys. Rev. Lett. **119**, 233602 (2017) (cit. on p. 3).

[70] C. Qian, V. Villafañe, M. Schalk, G. V. Astakhov, U. Kentsch, M. Helm, P. Soubelet, A. V. Stier, and J. J. Finley, "Emitter-Optomechanical Interaction in Ultra-High-Q hBN Nanocavities", arXiv: 2210.00150, [cond-mat.mes–hall] (2023) (cit. on p. 3).

[71] P. K. Shandilya, D. P. Lake, M. J. Mitchell, D. D. Sukachev, and P. E. Barclay, "Optomechanical interface between telecom photons and spin quantum memory", Nat. Phys. **17**, 1420–1425 (2021) (cit. on pp. 3, 30).

[72] J. D. Thompson, B. M. Zwickl, A. M. Jayich, F. Marquardt, S. M. Girvin, and J. G. E. Harris, "Strong dispersive coupling of a high-finesse cavity to a micromechanical membrane", Nature **452**, 72–75 (2008) (cit. on pp. 3, 24, 84).

[73] G. R. Cooper and C. D. McGillem, *Probabilistic Methods of Signal and System Analysis*, Third Edition (Oxford University Press, 1998) (cit. on pp. 5–7).

[74] R. A. Witte, *Spectrum and network measurements*, 2nd edition, Electromagnetic Waves (SciTech Publishing, 2014) (cit. on p. 5).

[75] B. D. Hauer, C. Doolin, K. S. D. Beach, and J. P. Davis, "A general procedure for thermomechanical calibration of nano/micro-mechanical resonators", Annals of Physics **339**, 181–207 (2013) (cit. on pp. 5, 8, 10–12, 69, 72).

[76] S. Schmid, L. G. Villanueva, and M. L. Roukes, *Fundamentals of Nanomechanical Resonators* (Springer Cham, 2016) (cit. on pp. 5, 8, 13, 71).

[77] A. E. Siegman, *Lasers* (Univ. Science Books, 1986) (cit. on pp. 5, 19, 20, 34, 104).

[78] E. Hecht, *Optics*, 5ed, global edition (Pearson, 2017) (cit. on pp. 5, 15, 17, 104).

[79] A. A. Clerk, M. H. Devoret, S. M. Girvin, F. Marquardt, and R. J. Schoelkopf, "Introduction to quantum noise, measurement, and amplification", Rev. Mod. Phys. **82**, 1155–1208 (2010) (cit. on pp. 5, 9).

[80] A. V. Oppenheim, *Signals and systems*, 2nd ed. (Prentice-Hall, 1997) (cit. on p. 6).

[81] M. Imboden and P. Mohanty, "Dissipation in nanoelectromechanical systems", Physics Reports, Dissipation in Nano-Electromechanical Systems **534**, 89–146 (2014) (cit. on p. 8).

[82] P. R. Saulson, "Thermal noise in mechanical experiments", Phys. Rev. D **42**, 2437–2445 (1990) (cit. on pp. 8, 9).

[83] H. B. Callen and T. A. Welton, "Irreversibility and Generalized Noise", Phys. Rev. **83**, 34–40 (1951) (cit. on p. 9).

[84] A. N. Cleland, *Foundations of Nanomechanics* (Springer Berlin Heidelberg, 2003) (cit. on p. 9).

[85] C. C. Katsidis and D. I. Siapkas, "General transfer-matrix method for optical multilayer systems with coherent, partially coherent, and incoherent interference", Appl. Opt. **41**, 3978 (2002) (cit. on pp. 14, 104).

[86] S. J. Byrnes, "Multilayer optical calculations", arXiv:1603.02720 [physics] (2019) (cit. on pp. 14, 104).

[87] A. M. Jayich, J. C. Sankey, B. M. Zwickl, C. Yang, J. D. Thompson, S. M. Girvin, A. A. Clerk, F. Marquardt, and J. G. E. Harris, "Dispersive optomechanics: a membrane inside a cavity", New J. Phys. **10**, 095008 (2008) (cit. on pp. 16, 24).

[88] Y. Rah, Y. Jin, S. Kim, and K. Yu, "Optical analysis of the refractive index and birefringence of hexagonal boron nitride from the visible to near-infrared", Opt. Lett., OL **44**, 3797–3800 (2019) (cit. on pp. 16, 66, 81).

[89] L. Novotny and B. Hecht, *Principles of Nano-Optics* (Cambridge University Press, 2012) (cit. on pp. 17, 25, 58, 104).

[90] H. Pfeifer, L. Ratschbacher, J. Gallego, C. Saavedra, A. Faßbender, A. von Haaren, W. Alt, S. Hofferberth, M. Köhl, S. Linden, and D. Meschede, "Achievements and perspectives of optical fiber Fabry–Perot cavities", Appl. Phys. B **128**, 29 (2022) (cit. on pp. 18, 24).

[91] V. Dumont, S. Bernard, C. Reinhardt, A. Kato, M. Ruf, and J. C. Sankey, "Flexure-tuned membrane-at-the-edge optomechanical system", Opt. Express, OE **27**, 25731–25748 (2019) (cit. on pp. 23, 30).

[92] V. B. Braginsky, Y. I. Vorontsov, and K. S. Thorne, "Quantum Nondemolition Measurements", Science **209**, 547–557 (1980) (cit. on p. 24).

[93] V. Dumont, H.-K. Lau, A. A. Clerk, and J. C. Sankey, "Asymmetry-Based Quantum Backaction Suppression in Quadratic Optomechanics", Phys. Rev. Lett. **129**, 063604 (2022) (cit. on p. 24).

[94] X. Ma, J. J. Viennot, S. Kotler, J. D. Teufel, and K. W. Lehnert, "Non-classical energy squeezing of a macroscopic mechanical oscillator", Nat. Phys. **17**, 322–326 (2021) (cit. on p. 24).

[95] N. P. Bullier, A. Pontin, and P. F. Barker, "Quadratic optomechanical cooling of a cavity-levitated nanosphere", Phys. Rev. Res. **3**, L032022 (2021) (cit. on p. 24).

[96] K. Makles, T. Antoni, A. G. Kuhn, S. Deléglise, T. Briant, P.-F. Cohadon, R. Braive, G. Beaudoin, L. Pinard, C. Michel, V. Dolique, R. Flaminio, G. Cagnoli, I. Robert-Philip, and A. Heidmann, "2D photonic-crystal optomechanical nanoresonator", Opt. Lett., OL **40**, 174–177 (2015) (cit. on p. 24).

[97] S. Bernard, C. Reinhardt, V. Dumont, Y.-A. Peter, and J. C. Sankey, "Precision resonance tuning and design of SiN photonic crystal reflectors", Opt. Lett., OL **41**, 5624–5627 (2016) (cit. on pp. 24, 63).

[98] C. Gärtner, J. P. Moura, W. Haaxman, R. A. Norte, and S. Gröblacher, "Integrated Optomechanical Arrays of Two High Reflectivity SiN Membranes", Nano Lett. **18**, 7171–7175 (2018) (cit. on p. 24).

[99] D. Hunger, T. Steinmetz, Y. Colombe, C. Deutsch, T. W. Hänsch, and J. Reichel, "A fiber Fabry–Perot cavity with high finesse", New J. Phys. **12**, 065038 (2010) (cit. on pp. 24, 34, 35, 39, 49).

[100] P. Meystre, E. M. Wright, J. D. McCullen, and E. Vignes, "Theory of radiation-pressure-driven interferometers", J. Opt. Soc. Am. B, JOSAB **2**, 1830–1840 (1985) (cit. on pp. 25, 26).

[101] A. Dorsel, J. D. McCullen, P. Meystre, E. Vignes, and H. Walther, "Optical Bistability and Mirror Confinement Induced by Radiation Pressure", Phys. Rev. Lett. **51**, 1550–1553 (1983) (cit. on p. 26).

[102] K.-K. Ni, R. Norte, D. J. Wilson, J. D. Hood, D. E. Chang, O. Painter, and H. J. Kimble, "Enhancement of Mechanical Q Factors by Optical Trapping", Phys. Rev. Lett. **108**, 214302 (2012) (cit. on p. 27).

[103] F. Marquardt, J. G. E. Harris, and S. M. Girvin, "Dynamical Multistability Induced by Radiation Pressure in High-Finesse Micromechanical Optical Cavities", Phys. Rev. Lett. **96**, 103901 (2006) (cit. on p. 28).

[104] J. D. Teufel, T. Donner, D. Li, J. W. Harlow, M. S. Allman, K. Cicak, A. J. Sirois, J. D. Whittaker, K. W. Lehnert, and R. W. Simmonds, "Sideband cooling of micromechanical motion to the quantum ground state", Nature **475**, 359–363 (2011) (cit. on p. 29).

[105] J. Chan, T. P. M. Alegre, A. H. Safavi-Naeini, J. T. Hill, A. Krause, S. Gröblacher, M. Aspelmeyer, and O. Painter, "Laser cooling of a nanomechanical oscillator into its quantum ground state", Nature **478**, 89–92 (2011) (cit. on p. 29).

[106] M. Rossi, D. Mason, J. Chen, Y. Tsaturyan, and A. Schliesser, "Measurement-based quantum control of mechanical motion", Nature **563**, 53–58 (2018) (cit. on p. 29).

[107] F. Elste, S. M. Girvin, and A. A. Clerk, "Quantum Noise Interference and Backaction Cooling in Cavity Nanomechanics", Phys. Rev. Lett. **102**, 207209 (2009) (cit. on pp. 29, 30).

[108] A. Sawadsky, H. Kaufer, R. M. Nia, S. P. Tarabrin, F. Y. Khalili, K. Hammerer, and R. Schnabel, "Observation of Generalized Optomechanical Coupling and Cooling on Cavity Resonance", Phys. Rev. Lett. **114**, 043601 (2015) (cit. on p. 29).

[109] C. Biancofiore, M. Karuza, M. Galassi, R. Natali, P. Tombesi, G. Di Giuseppe, and D. Vitali, "Quantum dynamics of an optical cavity coupled to a thin semitransparent membrane: Effect of membrane absorption", Phys. Rev. A **84**, 033814 (2011) (cit. on pp. 30, 31).

[110] J. C. Sankey, C. Yang, B. M. Zwickl, A. M. Jayich, and J. G. E. Harris, "Strong and tunable nonlinear optomechanical coupling in a low-loss system", Nature Physics **6**, 707–712 (2010) (cit. on pp. 30, 79, 81).

[111] S. Stapfner, "Investigation of nanomechanical resonators in a micro cavity for optomechanics experiments", PhD thesis (Ludwig-Maximilians-Universität München, 2016) (cit. on pp. 33, 40, 53).

[112] F. Rochau, "Cavity nano-optomechanics inside a fiber-based micro-cavity", PhD thesis (University of Konstanz, 2021) (cit. on pp. 33, 40, 43, 53, 68, 76, 79, 83).

[113] M. Trupke, E. A. Hinds, S. Eriksson, E. A. Curtis, Z. Moktadir, E. Kukharenka, and M. Kraft, "Microfabricated high-finesse optical cavity with open access and small volume", Appl. Phys. Lett. **87**, 211106 (2005) (cit. on p. 34).

[114] P. Treutlein, T. Steinmetz, Y. Colombe, B. Lev, P. Hommelhoff, J. Reichel, M. Greiner, O. Mandel, A. Widera, T. Rom, I. Bloch, and T. Hänsch, "Quantum information processing in optical lattices and magnetic microtraps", Fortschritte der Physik **54**, 702–718 (2006) (cit. on p. 34).

[115]T. Steinmetz, Y. Colombe, D. Hunger, T. W. Hänsch, A. Balocchi, R. J. Warburton, and J. Reichel, "Stable fiber-based Fabry-Pérot cavity", Appl. Phys. Lett. **89**, 111110 (2006) (cit. on p. 34).

[116]Y. Colombe, T. Steinmetz, G. Dubois, F. Linke, D. Hunger, and J. Reichel, "Strong atom–field coupling for Bose–Einstein condensates in an optical cavity on a chip", Nature **450**, 272–276 (2007) (cit. on p. 34).

[117]K. Wasa, I. Kanno, and H. Kotera, *Handbook of Sputter Deposition Technology: Fundamentals and Applications for Functional Thin Films, Nano-Materials and MEMS*, Second Edition (William Andrew, 2012) (cit. on p. 34).

[118]W. B. Joyce and B. C. DeLoach, "Alignment of Gaussian beams", Appl. Opt. **23**, 4187 (1984) (cit. on pp. 35, 51).

[119]J. Körber, "Herstellung und Charakterisierung optimierter Oberflächen für optische Mikrospiegel mit Multi-Puls CO2 Laserbearbeitung", BA thesis (Karlsruher Institut für Technologie, 2017) (cit. on p. 35).

[120]D. Hunger, C. Deutsch, R. J. Barbour, R. J. Warburton, and J. Reichel, "Laser micro-fabrication of concave, low-roughness features in silica", AIP Advances **2**, 012119 (2012) (cit. on p. 35).

[121]L. Gao, F. Lemarchand, and M. Lequime, "Exploitation of multiple incidences spectrometric measurements for thin film reverse engineering", Opt. Express, OE **20**, 15734–15751 (2012) (cit. on p. 36).

[122]P. de Groot, "Phase Shifting Interferometry", in *Optical Measurement of Surface Topography*, edited by R. Leach (Springer, Berlin, Heidelberg, 2011), pp. 167–186 (cit. on pp. 36, 38).

[123]J. H. Bruning, D. R. Herriott, J. E. Gallagher, D. P. Rosenfeld, A. D. White, and D. J. Brangaccio, "Digital Wavefront Measuring Interferometer for Testing Optical Surfaces and Lenses", Appl. Opt., AO **13**, 2693–2703 (1974) (cit. on p. 38).

[124]M. Costantini, "A novel phase unwrapping method based on network programming", IEEE Transactions on Geoscience and Remote Sensing **36**, 813–821 (1998) (cit. on p. 38).

[125]N. E. Flowers-Jacobs, S. W. Hoch, J. C. Sankey, A. Kashkanova, A. M. Jayich, C. Deutsch, J. Reichel, and J. G. E. Harris, "Fiber-cavity-based optomechanical device", Appl. Phys. Lett. **101**, 221109 (2012) (cit. on p. 40).

[126]V. J. Sorger and R. Maiti, "Roadmap for gain-bandwidth-product enhanced photodetectors: opinion", Opt. Mater. Express, OME **10**, 2192–2200 (2020) (cit. on p. 43).

[127]J. Gallego, S. Ghosh, S. K. Alavi, W. Alt, M. Martinez-Dorantes, D. Meschede, and L. Ratschbacher, "High-finesse fiber Fabry–Perot cavities: stabilization and mode matching analysis", Appl. Phys. B **122**, 47 (2016) (cit. on p. 46).

[128]B. Brandstätter, A. McClung, K. Schüppert, B. Casabone, K. Friebe, A. Stute, P. O. Schmidt, C. Deutsch, J. Reichel, R. Blatt, and T. E. Northup, "Integrated fiber-mirror ion trap for strong ion-cavity coupling", Review of Scientific Instruments **84**, 123104 (2013) (cit. on p. 48).

[129]M. Uphoff, M. Brekenfeld, G. Rempe, and S. Ritter, "Frequency splitting of polarization eigenmodes in microscopic Fabry–Perot cavities", New J. Phys. **17**, 013053 (2015) (cit. on p. 48).

[130]H. Rehbein, J. Harms, R. Schnabel, and K. Danzmann, "Optical Transfer Functions of Kerr Nonlinear Cavities and Interferometers", Phys. Rev. Lett. **95**, 193001 (2005) (cit. on pp. 48, 93).

[131] D. Zoepfl, M. L. Juan, N. Diaz-Naufal, C. M. F. Schneider, L. F. Deeg, A. Sharafiev, A. Metelmann, and G. Kirchmair, "Kerr Enhanced Backaction Cooling in Magnetomechanics", Phys. Rev. Lett. **130**, 033601 (2023) (cit. on pp. 48, 50, 89, 92, 93, 98).

[132] K. An, B. A. Sones, C. Fang-Yen, R. R. Dasari, and M. S. Feld, "Optical bistability induced by mirror absorption: measurement of absorption coefficients at the sub-ppm level", Opt. Lett., OL **22**, 1433–1435 (1997) (cit. on p. 49).

[133] R. Lifshitz and M. C. Cross, "Nonlinear Dynamics of Nanomechanical and Micromechanical Resonators", in *Reviews of Nonlinear Dynamics and Complexity* (John Wiley & Sons, Ltd, 2008), pp. 1–52 (cit. on p. 50).

[134] D. Zöpfl, "Demonstration of nonlinear enhanced backaction cooling in microwave magnetomechanics", PhD thesis (University of Innsbruck, 2023) (cit. on p. 50).

[135] F. Rochau, I. Sánchez Arribas, A. Brieussel, S. Stapfner, D. Hunger, and E. M. Weig, "Dynamical Backaction in an Ultrahigh-Finesse Fiber-Based Microcavity", Phys. Rev. Appl. **16**, 014013 (2021) (cit. on pp. 51, 76, 79, 83, 93, 97).

[136] B. A. Boom, A. Bertolini, E. Hennes, and J. F. J. van den Brand, "Gas Damping in Capacitive MEMS Transducers in the Free Molecular Flow Regime", Sensors **21**, 2566 (2021) (cit. on p. 53).

[137] E. D. Black, "An introduction to Pound–Drever–Hall laser frequency stabilization", American Journal of Physics **69**, 79–87 (2001) (cit. on p. 58).

[138] V. J. Urick, J. D. Mckinney, and K. J. Williams, "External Intensity Modulation with Direct Detection", in *Fundamentals of microwave photonics* (John Wiley & Sons, Ltd, 2015), pp. 212–272 (cit. on p. 58).

[139] D. Jaeger, F. Fogliano, T. Ruelle, A. Lafranca, F. Braakman, and M. Poggio, "Mechanical Mode Imaging of a High-Q Hybrid hBN/Si3N4 Resonator", Nano Lett. **23**, 2016–2022 (2023) (cit. on pp. 63, 70, 72, 73, 98).

[140] D. S. Kim, S. G. Yoon, G. E. Jang, S. J. Suh, H. Kim, and D. H. Yoon, "Refractive index properties of SiN thin films and fabrication of SiN optical waveguide", J Electroceram **17**, 315–318 (2006) (cit. on p. 63).

[141] E. Serra, M. Bawaj, A. Borrielli, G. Di Giuseppe, S. Forte, N. Kralj, N. Malossi, L. Marconi, F. Marin, F. Marino, B. Morana, R. Natali, G. Pandraud, A. Pontin, G. A. Prodi, M. Rossi, P. M. Sarro, D. Vitali, and M. Bonaldi, "Microfabrication of large-area circular high-stress silicon nitride membranes for optomechanical applications", AIP Advances **6**, 065004 (2016) (cit. on p. 63).

[142] Y. Tsaturyan, A. Barg, E. S. Polzik, and A. Schliesser, "Ultracoherent nanomechanical resonators via soft clamping and dissipation dilution", Nature Nanotech **12**, 776–783 (2017) (cit. on pp. 63, 98).

[143] A. Castellanos-Gomez, M. Buscema, R. Molenaar, V. Singh, L. Janssen, H. S. J. van der Zant, and G. A. Steele, "Deterministic transfer of two-dimensional materials by all-dry viscoelastic stamping", 2D Mater. **1**, 011002 (2014) (cit. on p. 64).

[144] D. Davidovikj, J. J. Slim, S. J. Cartamil-Bueno, H. S. J. van der Zant, P. G. Steeneken, and W. J. Venstra, "Visualizing the Motion of Graphene Nanodrums", Nano Lett. **16**, 2768–2773 (2016) (cit. on pp. 65, 73).

[145] R. Messmer, "2D materials for Cavity Optomechanics", MA thesis (University of Konstanz, May 2020) (cit. on pp. 67, 70).

[146] J. S. Huber, "Cavity-nano-optomechanics with SiN-resonators in a Fabry-Pérot-cavity", MA thesis (University of Konstanz, 2017) (cit. on pp. 67, 70).

[147] J.-F. Li, P. Moses, and D. Viehland, "Simple, high-resolution interferometer for the measurement of frequency-dependent complex piezoelectric responses in ferroelectric ceramics", Review of Scientific Instruments **66**, 215–221 (1995) (cit. on p. 69).

[148] R. Yimnirun, P. J. Moses, R. J. M. Jr, and R. E. Newnham, "A single-beam interferometer with sub-ångström displacement resolution for electrostriction measurements", Meas. Sci. Technol. **14**, 766 (2003) (cit. on p. 69).

[149] K. G. Libbrecht and E. D. Black, "A basic Michelson laser interferometer for the undergraduate teaching laboratory demonstrating picometer sensitivity", American Journal of Physics **83**, 409–417 (2015) (cit. on p. 69).

[150] A. Barg, Y. Tsaturyan, E. Belhage, W. H. P. Nielsen, C. B. Møller, and A. Schliesser, "Measuring and imaging nanomechanical motion with laser light", Appl. Phys. B **123**, 8 (2016) (cit. on p. 69).

[151] C. Schwarz, B. Pigeau, L. Mercier de Lépinay, A. G. Kuhn, D. Kalita, N. Bendiab, L. Marty, V. Bouchiat, and O. Arcizet, "Deviation from the Normal Mode Expansion in a Coupled Graphene-Nanomechanical System", Phys. Rev. Appl. **6**, 064021 (2016) (cit. on p. 70).

[152] R. Singh, R. J. Nicholl, K. I. Bolotin, and S. Ghosh, "Motion Transduction with Thermo-mechanically Squeezed Graphene Resonator Modes", Nano Lett. **18**, 6719–6724 (2018) (cit. on pp. 70, 72).

[153] R. Singh, A. Sarkar, C. Guria, R. J. Nicholl, S. Chakraborty, K. I. Bolotin, and S. Ghosh, "Giant Tunable Mechanical Nonlinearity in Graphene–Silicon Nitride Hybrid Resonator", Nano Lett. **20**, 4659–4666 (2020) (cit. on pp. 70, 72).

[154] A. Lipp, K. A. Schwetz, and K. Hunold, "Hexagonal boron nitride: Fabrication, properties and applications", Journal of the European Ceramic Society **5**, 3–9 (1989) (cit. on pp. 70, 72).

[155] L. Boldrin, F. Scarpa, R. Chowdhury, and S. Adhikari, "Effective mechanical properties of hexagonal boron nitride nanosheets", Nanotechnology **22**, 505702 (2011) (cit. on p. 70).

[156] R. A. Barton, B. Ilic, A. M. van der Zande, W. S. Whitney, P. L. McEuen, J. M. Parpia, and H. G. Craighead, "High, Size-Dependent Quality Factor in an Array of Graphene Mechanical Resonators", Nano Lett. **11**, 1232–1236 (2011) (cit. on p. 73).

[157] S. Afyouni Akbari, V. Ghafarinia, T. Larsen, M. M. Parmar, and L. G. Villanueva, "Large Suspended Monolayer and Bilayer Graphene Membranes with Diameter up to 750 Mm", Sci Rep **10**, 6426 (2020) (cit. on p. 73).

[158] P. K. Shandilya, J. E. Fröch, M. Mitchell, D. P. Lake, S. Kim, M. Toth, B. Behera, C. Healey, I. Aharonovich, and P. E. Barclay, "Hexagonal Boron Nitride Cavity Optomechanics", Nano Lett. **19**, 1343–1350 (2019) (cit. on p. 75).

[159] Y. Liu, Y. Wang, X.-Q. Zheng, Q. Lin, and P. X.-L. Feng, "Nanomechanical and Optomechanical Coupling in Silicon Carbide / Hexagonal Boron Nitride Hybrid Resonator", in 2021 21st International Conference on Solid-State Sensors, Actuators and Microsystems (Transducers) (June 2021), pp. 541–544 (cit. on p. 75).

[160] M. Karuza, M. Galassi, C. Biancofiore, C. Molinelli, R. Natali, P. Tombesi, G. D. Giuseppe, and D. Vitali, "Tunable linear and quadratic optomechanical coupling for a tilted membrane within an optical cavity: theory and experiment", J. Opt. **15**, 025704 (2012) (cit. on pp. 76, 81).

[161] J. Steinlechner, C. Krüger, I. W. Martin, A. Bell, J. Hough, H. Kaufer, S. Rowan, R. Schnabel, and S. Steinlechner, "Optical absorption of silicon nitride membranes at 1064 nm and at 1550 nm", Phys. Rev. D **96**, 022007 (2017) (cit. on pp. 79, 83).

[162] S.-Y. Lee, T.-Y. Jeong, S. Jung, and K.-J. Yee, "Refractive Index Dispersion of Hexagonal Boron Nitride in the Visible and Near-Infrared", physica status solidi (b) **256**, 1800417 (2019) (cit. on p. 81).

[163] M. L. Gorodetksy, A. Schliesser, G. Anetsberger, S. Deleglise, and T. J. Kippenberg, "Determination of the vacuum optomechanical coupling rate using frequency noise calibration", Opt. Express, OE **18**, 23236–23246 (2010) (cit. on p. 84).

[164] A. B. Shkarin, N. E. Flowers-Jacobs, S. W. Hoch, A. D. Kashkanova, C. Deutsch, J. Reichel, and J. G. E. Harris, "Optically Mediated Hybridization between Two Mechanical Modes", Phys. Rev. Lett. **112**, 013602 (2014) (cit. on p. 89).

[165] A. A. Popkova, I. M. Antropov, J. E. Fröch, S. Kim, I. Aharonovich, V. O. Bessonov, A. S. Solntsev, and A. A. Fedyanin, "Optical Third-Harmonic Generation in Hexagonal Boron Nitride Thin Films", ACS Photonics **8**, 824–831 (2021) (cit. on p. 93).

[166] N. V. Proscia, Z. Shotan, H. Jayakumar, P. Reddy, C. Cohen, M. Dollar, A. Alkauskas, M. Doherty, C. A. Meriles, and V. M. Menon, "Near-deterministic activation of room-temperature quantum emitters in hexagonal boron nitride", Optica, OPTICA **5**, 1128–1134 (2018) (cit. on p. 99).

[167] A. Branny, S. Kumar, R. Proux, and B. D. Gerardot, "Deterministic strain-induced arrays of quantum emitters in a two-dimensional semiconductor", Nat Commun **8**, 15053 (2017) (cit. on p. 99).

[168] H. Kim, J. S. Moon, G. Noh, J. Lee, and J.-H. Kim, "Position and Frequency Control of Strain-Induced Quantum Emitters in WSe2 Monolayers", Nano Lett. **19**, 7534–7539 (2019) (cit. on p. 99).

[169] P. Hernández López, S. Heeg, C. Schattauer, S. Kovalchuk, A. Kumar, D. J. Bock, J. N. Kirchhof, B. Höfer, K. Greben, D. Yagodkin, L. Linhart, F. Libisch, and K. I. Bolotin, "Strain control of hybridization between dark and localized excitons in a 2D semiconductor", Nat Commun **13**, 7691 (2022) (cit. on p. 99).

[170] M. Förg, L. Colombier, R. K. Patel, J. Lindlau, A. D. Mohite, H. Yamaguchi, M. M. Glazov, D. Hunger, and A. Högele, "Cavity-control of interlayer excitons in van der Waals heterostructures", Nat Commun **10**, 3697 (2019) (cit. on p. 99).

[171] C. Gebhardt, M. Förg, H. Yamaguchi, I. Bilgin, A. D. Mohite, C. Gies, M. Florian, M. Hartmann, T. W. Hänsch, A. Högele, and D. Hunger, "Polariton hyperspectral imaging of two-dimensional semiconductor crystals", Sci Rep **9**, 13756 (2019) (cit. on p. 99).